

Taming the quantum noise

How quantum metrology can expand the reach
of gravitational-wave observatories

Dissertation

zur Erlangung des Doktorgrades

an der Fakultät für Mathematik, Informatik und Naturwissenschaften

Fachbereich Physik

der Universität Hamburg

vorgelegt von

Mikhail Korobko

Hamburg

2020

Gutachter/innen der Dissertation:	Prof. Dr. Ludwig Mathey Prof. Dr. Roman Schnabel
Zusammensetzung der Prüfungskommission:	Prof. Dr. Peter Schmelcher Prof. Dr. Ludwig Mathey Prof. Dr. Henning Moritz Prof. Dr. Oliver Gerberding Prof. Dr. Roman Schnabel
Vorsitzende/r der Prüfungskommission:	Prof. Dr. Peter Schmelcher
Datum der Disputation:	12.06.2020
Vorsitzender Fach-Promotionsausschusses PHYSIK:	Prof. Dr. Günter Hans Walter Sigl
Leiter des Fachbereichs PHYSIK:	Prof. Dr. Wolfgang Hansen
Dekan der Fakultät MIN:	Prof. Dr. Heinrich Graener

List of Figures

2.1	Effect of a gravitational wave on a ring of free-falling masses, positioned orthogonally to the propagation direction of the GW.	16
2.2	Michelson interferometer as gravitational-wave detector.	17
2.3	The sensitivity of the detector as a function of the position of the source on the sky for circularly polarized GWs.	18
2.4	Noise contributions to the total design sensitivity of Advanced LIGO in terms of sensitivity to gravitational-wave strain $h(t)$	21
2.5	Sensitivity of the GW detector enhanced with squeezed light.	28
3.1	Effect of squeezing on quantum noise in the electromagnetic field for coherent field, phase squeezed state and amplitude squeezed state.	46
3.2	Schematic of a homodyne detector.	52
3.3	Sensing the motion of a mirror with light.	55
3.4	Comparison of effects of variational readout and frequency-dependent squeezing on quantum noise in GW detectors.	60
3.5	Optical cavity with a movable end mirror.	61
3.6	Setup for measuring laser amplitude noise.	68
3.7	Setup for measuring laser phase noise.	70
3.8	The effect of path length imbalance in a Mach-Zehnder interferometer on the phase noise of the laser.	72
3.9	Compensation of the phase delay in the signal cavity with an additional cavity in the local oscillator path.	73
3.10	Effect compensating the phase delay in signal cavity.	75
3.11	Schematic diagram of a setup for generating conditional frequency-dependent squeezing with EPR-entangled fields.	77
3.12	Example of conditional frequency-dependent squeezing through Einstein–Podolsky–Rosen entanglement	81

4.1	The concept of a quantum speedmeter.	84
4.2	Comparison between the total noise spectral densities of the speed- meter and position meter.	88
4.3	Optomechanical ring cavity.	89
4.4	Resonance structure of the ring cavity.	94
4.5	Displacement sensitivity of the ring cavity on the position and velocity output ports.	107
4.6	A path towards ring-cavity-based GW detector.	109
4.7	Simplified setup of a ring-cavity experiment	114
4.8	The optomechanical ring-cavity experiment with a membrane in the laboratory.	115
4.9	Simulation of resonances of the higher order TEM modes in the ring cavity.	116
4.10	Measurement of the ring-cavity linewidth and the mode splitting of the ring cavity with membrane.	117
4.11	Spectral density of noise and membrane motion.	120
4.12	Ringdown measurement of the quality factor of the membrane's fundamental mode.	121
4.13	The setup used for measuring laser amplitude noise.	123
4.14	Amplitude noise of the laser measured at frequencies of interest for the experiment.	124
4.15	Transfer function for the laser frequency noise in different cases . .	126
4.16	Laser frequency noise measurement.	127
4.17	Measurement of the optical transfer function of the ring cavity on the position and velocity ports.	129
4.18	Theoretical calculation of the signal transfer function for an external force acting on the membrane as seen on the homodyne detector. .	130
4.19	Signal transfer function for external excitation on the membrane as seen on the homodyne detector: theory and experiment.	132
5.1	Gravitational-wave detector with paired carriers.	138
5.2	Comparison between the total noise spectral densities of the speed- meter and position meter.	144

5.3	Plots of the total quantum noise spectral density in the double antisymmetric carriers regime.	151
5.4	Plots of the total quantum noise spectral densities of the xylophone configuration with two pairs of antisymmetric carriers.	153
5.5	Total sensitivity of triple-paired detector optimized for a pulsar J0034-0534.	154
5.6	Numerically optimized quantum noise spectral densities for one and two pairs of carriers	157
6.1	Three different approaches to improving the sensitivity (noise-to-signal ratio) of a baseline detector beyond the SSBL	161
6.2	Internal squeezing approach to cavity-enhanced quantum metrology.	163
6.3	The schematic representation of the cavity system.	166
6.4	Experimental setup — The internal squeezing cavity (ISC) was resonant for both the fundamental wavelength 1550 nm and the second harmonic wavelength 775 nm used for pumping the nonlinear crystal.	172
6.5	Noise spectral densities measured on the homodyne detector	173
6.6	Example of experimental data.	174
6.7	Signal and noise measurements.	175
6.8	Beating the standard sensitivity-bandwidth limit with internal squeezing.	176
7.1	Illustration of optical loss as a cause of reduced SNR and the way to compensate for it.	185
7.2	Relative improvement from optimizing the internal squeezing compared to the case without internal squeezing.	190
7.3	Relative improvement from optimizing the internal squeezing compared to the case of internal squeezing at threshold.	193
7.4	Dependence of the gain in the signal-to-noise ratio and the reduction in the bandwidth on the detected squeeze factor.	195
7.5	Effect of optimal internal squeezing on the detection bandwidth and the sensitivity-bandwidth product.	196
8.1	Conceptual representation of the GW observatory with our quantum expander.	202

8.2	Simulated signal from a binary neutron star coalescence.	203
8.3	Quantum fields in the model of a two-cavity system.	208
8.4	Concept of the quantum expander.	212
8.5	Effect of the quantum expander on the detector's sensitivity to gravitational-wave strain $S_h(f)$, in combination with variational readout.	217
8.6	Relative contribution of different vacuum modes to the overall sensitivity of the detector at different frequencies.	218
8.7	An improvement in the sensitivity of the detector by quantum expander, relative to the detector with external squeezing injection, depending on the amount of total loss.	219
8.8	An example of sensitivity improvement in a particular design of a detector.	220
8.9	Histogram for signal-to-noise ratio of the loudest event for 100 realizations in the Monte-Carlo simulation.	222
8.10	Two tunings of the GW detector with internal squeezing.	226
9.1	Schematic diagram of a GW detector proposed here.	232
9.2	Notations of the optical fields in the system.	233
9.3	Example of tuning of the sensitivity by changing the strength of intra-cavity amplification.	235
9.4	Signal enhancement by optical spring amplification.	238
9.5	Optomechanical frequency $\Omega_-/2\pi$ as a function of squeeze angle θ for different values of parametric gain Γ relative to the threshold value Γ_{th}	239
9.6	Example of tuning of the sensitivity by changing only the squeeze angle of the intra-cavity amplifier.	241
9.7	Dynamical tuning of the sensitivity by changing only the squeeze angle of the intra-cavity amplifier.	242
A.1	Quantum fields in the model of a two-cavity system.	249
A.2	Notations of the optical fields in the system.	257

List of Tables

4.1	Comparison between the shot-noise-limited sensitivities of different detectors.	100
4.2	Main experimental parameters of the ring-cavity system.	113
5.1	Main notations used in this chapter.	139
8.1	Set of parameters of the proposed detector.	216
A.1	Values of Γ , β , and θ which minimize function (A.122)	264

Abstract

The dawn of gravitational-wave astronomy has begun in 2015 with the historic detection of a binary black hole merger [1]. Several more detections followed in the years after [2]. Among them, the detectors observed the inspiral of a neutron star binary. This merger was also observed in a broad spectrum of electromagnetic counterparts [3, 4]. This multi-messenger observation demonstrated that gravitational-wave astronomy is invaluable for understanding the Universe [5, 6].

Current detectors, however, are able to see only a small part of binaries' inspirals. A typical signal from an inspiral of a binary neutron star appears in the detector at low frequencies a few minutes before the merger. During the inspiral, the frequency of the signal increases, faster for higher frequencies. It quickly passes through the detection band of the observatory. The merger itself and post-merger oscillations often remain inaccessible due to the reduced sensitivity of the detector to high-frequency signals. An increase in the low-frequency sensitivity will allow to detect signals significantly earlier, extracting more information about the binary. This will allow to precisely locate the source on the sky for the follow-up multi-messenger observations. An increase in the high-frequency sensitivity will give a possibility to observe the merger and post-merger signals, gaining insight into the physics of ultra-dense quantum matter.

The limitations to the sensitivity arise from quantum nature of light used to sense the displacement of mirrors caused by gravitational waves. At low frequencies, quantum fluctuations in the amplitude of the light field cause random forces on the mirrors, which mask the signal from gravitational waves. At high frequencies, quantum fluctuations in the phase of the light field cause measurement noise on the detectors. The detectors use optical cavities to enhance the signal within the bandwidth of the cavities. At frequencies outside this bandwidth the signal is getting suppressed. Signals from the binary neutron star mergers typically have frequencies outside the detection bandwidth.

In this thesis I study the fundamental limitations on the sensitivity of detectors, in the quest of a broadband observatory. I discuss a speedmeter approach to increasing the low-frequency sensitivity, and propose two ways of achieving it: with quantum-entangled light, and in a novel ring cavity topology of the detector, which I test experimentally. I further study the fundamental limits arising from the finite bandwidth of the cavities, and demonstrate experimentally how this limit can be overcome. I propose a concept of quantum expander that allows to increase the detection bandwidth by using quantum correlations, generated directly inside the detector's cavities. I investigate, how quantum correlations, controlled by internal squeezing, can help to tailor the sensitivity of the detector for the optimal performance at selected frequencies. Finally, I show that, although the benefit from application of squeezed light in metrology is limited by quantum decoherence, its impact on the sensitivity can be reduced by exploiting quantum correlations created with internal squeezing.

Quantum nature of light is a nuisance, which prevents us from seeing gravitational waves, but also a powerful tool, if properly applied. Quantum correlations hidden in the noise can be exploited for the benefit of the detectors, as I show in various scenarios throughout the thesis.

Quantum noise can be tamed, and not only in gravitational-wave detectors. All cavity-enhanced quantum metrological experiments can use quantum noise and underlying correlations as the resource for tailoring their sensitivity.

Kurzfassung

2015 begann mit der erstmaligen Beobachtung der Verschmelzung zweier schwarzer Löcher das Zeitalter der Gravitationswellenastronomie [1]. In den darauffolgenden Jahren gab es viele weitere Detektionen [2]. Unter anderem wurde das Gravitationswellensignal der Verschmelzung zweier Neutronensterne detektiert. Parallel zur Messung der Gravitationswellen wurde auch das elektromagnetische Spektrum dieses Ereignisses beobachtet [3, 4]. Diese Multi-Messenger Beobachtung hat gezeigt, dass Gravitationswellenastronomie wesentlich für das Verständnis des Universums ist [5, 6].

Aktuell kann jedoch nur eine kleine Zahl von astronomischen Ereignissen detektiert werden, denn die Signale sind typischerweise nur wenige Minuten vor der eigentlichen Verschmelzung messbar und haben dann sehr kleine Frequenzen. Solange sich die astronomischen Objekte umkreisen, erhöht sich die Signalfrequenz und zwar mit schneller werdender Rate hin zu höheren Frequenzen. Auf diese Art und Weise durchläuft das Signal schnell das Detektionsband des Gravitationswellendetektors und die eigentliche Verschmelzung sowie darauffolgende Oszillationssignale können nicht beobachtet werden, weil die Sensitivität der Detektoren bei den dafür nötigen höheren Frequenzen nicht ausreicht. Eine Erhöhung der Sensitivität bei kleinen Frequenzen würde eine frühere Detektion von Signalen ermöglichen, sodass mehr Informationen über die astronomischen Objekte gewonnen werden können. Außerdem würde die Signalquelle am Himmel präzise lokalisierbar, sodass Beobachtungen durch weitere Teleskope frühzeitig beginnen könnten. Eine höhere Sensitivität im hochfrequenten Bereich würde es ermöglichen, auch die eigentliche Verschmelzung zu beobachten sowie Signale nach der Verschmelzung zu messen. Dadurch könnten neue Erkenntnisse zur Physik von ultradichter Quantenmaterie gewonnen werden.

Limitiert wird die Sensitivität, sowohl bei hohen als auch bei niedrigen Frequenzen, durch die Quanteneigenschaften des Laserlichts, welches genutzt wird, um die relativen Positionsänderungen von Spiegeln zu messen. Diese Änderungen werden durch Gravitationswellen hervorgerufen. Bei kleinen Frequenzen sorgt die Amplitudenunschärfe des Lichts für Schwankungen des auf die Spiegel wirkenden Strahlungsdrucks, wodurch das Gravitationswellensignal überdeckt wird. Bei hohen Frequenzen koppelt durch die Phasenunschärfe des Lichts Rauschen in die Detektoren ein. In die Detektoren sind außerdem optische Resonatoren integriert, welche das Messsignal innerhalb der Resonatorbandbreite verstärken. Signale außerhalb der Bandbreite werden unterdrückt. Gravitationswellensignale von sich umkreisenden Neutronensternen haben in der Regel Frequenzen außerhalb dieser Detektionsbandbreite.

In dieser Arbeit befaße ich mich mit der Limitierung der Sensitivität der Detektoren und zeige Wege auf, diese zu verbessern. Dafür diskutiere ich einen Detektor, welcher auf einer Geschwindigkeitsmessung basiert und zeige zwei Wege auf, um die Messgenauigkeit zu steigern: Zum einen mit quantenverschränktem Licht und zum anderen mit einem Umlaufresonator, also einer neuartigen Detektortopologie. Außerdem studiere ich die Sensitivitätsbeschränkungen, welche durch die Resonatoren zur Signalverstärkung entstehen. Um diese Beschränkungen zu reduzieren, schlage ich ein neuartiges Konzept vor, bei dem quantenkorreliertes Licht direkt in den Resonatoren erzeugt wird und so die Detektionsbandbreite erhöht. Ich untersuche, wie die durch internes squeezing kontrollierten Quantenkorrelationen dabei helfen können, die Empfindlichkeit des Detektors bei ausgewählten Frequenzen zu optimieren. Dabei zeige ich, dass der Einfluss von Dekohärenz auf durch Quetschlicht optimierte Sensitivität durch die Nutzung von Quantenkorrelationen, die durch internes Squeezing erzeugt werden, reduziert werden kann.

Die Quantennatur des Lichts stellt ein fundamentales Limit für die Sensitivität der Gravitationswellendetektoren dar und verhindert die Beobachtung schwacher Signale. Sie kann aber auch als nützliches Werkzeug eingesetzt werden, um durch Quantenkorrelationen schwächste, im Rauschen versteckte Signale, sichtbar zu machen. Dies zeige ich für unterschiedliche Szenarien in dieser Arbeit.

Nicht nur die Gravitationswellenastronomie kann von diesen Ansätzen profitieren. In allen Resonator gestützten quantenmetrologischen Experimenten können Quantenkorrelationen genutzt werden, um die Messsensitivität zu verbessern.

Contents

1	Introduction	1
2	Introduction to gravitational-wave detection	13
2.1	Gravitational waves	13
2.2	How GW detectors work	15
2.3	Sensitivity and noises	20
2.4	Quantum-correlated light for GW detectors	26
2.5	Quantum limits in metrology	30
2.5.1	Simple quantum measurement model	30
2.5.2	Linear continuous measurement	32
2.5.3	Quantum Cramer-Rao bound	34
3	Basics of quantum noise in gravitational-wave detectors	39
3.1	Quantum states of light	39
3.1.1	Quantization of the electromagnetic field	39
3.1.2	Two-photon quadratures	41
3.1.3	Vacuum state	43
3.1.4	Coherent state	44
3.1.5	Squeezed state	45
3.1.6	Entangled state	48
3.1.7	Squeezed light from parametric down-conversion	49
3.2	Detection of light	50
3.2.1	Spectral densities	50
3.2.2	Balanced homodyne detection	51
3.3	Quantum-correlated light for sensing the motion of a mirror	54
3.3.1	Squeezed light	59
3.4	Optical cavity	61

3.4.1	Detuned cavity	65
3.5	Classical laser noises	67
3.5.1	Amplitude noise	68
3.5.2	Phase noise	69
3.6	Example: conditional frequency-dependent squeezing through Einstein–Podolsky–Rosen entanglement	76
4	Proof-of-principle of a ring-cavity speedmeter	83
4.1	Quantum speedmeter	85
4.2	Optomechanical ring cavity as a speedmeter	87
4.2.1	Input-output relations	90
4.2.2	Ring-cavity resonance structure	93
4.2.3	Single mode approximation	95
4.3	Full quantum noise sensitivity	98
4.3.1	Shot-noise limited sensitivity	98
4.3.2	Radiation-pressure noise	101
4.3.3	Spectrum and discussion	106
4.3.4	Towards large-scale design	107
4.4	Optomechanical coupling	108
4.5	Experimental results	111
4.5.1	Optical cavity	112
4.5.2	Membrane motion	118
4.5.3	Laser noises	122
4.5.4	Speedmeter signatures	128
4.6	Conclusion	133
5	Theoretical analysis of paired carriers for tailoring sensitivity	135
5.1	Optical spring in gravitational-wave detectors	136
5.2	Quantum noise in position meter and speedmeter	140
5.2.1	General equations for the quantum noise of a position meter	143
5.3	Multi-carrier shaping of quantum noise	145
5.3.1	Conditional measurement of a multi-channel detector . .	146
5.3.2	Speedmeter-like sensitivity in Michelson-Fabry-Perot in- terferometer	149

5.3.3	Combining multiple detectors in one	152
5.4	Discussion	155
6	First demonstration of beating the standard sensitivity-bandwidth limit with internal squeezing	159
6.1	Introduction	160
6.1.1	Energetic quantum limit	162
6.2	Theoretical calculation	165
6.2.1	Optical parametric oscillation threshold	168
6.2.2	Maximal squeeze factor inside the cavity	168
6.2.3	Single-mode approximation	169
6.3	Experimental demonstration	170
6.3.1	Experimental setup	170
6.3.2	Data analysis	177
6.4	Discussion and outlook	179
7	Analysis of compensation of quantum decoherence with internal squeezing	183
7.1	Quantum limit from decoherence	184
7.1.1	Physical picture	184
7.1.2	Computing the decoherence-induced limit	186
7.2	Optimal gain	189
7.2.1	Benefit of internal squeezing in numbers	191
7.3	Frequency dependence	194
7.3.1	Injection loss and additional amplification	197
7.4	Discussion	198
8	Proposal for quantum expansion of detection bandwidth	201
8.1	Quantum expander concept	203
8.1.1	Hamiltonian of the Quantum Expander	203
8.1.2	Input-output relations	207
8.2	The quantum expander in realistic GW detectors	214
8.2.1	Full derivation of the spectral density	214
8.2.2	Optical loss	215
8.2.3	Crystal inside the observatory	221

8.3	Astrophysical analysis	221
8.4	Different tuning of cavities in GW detectors	224
8.5	Conclusion and outlook	227
9	Theoretical investigation of an optical spring enhancement via internal squeezing	229
9.1	The optical spring in GW detectors	230
9.2	The optomechanical system	231
9.2.1	Sensing the radiation-pressure noise on input test masses	241
9.3	Summary and outlook	243
10	Conclusion and outlook	245
A	Appendix	249
A.1	Appendix: quantum expander	249
A.2	Appendix: optical spring detector	256
A.3	Appendix: paired carriers	262
A.3.1	Speedometer-like frequency dependence of the shot noise .	262
A.3.2	Sub-optimal regimes of the dual carrier interferometer . .	263
	Bibliography	267
	My publications	297
	Acknowledgments	307
	Curriculum Vitæ	309

Introduction

Gravitational waves were predicted by Einstein more than a hundred years ago [7]. For a long time they were thought to be undetectable, and even their existence was questioned. However, since the 60s it became evident that gravitational waves are not only inherent to general relativity, but must also be detectable (since they carry energy which can be coupled to detectors). There have been several approaches to detection, including interferometric, as proposed by Gerstein and Pustovoi in 1963 [8], and independently by J. Weber, and analyzed in detail by R. Weiss in 1968 [9]. Since that time scientist have been developing even more sensitive interferometers, first as small-scale test setups, and then first meters-long prototypes. Eventually it became obvious that the complexity of the interferometer capable of detecting gravitational waves goes beyond anything a small group of people can build independently. In the early 90s the international collaboration LIGO (Laser Interferometer Gravitational-Wave Observatory) [10] was established, and the construction of a kilometer-scale detector in the US had begun. Around the same time the Virgo detector in Italy [11, 12] and a smaller-scale detector GEO600 in Germany [13, 14] have been founded. These detectors were joined by a Japanese project KAGRA [15] in the early 2010s. It took another 20 years of constant progress to achieve a sufficient sensitivity of the detectors [16], until on September 14, 2015, the first gravitational-wave signal was observed [1].

After 50 years of preparations, humanity has entered the era of gravitational-wave astronomy. The gravitational-wave events are observed on a weekly basis [2], and truly multimessenger astronomy becomes possible with observations of the same event in gravitational, electromagnetic and neutrino spectrum [4]. The first 4 years of observations provided many results beyond the first direct confirmation of Einstein's theory of general relativity (GR). Scientists confirmed the speed of gravitational waves to be equal to the speed of light with a very high precision [5]

and put a bound on the mass of the hypothetical graviton particle; put constraints on the possible deviations from GR [17, 18]; learned the origin of heavy elements as coming from the kilonova events after the binary neutron star mergers [19, 20]; and measured the Hubble constant H_0 using the standard sirens independently of the cosmic distance ladder [6]. The observation of gravitational waves allowed us to narrow the parameter spaces for cosmological models [21, 22] and put bounds on the dark matter [23–27] and dark energy [28, 29] models, but at the same time raised new questions and potential routes to solving the quantum gravity riddle [30–33].

While the observations of gravitational waves have been so widely recognized and praised, bringing so many exciting discoveries in cosmology and astrophysics, the detectors' development has been no less fruitful in uncovering new science over the last decades. The GW community started new directions in research and made major contributions in: quantum measurement theory [34, 35]; quantum optomechanics [36–39]; quantum squeezed light [40–45]; frequency standards and laser stabilization techniques [46, 47]; optical cavities [48]; material science (e.g. suspensions [49–51] and optical coating [52–55]) and others. GW observations were made possible by a continuous improvement in every aspect of the detector hardware, data analysis and supporting theory, which always stayed at the cutting edge of the most advanced research for many decades.

More importantly, the detectors have not yet reached their full design sensitivity, which is expected to happen by the end of 2024 [56, 57]. Further upgrades to the current design are planned in the A+ [58] generation of the detectors, and the proposed LIGO Voyager upgrade [59]. After that the third generation of ground-based detectors is coming: the Einstein Telescope (ET) [60, 61] in Europe and the Cosmic Explorer (CE) [58, 62] in the US. Their sensitivities will bring a significant improvement to the detection rate, reaching up to multiple events per day.

Even with these high rates, there will still be room for improvements, which would be able to give us further insight into the physics of compact objects. For example, when a binary merges, the signal from the inspiral stage will stay at low frequencies for a long time: ET could be able first see the signal from binary neutron stars hours before the merger event, allowing the optical telescopes to point at the location of the expected event. Increasing the sensitivity at low

frequency even further would allow to detect the signals days or even weeks in advance, giving enough time for a precise triangulation. On the other hand, both ET or CE would have high sensitivity for the signals with frequencies up to ~ 1 kHz, which will make them not very efficient for detecting the moments of merger for the neutron stars, or any post-merger features and oscillations, which would typically be observed at higher frequency [61, 63]. Expanding the detection bandwidth to higher frequencies would allow to gather more information about the equations of state of the neutron stars, and even to glimpse at some possible deviations from GR [64].

Finally, currently the detectors are optimized for broad frequency ranges, which makes them very versatile, but less efficient for some potentially interesting signals at a specific frequency. Having an additional knob to switch the detector from the broadband operation to the narrowband would allow to observe a highly interesting signal when needed — an option that current detectors do not possess.

After the current generation, the sensitivity of GW detectors will be mainly limited by quantum noise at most of their detection frequencies [10]. There are two types of quantum noise, originating from the quantization of light used in the interferometers to sense the changes in the space-time metric disturbed by the passing gravitational waves. The first type is quantum shot noise, also called measurement noise, which arises from the fluctuations in the phase of the light as seen by photodetectors [65, 66]. The second type is quantum radiation pressure noise (QRPN) or back-action noise, which arises from the amplitude fluctuations of the light field applying random kicks to the mirrors used in the interferometer [67]. Increase in the sensitivity will come from quantum techniques deployed in the detector, which would allow to suppress or mitigate these noises.

In this thesis, I explore the various approaches to employing quantum light for pushing the quantum limits in gravitational-wave detectors. With the main goal of observing the binary mergers over a longer time and accessing the high-frequency signal from the post-merger dynamics of the formed object, I study how quantum noise can be suppressed at low, medium and high frequencies. I utilize quantum correlations in various ways to achieve a broadband observatory and tailor the sensitivity for specific signals. Since a gravitational-wave detector is one of the most precise metrological devices, the findings of this thesis are placed in a more general context of quantum measurements and metrology.

In Chapter 2, I review the basic principles of gravitational-wave detection. I discuss the concept of interferometric detectors and which noises limit the sensitivity of current detectors. I further introduce the general metrological task of linear measurements, and which limits are imposed on the sensitivity by the quantum nature of light.

In Chapter 3, I review the basics of quantum noises in optical experiments. I introduce the ways to calculate quantum noises in optomechanical devices, with the emphasis on practical application and specific examples. I discuss in more detail quantum measurements and limits. I review the basics for experimental techniques, including homodyne detection and laser noises.

In Chapter 4, I begin to introduce the path towards broadband detectors by discussing the way to avoid quantum radiation-pressure noise by measuring the speed of the test mirrors. I briefly review this concept of a quantum speedmeter, and introduce a novel optomechanical ring cavity that features both position and velocity measurements, which allows an independent comparison between the two. I describe the concept theoretically, and experimentally test some of speedmeter features. Part of the results of this chapter is published in [68]

In Chapter 5, I continue discussing the speedmeter concept, but from another point of view. I present a concept of paired carriers, where the optomechanical interaction entangles two light beams inside the detector, and enables a speedmeter-like sensitivity. This approach allows to fine-tune the sensitivity of the detector in a broadband way by combining pairs of carriers with different parameters. The results of this Chapter are published in [69].

In Chapter 6, I switch from suppressing the QRPN to the shot noise, and introduce the concept of internal squeezing in quantum metrology. In this approach squeezed light is generated directly inside one of the detector's cavities. This provides an alternative to conventional external squeezed-light injection, and serves as a new tool for tuning the detector's sensitivity. I introduce the standard sensitivity-bandwidth limit, and demonstrate experimentally, that this limit can be overcome using the internal squeezing. The results of this Chapter are published in [70].

In Chapter 7 I give a more detailed account of the benefits of internal squeezing for mitigating quantum decoherence. I give theoretical arguments for the

existence of a new decoherence-induced quantum limit, and discuss how internal squeezing is vital in achieving it.

In Chapter 8, I focus on expanding the detector's bandwidth towards high frequencies by employing both internal squeezing and the particular resonance structure of coupled cavities in the detector. I give a general quantum-optical model for the system, which allows to readily transfer the results beyond gravitational-wave detection, but also provide a theoretical derivation of a full interferometer model that includes the effects of internal squeezing, decoherence, and QRPN. I further highlight the benefits of the proposed approach by computing the improvement in the detection rate of neutron star mergers. Notably, while this quantum expander approach allows to detect more merger and post-merger signals, it does not affect the low-frequency sensitivity. Therefore the back-action evasion techniques, such as discussed in Chapters 3 and 5, could still be used, bringing all the benefits of early detection of the inspiral signal. The results of this Chapter are published in [71].

In Chapter 9, I discuss another way to use internal squeezing by changing the phase between the pump of the nonlinear crystal and the main beam. This creates an optical spring effect, which enhances the sensitivity greatly in a narrow bandwidth around a selected frequency. By adjusting the phase of the pump, this frequency can be tuned in a broad range, for dynamical tracing of the signal of interest. The results of this Chapter are published in [72].

This dynamical tracing completes the full detection cycle for my vision of the quantum-expanded detector: the signal appears early in the detector due to the reduced QRPN, which allows to pinpoint its position on the sky and to tune the electromagnetic telescopes to observe the merger. Once the signal reaches high enough frequencies, the dynamical tuning switches on, and tracks the signal in the mid-frequency range. Finally, closer to the merger point the detector is brought in the quantum-expanded mode (also by tuning the phase of the pump), which allows to observe the merger and post-merger oscillations of the formed object.

In Chapter 10, I conclude with an outlook on the use of quantum technologies for gravitational-wave detectors and quantum metrology in general, and discuss the benefits and the challenges on the way towards a truly broadband detector.

Disclaimer

Throughout the thesis I use different pronouns to describe the results. When I use “we” (as in “*we obtained the result*”), it is to acknowledge that this result was obtained in collaboration with other authors. Such results in most cases were published in peer-reviewed journals, as cited in the text. Whenever I use “I”, it is to highlight, that this opinion is only mine, and I am the only person bearing the full responsibility for any mistakes in the statements. In particular, in the chapters that are based on the published results, this distinction is made to ensure the difference between the shared opinions of the authors group, and my personal opinions. Correspondingly, such statements had not been verified or endorsed by any of my collaborators.

In some cases in a descriptive context, where no new insights are presented, I use “we”, assuming it to be “*me and the reader*”.

Glossary

Acronyms

AOM	acousto-optic modulator
AR	anti-reflective
BS	beamsplitter
CE	Cosmic Explorer
DC	direct current, used to define the 0 Hz component of a signal
EAOM	electro-optic amplitude modulator
EOM	electro-optic modulator
EPR	Einstein–Podolsky–Rosen
ET	Einstein Telescope
ETM	end test mass
FSR	free spectral range
FWHM	full-width half maximum
GR	general relativity
GW	gravitational wave
GWD	gravitational-wave detector
GWO	gravitational-wave observatory
HR	highly reflective
HWHM	half-width half maximum
ITM	input test mass
LIGO	Laser Interferometer Gravitational-wave Observatory
LO	local oscillator
MZI	Mach-Zehnder interferometer
OPA	optical parametric amplifier
PBS	polarizing beamsplitter
PD	photodiode
PDH	Pound-Drever-Hall
PPKTP	periodically poled potassium titanyl phosphate (KTP)

PR	power recycling
PRM	power recycling mirror
QCRB	quantum Cramer-Rao bound
QN	quantum noise
QRPN	quantum radiation-pressure noise
SE	signal extraction
SEM	signal extraction cavity
SHG	second harmonic generation
SNR	signal-to-noise ratio
SQL	standard quantum limit
SR	signal recycling
SRM	signal recycling mirror
SSBL	standard sensitivity-bandwidth limit
TEM	transverse electromagnetic mode
TF	transfer function
TT	transverse-traceless (gauge)

Mathematical notation

Quantity	Description
c	speed of light
\hbar	reduced Plank constants
M	mass of a mirror
L	length
$\omega, \omega_p, \omega_0$	angular frequency of light in different contexts
λ	light wavelength
$k = \omega/c$	light wave vector
$\tau = L/c$	travel time
χ	mechanical response function
R	amplitude reflectivity of a mirror
T	power reflectivity of a mirror
$\gamma = \frac{cT^2}{4L}$	half-width half-maximum of the interferometer
δ	detuning of the light field relative to resonance frequency of a cavity
$\beta = \arctan \frac{\delta}{\gamma}$	normalized detuning
\mathcal{F}	finesse of a cavity
$h(t)$	gravitational-wave strain
Ω	angular frequency of the signal audio sideband
I_c	optical power circulating in a cavity
$J = \frac{4\omega_p I_c}{MLc}$	normalized optical power
ζ	homodyne angle
e^{2r}	squeeze factor
η	optical efficiency
$\hat{a}(\omega), \hat{a}^\dagger(\omega)$	annihilation and creation operators for the mode at frequency ω
$\hat{a}^c(\Omega) = \frac{\hat{a}(\omega_0 + \Omega) + \hat{a}^\dagger(\omega_0 - \Omega)}{\sqrt{2}}$	two-photon amplitude quadrature operator
$\hat{a}^s(\Omega) = \frac{\hat{a}(\omega_0 + \Omega) - \hat{a}^\dagger(\omega_0 - \Omega)}{i\sqrt{2}}$	two-photon amplitude quadrature operator

Quantity	Description
\mathbb{I}	identity matrix
$\langle \hat{X} \rangle$	expectation value of \hat{X}
$\Delta^2 \hat{X}$	variance of \hat{X}
$\sigma_{\hat{X}}$	standard deviation of \hat{X}
\bar{X}	average value of X
$S_{xx}(\Omega)$	single-sided spectral density of value x
$S^x, S_x(\Omega)$	single-sided spectral density normalized to value x

Introduction to gravitational-wave detection

2.1 Gravitational waves

Einstein's general relativity (GR) has been extremely successful, contributing to many technological advances in communication and space exploration. The basis of GR is the idea that gravitational force is nothing else but a curvature of space-time, and this curvature is created by energy (mass and radiation). The objects traveling through space-time take the shortest path, which is a straight line in a curved space-time, but looks like the change in direction to us, when we observe e.g. a rotation of a planet around the sun.

The core of GR — Einstein's field equation — relates the metric tensor field $g_{\mu\nu}$ to the energy-momentum tensor $T_{\mu\nu}$:

$$G_{\mu\nu} \equiv R_{\mu\nu} - Rg_{\mu\nu} = \frac{8\pi}{c^4}GT_{\mu\nu}, \quad (2.1)$$

where $G_{\mu\nu}$ is the Einstein's tensor, $R_{\mu\nu}$ is the Ricci tensor, and R is the curvature scalar. This system of coupled second order nonlinear differential equations in general describes how the space-time (metric) curves in the presence of energy and mass. There is no known general solution to these equations, but a solution to many special cases exists: black holes, gravitational waves, *etc.*

Gravitational waves are small perturbations of the space-time [73, 74]. For a gravitational wave propagating in a free space, the metric $g_{\mu\nu}$ can be decomposed into a flat Minkowski metric $\eta_{\mu\nu}$ and a small perturbation $h_{\mu\nu}$:

$$g_{\mu\nu} = \eta_{\mu\nu} + h_{\mu\nu}, \quad |h_{\mu\nu}| \ll 1, \quad (2.2)$$

and with this linearisation Einstein's equation can be brought to a relatively simple form [73, 74]. In the so-called transverse-traceless (TT) gauge, the solution takes a simple form with only four components of the tensor present, and defined by the two possible polarizations $h_{+, \times}$ (plus and cross):

$$h = \begin{bmatrix} 0 & 0 & 0 & 0 \\ 0 & h_+ & h_{\times} & 0 \\ 0 & h_{\times} & -h_+ & 0 \\ 0 & 0 & 0 & 0 \end{bmatrix}. \quad (2.3)$$

In a simple case of observing a merger of a binary far away from the source, the two polarizations take the form:

$$h_+ = -\frac{2G\mu}{c^2 r} (1 + \cos^2 \iota) \left(\frac{v}{c}\right)^2 \cos 2\omega t, \quad (2.4)$$

$$h_{\times} = -\frac{2G\mu}{c^2 r} \cos \iota \left(\frac{v}{c}\right)^2 \sin 2\omega t, \quad (2.5)$$

where $\mu = m_1 m_2 / M$ is the reduced mass of the system with two masses $m_{1,2}$ and the total mass $M = m_1 + m_2$; r is the distance from the source; $v = (\omega GM)^{1/3}$ is the mean orbital speed; ω is the radial frequency of the GW; and ι is the inclination angle. This equation allows us to estimate the amplitude of the GW from a typical source. Let's consider the system GW150914 [1]: $m_1 = 35M_{\odot}$, $m_2 = 30M_{\odot}$, $r = 440 \times 3.1 \times 10^{22}$, and select a frequency of 100 Hz: the corresponding parameters are: $M = 65M_{\odot}$, $\mu = 16.15M_{\odot}$, $\omega = 628.32$, $v/c = 0.586$, and we obtain $h \approx 1.2 \times 10^{-21}$, which is close to the measured value (about 0.9×10^{-21}).

This simple calculation tells us an important fact about the GWs: they are very small in amplitude, if observed far from the source. The strain amplitude of 10^{-21} means that the relative change in distance between two test masses separated by 1 km would be on the order of 10^{-18} m. This is the main difficulty of constructing a gravitational-wave detector: it needs to be extremely sensitive.

Another feature of GWs is that they carry energy. The first confirmation of that came with the detection of the decaying orbit of a binary pulsar [75]: two compact objects rotating around each other emit gravitational waves, which carry away the energy and cause the objects to inspiral into each other. Consequently, as the distance between the objects becomes smaller, their orbital frequency increases,

and so does the GW frequency - in an accelerating manner, a so-called chirp. At the same time the amplitude of the GW would grow, carrying away more energy, up until the moment the objects merge.

The time evolution of the gravitational-wave signal is described by a more complicated equation, taking into account this decay:

$$h_+(t) = -\frac{2G\mathcal{M}}{c^2 r} \frac{1 + \cos^2 \iota}{2} \left(\frac{c^3(t_c - t)}{5G\mathcal{M}} \right)^{-\frac{1}{4}} \cos \left[2\phi_c - 2 \left(\frac{c^3(t_c - t)}{5G\mathcal{M}} \right)^{\frac{5}{8}} \right] \quad (2.6)$$

$$h_\times(t) = -\frac{2G\mathcal{M}}{c^2 r} \cos \iota \left(\frac{c^3(t_c - t)}{5G\mathcal{M}} \right)^{-\frac{1}{4}} \sin \left[2\phi_c - 2 \left(\frac{c^3(t_c - t)}{5G\mathcal{M}} \right)^{\frac{5}{8}} \right], \quad (2.7)$$

where t_c, ϕ_c are the moment and the phase of the merger, $\mathcal{M} = \mu^{3/5} M^{2/5}$ is the chirp mass.

As gravitational waves propagate, they stretch and squash the metric of the space-time in the plane (x, y) orthogonal to the direction of propagation (z) . GW are quadrupolar: for + polarization, if x is stretched, y is squashed; for \times polarization the diagonal directions are stretched, see Fig. 2.1. It is this stretching and squashing that can be detected by the interferometric detector most efficiently due to its topology.

2.2 How GW detectors work

The TT gauge is commonly used for describing gravitational waves. In this gauge the test masses remain inertial, i.e. a passing GW does not induce the displacement of the test masses, but instead changes proper distances between them. The coordinate system is changing with the GW. Therefore, this gauge cannot be easily applied for the ground-based detectors, where the coordinate system is set by various forces acting on test masses (e.g. from suspensions of test mirrors) [76].

Instead, it's convenient to use the Lorentz (Newtonian) gauge. From the point of view of the local observer in the origin of a coordinate system, in this gauge a GW acts as a tidal force that displaces the test masses [77]. The dynamics of the test masses is then defined simply by a tidal acceleration of the test mass. In

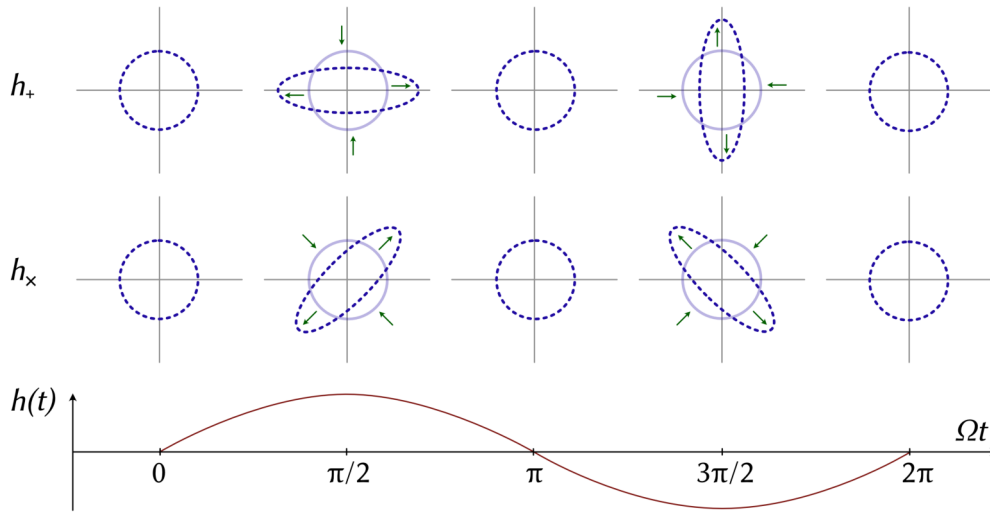


Fig. 2.1. Effect of a gravitational wave on a ring of free-falling masses, positioned orthogonally to the propagation direction of the GW. GW with frequency Ω changes metrics such that the ring is deformed, differently for two GW polarizations $h_{+, \times}$ at different phases Ωt .

the rest of this chapter I assume the GW wavelength to be large compared to the dimensions of the experiment. In this approximation the dynamics is can be described as:

$$\ddot{x} = \frac{1}{2}\ddot{h}x, \quad (2.8)$$

$$\ddot{y} = -\frac{1}{2}\ddot{h}y, \quad (2.9)$$

which can be linearized to a small perturbation in metric:

$$\delta x(t) = \frac{1}{2}h(t)x_0, \quad (2.10)$$

$$\delta y(t) = -\frac{1}{2}h(t)y_0, \quad (2.11)$$

where x_0, y_0 are the initial positions of the test mass. Notice, that the displacement is larger the larger when the initial distance from the origin is larger.

This directly suggests a way to measure the GWs by observing a displacement of the test mass relative to a reference point. This idea lies in the origin of the interferometer-based detectors. While there are multiple different ways of

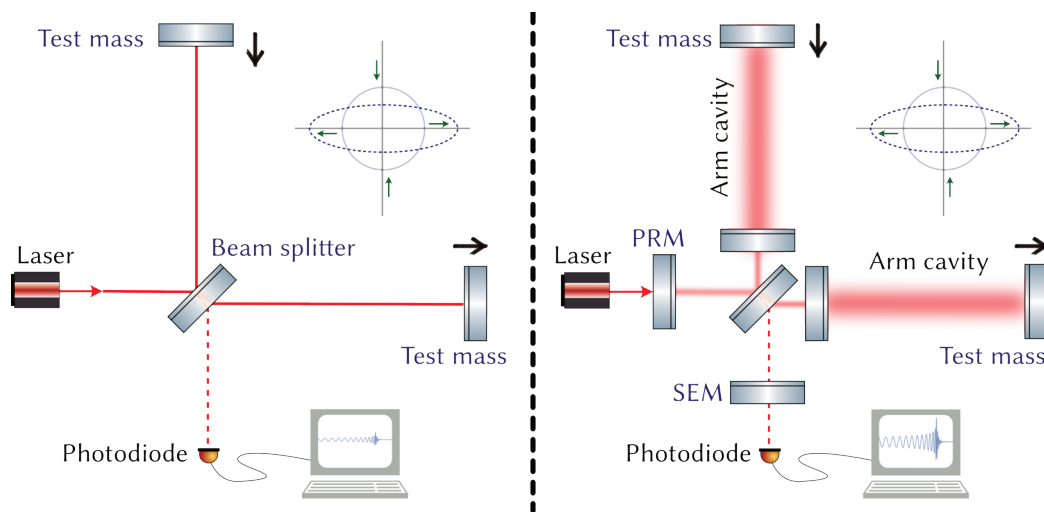


Fig. 2.2. Michelson interferometer as gravitational-wave detector. Left: a GW displaces the test masses relative to the central beamsplitter, which results in a relative change in phases of the light beams and interference observed on the photodiode. Right: cavity-enhanced detector. Arm cavities serve to enhance signal and light power. Power-recycling mirror (PRM) further enhances the light power, Signal-extraction mirror (SEM) enhances the signal independently on the light power.

observing the GWs: bar detectors [78], pulsar timing arrays [79], and more exotic Bose-Einstein-condensate [80] or atom interferometer [81] detectors. The most successful topology to date is the optical interferometer.

The idea is to use light itself as a clock for measuring the changes in the distance between the origin and the test mass. For that the light beam is sent from the origin, reflected off the test mass, and detected at the origin again. Computing the travel time (and comparing to the reference) allows to deduce the GW signal. A convenient way to time the arrival of the light beam is to use a Michelson interferometer with two arms, see Fig. 2.2. Passing GW stretches one arm and squashes another, causing a relative phase change between the light beams in the arms. This change can be observed as an interference on the output port of the interferometer.

The phase of the light acquired by light on a round-trip in the arm is gauge independent. In the Lorentz gauge, the mirrors are displaced by a GW, which results in an additional phase acquired by light. In the TT gauge, the distance to the mirror is stretched, and it takes longer for the light to travel, resulting in

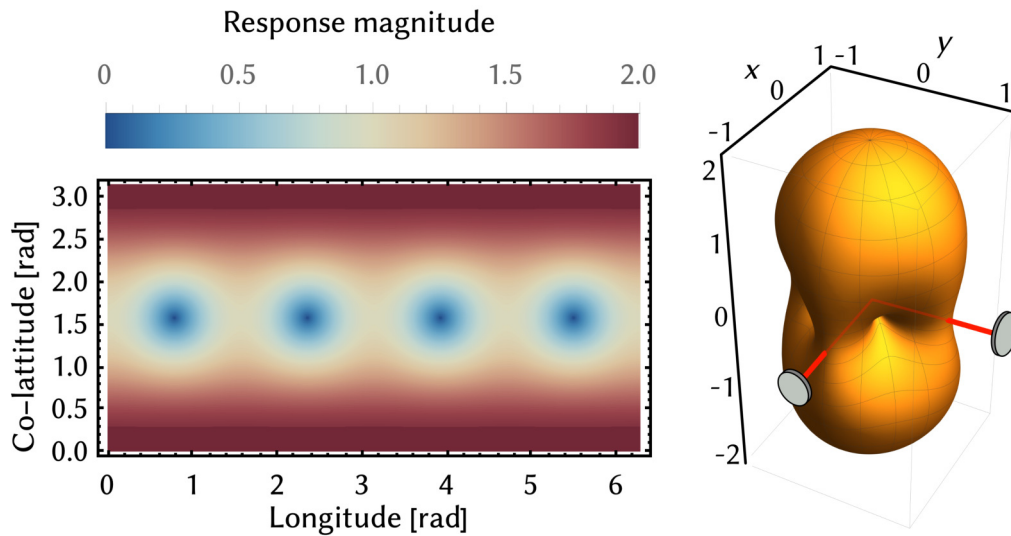


Fig. 2.3. The sensitivity of the detector as a function of the position of the source on the sky for circularly polarized GWs. (Left) magnitude of the response as a function of the coordinates on the sky; (right) antenna pattern relative to the position of the detector in Cartesian coordinates. The GWs arriving from zenith or nadir are twice as strong as the ones propagating along the arms, since they couple maximally to both arms. The GWs arriving from the bisector between the arms are not detected, since they excite the two arms equally, in the common mode.

an additional phase. Practically, when including other forces acting on the test mirrors, it is difficult to use the TT gauge, so from here on I use the Lorentz gauge, and view the GW as a tidal force.

In general, a single Michelson interferometer is not equally sensitive to all polarizations and propagation directions of GWs [82, 83]. For example, if the polarization of the GW is (+), and the arms are aligned along the coordinates of metrics change, the signal in the detector will be maximal. It will be not sensitive to (\times) polarization, and somewhat sensitive to the combination of these polarizations. Of course, the angle at which the GW arrives at the detector also affects the sensitivity. Ultimately every detector has an antenna pattern for the highest sensitivity, see Fig. 2.3. For the further discussion I always assume that the detector is perfectly aligned with one of the polarizations, achieving the full sensitivity.

The change in the arm length, according to the equations (2.10) is:

$$\delta L(t) = \frac{1}{2}h(t)L, \quad (2.12)$$

where L is the arm length of the interferometer. The corresponding change in the phase of light with wavelength λ_0 on the round trip:

$$\delta\phi(t) = 2\pi\frac{2L}{\lambda_0}h(t). \quad (2.13)$$

As one can see, the magnitude of this change in phase is tiny when induced by a typical GW of amplitude $h \sim 10^{-21}$ in the 4-km long interferometer: $\delta\phi \sim 5 \times 10^{-11}$. In the interferometer this phase change converts into a power change at the output of the interferometer. For example, for an interferometer tuned to the mid-fringe (i.e. when there is half total power in the signal port in the absence of signal):

$$P_{\text{out}} = \frac{1}{2}P_{\text{in}}(1 + \sin 2\delta\phi). \quad (2.14)$$

The difference in detected powers for an input power of 100 W due to the phase change of $\delta\phi \sim 5 \times 10^{-11}$ will be on the order of 5 nW.

Clearly, such small signals are not feasible for practical detection. There are two clear ways to increase the signal, which can be seen straight from the equations above. The first one is to make the arms longer, the second one is to increase the light power in the interferometer. The arm length of 4 km in Advanced LIGO is already rather long, and while it is planned to implement tens of kilometers arms in future detectors [58], their size is clearly limited by the ground infrastructure. There are plans for space-based observatories, such as LISA [84, 85], DECIGO [86], Taiji [87] and TianQin [88], with arm lengths of thousands to millions of kilometers, to observe GWs at much lower frequencies (below 10 Hz). While very long arms are not feasible on the ground, the same effect may be achieved with a delay line in the arms: since the measured effect depends on the travel time in arms, a delay line with \mathcal{N} trips would result in the phase gain:

$$\delta\phi(t) = 2\pi \times \mathcal{N} \times \frac{2L}{\lambda_0}h(t). \quad (2.15)$$

Modern detectors use Fabry-Perot resonators instead of delay lines, see Fig. 2.2. An additional mirror (input test mass, ITM) in the arm of the interferometer forms an optical cavity with the back mirror (end test mass, ETM). When the cavity is on resonance, the light effectively stays inside for some time, acquiring a phase enhanced by the amount of round-trips $4\mathcal{N} = 2\mathcal{F}/\pi$, where \mathcal{F} is cavity finesse, which depends on the power reflectivities $R_{1,2}$ of the two mirrors:

$$\mathcal{F} = \frac{\pi\sqrt[4]{R_1R_2}}{1 - \sqrt{R_1R_2}}. \quad (2.16)$$

For a typical finesse $\mathcal{F} \sim 100$ and $P_{\text{in}} \sim 100 \text{ W}$ would result in $P_{\text{out}} \sim 0.5 \mu\text{W}$, which is much larger than 5 nW in the example without a cavity. Such power is already detectable. Modern detectors use additional cavities to enhance the signal even further. One mirror on the input of the interferometer forms a so-called power-recycling (PR) cavity. This cavity enhances the light power by interfering it constructively with itself on a round trip. This does not have an effect on the signal. The second mirror is placed in the output of the interferometer and forms a so-called signal-extraction (SE) cavity with the ITM to enhance the signal.

2.3 Sensitivity and noises

As we saw in Sec. 2.1, the strain amplitude from a GW source at typical distance is extremely weak: on the order of 10^{-21} . Conceptually, such a signal can be detected by measuring the differential length change of the arms of the interferometer. Practically though, the ability of the detector to measure such signals is limited by various disturbances that also change the differential path length or manifest themselves as such. The main noise source at signal frequencies above $\sim 50 \text{ Hz}$ in the current generation of GW observatories is the quantum uncertainty of the light field, which results in shot noise (photon-counting noise) [10, 16]. Noise at lower frequencies has contributions of several origins such as Brownian motion of the mirror surfaces and suspensions, as well as quantum radiation pressure noise, which comes from mirrors' random motion due to quantum uncertainty of the light power [67, 89]. All these noise sources give contributions to the photocurrent of the photodiode placed on the signal port of the detector. The observatory's

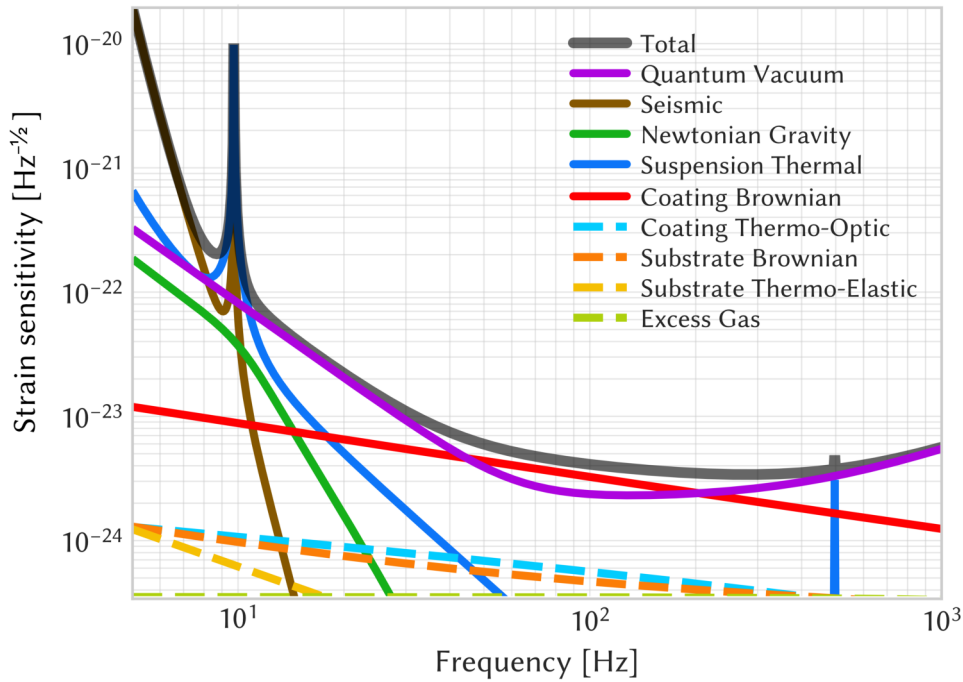


Fig. 2.4. Noise contributions to the total design sensitivity of Advanced LIGO [10] in terms of sensitivity to gravitational-wave strain $h(t)$. The figure is produced in PyGWINC package [90] using the standard "aLIGO" model.

sensitivity to the GW signal is given by the observatory's signal-to-noise ratio (SNR).

It is convenient to quantify a noise in the frequency domain, since a GW signal has distinct contribution at a single frequency (varying in time). Signal frequencies at which the detector is most sensitive define the detection bandwidth. Since most of the noises can be qualified as stationary or quasi-stationary [16], it is sufficient to give the spectral density of the noise (usually normalized to the signal transfer function).

The main noise contributions to the design sensitivity of Advanced LIGO are plotted in Fig. 2.4, and further I briefly discuss some of the most important of the sources.

- **Shot noise** (measurement noise) originates from the quantization of light, as seen by photodetectors. Random arrival statistics of the photons creates photo-voltage fluctuations, which mask the signal. The photons in the light beam obey Poisson statistics [91], which for large average number of photons \bar{N} can be approximated by a normal distribution with a standard deviation $\sigma_N = \sqrt{\bar{N}}$:

$$p(N) = \frac{1}{\sqrt{2\pi\bar{N}}} e^{-\frac{(N-\bar{N})^2}{2\bar{N}}}. \quad (2.17)$$

The power P of the light beam is related to the average amount of photons \bar{N} per time τ :

$$P = \frac{2\pi\hbar c}{\lambda_0\tau} \bar{N}. \quad (2.18)$$

Their standard deviations are related correspondingly:

$$\sigma_P = \frac{2\pi\hbar c}{\lambda_0\tau} \sigma_N = \sqrt{\frac{2\pi\hbar c}{\lambda_0\tau} P}. \quad (2.19)$$

The output of a typical interferometer, see Eq. (2.14), contains both the signal and the noise δP_{out} :

$$P_{\text{out}}(t) = \frac{2\pi L P_{\text{in}}}{\lambda_0} h(t) + \delta P_{\text{out}}(t). \quad (2.20)$$

The standard deviation of the shot noise is defined by the relation above:

$$\sigma_{P_{\text{out}}} = \frac{2\pi\hbar c}{\lambda_0\tau} \sigma_N = \sqrt{\frac{4\pi\hbar c}{\lambda_0\tau} P_{\text{in}}}. \quad (2.21)$$

The sensitivity of the detector is characterized by the inverse SNR, which can be computed by dividing the noise standard deviation by the signal transfer function $\partial P_{\text{out}}/\partial h(t)$:

$$\sigma_h = \frac{\sigma_{P_{\text{out}}}}{\partial P_{\text{out}}/\partial h(t)} = \sqrt{\frac{\hbar c \lambda_0}{4\pi L^2 P_{\text{in}} \tau}}. \quad (2.22)$$

This relation allows us to confirm the qualitative picture from the previous section, and highlight the ways to enhance the sensitivity. Firstly, one can increase the input light power, either directly, or by using an additional mirror (PRM) to form a power-recycling cavity. Secondly, one can increase the length, either directly, or by using optical cavities in the arms. When the arm cavity is present, the signal is amplified by its finesse \mathcal{F} , see Eq. 2.15:

$$P_{\text{out}}(t) = \frac{2\mathcal{F}LP_{\text{in}}}{\lambda_0}h(t) + \delta P_{\text{out}}(t), \quad (2.23)$$

and using the relation between the input and intra-cavity power $P_c = (2\mathcal{F}/\pi) \times (P_{\text{in}}/2)$ one can obtain the enhanced sensitivity at low frequencies (i.e. not taking the effects of a finite cavity linewidth into account):

$$\sigma_h = \sqrt{\frac{\hbar c \lambda_0}{4\mathcal{F}L^2P_c\tau}} = \sqrt{\frac{\hbar \lambda_0 \gamma}{8\pi L P_c \tau}}, \quad (2.24)$$

where we introduced the cavity half-width half-maximum (bandwidth) $\gamma = cT/(4L)$, for a single-sided cavity with mirror's power transmissivity T .

- **Radiation-pressure noise** In the classical effect of radiation pressure, electromagnetic radiation applies force to the surface it is reflected off. This is the case also in gravitational-wave detectors, where the laser beam creates a strong push on the test mirrors:

$$F_{\text{rp}}(t) = \frac{P_c(t)}{c} = \frac{P_{\text{in}} + \delta P_{\text{in}}(t)}{2c}. \quad (2.25)$$

The average force is proportional to the average light power P_{in} , but it also has a contribution from any fluctuations in this power $\delta P_{\text{in}}(t)$. In particular, when the light field is limited by quantum fluctuations, they cause quantum radiation pressure noise (QRPN). The force applied to a test mass causes its displacement: $M\ddot{x}_{\text{rp}}(t) = F_{\text{rp}}(t)$ The constant shift can be compensated by classical control loops, but the QRPN part inevitably produces random

displacement and thus noise in the interferometer output. The standard deviations of the QRPN can be computed accordingly:

$$\sigma_F = \frac{\sigma_{P_{\text{in}}}}{c} = \sqrt{\frac{4\pi\hbar}{c\lambda_0\tau}} P_{\text{in}}. \quad (2.26)$$

As a consequence of the Heisenberg uncertainty relation, the noise imposed on a test mass by a meter (QRPN) and the measurement precision (shot noise) should obey the uncertainty relation:

$$\frac{\hbar}{2} = \sigma_x \sigma_p = \frac{L}{2} \sigma_h \times \tau \sigma_F = \frac{L}{2} \sqrt{\frac{\hbar c \lambda_0}{4\pi L^2 P_{\text{in}} \tau}} \times \tau \sqrt{\frac{4\pi\hbar}{c\lambda_0\tau}} P_{\text{in}} = \frac{\hbar}{2}. \quad (2.27)$$

Since the equivalent contribution of the QRPN to the displacement scales with averaging time: $M\sigma_{x,\text{rp}} = \tau^2\sigma_F$, it is evident that the longer the averaging time, the higher is the contribution of QRPN to the sensitivity. It is understandable, since the position can be estimated most precisely from the instantaneous measurement, and the momentum — from two successive measurements of the position separated by some time, the QRPN contaminates the latter. There is an optimum power, for which these two noise contributions become equal: $\sigma_x = \sigma_{x,\text{rp}}$, and this optimum point is called the Standard Quantum Limit (SQL):

$$\sigma_x^{(\text{SQL})} = \sqrt{\frac{\hbar\tau^2}{2M}}, \quad P^{(\text{SQL})} = \frac{c\lambda_0 M}{8\pi\tau^2}. \quad (2.28)$$

SQL serves as an important benchmark, since it's not possible to surpass this limit using classical approaches, e.g. by increasing light power or integration time. It is possible, however, to overcome this limit using non-classical states of light.

- **Coating thermal noise** Molecules in the highly-reflective coatings of the mirrors that are used as test masses undergo random Brownian motion due to the coupling to a room-temperature thermal bath [92]. These excitations lead to random fluctuations of the surface itself, which is seen by the reflected light as a change in mirror's position. The laser beam is

relatively broad on the surface of the mirror, which averages out most of the fluctuations, but a small fraction still contributes to the phase of the reflected light. This coating thermal noise is currently limiting the sensitivity in the middle-frequency band [16]. It is possible to reduce the noise by decreasing the coupling to the thermal bath (increasing the mechanical quality of the coatings) and decreasing the temperature of the bath itself. The Japanese detector KAGRA operates at cryogenic temperatures, and it is also planned for future GW detectors, such as Einstein Telescope and LIGO Voyager. At the same time new coatings are constantly being developed with better mechanical and optical properties (which reduces heating from the absorbed light) [54].

- **Suspension thermal noise** Brownian motion also excites vibrations in the suspensions of the test masses [93]. This noise acts as an additional random force shifting the mirrors, and thus has a higher contribution at low frequency, where the mirror's response to a force is higher. While the underlying reason for this noise is the same as for coating thermal noise, the material design for suspensions has another focus: it needs to satisfy strict requirements on the shape and dimensions of the suspension, while optical properties are not important.
- **Seismic noise** The detectors are so sensitive, that even the smallest seismic vibrations can be seen in the output channel [50, 94]. Aside from the seismic activity of the Earth, various vibrations from cars on nearby roads, construction works and other human activities, or even the ocean waves hitting the shore, all can be sensed by the detector. Multiple stages of isolation, both active and passive (most notably suspending all optics on multi-stage suspensions) are required to reduce the influence of seismic noise in the detection frequency band. One of the additional approaches for reducing the seismic noise is placing the detector underground, as is done for KAGRA, and planned for ET.
- **Newtonian gravity noise** One of the more fundamental noises is the gravity gradient noise [95, 96]. Motion of heavy objects around test masses can displace them due to the gravitational attraction between the object

and the test mass. For example, surface gravity waves cause mirrors to shift. The conceptual problem with this noise is that it is impossible to isolate from it. It can be reduced by going underground, since there surface ground motion would give minimal contribution. On the other hand, body waves become more pronounced. One approach to mitigating this noise is sensing it and subtracting from the data [97].

- **Control noise** There are various control noises, arising from electronics and auxiliary readouts [16]. These noises have significant contribution at low frequency, but are difficult to model and reduce.
- **Other noises** There are multiple other sources of noise (e.g. parasitic interference with back-scattered light [98]), and also various non-stationary processes that contaminate the signal [99, 100].

While all the noises are very challenging to mitigate and reduce, quantum shot and radiation pressure noises remain the most fundamental limitations to the sensitivity. In the next section I overview the techniques for reducing quantum noise.

2.4 Quantum-correlated light for GW detectors

Quantum noises are one of the main limiting factors in gravitational-wave detectors, and there are several approaches on how to reduce or avoid them. Semi-classically, shot noise can be suppressed by increasing the light power, or the length of the arms. That, however, increases QRPN at low frequencies. The classical trade-off is always the SQL: there is no way to avoid it without creating quantum correlations in the light field (non-classical light).

For continuous light field, the fluctuations in the photon number and arriving times [101] correspond to the fluctuations in the amplitude and phase of the light field. It is convenient to describe these fluctuations in the phase space in terms of fluctuations in the amplitude and phase *quadratures* of the light field. I introduce

the quadratures rigorously in Chapter 3, and here define as a real and imaginary part of the complex amplitude of the light field E :

$$E(t) = E_0 e^{-i\omega_0 t} + E_0^* e^{i\omega_0 t} = X \cos \omega_0 t + Y \sin \omega_0 t, \quad (2.29)$$

$$X = \sqrt{2}\Re[A], \quad Y = \sqrt{2}\Im[A], \quad (2.30)$$

where E_0 is the complex amplitude of the light field at frequency ω_0 , and X, Y are the amplitude and phase quadratures, correspondingly. From here on, I discuss the noises in terms of light quadratures.

One of the first approaches for suppressing shot noise was squeezing the quantum uncertainty of a signal quadrature by injecting squeezed vacuum in the output port of the interferometer [65, 66, 102–107]. When the signal (phase) quadrature is squeezed, the shot noise is suppressed, and the sensitivity is enhanced, much like with increased light power: 3 dB of shot noise squeezing provides the same increase in sensitivity as doubling the light power. On the other hand, the amplitude quadrature gets anti-squeezed, which increases QRPN at low frequencies. Nevertheless, squeezed light has been used in GEO600 for many years [108, 109], and since April 2019 Advanced LIGO [42] and Advanced Virgo [44] use squeezed light injection to suppress shot noise. Since these detectors currently have not yet reached their design sensitivity and thus are not limited by QRPN at low frequencies, squeezed light injection does not

In order to take full advantage of squeezed light, it would be necessary to squeeze the amplitude quadrature of the light at low frequencies (thus reducing QRPN), and the phase quadrature – at high frequencies (suppressing shot noise), see Fig. 2.5. Such frequency-dependent squeezing [110, 111] is planned to be implemented in the next large upgrade of the detectors. In order to create the necessary frequency dependence, squeezed vacuum is reflected off a hundreds-of-meters long filter cavities [112–114], detuned from their resonance in an optimal way.

Other approaches target reducing the QRPN without affecting the shot noise. One of the most direct ways is to increase the mass of the mirrors, but that is technically challenging. A class of approaches is united under a general label of back-action evading measurements [34, 115, 116]. The most notable example of such measurements is ‘variational readout’ [112, 117, 118], where the outgoing

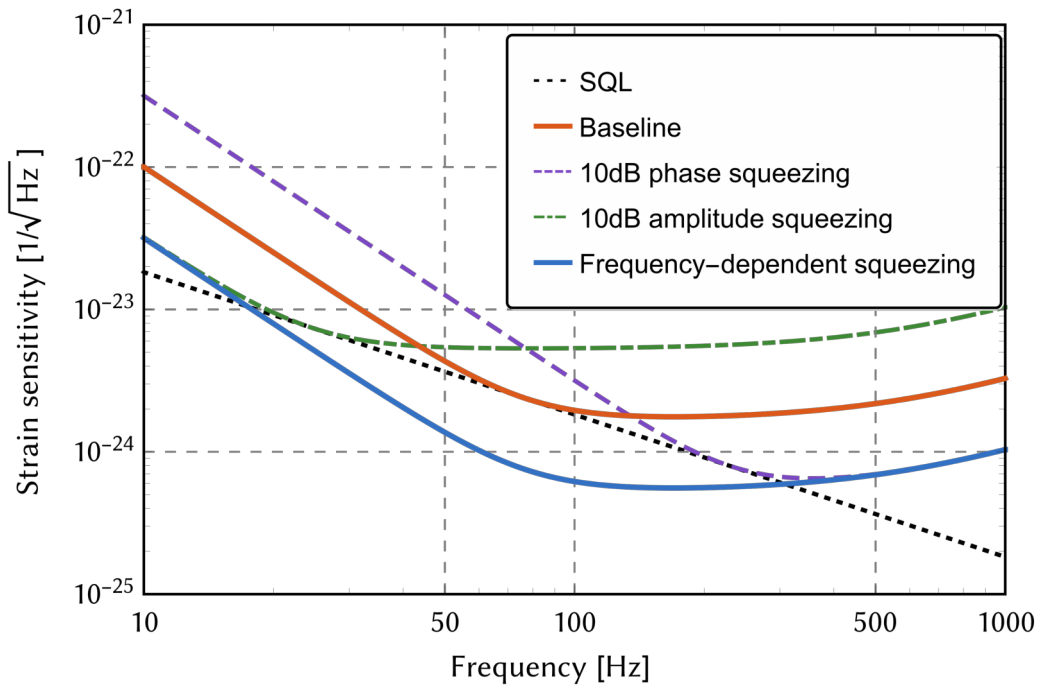


Fig. 2.5. Sensitivity of the GW detector enhanced with squeezed light. Phase squeezing (magenta) increases the sensitivity at high frequencies, at a price of reduced low-frequency sensitivity, which increases due to QRPN. Amplitude squeezing (green) allows to suppress QRPN at low frequencies, increasing the shot noise at high frequencies. For both phase and amplitude squeezing, sensitivity does not surpass the SQL, since no cross-correlation between the noises is used. Frequency-dependent squeezing allows to rotate the squeezed quadratures such, that the noise is suppressed at all frequencies, allowing to surpass the SQL.

quadratures of the light are rotated in such a way that quantum correlations between the two quadratures cancel the effect of QRPN and it is never seen by the photodetectors. Variational readout requires a scheme with detuned filter cavities, which is very similar to the frequency-dependent squeezing, but on the output of the detector instead of the input.

There are other approaches, in which QRPN does not arise in the measurement. Such approaches are called quantum-non demolition (QND) [34]. They require changes to the measurement procedure itself. The most developed concept of such measurements is a speedmeter topology [119–122], where instead of position, the light senses the velocity of the test masses. This allows to significantly lower the QRPN, and in the ideal case get rid of it completely. Many different topologies have been proposed over the years [123–126], but they are still waiting to be verified experimentally.

Finally, there are concepts that involve changing the response of the test masses in such a way, that a particular frequency band gains in sensitivity significantly, while others become less sensitive [127–132].

Apart from these mainstream concepts, many more have been proposed, involving atomic [133–136] or optomechanical systems [137–139] inside and outside [140] the detector, changes in readout [141–144] and combinations of several different approaches.

All these approaches share one weakness: as long as they use quantum correlations, they are very susceptible to quantum decoherence (optical loss) [43]. Any quantum state is easily destroyed by a small amount of decoherence, and optical states are not an exception. For example, even if one could produce 100 dB of squeezed light (suppression of shot noise by 10^{10}), 1% of loss would reduce this squeezing to 20 dB (suppression by 100), and 10% – to 10 dB (suppression by 10). One has to keep in mind, that current losses in Advanced LIGO are on the order of 25% [45], and it could be technologically possible to reduce them to several percent. Anything below 1% is beyond current technology. Optical loss is the main limitation for all quantum techniques, and a showstopper for some of them. It is therefore of utmost importance to always consider the practical aspect of a specific approach, and find a way to reduce the influence of loss. In the following chapters I will outline some possible directions for avoiding particular kinds of optical loss.

In the next section I talk more about the quantum limits in the more general context of quantum metrology, and discuss the importance of these limits for gravitational-wave detectors.

2.5 Quantum limits in metrology

Metrology - the science of precise measurement of physical values - has entered our everyday life in various applications [145, 146], from biological sensors [147] and accelerometers [148, 149] to ultra-precise magnetic field sensors [150] and gravitational-wave detectors. Technological advances lead to many sensors being limited by the quantum properties of the measurement device (e.g. laser shot noise). Further advances would require employing quantum techniques for achieving the optimal sensitivity. In this section I review the task of metrology, fundamental limitations on the measurement precision, and how this connects to gravitational-wave detectors.

The main task of metrology is finding the best way of measuring the specific parameter or set of parameters, which entails both optimization of the measurement apparatus, and data analysis [145]. There are many branches of quantum metrology, some use discrete, some continuous variables (and measurement techniques), some target measuring classical parameters, others – quantum. I focus on a metrological task of measuring a classical force acting on a movable mirror by reflecting continuous light off this mirror.

2.5.1 Simple quantum measurement model

I start by considering the simplest model of measuring the displacement of a free test mass under action of classical force G . The measurement in this toy example is instantaneous and yields a value for the position of the test mass. It also applies some back-action (i.e. changes momentum of the test mass). An example of such a measurement is timing the delay of a photon reflected off a test mass. Depending on the delay, one may judge the value of the position, but also every reflection transfers momentum of $2\hbar k$ to the test mass (for a wavevector k). Statistically, the precision of such measurement Δx and the random spread of momentum Δp should obey the Heisenberg's uncertainty relation: $\Delta x \Delta p \geq \hbar/2$. With this in

mind we can construct a four-stage procedure for repeated measurement of the force G : initiate the state of the test mass x_0, p_0 , measure this state right before the force arrives (and apply back-action), wait for the force to act on the test mass and measure again after time τ and again after time τ , in order to construct a discrete second derivative (i.e. acceleration) as $x_3 - 2x_2 + x_1$:

$$x_1 = x_0 + x_1^m, \quad (2.31)$$

$$x_2 = x_0 + \tau \frac{p_0 + p_1^{\text{ba}}}{m} + \frac{G\tau^2}{2m} + x_2^m, \quad (2.32)$$

$$x_3 = x_0 + 2\tau \frac{p_0 + p_1^{\text{ba}}}{m} + \tau \frac{p_2^{\text{ba}}}{m} + 2\frac{G\tau^2}{m} + x_3^m, \quad (2.33)$$

$$\tilde{G} = \frac{m}{\tau^2}(x_3 - 2x_2 + x_1) = G + \frac{p_2^{\text{ba}}}{\tau} + \frac{m}{\tau^2}(x_3^m - 2x_2^m + x_1^m), \quad (2.34)$$

where \tilde{G} is our estimation of the force given the measurement record, and $x_{1,2,3}^m$ are the measurement noises. The uncertainty of this estimation is:

$$\Delta^2 \tilde{G} = \frac{m}{\tau^2} (\Delta^2 x_3^m + 4\Delta^2 x_2^m + \Delta^2 x_1^m) + \frac{\Delta^2 p_2^{\text{ba}}}{\tau}. \quad (2.35)$$

Since the first and the last measurements do not contribute to the back-action, they can be assumed infinitely strong: $\Delta^2 x_{1,3}^m = 0$. If we then recall that $\Delta^2 x_2^m \Delta^2 p_2^{\text{ba}} = \hbar^2/4$, we obtain:

$$\Delta^2 \tilde{G} = \frac{4m}{\tau^2} \Delta^2 x_2^m + \frac{\hbar^2}{4\Delta^2 x_2^m \tau}, \quad (2.36)$$

which allows to optimize the measurement strength for the second measurement: $\Delta^2 x_2^m = 0.25\hbar\tau m^{-1}$, which gives the minimal detectable force

$$\Delta^2 \tilde{G}^{\text{min}} = \frac{\hbar m}{\tau^3}. \quad (2.37)$$

This measurement uncertainty corresponds to the SQL.

Now suppose that we could measure a linear combination of displacement and back-action: $y = x + \alpha p^{\text{ba}}$, where we are free to choose a coefficient α . Then the

same procedure as above with modified measurement during the second stage would give:

$$x_2 = x_0 + \tau \frac{p_0 + p_1^{\text{ba}}}{m} + \frac{G\tau^2}{2m} + x_2^{\text{m}} + \alpha p_2^{\text{ba}}, \quad (2.38)$$

$$\tilde{G} = \frac{m}{\tau^2}(x_3 - 2x_2 + x_1) = G + \frac{p_2^{\text{ba}}}{\tau} \left(1 + \frac{2m\alpha}{\tau}\right) + \frac{m}{\tau^2}(x_3^{\text{m}} - 2x_2^{\text{m}} + x_1^{\text{m}}), \quad (2.39)$$

which allows to completely avoid the back-action by selecting $\alpha = -\tau(2m)^{-1}$:

$$\Delta^2 \tilde{G} = \frac{m}{\tau^2} (\Delta^2 x_3^{\text{m}} + 4\Delta^2 x_2^{\text{m}} + \Delta^2 x_1^{\text{m}}). \quad (2.40)$$

The precision is then unlimited: $\Delta^2 \tilde{G}^{\text{min}} = 0$, when all measurements are strong. Note that this does not mean that the measurement does not produce back-action, we just avoid looking at it: we use correlations between the measurements to erase their effect on the measurement result. Such a *variational measurement* scenario is not hypothetical and can be realized in a real experiment by using quantum correlations in the light field.

2.5.2 Linear continuous measurement

The same example as above can be considered in the case of continuous measurement of displacement $\hat{x}(t)$ reflecting a laser beam off the mirror and registering the change in the phase. The light pushes back on the mirror, causing measurement back-action $\hat{F}^{\text{ba}}(t)$. The dynamics of this system can be described by a dynamical equation:

$$M\ddot{\hat{x}}(t) = G(t) + \hat{F}^{\text{ba}}(t), \quad (2.41)$$

$$\hat{y}(t) = \hat{x}(t) + \hat{x}^{\text{m}}(t), \quad (2.42)$$

where \hat{y} is the measurement result, and \hat{x}^m is the measurement noise (shot noise in our example). It is convenient to consider the spectral components in the frequency-domain:

$$-M\Omega^2 \hat{x}(\Omega) = G(\Omega) + \hat{F}^{\text{ba}}(\Omega), \quad (2.43)$$

$$\hat{y}(t) = \hat{x}(\Omega) + \hat{x}^m(\Omega) = \frac{G(\Omega)}{-M\Omega^2} + \frac{\hat{F}^{\text{ba}}(\Omega)}{-M\Omega^2} + \hat{x}^m(\Omega). \quad (2.44)$$

We are interested in the sensitivity of this measurement scheme, which is defined by the spectral densities of the noises and the response of the system to a signal. In general, measurement noise and back-action noise can be correlated. Therefore, there is a cross-correlation spectral density $S_{xF}(\Omega)$ that quantifies the correlation between these noises. Total spectral density including this cross-correlation takes the form:

$$S_{\text{total}}(\Omega) = S_x(\Omega) + \frac{2\Re[S_{xF}(\Omega)]}{-M\Omega^2} + \frac{S_F(\Omega)}{M^2\Omega^4}, \quad (2.45)$$

where $\Re[Z]$ is a real part of a complex value Z . First consider the case without cross-correlation: $S_{xF} = 0$. As in the discrete case, it's possible to prove that the spectral densities for the measurement and back-action noises obey the uncertainty relation:

$$S_x(\Omega)S_F(\Omega) \geq \frac{\hbar^2}{4}. \quad (2.46)$$

Then the SQL is readily recovered by optimizing the measurement precision, as before:

$$S_x^{\text{SQL}}(\Omega) = \frac{\hbar}{M\Omega^2}, \quad S_F^{\text{SQL}}(\Omega) = \hbar M\Omega^2. \quad (2.47)$$

When the noises are correlated, the uncertainty relation is modified:

$$S_x(\Omega)S_F(\Omega) - |S_{xF}(\Omega)|^2 \geq \frac{\hbar^2}{4}, \quad (2.48)$$

and the sensitivity is, correspondingly:

$$S_{\text{total}}(\Omega) = \frac{\hbar^2/4 + |S_{xF}(\Omega)|^2}{S_F(\Omega)} + \frac{2\Re[S_{xF}(\Omega)]}{-M\Omega^2} + \frac{S_F(\Omega)}{M^2\Omega^4}. \quad (2.49)$$

The optimal cross-correlation is given by $S_{xF}(\Omega) = S_F(\Omega)(M\Omega^2)^{-1}$, where the sensitivity again becomes unbounded:

$$S_{\text{total}}(\Omega) = \frac{\hbar^2}{4S_F(\Omega)} \rightarrow 0. \quad (2.50)$$

The difficulty is in creation of the necessary frequency dependence in the correlation function between the noises.

2.5.3 Quantum Cramer-Rao bound

The SQL is not a fundamental limit, and can be avoided in a straightforward (yet still practically challenging) way by using back-action evasion approaches. Once back-action is out of the question, the sensitivity remains to be limited by laser shot (measurement) noise. Shot noise puts a true fundamental limit on the sensitivity.

It is possible to put this in a more broad metrological context by considering the amount of information that *in principle* can be extracted out of the noisy record. From the Heisenberg uncertainty relation:

$$\Delta\mathcal{E}\delta\phi \geq \frac{\hbar\omega_0}{2}, \quad (2.51)$$

follows that if we want to detect a small phase shift on a laser beam with frequency ω_0 , we need to minimize the uncertainty in phase $\Delta\phi$ and thus by necessity increase the uncertainty $\Delta\mathcal{E}$ in the energy used to probe this phase shift. This statement is at the core of the energetic quantum limit, as introduced by Braginsky *et.al.* [151]: the ultimate measurement precision is limited by the available energy.

In a more general metrological context this statement is known as the quantum Cramer-Rao bound (QCRB) [152, 153]. For measuring a parameter θ with a meter that has an interaction Hamiltonian H_{int} , there exists a bound on the precision of estimation of this parameter:

$$\Delta^2\theta \geq \frac{1}{4\Delta^2 H_{\text{int}}}, \quad (2.52)$$

for the case of pure states. This statement is in fact analogous to the energetic quantum limit above. For linear detection of a continuous displacement $x(t)$ with interaction Hamiltonian $H_{\text{int}} = -x(t)\hat{F}$, QCRB takes the form [154]:

$$\Delta^2 x(\omega) \geq \frac{\hbar^2}{4S_{FF}(\omega)}, \quad (2.53)$$

where $S_{FF}(\omega)$ is a symmetrized spectral density of quantum fluctuations in \hat{F} . For a gravitational-wave detector the fluctuations in \hat{F} correspond to power fluctuations on the mirrors, so the QCRB can be written as:

$$S_h^{\text{QCRB}}(\Omega) = \frac{\hbar c}{4\omega_0 L P_c} \frac{1}{S_{aa}(\Omega)}, \quad (2.54)$$

where ω_0 is the light frequency, L is the arm length, P_c is the optical power in the arms, and $S_{aa}(\Omega)$ is the spectrum of amplitude quadrature noise in the arms.

The main statement of the QCRB is that in order to increase the sensitivity of the detector, one needs to increase the pure-state energy fluctuations of the meter. For a GW detector it means increasing the amplitude fluctuations in the light field. This can be done either by increasing the light power, or by anti-squeezing the amplitude quadrature of the light. In general, QCRB does not impose any requirement on the phase quadrature, and in some approaches involving entangled states, both amplitude and phase quadratures can be increased. This summarizes all approaches to increasing the shot-noise limited sensitivity of the detector. It is important, that the QCRB in general does not make any statements about the readout. The bound itself depends only on the properties of the interaction Hamiltonian.

An entirely different question is how to reach this bound in a realistic design. There are two main conditions for that: i) the detector is in a pure state (at the quantum limit); ii) measurement back-action is evaded. This means in particular that the detector would have to have no optical loss, which is not possible. There exists a different limit, that originates from optical losses, and I discuss it in detail in Chapter 7.

Practically, the design of a detector can then be separated into two tasks: finding the design with low QCRB, and looking for ways to achieve it. Now I give several examples of how QCRB could be applied to a detector design.

First, let's start with considering the baseline sensitivity of a Michelson interferometer without any cavities:

$$S_h^{\text{baseline}}(\Omega) = \frac{\hbar c}{4\omega_0 L P_0}, \quad (2.55)$$

where the amplitude noise on the mirror is assumed to originate from a coherent state, thus $S_{aa}(\Omega) = 1$, and the input light power is P_0 . As I discussed in the previous sections, optical cavities allow to increase the sensitivity. Indeed, from the point of view of QCRB, with coherent input, the amplitude noise inside the cavity is amplified by a cavity resonance factor, and the sensitivity becomes:

$$S_h^{\text{cavity}}(\Omega) = \frac{\pi \hbar c}{4\omega_0 L P_0 \mathcal{F}} \frac{\gamma^2 + \Omega^2}{\gamma}, \quad (2.56)$$

where γ is cavity bandwidth, and \mathcal{F} is the cavity finesse. It is important, that the QCRB is significantly, by \mathcal{F}^2 , lowered on resonance ($\Omega = 0$), but becomes worse at higher frequencies:

$$\frac{S_h^{\text{cavity}}(\Omega)}{S_h^{\text{baseline}}(\Omega)} = \pi \frac{\gamma^2 + \Omega^2}{\mathcal{F} \gamma} = \frac{\pi^2}{2\mathcal{F}^2 \tau} + 2\tau \Omega^2. \quad (2.57)$$

This highlights an important property of QCRB: it depends on frequency, and thus sometimes it is difficult to use it as a benchmark parameter. Instead, an integrated QCRB can be used. For a cavity-based detector, in which the sensitivity has a Lorentzian spectral shape, integrating over the SNR gives the product of peak sensitivity and bandwidth:

$$\int_0^{\omega_{\text{QCRB}}} \frac{1}{S_h^{\text{MFP}}(\Omega)} d\Omega = \frac{V_{aa}}{S_h^{\text{QCRB}}(0)} \times \gamma = \mathcal{S} \times \mathcal{B}, \quad (2.58)$$

where V_{aa} is the variance of amplitude fluctuations in the cavity. Interestingly, for any choice of detector's bandwidth the sensitivity-bandwidth product remains constant and proportional to the power on the mirror, since for a coherent state of light $V_{aa} = 1$. It can be understood as follows: if one wants to increase the peak sensitivity, the only classical way to that is to increase the cavity finesse. But that comes at a price of reduced bandwidth, such that the sensitivity times bandwidth

remains constant. This limitation, known as the Mizuno theorem [155], we call a standard sensitivity-bandwidth limit (SSBL), which cannot be overcome by classical means for a given light power.

Quantum-correlated light, on the other hand, would allow us to overcome the SSBL: e.g. injection of squeezed light reduces the phase uncertainty, and correspondingly increases the amplitude one. Interestingly, SSBL or QCRB depend only on the amplitude quadrature, and generally don't state anything about the phase quadrature, where the signal is. That is because they only set a limit, and finding the means for approaching it, is a separate task, as I mentioned earlier. It might be that the limit is not achievable in a particular configuration.

Three limits, SQL, QCRB and SSBL, reflect different aspects of the quantum nature of detector design. The SQL highlights the influence of measurement back-action, the QCRB sets the precision for every measurement frequency, and the SSBL allows to quantify the sensitivity in a broad band. The SQL and the SSBL can be overcome and the QCRB can be lowered with quantum technology. Using these limits as benchmark parameters for new experimental designs allows to find new approaches to designing a detector.

Basics of quantum noise in gravitational-wave detectors

In this chapter I give a brief introduction into the basics of quantum noise in gravitational-wave detectors, and describe the ways to measure it and describe the main limitations. This introduction is by no means complete or even fully rigorous in the mathematical sense. Instead, I give a practical guide to calculating the quantum noises for several common situations, and describe some experimental challenges.

A curious reader can find plenty of literature devoted to theoretical and experimental aspects of quantum technologies in quantum optics and gravitational-wave detection [34–36, 38, 40, 91, 124, 156–164].

3.1 Quantum states of light

3.1.1 Quantization of the electromagnetic field

First, I introduce some concepts and definitions that will be used throughout the text. The main focus of this thesis is quantum optics in the continuous-wave regime and relatively strong fields, where the number of photons per Fourier-limited mode is significantly larger than zero. For the purposes of the theoretical calculations, I consider plane monochromatic laser light at a wavelength λ_0 (and corresponding angular frequency ω_0), which propagates along x direction in perfect vacuum. This laser light is described by an electric field strength

$$E(x, y, z, t) = E(y, z)E(x - ct) = E_0 e^{ik_0 x} e^{-i\omega_0 t}, \quad (3.1)$$

where I assume the waves to be plane, such that the field strength in the direction orthogonal to the propagation direction is uniform: $E(y, z) = 1$. The feature of a plane wave is that its propagation in free space can be equivalently described simply by time evolution. For example, the propagation from $x_0 = 0$ to $x_L = L$ is:

$$E(L - ct) = E_0 e^{ik_0 L} e^{-i\omega_0 t} \equiv E(t - L/c). \quad (3.2)$$

This enables us to talk only about time dependence in most cases: $E(x - ct) \equiv E(t)$.

The main focus of this thesis are the effects of quantum noise on the metrological devices. Quantization of light follows the procedure of the second quantization, in which propagating light fields are described by a continuum of Fourier-limited modes at frequencies ω with annihilation operators $\hat{A}(\omega)$:

$$\hat{E}(t) = \int_0^\infty \sqrt{\frac{2\pi\hbar\omega}{\mathcal{A}c}} \hat{A}(\omega) e^{-i\omega t} \frac{d\omega}{2\pi} + h.c. \quad (3.3)$$

where \mathcal{A} is the laser beam cross-section area, \hbar is the reduced Plank constant, and "h.c." stands for "Hermitian conjugate". Mode operators $\hat{A}(\omega)$ satisfy the following commutation relations:

$$[\hat{A}(\omega), \hat{A}^\dagger(\omega')] = 2\pi\delta(\omega - \omega'), \quad (3.4)$$

and can act on a number state $|n(\omega)\rangle$ to create or annihilate a photon:

$$\hat{A}(\omega)|n(\omega)\rangle = \sqrt{n(\omega)}|n(\omega) - 1\rangle, \quad (3.5)$$

$$\hat{A}^\dagger(\omega)|n(\omega)\rangle = \sqrt{n(\omega) + 1}|n(\omega) + 1\rangle. \quad (3.6)$$

It is convenient to discuss the equations in terms of photon number flux ($\hat{A}(t)$ has the dimension of its square root) and not electric field amplitudes, since its relation to optical power is more direct. We can further assume the field to have a strong "classical" part (i.e. mean field) and small quantum noise: $\hat{A}(t) \rightarrow A_0 + \hat{a}(t)$. Such a value is convenient, since it relates to optical power $\hat{I}(t)$ as measured by photodiodes:

$$\hat{I}(t) = \overline{\hbar\omega_0 \hat{A}^2(t - x/c)} \approx \frac{1}{2} \overline{\hbar\omega_0 |A_0|^2} + \overline{\hbar\omega_0 A^* \hat{a}(t - x/c)} = I_0 + \hat{I}(t), \quad (3.7)$$

where the average is taken over many optical oscillation periods, $I_0 = 0.5\hbar\omega_0|A_0|^2$ is the mean power, and $\hat{I}(t)$ is the quantum noise power fluctuations.

Written in terms of photon number flux and separate classical and quantum parts, the field quantization takes another form:

$$\hat{A}(t) = \sqrt{\frac{\mathcal{A}c}{2\pi\hbar\omega}}E(t) = \frac{A_0e^{-i\omega_0t}}{\sqrt{2}} + \int_0^\infty \sqrt{\frac{\omega}{2\omega_0}}\hat{a}(\omega)e^{-i\omega t}\frac{d\omega}{2\pi} + h.c.. \quad (3.8)$$

3.1.2 Two-photon quadratures

We are interested in the processes with characteristic frequencies Ω around the central frequency ω_0 : $\omega = \omega_0 \pm \Omega$. In most cases we consider, the noises and signals are symmetric modulation sidebands at $\pm\Omega$. Therefore it is convenient to use so-called two-photon quadratures, as introduced by Caves and Schumaker,[165, 166], which takes this symmetry into account:

$$\hat{a}^c(\Omega) = \frac{\hat{a}_+ + \hat{a}_-^\dagger}{\sqrt{2}}, \quad (3.9)$$

$$\hat{a}^s(\Omega) = \frac{\hat{a}_+ - \hat{a}_-^\dagger}{i\sqrt{2}}, \quad (3.10)$$

$$\hat{a}_+ \equiv \hat{a}(\omega_0 + \Omega) = \frac{\hat{a}^c(\Omega) + i\hat{a}^s(\Omega)}{\sqrt{2}}, \quad (3.11)$$

$$\hat{a}_-^\dagger \equiv \hat{a}^\dagger(\omega_0 - \Omega) = \frac{\hat{a}^c(\Omega) - i\hat{a}^s(\Omega)}{\sqrt{2}}, \quad (3.12)$$

where c, s refer to *cosine* and *sine* components of the fields, as I show below. In the quantum optical experiments the measurements are not instantaneous, and are limited by the time resolution of the photodetectors $\Delta\tau$ [43]. Therefore the observable mode is in fact defined as an average over a resolution time $\Delta\tau = 1/\Delta\Omega$:

$$\hat{X}_{\Omega,\Delta\Omega}(t) = \frac{\Delta\Omega}{2} \int_{t-1/\Delta\Omega}^{t+1/\Delta\Omega} \hat{a}^c(\tau)d\tau, \quad \hat{Y}_{\Omega,\Delta\Omega}(t) = \frac{\Delta\Omega}{2} \int_{t-1/\Delta\Omega}^{t+1/\Delta\Omega} \hat{a}^s(\tau)d\tau. \quad (3.13)$$

In the remaining of the thesis, I use the two-quadrature operators $\hat{a}^{c,s}$ as more simple from theoretical perspective, but encourage the reader to keep in mind that quadratures $\hat{X}_{\Omega,\Delta\Omega}$ and $\hat{Y}_{\Omega,\Delta\Omega}$ are the ones observed in real experiment [43].

These frequencies are typically much smaller than the optical frequency $\omega_0 \gg \Omega$, so in terms of two-photon quadratures, quantization of a field in Eq. 3.8 takes a simpler form:

$$\begin{aligned} \hat{A}(t) &= \frac{A_0 e^{-i\omega_0 t}}{\sqrt{2}} + \frac{1}{2} \int_0^\infty \sqrt{1 + \frac{\Omega}{\omega_0}} [\hat{a}^c(\Omega) + i\hat{a}^s(\Omega)] e^{-i(\omega_0 + \Omega)t} \frac{d\omega}{2\pi} + h.c. \approx \\ &\approx [A^c + \hat{a}^c(t)] \cos \omega_0 t + [A^s + \hat{a}^s(t)] \sin \omega_0 t. \end{aligned} \quad (3.14)$$

The two quadratures: cosine and sine, are called *amplitude* and *phase* quadratures correspondingly. The reason for it is that the standard representation of a field with a small phase ϕ and noise a :

$$A(t) = (A_0 + a) \cos(\omega_0 t - \phi) \approx (A_0 + a) \cos \omega_0 t + A_0 \phi \sin \omega_0 t, \quad (3.15)$$

reduces to Eq. 3.14 when choosing $A^c = A_0, A^s = 0, a^s = \phi A_0, a^c = a$. Thus, fluctuations in a sine quadrature correspond to phase fluctuations.

Two-photon quadratures obey the following commutation relations, in the approximation $\Omega \ll \omega_0$:

$$[\hat{a}^c(\Omega), \hat{a}^c(\Omega')] = [\hat{a}^s(\Omega), \hat{a}^s(\Omega')] \approx 0, \quad (3.16)$$

$$[\hat{a}^c(\Omega), \hat{a}^s(\Omega')] = [\hat{a}^s(\Omega), \hat{a}^c(\Omega')] = 2i\pi\delta(\Omega + \Omega'). \quad (3.17)$$

Two-photon operators create one photon in the lower sideband and annihilate one photon in the upper sideband:

$$\begin{aligned} \hat{a}^c(\Omega)|n(\omega)\rangle &= \frac{\hat{a}(\omega_0 + \Omega) + \hat{a}^\dagger(\omega_0 - \Omega)}{\sqrt{2}}|n(\omega)\rangle = \\ &= \sqrt{\frac{n(\omega_0 + \Omega)}{2}}|n(\omega_0 + \Omega) - 1\rangle + \sqrt{\frac{n(\omega_0 - \Omega) + 1}{2}}|n(\omega_0 - \Omega) + 1\rangle, \end{aligned} \quad (3.18)$$

hence the name "two-photon".

3.1.3 Vacuum state

The vacuum state of a continuum is the direct product of all ground states of specific modes ω in this continuum $|\text{vac}\rangle = \otimes_{\omega} |0\rangle_{\omega}$. The energy in each mode is defined as:

$$\hat{\mathcal{E}}(\omega) = \hbar\omega \left(\hat{A}(\omega)\hat{A}^{\dagger}(\omega) + \frac{1}{2} \right) \equiv \hbar\omega \left(\hat{n}(\omega) + \frac{1}{2} \right) \quad (3.19)$$

and the ground state is the state of minimal energy, where $\hat{n}(\omega) = 0$. The action of an annihilation operator on the ground state yields zero:

$$\hat{A}(\omega)|0\rangle_{\omega} = 0. \quad (3.20)$$

The mean value for this operator, as well as for the corresponding two-photon quadrature operators, is zero too:

$$\langle \text{vac} | \hat{A}(\omega) | \text{vac} \rangle = \langle \hat{A}(\omega) \rangle = \langle \hat{A}^{\dagger}(\omega) \rangle = 0, \quad (3.21)$$

$$\langle \hat{a}^c(\Omega) \rangle = \langle \hat{a}^c(\Omega) \rangle = 0, \quad (3.22)$$

where the average is over the full spectrum of vacuum states $|\text{vac}\rangle$. To quantify the fluctuations in the fields, we can define the spectrum of these fluctuations as:

$$\begin{aligned} 2\pi\bar{S}^{i,j}(\Omega)\delta(\Omega + \Omega') &\equiv \langle \hat{a}^i(\Omega)\hat{a}^j(\Omega') \rangle_{\text{sym}} \equiv \\ &\equiv \frac{1}{2} \langle \hat{a}^i(\Omega)\hat{a}^j(\Omega') + \hat{a}^j(\Omega')\hat{a}^i(\Omega) \rangle, \end{aligned} \quad (3.23)$$

where we defined the double-sided spectral density, which for an observable \hat{x} connects to the variance of its observable through:

$$\Delta^2\hat{x} = \int_{-\infty}^{\infty} \bar{S}_x(\Omega) \frac{d\Omega}{2\pi}. \quad (3.24)$$

Since the double-sided spectral density is unavailable in experiments without heterodyne detection, for most of this thesis I define a single-sided spectral density, i.e. only for positive frequencies $\Omega > 0$:

$$S(\Omega) = 2\bar{S}(\Omega). \quad (3.25)$$

Using the definition of the spectral density in Eq. 3.23 and the commutation relations, the spectral density for the vacuum state is:

$$S_{\text{vac}}^{cc}(\Omega) = S_{\text{vac}}^{ss}(\Omega) = 1, \quad S_{\text{vac}}^{cs}(\Omega) = S_{\text{vac}}^{sc}(\Omega) = 0. \quad (3.26)$$

3.1.4 Coherent state

Coherent states are the eigenstates of the annihilation operator:

$$\hat{A}|\alpha\rangle = \alpha|\alpha\rangle, \quad (3.27)$$

with complex eigenvalues α . Coherent states can be seen as displaced vacuum states (in phase space):

$$\begin{aligned} |\alpha\rangle &\equiv \hat{D}(\alpha)|0\rangle = e^{\alpha\hat{a}^\dagger - \alpha^*\hat{a}}|0\rangle = \\ &= \exp\left[\int_0^\infty \left(\alpha(\omega)\hat{a}^\dagger(\omega) - \alpha^*(\omega)\hat{a}(\omega)\right) \frac{d\omega}{2\pi}\right] |0\rangle. \end{aligned} \quad (3.28)$$

The displacement operator \hat{D} is unitary, and the evolution of the annihilation operator under its action is simply a displacement by a complex value α :

$$\hat{D}(\alpha)^\dagger \hat{A} \hat{D}(\alpha) = \hat{A} + \alpha, \quad \hat{D}(\alpha)^\dagger \hat{A}^\dagger \hat{D}(\alpha) = \hat{A}^\dagger + \alpha^*, \quad (3.29)$$

which allows to compute the statistical properties of the field in terms of two-photon quadratures:

$$\langle \hat{a}^c(\Omega) \rangle = \Re[\alpha] \delta(\Omega), \quad \langle \hat{a}^s(\Omega) \rangle = \Im[\alpha] \delta(\Omega), \quad (3.30)$$

$$S_{\text{vac}}^{cc}(\Omega) = S_{\text{vac}}^{ss}(\Omega) = 1, \quad S_{\text{vac}}^{cs}(\Omega) = S_{\text{vac}}^{sc}(\Omega) = 0. \quad (3.31)$$

The average complex amplitude $\langle \hat{a}(\Omega) \rangle = \alpha(\Omega)$ is then defined by the average light power \mathcal{I}_0 at $\Omega = 0$:

$$\alpha(\Omega) = \pi \sqrt{\frac{2\mathcal{I}_0}{\hbar\omega_0}} \delta(\Omega), \quad (3.32)$$

and the noise of this state corresponds to that of the vacuum state. This enables us to talk about quantum noise as being in vacuum state, separately from the "classical" mean amplitude, as I introduced before:

$$\hat{A}(t) = [\Re[\alpha] + \hat{a}^c(t)] \cos \omega_0 t + [\Im[\alpha] + \hat{a}^s(t)] \sin \omega_0 t = \quad (3.33)$$

$$= [A^c + \hat{a}^c(t)] \cos \omega_0 t + [A^s + \hat{a}^s(t)] \sin \omega_0 t. \quad (3.34)$$

3.1.5 Squeezed state

Variances of two orthogonal quadratures in the coherent (and vacuum) states obey Heisenberg uncertainty relation:

$$\Delta^2 \hat{a}^c(t) \Delta^2 \hat{a}^s(t) \geq \frac{1}{4}, \quad S^{cc}(\Omega) S^{ss}(\Omega) \geq 1, \quad (3.35)$$

and while for these states the variances of two quadratures are equal, in principle, it is possible to reduce one of them at the price of increasing the other – as long as the uncertainty relation is satisfied.

It is straightforward to define a unitary operator generating a squeezed state:

$$\mathcal{S}(\chi) = \exp \left[\int_0^\infty \left(\chi \hat{A}_+^\dagger \hat{A}_-^\dagger - \chi^* \hat{A}_+ \hat{A}_- \right) \frac{d\Omega}{2\pi} \right]. \quad (3.36)$$

For a real $\chi = r$, which we call squeeze factor, the evolution under this operator is defined by a mixing of creation and annihilation operators:

$$\mathcal{S}^\dagger(r) \hat{A} \mathcal{S}(r) = \hat{A}_+ \cosh r + \hat{A}_-^\dagger \sinh r, \quad (3.37)$$

$$\mathcal{S}^\dagger(r) \hat{A}^\dagger \mathcal{S}(r) = \hat{A}_+^\dagger \cosh r + \hat{A}_- \sinh r, \quad (3.38)$$

which for two-photon quadratures results in simple expressions:

$$\mathcal{S}^\dagger(r) \hat{a}^c \mathcal{S}(r) = e^r \hat{a}^c \quad (3.39)$$

$$\mathcal{S}^\dagger(r) \hat{a}^s \mathcal{S}(r) = e^{-r} \hat{a}^s, \quad (3.40)$$

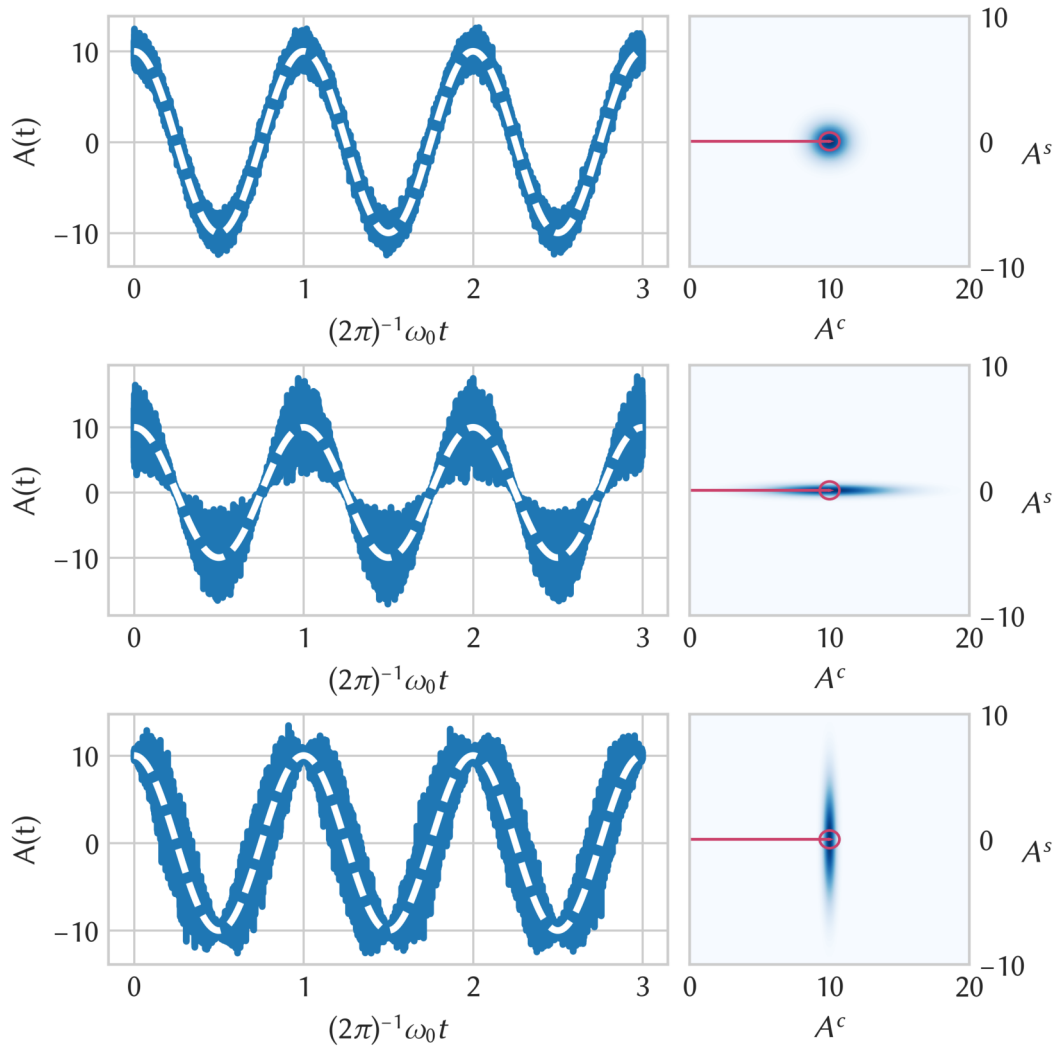


Fig. 3.1. Effect of squeezing on quantum noise in the electromagnetic field for coherent field (top), phase squeezed state (middle) and amplitude squeezed state (bottom). Left: field amplitude $\hat{A}(t) = [A + \hat{a}^c(t)] \cos \omega_0 t + \hat{a}^s(t) \sin \omega_0 t$ as a function of time, classical amplitude A is shown in dashed white. Right: uncertainty of the field amplitude in phase space in a frame, rotating at frequency ω_0 . Classical amplitude A is shown as red arrow in amplitude quadrature; uncertainty of the vacuum state, $\Delta \hat{a}^c = \Delta \hat{a}^s = 1/\sqrt{2}$, is shown in red circle. With 10 dB of squeezing, the uncertainty of quantum noise is suppressed by a factor of $\sqrt{10}$ in one quadrature, and proportionally enhanced in another, according to the Heisenberg uncertainty relation.

Squeezed spectral densities for the quadratures are then anti-squeezed (amplified) and squeezed correspondingly:

$$S^{cc}(\Omega) = e^{2r}, \quad S^{ss}(\Omega) = e^{-2r}, \quad (3.41)$$

where it becomes clear that one quadrature can have significantly suppressed quantum fluctuations. Such a state is called phase-squeezed (since the fluctuations are reduced in phase quadrature), and the opposite choice of the sign (phase) of squeezing strength would yield amplitude-squeezed state, see Fig. 3.1. More generally, for a complex value of $\chi = re^{i\phi}$, where ϕ is the phase of the squeezing, the evolution of a quadrature state can be described by a squeezing matrix:

$$\hat{\mathbf{a}}_{\text{sqz}} = \begin{bmatrix} \hat{a}_{\text{sqz}}^c \\ \hat{a}_{\text{sqz}}^s \end{bmatrix} = \mathbb{S}(r, \phi) \hat{\mathbf{a}}, \quad (3.42)$$

$$\mathbb{S}(r, \phi) = \begin{bmatrix} \cosh r + \sinh r \cos 2\phi & \sinh r \sin 2\phi \\ \sinh r \sin 2\phi & \cosh r - \sinh r \cos 2\phi \end{bmatrix}. \quad (3.43)$$

Notice that the squeeze operation $\mathbb{S}(r, \phi)$ can equivalently be described as a consecutive rotation of quadratures by ϕ , squeezing along the origin, and counter-rotation by ϕ :

$$\mathbb{S}(r, \phi) = \mathbb{O}(\phi) \mathbb{S}(r, 0) \mathbb{O}(-\phi), \quad (3.44)$$

$$\mathbb{O}(\phi) = \begin{bmatrix} \cos \phi & -\sin \phi \\ \sin \phi & \cos \phi \end{bmatrix} \quad (3.45)$$

The resulting state has cross-correlation between the amplitude and phase quadratures, which, as I discussed in Chapter 1, can be used to evade the back-action noise in gravitational-wave detectors.

3.1.6 Entangled state

A more general state is the quantum-entangled state. The entangling operation is akin to the squeezing one, but for two modes \hat{A}, \hat{B} :

$$\mathcal{E}(\chi) = \exp \left[\int_0^\infty \left(\chi \hat{A}_+^\dagger \hat{B}_-^\dagger - \chi^* \hat{A}_+ \hat{B}_- \right) \frac{d\Omega}{2\pi} \right]. \quad (3.46)$$

and introduces correlations between the two optical modes, see e.g. the case of $\chi = r$:

$$\hat{A}_+^o = \mathcal{E}^\dagger(r) \hat{A}_+ \mathcal{E}(r) = \hat{A}_+ \cosh r + \hat{B}_-^\dagger \sinh r, \quad (3.47)$$

$$\hat{B}_+^o = \mathcal{E}^\dagger(r) \hat{B}_+ \mathcal{E}(r) = \hat{B}_+ \cosh r + \hat{A}_-^\dagger \sinh r. \quad (3.48)$$

Notice the similarity to the operator of the squeezed states: this operator produces two-mode squeezed state. The only difference is the definition of the mode: and I take the definition to be dependent on the measurement process. For example, when two independent classical fields are used, this is the case of two-mode squeezing. Another interesting hint to take from this similarity is that squeezing operation produces entanglement between the upper and lower sidebands, and this entanglement is the source of the quantum correlations that allow to suppress the noise in one quadrature.

After defining two-photon quadratures for each of the modes, one can see that their combinations have a curious property:

$$\hat{a}^{o,c}(\Omega) + \hat{b}^{o,c}(\Omega) = e^r (\hat{a}^c(\Omega) + \hat{b}^c(\Omega)), \quad (3.49)$$

$$\hat{a}^{o,c}(\Omega) - \hat{b}^{o,c}(\Omega) = e^{-r} (\hat{a}^c(\Omega) - \hat{b}^c(\Omega)), \quad (3.50)$$

$$\hat{a}^{o,s}(\Omega) + \hat{b}^{o,s}(\Omega) = e^{-r} (\hat{a}^s(\Omega) + \hat{b}^s(\Omega)), \quad (3.51)$$

$$\hat{a}^{o,s}(\Omega) - \hat{b}^{o,s}(\Omega) = e^r (\hat{a}^s(\Omega) - \hat{b}^s(\Omega)), \quad (3.52)$$

such that the two combined observables commute: $[\hat{a}^{o,c}(\Omega) - \hat{b}^{o,c}(\Omega), \hat{a}^{o,s}(\Omega) + \hat{b}^{o,s}(\Omega)] = 0$. This EPR-type correlation [167] allows to infer the values of one of the observables with in principle infinite precision based on the measurements of another one, since there is no uncertainty relation limiting the precision of

their measurement. In Sec. 3.6, I show how we used this property to benefit the sensitivity of a gravitational-wave detector.

3.1.7 Squeezed light from parametric down-conversion

Section 3.1.5 introduces the squeezing operation as a purely mathematical abstraction. Squeezing naturally emerges in various nonlinear processes. One example is parametric down-conversion (PDC) of light by actively pumping a nonlinear material with non-zero second-order nonlinearity in dielectric polarization:

$$\mathcal{P}(E) = \epsilon_0 \left(\chi^{(0)} E + \chi^{(2)} E^2 + \chi^{(3)} E^3 + \dots \right), \quad (3.53)$$

where the second-order susceptibility $\chi^{(2)}$ defines the three-mode interaction in the crystal. The Hamiltonian of this system takes the form [168, 169]:

$$\hat{H} = \hbar\omega_1 \hat{a}_1^\dagger \hat{a}_1 + \hbar\omega_2 \hat{a}_2^\dagger \hat{a}_2 + \hbar\omega_p \hat{b}^\dagger \hat{b} + \frac{i\hbar}{2} (\kappa \hat{a}_1^\dagger \hat{a}_2^\dagger \hat{b} - \kappa^* \hat{a}_1 \hat{a}_2 \hat{b}^\dagger), \quad (3.54)$$

where $\hat{a}_{1,2}$ is the fundamental modes of frequencies $\omega_{1,2}$, \hat{b} is the pumping mode of frequency ω_p , κ is the nonlinear coupling term that is proportional to susceptibility $\chi^{(2)}$ and is real when the fields are phase matched. For the purposes of this analysis, we take the two fundamental modes to be the upper and lower sidebands, so $\omega_1 = \omega_0 + \Omega$, $\omega_2 = \omega_0 - \Omega$, and pump frequency to be twice the fundamental one: $\omega_p = 2\omega_0$. The pump is usually assumed to be strong in the context of squeezed light, such that the effects of quantization of pump light and its depletion can be ignored: $\hat{b} = \beta e^{i\phi} e^{-2i\omega_0 t}$, which brings the Hamiltonian in the following form:

$$\begin{aligned} \hat{H} = \hbar\omega_0 (\hat{a}_+^\dagger \hat{a}_+ + \hat{a}_-^\dagger \hat{a}_-) + 2\hbar\omega_0 |\beta|^2 + \\ + i\hbar\kappa\beta (\hat{a}_+^\dagger \hat{a}_-^\dagger e^{i\phi} e^{-2i\omega_0 t} - \hat{a}_+ \hat{a}_- e^{-i\phi} e^{2i\omega_0 t}) = \hat{H}_0 + \hat{H}_{\text{int}}, \end{aligned} \quad (3.55)$$

where we defined the self-evolution part of the Hamiltonian \hat{H}_0 and the interaction part \hat{H}_{int} . The unitary evolution operator for this system in the interaction picture (i.e. in the frame rotating at ω_0) is defined by the interaction Hamiltonian:

$$\hat{U} = \exp \left[-i\hat{H}_{\text{int}} t \hbar^{-1} \right] = \exp \left[\frac{\kappa\beta}{2} \left(\hat{a}_+^\dagger \hat{a}_-^\dagger e^{i\phi} - \hat{a}_+ \hat{a}_- e^{-i\phi} \right) \right], \quad (3.56)$$

which corresponds to the squeeze operator Eq. 3.36, where $r = \kappa\beta t$. Indeed, the PDC process does produce squeezed states of light. Notice that modes $\hat{a}_{1,2}$ can differ in their fundamental frequency. Then the parametric process entangles these modes, and a suitable mirror can separate them for preparing a "two-color" entangled state [170].

It is important to keep in mind, that although the process involved in creation of squeezed state is nonlinear, from the point of view of the light fields (quadratures), the transformation between them is linear. This allows to describe the evolution of fundamental light fields through a general linear amplification (resulting in all transfer functions for the fields being linear).

3.2 Detection of light

3.2.1 Spectral densities

Suppose we are interested in measuring a classical signal $G(\Omega)$ using a coherent light field in a pure state \hat{a} (in two-photon quadratures). The device has a linear transfer function for the noise $\mathcal{R}(\Omega)$ and signal $\mathcal{T}(\Omega)$, which might involve splitting (and joining) the beam on semi-transparent mirrors, propagation through optical cavities, and linear amplifiers (squeezers). The transformation of these transfer functions to the two-photon quadratures obeys a general rule: for a given input-output relation $\hat{b}(\omega_0 + \Omega) = \mathcal{R}(\omega_0 + \Omega)\hat{a}(\omega_0 + \Omega) = \mathcal{R}_+\hat{a}_+$, the two-photon quadratures are transformed as:

$$\begin{bmatrix} \hat{b}^c(\Omega) \\ \hat{b}^s(\Omega) \end{bmatrix} = \frac{1}{2} \begin{bmatrix} \mathcal{R}_+ + \mathcal{R}_-^* & i(\mathcal{R}_+ - \mathcal{R}_-^*) \\ -i(\mathcal{R}_+ - \mathcal{R}_-^*) & \mathcal{R}_+ + \mathcal{R}_-^* \end{bmatrix} \begin{bmatrix} \hat{a}^c(\Omega) \\ \hat{a}^s(\Omega) \end{bmatrix} \quad (3.57)$$

Then on the output we measure signal and noise, transmitted through the device:

$$\hat{y}(\Omega) = \mathbb{R}^\dagger(\Omega)\hat{a}(\Omega) + \mathbb{T}^\dagger(\Omega)G(\Omega), \quad (3.58)$$

where in general the signal can be both in amplitude and phase quadratures. For our analysis we assume that only a linear combination of quadratures can be measured, so the noise and the signal transfer functions are vectors of the same length as field operators: $\mathbb{R}(\Omega) = \{\mathcal{R}^c(\Omega), \mathcal{R}^s(\Omega)\}^\top$, $\mathbb{T}(\Omega) = \{\mathcal{T}^c(\Omega), \mathcal{T}^s(\Omega)\}^\top$.

For simplicity (and since that's the only case I discuss throughout the thesis), we are going to assume that the signal is in the phase quadrature: $\mathbb{T}^\dagger(\Omega)G(\Omega) = (\mathcal{T}^s)^*(\Omega)G^s(\Omega) = \mathcal{T}^*(\Omega)G(\Omega)$. Alternatively, one can always apply a rotation such, that the signal is fully contained in one quadrature.

We assume that the classical value that we obtain as a result of the measurement is linear with respect to the observable \hat{y} . Since we are interested in the sensitivity of the device, we normalize the output to the signal transfer function:

$$\tilde{\hat{y}}(\Omega) = \frac{1}{\mathcal{T}^*(\Omega)} \mathbb{R}^\dagger(\Omega) \hat{\mathbf{a}}(\Omega) + G(\Omega) = \hat{\mathbf{n}}(\Omega) + G(\Omega), \quad (3.59)$$

where I defined the normalized noise on the output $\hat{\mathbf{n}}(\Omega)$, which provides the full information about the sensitivity. The spectral density of this observable can be computed:

$$\begin{aligned} 2\pi S_{nn}(\Omega) \delta(\Omega - \Omega') &= \langle \hat{\mathbf{n}}(\Omega) \hat{\mathbf{n}}^\dagger(\Omega') \rangle_{\text{sym}} = \\ &= \frac{1}{|\mathcal{T}(\Omega)|^2} \mathbb{R}^\dagger(\Omega) \langle \hat{\mathbf{a}}(\Omega) \hat{\mathbf{a}}^\dagger(\Omega') \rangle_{\text{sym}} \mathbb{R}(\Omega'), \end{aligned} \quad (3.60)$$

from where we find the expression for the spectral density in terms of input spectral densities:

$$S_{nn}(\Omega) = \frac{1}{|\mathcal{T}(\Omega)|^2} \mathbb{R}^\dagger(\Omega) \begin{bmatrix} S^{cc}(\Omega) & S^{cs}(\Omega) \\ S^{sc}(\Omega) & S^{ss}(\Omega) \end{bmatrix} \mathbb{R}(\Omega) \quad (3.61)$$

This will be the basis for the transfer matrix approach to computing the sensitivities: finding the signal and noise transfer functions, and using the equation above to calculate the spectrum.

3.2.2 Balanced homodyne detection

There are various particular schemes that realize the linear transfer function between the quantum observable and classical signal. The simplest example is

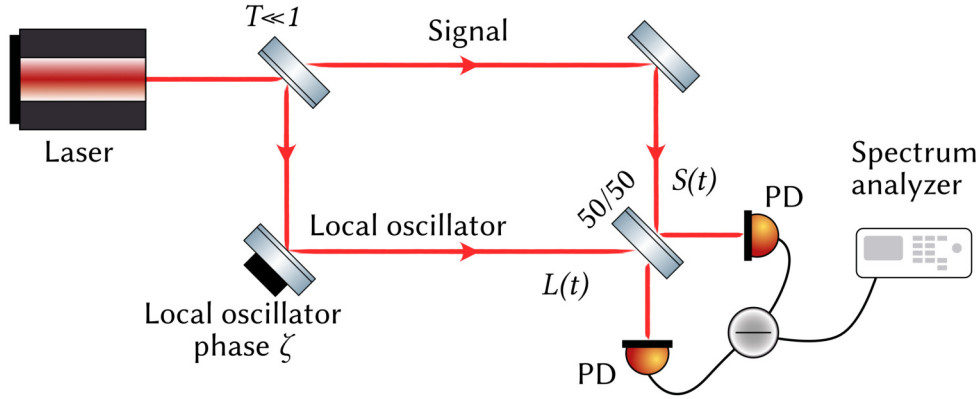


Fig. 3.2. Schematic of a homodyne detector. Laser beam is split into the strong local oscillator (LO) field, and signal field, which is then sent into experiment (not in the figure). The phase ζ of the LO field can be adjusted by a piezo-actuated mirror. The signal and LO fields are overlapped on the 50/50 beamsplitter, and the two outputs are measured by photodetectors (PD). The resulting photocurrents are subtracted and sent on the data acquisition device.

a photodiode: the current of the photodiode is proportional to the light field intensity I :

$$i \propto I(t) = \hbar\omega_0 \overline{|(A^c + \hat{a}^c) \cos \omega_0 t + a^s \sin \omega_0 t|^2} \approx I_0 + \hbar\omega_0 A^c \hat{a}^c(t), \quad (3.62)$$

where we can only observe the amplitude fluctuations $\hat{a}^c(t)$ (since the phase is not an observable). In order to realize the observation of phase quadrature, one first needs to convert phase fluctuations into the amplitude ones, which would then be measured by the photodetector.

An example of such a scheme is a balanced homodyne detector. In this scheme the signal beam $S(t)$ is split on a 50/50 beamsplitter, and overlapped with a strong local oscillator field, see Fig. 3.2:

$$S(t) = (S + \hat{s}^c(t)) \cos \omega_0 t + \hat{s}^s(t) \sin \omega_0 t, \quad (3.63)$$

$$L(t) = (L_0 \cos \zeta + \hat{l}^c(t)) \cos \omega_0 t + (L_0 \sin \zeta + \hat{l}^s(t)) \sin \omega_0 t, \quad (3.64)$$

where I selected the signal phase such that the classical amplitude S is only in the amplitude quadrature, and introduced local oscillator's classical field L_0 , phase

ζ and amplitude and phase noises $l_{c,s}$. After the overlap on the beamsplitter the two fields are detected on the photodiodes, so:

$$i_1 \propto \frac{|L(t) + S(t)|^2}{2} \approx \frac{S^2 + L_0^2 + 2SL_0 \cos \zeta}{2} + L_0(\hat{s}^c(t) + \hat{l}^c(t)) \cos \zeta + L_0(\hat{s}^s(t) + \hat{l}^s(t)) \sin \zeta + S(\hat{s}^c(t) + \hat{l}^c(t)), \quad (3.65)$$

$$i_2 \propto \frac{|L(t) - S(t)|^2}{2} \approx \frac{S^2 + L_0^2 - 2SL_0 \cos \zeta}{2} + L_0(\hat{s}^c(t) - \hat{l}^c(t)) \cos \zeta - L_0(\hat{s}^s(t) - \hat{l}^s(t)) \sin \zeta + S(\hat{s}^c(t) - \hat{l}^c(t)), \quad (3.66)$$

where all the noises are assumed to be small compared to the mean amplitudes. The two currents $i_{1,2}$ are then subtracted, such that the resulting signal is:

$$i_1 - i_2 \propto 2L_0 (S \cos \zeta + \hat{s}^c(t) \cos \zeta + \hat{s}^s(t) \sin \zeta) + 2S\hat{l}^c(t), \quad (3.67)$$

and since typically the classical field in the signal is relatively weak, the homodyne signal can further be approximated:

$$i_1 - i_2 \propto 2L_0 (\hat{s}^c(t) \cos \zeta + \hat{s}^s(t) \sin \zeta), \quad (3.68)$$

. One can see, that as long as the local oscillator is much stronger than the signal field, the main contribution comes from the signal, which is linearly amplified by the local oscillator amplitude.

There are several useful features of the homodyne detector:

- it allows to select the measured quadrature of the signal by adjusting the LO phase ζ ;
- there is no DC contribution to the measured output, which improves the sensitivity of the detector, allowing better electronic characteristics of the detector board;
- classical noises of the local oscillator are canceled (or suppressed, depending on the average power in the signal)

- the signal is linearly amplified by the LO amplitude, and the output spectrum of the current directly relates to the spectrum of the signal.

On the other hand, it requires good mode overlap between the LO and signal fields, and good balancing of the splitting ratio.

Homodyne detection from the point of view of the linear measurement can be described by a transfer vector:

$$\mathbb{H}(\zeta) = \begin{bmatrix} \cos \zeta \\ \sin \zeta \end{bmatrix}, \quad (3.69)$$

and the output of the homodyne detector:

$$i_1 - i_2 \propto \hat{y}(\Omega) = \mathbb{H}^T(\zeta) \mathbb{R}^\dagger(\Omega) \mathbf{a}(\Omega), \quad (3.70)$$

where $\mathbb{R}(\Omega)$ is the full transfer matrix of a system for input noise $\mathbf{a}(\Omega)$.

3.3 Quantum-correlated light for sensing the motion of a mirror

In this section I describe how to measure the motion of a single perfectly reflective free mass, with force $G(t)$ acting on it, see Fig. 3.3. The incoming light in the two-photon picture:

$$\hat{A}(t) = (A_0 + \hat{a}^c(t)) \cos \omega_0 t + \hat{a}^s(t) \sin \omega_0 t. \quad (3.71)$$

The outgoing light will be delayed by $2\hat{x}(t)/c$ relative to the incoming light, and assuming this delay to be very small, we can make a Taylor expansion:

$$\begin{aligned} \hat{B}(t) &= \hat{A}(t - 2\hat{x}/c) \\ &\approx (A_0 + \hat{a}^c(t)) \cos \omega_0 t + \left(\hat{a}^s(t) - 2A_0 \frac{\omega_0}{c} \hat{x}(t) \right) \sin \omega_0 t. \end{aligned} \quad (3.72)$$

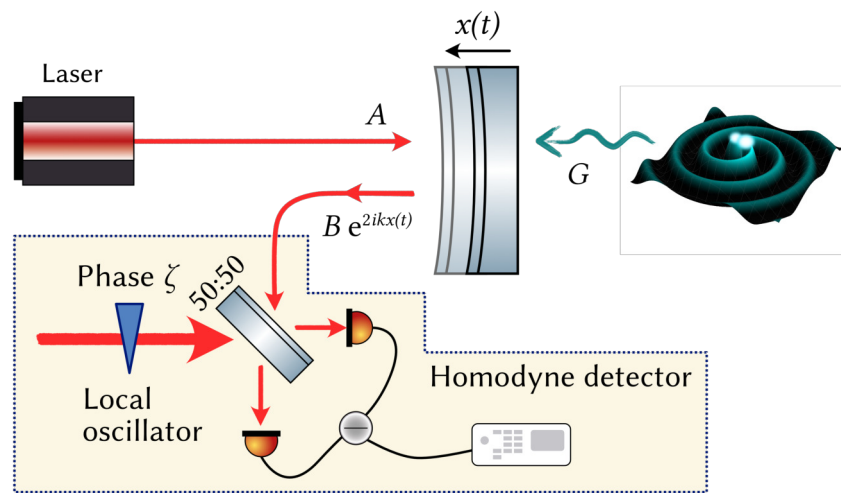


Fig. 3.3. Sensing the motion of a mirror with light. Classical force $G(t)$ acts on a free mass (mirror), causing its displacement $x(t)$. This displacement is sensed by reflecting laser light off the reflective surface of the mirror. Reflected light carries the information about the displacement in the phase $\exp[2ikx(t)]$. This phase can be sensed by overlapping the signal beam with a strong local oscillator field on a 50:50 beamsplitter, and then observing the interference on the two photodiodes. The difference of the photocurrents is linearly proportional to the phase of the signal beam, if the appropriate phase ζ of the local oscillator is selected.

The input-output relations describe the propagation of light through the system for classical and quantum fields:

$$B_0 = A_0, \quad (3.73)$$

$$\hat{b}^c(t) = \hat{a}^c(t), \quad (3.74)$$

$$\hat{b}^s(t) = \hat{a}^s(t) - 2A_0 \frac{\omega_0}{c} \hat{x}(t), \quad (3.75)$$

which can be translated into the frequency domain:

$$B_0 = A_0, \quad (3.76)$$

$$\hat{b}^c(\Omega) = \hat{a}^c(\Omega), \quad (3.77)$$

$$\hat{b}^s(\Omega) = \hat{a}^s(\Omega) - 2\sqrt{\frac{2I_0}{\hbar\omega_0}} \frac{\omega_0}{c} \hat{x}(\Omega), \quad (3.78)$$

where I introduced the field intensity I_0 .

Motion of the mirror is caused by the signal force $G(t)$, which is assumed to be classical, and radiation-pressure force: $\hat{F}_{\text{rp}} = 2\hat{I}(t)c^{-1}$:

$$M\ddot{\hat{x}}(t) = \hat{F}_{\text{rp}}(t) + G(t), \quad (3.79)$$

$$-M\Omega^2 \hat{x}(\Omega) = \hat{F}_{\text{rp}}(\Omega) + G(\Omega). \quad (3.80)$$

Radiation-pressure force has generally a constant contribution from the classical light amplitude, and a fluctuating part from quantum noise. Since in time-domain $\hat{I}(t) = \hbar\omega_0 \overline{|A(t)|^2} \approx I_0 + A_0 \hbar\omega_0 \hat{a}^c(t) = I_0 + \sqrt{2I_0 \hbar\omega_0} \hat{a}^c(t)$, the radiation-pressure force is:

$$\hat{F}_{\text{rp}}(\Omega) \approx \frac{2I_0}{c} + \frac{2\sqrt{2I_0 \hbar\omega_0} \hat{a}^c(\Omega)}{c}, \quad (3.81)$$

which results in the equation of motion for a free mass (ignoring the constant force):

$$\hat{x}(\Omega) = \frac{1}{-M\Omega^2} \left(\frac{2\sqrt{2I_0 \hbar\omega_0} \hat{a}^c(\Omega)}{c} + G(\Omega) \right). \quad (3.82)$$

We can define an optomechanical coupling factor (Kimble factor), which describes the coupling between the position and radiation-pressure:

$$\mathcal{K}(\Omega) = \frac{8\omega_0 I_0}{Mc^2 \Omega^2}, \quad (3.83)$$

and then re-write the input-output relations in a different form:

$$\begin{bmatrix} \hat{b}^c(\Omega) \\ \hat{b}^s(\Omega) \end{bmatrix} = \begin{bmatrix} 1 & 0 \\ -\mathcal{K}(\Omega) & 1 \end{bmatrix} \begin{bmatrix} \hat{a}^c(\Omega) \\ \hat{a}^s(\Omega) \end{bmatrix} + \begin{bmatrix} 0 \\ \sqrt{2\mathcal{K}(\Omega)} \end{bmatrix} \frac{G(\Omega)}{F_{\text{SQL}}(\Omega)}, \quad (3.84)$$

where $F_{\text{SQL}}(\Omega)$ is the SQL for force sensing, which was derived in the Introduction:

$$F_{\text{SQL}}(\Omega) = \sqrt{2\hbar M \Omega^2}. \quad (3.85)$$

We can see that the interaction with the mirror causes mixing of two quadratures. This introduces correlations between them – the effect, called *ponderomotive squeezing* [102, 171].

We can now use the approach developed in the previous section to compute the sensitivity of this setup as measured on the homodyne detector:

$$\hat{y}(\Omega) = \mathbb{H}^\top(\zeta) \mathbf{b}(\Omega) = \mathbb{H}^\top(\zeta) \mathbb{R}^\dagger(\Omega) \mathbf{a}(\Omega) + \frac{\sqrt{2\mathcal{K}(\Omega)}}{F_{\text{SQL}}(\Omega)} G(\Omega) \sin \zeta. \quad (3.86)$$

This results in a spectral density, normalized to the force G :

$$S(\Omega) = \frac{F_{\text{SQL}}^2(\Omega)}{2\mathcal{K}(\Omega) \sin^2 \zeta} \mathbb{H}^\top(\zeta) \mathbb{R}^\dagger(\Omega) \mathbb{S}(\Omega) \mathbb{R}(\Omega) \mathbb{H}(\zeta), \quad (3.87)$$

and assuming the input state to be vacuum: $\mathbb{S}(\Omega) = \mathbb{I}$ (identity matrix), and measurement to take place in phase quadrature, where the signal is maximized: $\zeta = \pi/2$ we obtain the sensitivity:

$$S(\Omega) = \frac{F_{\text{SQL}}^2(\Omega)}{2} \left(\frac{1}{\mathcal{K}(\Omega)} + \mathcal{K}(\Omega) \right), \quad (3.88)$$

which is the generic form of all standard sensitivities, where only the particular function $\mathcal{K}(\Omega)$ changes depending on the topology, as I discuss in detail in Chapter 5.

There is another way to compute the sensitivity, which is mentioned in the introduction: first compute the shot and QRPN noises separately, and then add them using the rules for addition. This approach is more useful for understanding the details of each particular contribution, while the transfer matrix approach is

convenient for numerical calculations. We can use this approach to compute the noises starting from equation for the output in a different form:

$$\begin{aligned}\tilde{y}(\Omega) &= \frac{F_{\text{SQL}}(\Omega)}{\sqrt{2\mathcal{K}(\Omega)} \sin \zeta} (\hat{a}^c(\Omega) \cos \zeta + \hat{a}^s(\Omega) \sin \zeta) + \hat{F}_{\text{rp}}(\Omega) + G(\Omega) \\ &= M\Omega^2 \hat{x}_n(\Omega) + \hat{F}_{\text{rp}}(\Omega) + G(\Omega)\end{aligned}\quad (3.89)$$

We can compute the spectral density of every part separately (assuming no cross-correlation on the input state: $S^{sc}(\Omega) = 0$):

$$S_{xx}(\Omega) = \frac{F_{\text{SQL}}^2(\Omega)}{2\mathcal{K}(\Omega)M^2\Omega^4 \sin^2 \zeta} (S^{cc}(\Omega) \cos^2 \zeta + S^{ss}(\Omega) \sin^2 \zeta), \quad (3.90)$$

$$S_{FF}(\Omega) = \mathcal{K}(\Omega)F_{\text{SQL}}^2(\Omega)S^{cc}(\Omega), \quad (3.91)$$

$$S_{xF}(\Omega) = \frac{F_{\text{SQL}}^2(\Omega)}{2M\Omega^2} S^{cc}(\Omega) \cot \zeta, \quad (3.92)$$

and for the total spectral density, assuming the input state to be vacuum, $S^{cc}(\Omega) = S^{ss}(\Omega) = 1$:

$$\begin{aligned}S(\Omega) &= M\Omega^4 S_{xx}(\Omega) - 2M\Omega^2 \Re[S_{xF}(\Omega)] + S_{FF}(\Omega) = \\ &= \frac{F_{\text{SQL}}^2(\Omega)}{2} \left(\frac{1}{\mathcal{K}(\Omega) \sin^2 \zeta} - 2 \cot^2 \zeta + \mathcal{K}(\Omega) \right)\end{aligned}\quad (3.93)$$

As an exercise, we can demonstrate the use of cross-correlation between the noises $S_{xF}(\Omega)$ for surpassing the SQL, as I did already in the Introduction. For that we minimize the expression above with respect to the readout angle: $\cot \zeta = \mathcal{K}(\Omega)$, which yields an unbounded spectral density:

$$S^{(\text{opt})}(\Omega) = \frac{F_{\text{SQL}}^2(\Omega)}{2\mathcal{K}(\Omega)}. \quad (3.94)$$

The difficulty here is in creating the necessary cross-correlation between the noises. It is possible by using a frequency-dependent homodyne angle in the variational readout scheme [112].

3.3.1 Squeezed light

Finally, we can describe demonstrate the effect of squeezed light injection on the sensitivity. When the input state is phase-squeezed, $S^{ss}(\Omega) = e^{-2r}$, $S^{cc} = e^{2r}$, we obtain for the shot and radiation-pressure noise:

$$S_{xx}(\Omega) = \frac{F_{\text{SQL}}^2(\Omega)e^{-2r}}{2\mathcal{K}(\Omega)M^2\Omega^4}, \quad (3.95)$$

$$S_{FF}(\Omega) = \mathcal{K}(\Omega)F_{\text{SQL}}^2(\Omega)e^{2r}, \quad (3.96)$$

so the shot noise is suppressed, and radiation-pressure noise is amplified (which is required by the SQL), as I showed previously in Fig. 2.5:

$$S(\Omega) = \frac{F_{\text{SQL}}^2(\Omega)}{2} \left(\frac{e^{-2r}}{\mathcal{K}(\Omega)} + e^{2r}\mathcal{K}(\Omega) \right). \quad (3.97)$$

It is possible to use frequency-dependent squeezing, where the amplitude quadrature is squeezed at low frequencies (and thus radiation-pressure reduced), and phase quadrature is squeezed at high frequencies. Such frequency-dependent rotation of the squeezed quadratures can be described by a squeezing matrix $\mathbb{S}(r, \phi)$, see Eq. 3.43, with frequency-dependent phase $\phi(\Omega)$:

$$\begin{bmatrix} \hat{b}^c(\Omega) \\ \hat{b}^s(\Omega) \end{bmatrix} = \begin{bmatrix} 1 & 0 \\ -\mathcal{K}(\Omega) & 1 \end{bmatrix} \mathbb{S}(r, \phi) \begin{bmatrix} \hat{a}^c(\Omega) \\ \hat{a}^s(\Omega) \end{bmatrix} + \begin{bmatrix} 0 \\ \sqrt{2\mathcal{K}(\Omega)} \end{bmatrix} \frac{G(\Omega)}{F_{\text{SQL}}(\Omega)}. \quad (3.98)$$

As in the case with a variational readout, a straightforward optimization of the squeezing phase $\phi(\Omega) = \arctan \mathcal{K}(\Omega)$ results in a phase quadrature squeezed for both shot and radiation-pressure part:

$$\hat{b}^s(\Omega) = e^{-r} (\hat{a}^s(\Omega) - \mathcal{K}\hat{a}^c(\Omega)) + \frac{\sqrt{2\mathcal{K}(\Omega)}G(\Omega)}{F_{\text{SQL}}(\Omega)}, \quad (3.99)$$

and the corresponding spectral density is suppressed by e^{2r} at all frequencies:

$$S(\Omega) = \frac{F_{\text{SQL}}^2(\Omega)e^{-2r}}{2} \left(\frac{1}{\mathcal{K}(\Omega)} + \mathcal{K}(\Omega) \right). \quad (3.100)$$

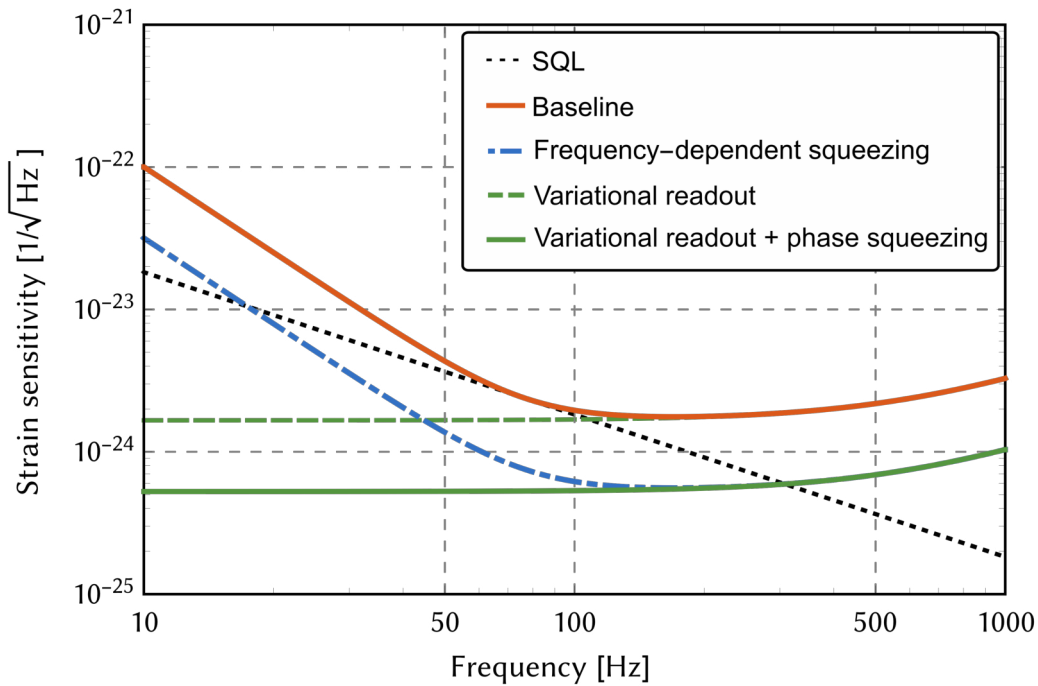


Fig. 3.4. Comparison of effects of variational readout and frequency-dependent squeezing on quantum noise in GW detectors. Frequency-dependent squeezing suppresses both shot noise and QRPN equally, effectively achieving the same sensitivity gain at all frequencies. Variational readout allows to evade the back-action completely, but does not affect shot noise at high frequency. A combination of variational readout with frequency-independent squeezing in phase quadrature allows to achieve the highest gain in sensitivity.

As with the case of variational readout, implementing a particular frequency dependence for the squeezing angle is challenging, and requires long high-quality filter cavities, which would provide the desired frequency dependence to the phase of squeezed light reflected off them [112]. These cavities need to have particularly low optical loss, since quantum correlations that allow to achieve the desired effect are very sensitive to loss. The important difference to the variational readout is that here back-action is evaded only partially, while the variational readout would allow full back-action evasion in the ideal case, see Fig. 3.4. Practically though, when the effect of optical losses is included, the difference between the two approaches becomes marginal [35]. A more detailed description of different spectral densities in gravitational-wave detectors can be found in Chapter 5.

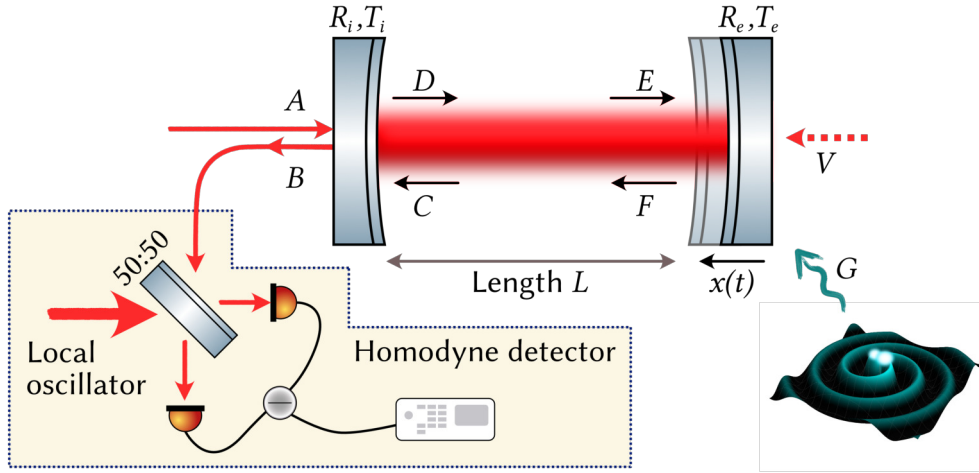


Fig. 3.5. Optical cavity with a movable end mirror. External force G (e.g. from GW) displaces a mirror by $x(t)$

3.4 Optical cavity

Optical cavities are the basis of modern metrological devices, including the gravitational-wave detectors. In this section I describe the input-output relations for the fields propagating through the cavity, define all main parameters and compute the signal and the noise.

I start by solving the steady-state equations of motion for the fields as they reflect off the mirrors and propagate through free space, see Fig. 3.5.

$$\hat{D}(\omega) = R_i \hat{C}(\omega) + T_i \hat{A}(\omega), \quad (3.101)$$

$$\hat{E}(\omega) = \hat{D}(\omega) e^{i\omega\tau}, \quad (3.102)$$

$$\hat{F}(\omega) = R_e \hat{E}(\omega) + T_e \hat{V}(\omega), \quad (3.103)$$

$$\hat{C}(\omega) = \hat{F}(\omega) e^{i\omega\tau}, \quad (3.104)$$

$$\hat{B}(\omega) = -R_i \hat{A}(\omega) + T_i(\omega) \hat{C}(\omega), \quad (3.105)$$

$$(3.106)$$

where we introduce the amplitude transmissivity and reflectivity of the mirrors $R_{i,e}^2 + T_{i,e}^2 = 1$, and the phase accumulated during travel in free space of length L depends on the travel time $\tau = L/c$. We can solve these equations:

$$\hat{C}(\omega) = \frac{R_e T_i \hat{A}(\omega) e^{2i\omega\tau} + T_e \hat{V}(\omega) e^{i\omega\tau}}{1 - R_e R_i e^{2i\omega\tau}}, \quad (3.107)$$

$$\hat{B}(\omega) = \frac{(-R_i + R_e e^{2i\omega\tau}) \hat{A}(\omega) + T_i T_e \hat{V}(\omega) e^{i\omega\tau}}{1 - R_e R_i e^{2i\omega\tau}}. \quad (3.108)$$

First, we can find the resonance condition of the cavity by looking for a maximal amplification inside the cavity, i.e. where the absolute value of the denominator of Eq.(3.107) reaches its minimum. This can be done by solving the equation

$$\frac{d|1 - R_e R_i e^{2i\omega\tau}|^2}{d\omega} = \frac{d(1 + R_e^2 R_i^2 - 2R_e R_i \cos \omega\tau)}{d\omega} = 0, \quad (3.109)$$

which yields a simple solution $\omega_0 = n\pi/(\tau)$, $n \in \mathbb{N}_0$, which is of course a well known condition for the resonance of the cavity: the round number of half-wavelength $\lambda_0/2$ should fit into the cavity length L : $L = n\lambda_0/2$, $n = 1, 2, 3 \dots$. The fields can then be described relative to this resonance frequency at sideband frequency $\Omega = \omega - \omega_0$. It is convenient to simplify the equations by assuming the cavity to have a relatively high finesse, and the sideband frequency to be low compared to the free spectral range of the cavity ($f_{\text{FSR}} = (2\tau)^{-1}$). These two conditions are known as a single-mode approximation: (i) $T_{i,e} \ll 1$, which allows to expand $R_{i,e} = \sqrt{1 - T_{i,e}} \approx 1 - T_{i,e}^2/2$; (ii) $\Omega\tau \ll 1$, so $e^{i\Omega\tau} \approx 1 + i\Omega\tau$. We can define the cavity bandwidth:

$$\gamma_{i,e} = \frac{cT_{i,e}^2}{4L}, \quad \gamma = \gamma_i + \gamma_e, \quad (3.110)$$

and use the single-mode approximation to expand the coefficients in the Eqs. (3.107),(3.108):

$$1 - R_e R_i e^{2i\Omega\tau} \approx 1 - 1 + \frac{T_e^2}{2} + \frac{T_i^2}{2} - 2i\Omega\tau = 2\tau(\gamma - i\Omega), \quad (3.111)$$

$$R_e T_i \approx T_i = \sqrt{4\gamma_i\tau}, \quad (3.112)$$

$$-R_i + R_e e^{2i\omega\tau} \approx -1 + \frac{T_i^2}{2} + 1 - \frac{T_e^2}{2} + 2i\Omega\tau = 2\tau(\gamma_i - \gamma_e + i\Omega), \quad (3.113)$$

$$T_i T_e \approx 4\tau\sqrt{\gamma_i\gamma_e}. \quad (3.114)$$

$$(3.115)$$

This approximation gives a more convenient form of the Eqs. (3.107),(3.108):

$$\hat{C}(\Omega) = \frac{1}{\sqrt{\tau}} \frac{\sqrt{\gamma_i}\hat{A}(\Omega) + \sqrt{\gamma_e}\hat{V}(\Omega)}{\gamma - i\Omega} \quad (3.116)$$

$$\begin{aligned} \hat{B}(\Omega) &= \frac{(\gamma_i - \gamma_e + i\Omega)\hat{A}(\Omega) + 2\sqrt{\gamma_i\gamma_e}\hat{V}(\Omega)}{\gamma - i\Omega} = \\ &= \mathcal{R}(\Omega)\hat{A}(\Omega) + \mathcal{T}(\Omega)\hat{V}(\Omega), \end{aligned} \quad (3.117)$$

where we introduced frequency-dependent reflection and transmission coefficients $\mathcal{R}(\Omega), \mathcal{T}(\Omega)$:

$$\mathcal{R}(\Omega) = \frac{(\gamma_i - \gamma_e + i\Omega)}{\gamma - i\Omega}, \quad (3.118)$$

$$\mathcal{T}(\Omega) = \frac{2\sqrt{\gamma_i\gamma_e}}{\gamma - i\Omega}. \quad (3.119)$$

The optical power is amplified inside the single-sided cavity on resonance ($\Omega = 0, \gamma_e = 0$) by its finesse $\mathcal{F} \approx 2\pi f_{FSR}(2\gamma)^{-1}$:

$$|C(0)|^2/|A(0)|^2 = \frac{1}{\gamma\tau} = \frac{2f_{FSR}}{\gamma} = \frac{2\mathcal{F}}{\pi}. \quad (3.120)$$

Sensing a signal

When a back mirror is displaced by a small amount x , the light reflected off this mirror acquires an additional phase shift $2i\omega\hat{x}(\omega)c^{-1}$, so equations Eqs. 3.101 are modified slightly:

$$\hat{F}(\omega) = R_e\hat{E}(\omega)e^{2i\omega x(\omega)c^{-1}} + T_e\hat{V}(\omega), \quad (3.121)$$

and if the displacement is small, the exponent can be expanded: $e^{2i\omega x(\omega)c^{-1}} \approx 1 + 2i\omega_0 x(\omega)c^{-1}$, as we did with a single mirror.

In the single-mode approximation $C(\Omega) = E(\Omega) = F(\Omega)$, and also assuming the intra-cavity field is monochromatic (i.e. $E(\Omega) \approx E(0)$), the signal part of the output takes the form:

$$\hat{B}_x(\Omega) = \frac{2i\omega_0 x c^{-1} E(0) T_i}{1 - R_e R_i e^{2i\Omega\tau}} = 2i \frac{\gamma_i}{c\tau} \frac{\omega_0 A(0)}{\gamma(\gamma - i\Omega)} \hat{x}(\Omega). \quad (3.122)$$

Finally, we can make split the fields into classical and quantum parts: $\hat{A}(\Omega) = A_0 + \hat{a}(\Omega)$, and transition to the two-photon quadratures. Notice, that in the simplest case we assume no coupling between the two quadratures in the equations of motion, and thus can directly write down the equations of motion for the quadratures, which will be the same as for the sidebands (in shape). In a more general case, one needs to compute the transfer matrices, as will be done in the rest of the thesis. Here, however, keeping things simple, we can write quantum noises and the signal on the output of the cavity:

$$\hat{b}^c(\Omega) = \mathcal{R}(\Omega)\hat{a}^c(\Omega) + \mathcal{T}\hat{v}^c(\Omega), \quad (3.123)$$

$$\hat{b}^s(\Omega) = \mathcal{R}(\Omega)\hat{a}^s(\Omega) + \mathcal{T}\hat{v}^s(\Omega) + 2i \frac{\gamma_i}{c\tau} \frac{\omega_0 A_0}{\gamma(\gamma - i\Omega)} \hat{x}(\Omega). \quad (3.124)$$

Making a further approximation by assuming the back mirror to be perfectly reflective, we arrive at the same set of equations as for the case of a single mirror (c.f. Eq. 3.84):

$$\begin{bmatrix} \hat{b}^c(\Omega) \\ \hat{b}^s(\Omega) \end{bmatrix} = e^{2i\phi} \begin{bmatrix} 1 & 0 \\ -\mathcal{K}(\Omega) & 1 \end{bmatrix} \begin{bmatrix} \hat{a}^c(\Omega) \\ \hat{a}^s(\Omega) \end{bmatrix} + e^{-i\phi} \begin{bmatrix} 0 \\ \sqrt{2\mathcal{K}(\Omega)} \end{bmatrix} \frac{G(\Omega)}{F_{\text{SQL}}(\Omega)}, \quad (3.125)$$

but with an additional phase and a new definition of a Kimble factor $\mathcal{K}(\Omega)$, which includes a normalized power J :

$$\phi \equiv \arctan \Omega/\gamma, \quad \mathcal{K}(\Omega) = \frac{2\gamma J}{\Omega^2(\gamma^2 + \Omega^2)}, \quad J = \frac{8\omega_0 I_c}{McL}, \quad (3.126)$$

where I_c is the light power inside the cavity. The spectral density takes the same form as for a single mirror:

$$S(\Omega) = \frac{F_{\text{SQL}}^2(\Omega)}{2} \left(\frac{1}{\mathcal{K}(\Omega)} + \mathcal{K}(\Omega) \right), \quad (3.127)$$

3.4.1 Detuned cavity

Considering a more general case of a cavity detuned from its resonance generally needs to start with input-output relations in the sideband picture, but it is more convenient to directly compute everything in the two-photon quadrature picture. It also gives a chance to demonstrate the approach to computing the sensitivity using transfer matrices.

The detuning of a carrier field from cavity resonance, $\delta = \omega - \omega_0$, adds an additional phase shift on the free-propagating fields: $e^{i(\omega+\Omega+\delta)\tau}$. In the two-photon picture such a phase shift can be seen as rotation of quadratures by a phase $\delta\tau$, so e.g. the equations 3.101 for a detuned cavity take the form:

$$\hat{\mathbf{e}}(\Omega) = e^{i\Omega\tau} \mathbb{O}[\delta\tau] \hat{\mathbf{d}}(\Omega) = \mathbb{P}(\Omega) \hat{\mathbf{d}}(\Omega), \quad (3.128)$$

where I defined the matrix for free-space propagation \mathbb{P} . We can re-write Eqs. 3.101 in a matrix form (omitting the signal part for now):

$$\hat{\mathbf{d}}(\Omega) = \mathbb{R}_i \hat{\mathbf{c}}(\Omega) + \mathbb{T}_i \hat{\mathbf{a}}(\Omega), \quad (3.129)$$

$$\hat{\mathbf{e}}(\Omega) = \mathbb{P}(\Omega) \hat{\mathbf{d}}(\Omega), \quad (3.130)$$

$$\hat{\mathbf{f}}(\Omega) = \mathbb{R}_e \hat{\mathbf{e}}(\Omega) + \mathbb{T}_e \hat{\mathbf{v}}(\Omega), \quad (3.131)$$

$$\hat{\mathbf{c}}(\Omega) = \mathbb{P}(\Omega) \hat{\mathbf{f}}(\Omega), \quad (3.132)$$

$$\hat{\mathbf{b}}(\Omega) = -\mathbb{R}_i \hat{\mathbf{a}}(\Omega) + \mathbb{T}_i \hat{\mathbf{c}}(\Omega). \quad (3.133)$$

I keep the reflection and transmission matrices in this form to demonstrate the approach, although $\mathbb{R}_{i,e} = R_{i,e} \mathbb{I}$, $\mathbb{T}_{i,e} = T_{i,e} \mathbb{I}$. The solution to this set of equations is:

$$\hat{\mathbf{c}}(\Omega) = \mathbb{K}(\Omega) \mathbb{P}(\Omega) \mathbb{R}_e \mathbb{P}(\Omega) \mathbb{T}_e \hat{\mathbf{a}}(\Omega) + \mathbb{K}(\Omega) \mathbb{P}(\Omega) \mathbb{T}_e \hat{\mathbf{v}}(\Omega), \quad (3.134)$$

$$\hat{\mathbf{b}}(\Omega) = (-\mathbb{R}_i + \mathbb{T}_i \mathbb{K}(\Omega) \mathbb{P}(\Omega) \mathbb{R}_e \mathbb{P}(\Omega) \mathbb{T}_e) \hat{\mathbf{a}}(\Omega) + \mathbb{T}_i \mathbb{K}(\Omega) \mathbb{P}(\Omega) \mathbb{T}_e \hat{\mathbf{v}}(\Omega), \quad (3.135)$$

$$\mathbb{K}(\Omega) = [\mathbb{I} - \mathbb{P}(\Omega) \mathbb{R}_e \mathbb{P}(\Omega) \mathbb{R}_i]^{-1}. \quad (3.136)$$

Following the approach to computing spectral densities I described in this chapter, we can find a generic expression for the noise spectral density of the output:

$$\begin{aligned} S_{bb}(\Omega) &= (-\mathbb{R}_i + \mathbb{T}_i \mathbb{K}(\Omega) \mathbb{P}(\Omega) \mathbb{R}_e \mathbb{P}(\Omega) \mathbb{T}_e) S_{aa}(\Omega) \times \\ &\quad \times (-\mathbb{R}_i + \mathbb{T}_i \mathbb{K}(\Omega) \mathbb{P}(\Omega) \mathbb{R}_e \mathbb{P}(\Omega) \mathbb{T}_e)^\dagger + \\ &\quad + \mathbb{T}_i \mathbb{K}(\Omega) \mathbb{P}(\Omega) \mathbb{T}_e S_{vv}(\Omega) \mathbb{T}_e^\dagger \mathbb{P}^\dagger(\Omega) \mathbb{K}^\dagger(\Omega) \mathbb{T}_i^\dagger. \end{aligned} \quad (3.137)$$

Such an expression is obviously not very useful for understanding the nature of quantum noise, but can be easily computed using computing software, such as Wolfram Mathematica. This particular case can be calculated analytically in a straightforward way, but when a more complicated case is considered, e.g. with multiple coupled cavities, optical losses, etc., a numerical approach becomes useful.

In order to complete the consideration of a detuned cavity, I simplify the equations above by going to the single-mode approximation. In the single mode approximation detuning is also considered to be small relative to the free spectral

range of a cavity, which allows to expand: $\cos \delta\tau \approx 1$, $\sin \delta\tau \approx -\delta\tau$, which allows to write the rotation matrix as:

$$\mathbb{O}[\delta\tau] \approx \begin{bmatrix} 1 & \delta \\ -\delta & 1 \end{bmatrix} \approx \mathbb{I} + \begin{bmatrix} 0 & \delta \\ -\delta & 0 \end{bmatrix}. \quad (3.138)$$

The resulting input-output equations become:

$$\hat{\mathbf{b}}(\Omega) = \mathbb{R}(\Omega)\hat{\mathbf{a}}(\Omega) + \mathbb{T}(\Omega)\hat{\mathbf{v}}(\Omega), \quad \hat{\mathbf{e}}(\Omega) = \sqrt{\tau^{-1}}\mathbb{L}(\Omega) (\sqrt{\gamma_i}\hat{\mathbf{a}}(\Omega) + \sqrt{\gamma_e}\hat{\mathbf{v}}(\Omega)), \quad (3.139)$$

where I defined the transfer matrices:

$$\mathbb{R}(\Omega) = 2\gamma_i\mathbb{L}(\Omega) - \mathbb{I}, \quad (3.140)$$

$$\mathbb{T}(\Omega) = 2\sqrt{\gamma_i\gamma_e}\mathbb{L}(\Omega), \quad (3.141)$$

$$\mathbb{L}(\Omega) = \frac{1}{(\gamma - i\Omega)^2 + \delta^2} \begin{bmatrix} \gamma - i\Omega & -\delta \\ \delta & \gamma - i\Omega \end{bmatrix} \quad (3.142)$$

It is useful to see the case of a cavity with a perfectly reflective back mirror: $\gamma_e = 0$, $\gamma = \gamma_i$. In this case the reflection matrix is simplified:

$$\mathbb{R}(\Omega) = \frac{1}{(\gamma - i\Omega)^2 + \delta^2} \begin{bmatrix} \gamma^2 + \Omega^2 - \delta^2 & -2\gamma\delta \\ 2\gamma\delta & \gamma^2 + \Omega^2 - \delta^2 \end{bmatrix} = e^{i\beta}\mathbb{O}[\alpha], \quad (3.143)$$

$$\alpha = \arctan \frac{2\delta\gamma}{\gamma^2 - \delta^2 + \Omega^2}, \quad \beta = \arctan \frac{2\Omega\gamma}{\gamma^2 + \delta^2 - \Omega^2}. \quad (3.144)$$

In other words, a detuned cavity applies a frequency-dependent rotation on the input fields. This explains why a detuned filter cavity can be used for frequency-dependent squeezing or variational readout, which were discussed in this chapter.

3.5 Classical laser noises

Real lasers do not emit a perfectly monochromatic field. Their emission linewidth is finite, due to the natural linewidth of a transition used to produce the photons, but also additionally due to various imperfections in the laser setup. As a result,

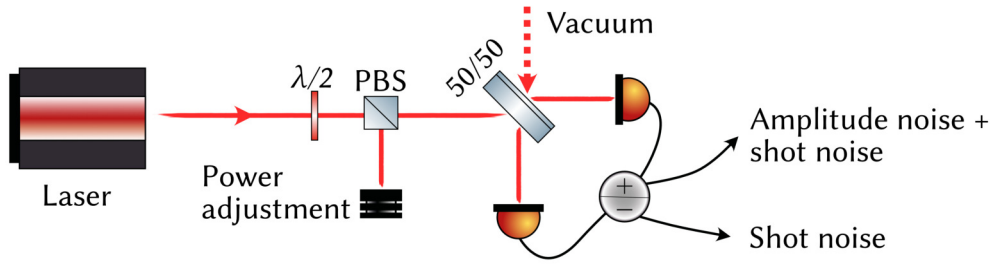


Fig. 3.6. Setup for measuring laser amplitude noise. Laser is split into two beams on a 50:50 beamsplitter, and the outputs are sent on the photodiodes. Added photocurrents result in a sum of amplitude and shot noise, subtracted photocurrents give just the shot noise. Subtracting two spectra allow to retrieve the amplitude noise spectrum.

both the amplitude and the frequency of the laser can fluctuate. Part of these fluctuations is quantum and has been discussed in the chapter so far. The main characteristic of quantum noise is that it's perfectly Markovian (i.e. does not correlate with itself at different moments of time). The other part is classical. In this section I discuss briefly classical phase and amplitude noises.

3.5.1 Amplitude noise

Consider the fluctuations in the amplitude of the light:

$$E(t) = (E_0(1 + \delta E(t)) + \hat{e}(t)) \cos(\omega_0 t + \phi), \quad (3.145)$$

where \hat{e}_q is the quantum noise, and δE is the classical fluctuation of the amplitude. The corresponding intensity on a photodiode:

$$I(t) = I_0 + \sqrt{2I_0\hbar\omega_0}\hat{e}_q(t) + I_0\delta E(t). \quad (3.146)$$

Power spectral density of the intensity reveals the different scaling of noises with optical intensity I_0 :

$$S_{II}(\Omega) = 2I_0\hbar\omega_0 + I_0^2 S_{EE}(\Omega), \quad (3.147)$$

where $S_{EE}(\Omega)$ is the spectrum of the amplitude fluctuations. As an example, when the light power on the photodiode is increased by a factor of 2, shot noise

is increased by 3 dB, but amplitude noise is increased by 6 dB. This allows to differentiate between the two noises in a simple way.

Amplitude noise generally does not couple to the measurements of the phase quadrature directly. However, when the detector is detuned from its resonance, such that the quadratures are rotated and mixed, it can influence the sensitivity. Moreover, as an amplitude fluctuation, it contributes to the radiation-pressure noise on the mirrors, and can disturb the measurements if this classical radiation-pressure is comparable to the quantum one.

In interferometric experiments the influence of the amplitude noise is avoided by the fact that its contribution to the radiation-pressure noise does not couple to the differential signal between two arms. Only in the presence of asymmetries (e.g. unequal powers in the arms, not perfect 50:50 splitting on the central beamsplitter) the amplitude noise can create some difficulties for the measurements. Since in LIGO such asymmetries of course are present, several sophisticated laser noise stabilization schemes are employed [172–174].

Amplitude noise can be measured by splitting the light field on the 50:50 beamsplitter, and detecting the outputs with two photodiodes, see Fig. 3.6. The photodiodes' currents are then added and subtracted. Added current contains the information about both amplitude and phase noise of the laser. Subtracted current contain only the information about the shot noise (since amplitude noise is correlated). Then the difference between two spectra represents only the amplitude noise. More details about the amplitude noise can be found in Chapter 4.

3.5.2 Phase noise

Phase noise is more difficult to observe, since it does not couple directly to the intensity as measured on the photodiode. Instead, interferometric techniques need to be used to convert phase fluctuations into the amplitude ones, that are then observable on the photodetectors.

Consider a Mach-Zehnder interferometer (MZI) with imbalanced arm length, see Fig. 3.7. After the first beamsplitter the two fields are:

$$E_{1,2}(t) = \frac{1}{\sqrt{2}}E_0e^{i\phi(t)} + \hat{e}_{1,2}(t), \quad (3.148)$$

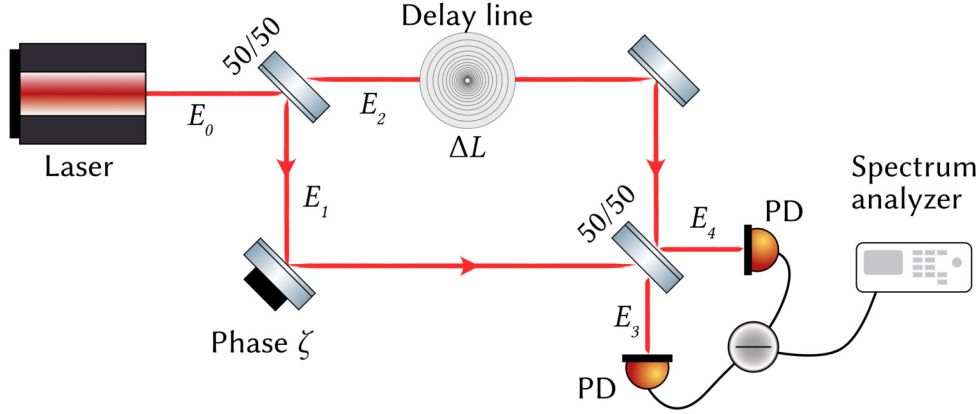


Fig. 3.7. Setup for measuring laser phase noise. Laser passes through the imbalanced Mach-Zehnder with arm length difference ΔL . The two photodiodes detect interference between the light fields in the arms. Phase noise can be recovered by subtracting the photocurrents (like in a balanced homodyne detector). Depending on the imbalance in the arms, coupling of the laser phase noise changes.

where $\hat{e}_{1,2}(t)$ is the quantum part of the noise. This noise is uncorrelated, so we simply carry it through the calculation. The two arms have length of $L_{1,2}$ that are generally different by $\Delta L = L_2 - L_1$. After propagating through the interferometer, the output of the second beamsplitter is the result of interference between two beams:

$$E_{3,4}(t) = \frac{E_0}{2} \left(e^{i\phi(t)} - e^{i\phi(t+\Delta L/c)} \right) + \hat{e}_{3,4}(t). \quad (3.149)$$

Considering that the phase at a later time can be seen as an additional phase delay: $\phi(t + \Delta L/c) = \phi(t) + \Delta\phi(t)$, the intensities measured on the photodiodes are:

$$I_{3,4}(t) = \frac{I_0}{2} (1 \pm \cos \Delta\phi(t)) + \frac{1}{2} \sqrt{2I_0\hbar\omega_0} \hat{e}_{3,4}, \quad (3.150)$$

which can be subtracted as on the homodyne detector, resulting in the photocurrent:

$$i(t) \propto I_0 \cos \Delta\phi(t) + \sqrt{2I_0\hbar\omega_0} (\hat{e}_3(t) - \hat{e}_4(t)). \quad (3.151)$$

The spectral density of the noise is then:

$$S_{II}(\Omega) = 4I_0 S_{\phi\phi}(\Omega) \sin^2 \left(\frac{\Omega\Delta L}{2c} \right) + 4I_0\hbar\omega_0. \quad (3.152)$$

In other words, the interferometer converts phase fluctuations on the input $S_{\phi\phi}(\Omega)$ into the amplitude (intensity) fluctuations on the output, given the appropriate choice of ΔL . The corresponding transfer function of a MZI:

$$T(\Omega) = 1 + \sin \frac{2\Delta L\Omega}{c}. \quad (3.153)$$

Phase noise can also be interpreted as frequency noise $S_{ff}(\Omega)$ using the relation between the phase and frequency: $2\pi f(\Omega) = -i\Omega\phi(\omega)$:

$$S_{II}(\Omega) = 4I_0 \frac{S_{ff}(\Omega)}{\Omega^2} \sin^2 \left(\frac{\Omega\Delta L}{2c} \right) + 4I_0\hbar\omega_0. \quad (3.154)$$

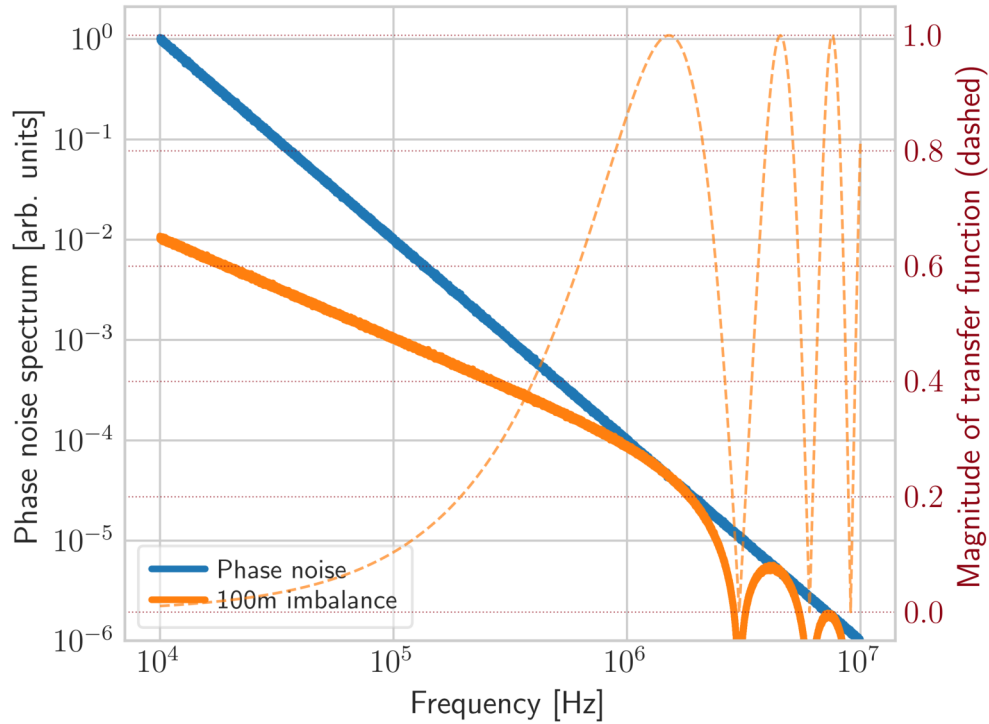


Fig. 3.8. The effect of path length imbalance in a Mach-Zehnder interferometer on the phase noise of the laser. Input laser phase noise (simulated, blue) does not couple to the detector when the arms are balanced (zero level, not shown). With 100 m imbalance in one arm (orange), the noise can contribute significantly to the sensitivity. The magnitude of transfer function of the imbalanced interferometer is in orange dashed (right y-axis and red grid lines). For low frequencies, the transfer function is low, and the detected noise is suppressed relative to the input phase noise. At the half of the FSR frequency of the MZI, $c/(2\Delta L) = 1.5 \times 10^6$ Hz, phase noise couples maximally to the detector.

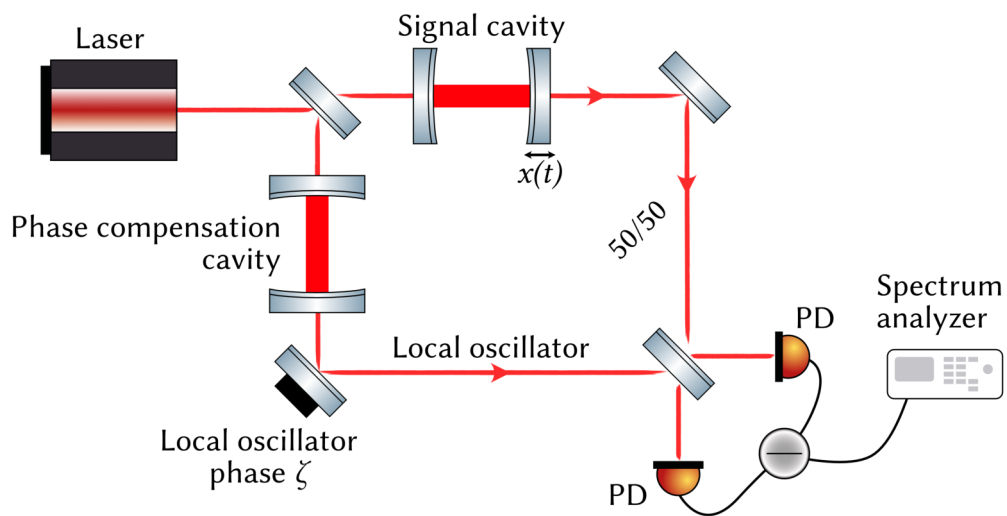


Fig. 3.9. Compensation of the phase delay in the signal cavity with an additional cavity in the local oscillator path. When a phase modulation signal in a cavity is measured with a balanced homodyne detector, phase noise can couple into the measurement record, due to the light being delayed in the cavity. It is possible to compensate this delay by placing an identical cavity in the local oscillator path. For a perfectly identical cavity, phase noise can be fully canceled, see Fig. 3.10

Since the MZI is the basis for homodyne detector, we can separate the phase difference into two contributions: phase delay due to macroscopic length, and small phase difference corresponding to homodyne angle ζ :

$$S_{II}(\Omega) = 4I_0 S_{\phi\phi}(\Omega) \sin^2\left(\frac{\Omega\Delta L}{2c} + \zeta\right) + 4I_0\hbar\omega_0. \quad (3.155)$$

For perfectly balanced arms the noise does not couple to the output in amplitude quadrature: $\zeta = 0$. This is why in a perfect interferometer operated in the dark port condition (i.e. when the signal port remains dark), phase noise of the laser does disturb the measurements. The main problem with the phase noise occurs when the arms are largely imbalance. For instance, when in one arm there is a cavity where the signal is generated. Then phase noise can have a significant contribution to the measurement on the homodyne detector, see Fig. 3.8. Sometimes it is possible to compensate this imbalance by placing an identical cavity in the other arm, see Fig. 3.9. Such a cavity, depending on how close it is in linewidth to the signal cavity, could provide a significant reduction to the phase noise influence, see Fig. 3.10. In other cases, however, it is not possible due to various reasons, as I discuss in Chapter 4. Generally a dedicated active laser stabilization is required to minimize the impact of the phase noise [172–174].

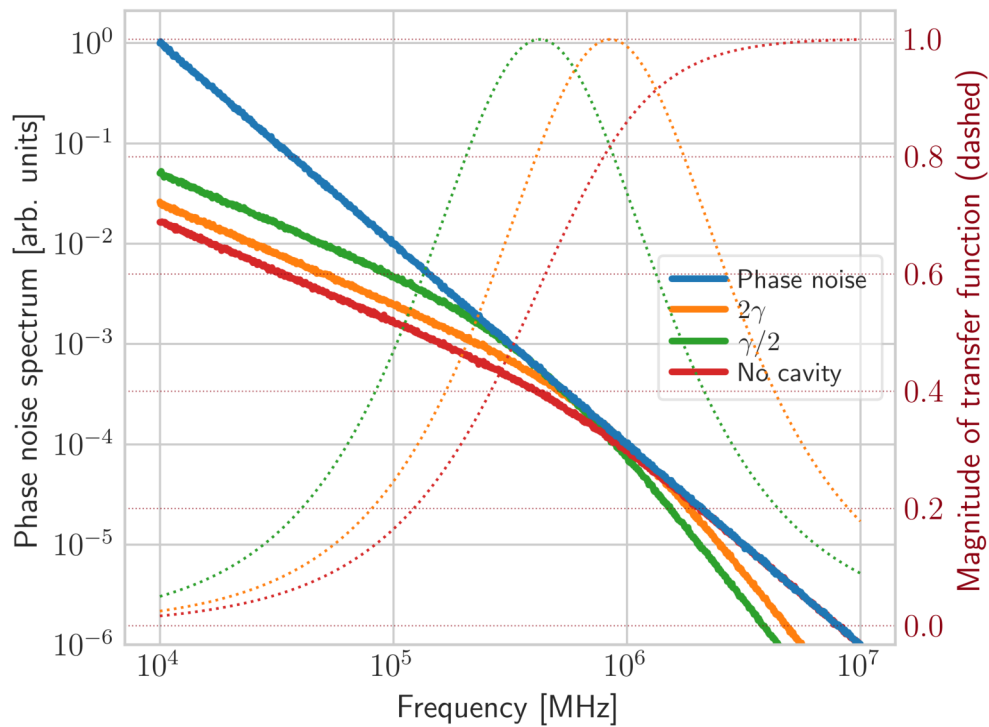


Fig. 3.10. Effect compensating the phase delay in signal cavity. Laser phase noise (blue) experiences a phase delay, and contaminates the measurement record (red). If another compensation cavity is placed in the local oscillator path, it is possible to suppress this noise. For a compensation cavity identical to the signal cavity cavity, the noise can be completely canceled (zero at the plot, not shown). When its linewidth is larger (orange) or smaller (green) than the signal cavity linewidth γ , the noise is suppressed only at some frequencies. The magnitudes of corresponding transfer functions are in dashed lines matching the colors.

3.6 Example: conditional frequency-dependent squeezing through Einstein–Podolsky–Rosen entanglement

I conclude this chapter with an example by calculating the spectral density of the EPR-based conditional frequency-dependent squeezing [143], which combines the techniques used throughout this chapter. As I discuss in Sec. 3.3, frequency-dependent squeezing requires costly long filter cavities for achieving the desired frequency dependence. The main source of cost is the stringent requirement on the low optical loss. For that cavities have to be made long, in vacuum, and very high quality, which adds the experimental complexity as well.

In fact, there are already very long and very high quality cavities in the GW detectors: their arm cavities. The idea behind the EPR-squeezing is to use the detector itself as a filter cavity. In order to avoid the interaction with the signal, squeezed light that experiences the rotation, needs to be tuned to the one of the next longitudinal resonances of the arm cavities. For that purpose, two beams with different central frequencies are entangled and injected into the interferometer. One beam is at the same frequency of the main laser field, and thus enters the interferometer on resonance, as the usual squeezed vacuum field. Another beam is detuned by several FSRs off the first one, and also from the cavity resonance such, that it experiences the necessary phase rotation. Then two beams are detected on two different homodyne detectors, and the measurement of the one is conditioned on the measurement in the second one, resulting in the optimal conditional sensitivity that features the desired effect of frequency-dependent squeezing.

The detailed analysis of the proposal can be found in [141], the results of the experiment performed by J.Südbeck and S.Steinlechner were published [143], and independently by Yap *et.al.* in [144]. Here I briefly demonstrate how I combined the approaches presented in this Chapter to produce the theoretical model used in [143].

There the two non-degenerate entangled beams are sent in the GW detector, such that low-frequency part (signal) is resonant in the main detector, and the high-frequency part (idler) is detuned from one of the next longitudinal resonances

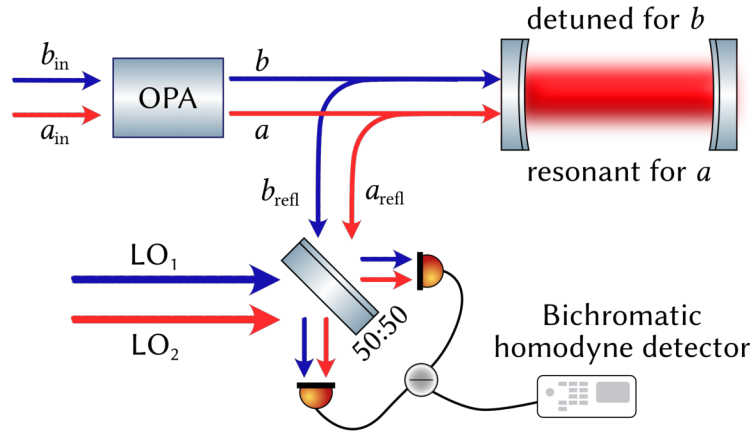


Fig. 3.11. Schematic diagram of a setup for generating conditional frequency-dependent squeezing with EPR-entangled fields. Two modes \hat{a} , \hat{b} at frequencies $\omega_0, \omega_0 + \Delta$, are entangled inside the optical-parametric amplifier (OPA). The cavity is tuned to be on resonance at ω_0 . One of the next longitudinal resonances of the cavity is detuned relative to the frequency $\omega_0 + \Delta$. The two reflected fields acquire frequency dependence in the correlations between them. These fields are then detected on a bichromatic homodyne detector with local oscillator (LO) fields at frequencies $\omega_0, \omega_0 + \Delta$. The resulting photocurrent allows to compute the conditional spectral density of the noise, exhibiting a frequency-dependence in suppression of the shot noise, see more details in [143].

of the cavity. This way the idler experiences the frequency-dependent rotation of the quadratures. By measuring the signal and idler at separate homodyne detectors and optimally combining the data, it is possible to create a frequency-dependent squeezing on the light field.

I start building the theoretical description of a setup, depicted in Fig. 3.11, by considering generation of entangled fields inside the OPA. Consider the input fields at frequencies $\omega_0, \omega_0 + \Delta$, centered around the frequency $\omega_p = 2\omega_0 + \Delta$. I define the input fields $\hat{a}_{in,\pm} = \hat{a}(\omega_0 \pm \Omega)$, $\hat{b}_{in,\pm} = \hat{b}(\omega_0 + \Delta \pm \Omega)$. Parametric process in the OPA creates correlations between frequency symmetric around the pump

frequencies. The input fields $\hat{a}_{\text{in},+}$ and $\hat{b}_{\text{in},-}$, being initially in the vacuum state become quantum correlated on the output, see Sec. 3.1.6:

$$\hat{a}_+ = \hat{a}_{\text{in},+} \cosh r + \hat{b}_{\text{in},-}^\dagger \sinh r, \quad (3.156)$$

$$\hat{b}_+ = \hat{b}_{\text{in},+} \cosh r + \hat{a}_{\text{in},-}^\dagger \sinh r. \quad (3.157)$$

Every mode is sent into the interferometer, which we represent here by two cavities (for the main field and the idler field). It is useful to define two-photon quadratures. Keep in mind, that in this case, the modes are centered around different frequencies, $\omega_0, \omega_0 + \Delta$:

$$\hat{a}^{c,s}(\Omega) = \hat{a}_{\text{in}}^{c,s}(\Omega) \cosh r \pm \hat{b}_{\text{in}}^{c,s}(\Omega)^\dagger \sinh r, \quad (3.158)$$

$$\hat{b}^{c,s}(\Omega) = \hat{b}_{\text{in}}^{c,s}(\Omega) \cosh r \pm \hat{a}_{\text{in}}^{c,s}(\Omega)^\dagger \sinh r. \quad (3.159)$$

In the further discussion, I use the quadrature vectors, e.g. $a(\Omega) = \{\hat{a}^c(\Omega), \hat{a}^s(\Omega)\}^\top$, to simplify the discussion (as in the previous Sections):

$$a(\Omega) = a_{\text{in}}(\Omega) \cosh r + \sigma_3 b_{\text{in}}(\Omega) \sinh r, \quad (3.160)$$

$$b(\Omega) = b_{\text{in}}(\Omega) \cosh r + \sigma_3 a_{\text{in}}(\Omega) \sinh r, \quad (3.161)$$

where I defined the Pauli matrix $\sigma_3 = \{\{1, 0\}, \{0, -1\}\}$.

In the proposal, mode \hat{a} is resonant with the cavity, and mode \hat{b} is detuned off the cavity resonance to produce the necessary rotation on the quadratures. Here, I am going to assume that both fields can have some detuning of the cavity resonance. Then the field reflected off the cavity is transformed according to Eq. 3.143. Using the rules for two-photon quadratures from Sec. 3.2.2, I compute the fields after the reflection off the cavities:

$$a_{\text{refl}}(\Omega) = e^{i\beta_1(\Omega)} \mathbb{O}[\alpha_1(\Omega)] a_{\text{in}}(\Omega) \cosh r + e^{i\beta_2(\Omega)} \mathbb{O}[\alpha_2(\Omega)] \sigma_3 b_{\text{in}}(\Omega) \sinh r, \quad (3.162)$$

$$b_{\text{refl}}(\Omega) = e^{i\beta_2(\Omega)} \mathbb{O}[\alpha_2(\Omega)] b_{\text{in}}(\Omega) \cosh r + e^{i\beta_1(\Omega)} \mathbb{O}[\alpha_1(\Omega)] \sigma_3 a_{\text{in}}(\Omega) \sinh r, \quad (3.163)$$

where the rotation angles are:

$$\alpha_{1,2} = \arctan \frac{2\delta_{1,2}\gamma}{\gamma^2 - \delta_{1,2}^2 + \Omega^2}, \quad (3.164)$$

$$\beta_{1,2} = \arctan \frac{2\Omega\gamma}{\gamma^2 + \delta_{1,2}^2 - \Omega^2}. \quad (3.165)$$

In these equations, I assume for simplicity that the linewidth of the cavities is the same, since it is the same cavity at a different longitudinal resonance. In reality, depending on the properties of the optical coatings, this might be different.

The next experimental stage is the detection of the reflected fields. In the experiment in [143], the fields were detected on a bichromatic homodyne detector. This detector features the two LOs at frequencies $\omega_0, \omega_0 + \Delta$, with corresponding powers P_a, P_b and phases ζ_a, ζ_b . The resulting photocurrents of the two outputs, see Sec. 3.2.2:

$$y_a(\Omega) = \sqrt{P_a} \mathbb{H}^\top[\zeta_a] a_{\text{refl}}(\Omega), \quad (3.166)$$

$$y_b(\Omega) = \sqrt{P_b} \mathbb{H}^\top[\zeta_b] b_{\text{refl}}(\Omega). \quad (3.167)$$

In the bichromatic homodyne detector, the photocurrents from two signals are directly added (since the fields are detected by the same photodiodes):

$$y(\Omega) = y_a(\Omega) + y_b(\Omega) = \mathcal{R}_a(\Omega) a_{\text{in}}(\Omega) + \mathcal{R}_b(\Omega) b_{\text{in}}(\Omega), \quad (3.168)$$

$$\mathcal{R}_a(\Omega) = \sqrt{P_a} \mathbb{H}^\top[\zeta_a] e^{i\beta_1} \mathbb{O}[\alpha_1] \cosh r + \sqrt{P_b} \mathbb{H}^\top[\zeta_b] e^{i\beta_2} \mathbb{O}[\alpha_2] \sigma_3 \sinh r, \quad (3.169)$$

$$\mathcal{R}_b(\Omega) = \sqrt{P_b} \mathbb{H}^\top[\zeta_b] e^{i\beta_2} \mathbb{O}[\alpha_2] \cosh r + \sqrt{P_a} \mathbb{H}^\top[\zeta_a] e^{i\beta_1} \mathbb{O}[\alpha_1] \sigma_3 \sinh r. \quad (3.170)$$

Computing the spectral density from this relation is straightforward by following the rules in Sec. 3.2.1:

$$S_{yy}(\Omega) = \mathcal{R}_a(\Omega) S_{aa}(\Omega) \mathcal{R}_a^\dagger(\Omega) + \mathcal{R}_b(\Omega) S_{bb}(\Omega) \mathcal{R}_b^\dagger(\Omega), \quad (3.171)$$

where $S_{aa} = S_{bb} = 1$, since the initial state is uncorrelated vacuum. I skip here the lengthy computation of the matrix multiplication, and present the resulting expression directly:

$$S_{yy}(\Omega) = (P_a + P_b) \cosh 2r + 2\sqrt{P_a P_b} \cos[\beta_2(\Omega) - \beta_1(\Omega)] \times \\ \times \cos[\alpha_1(\Omega) + \alpha_2(\Omega) - \zeta_a - \zeta_b] \sinh 2r. \quad (3.172)$$

The full analysis of this expression goes beyond the scope of this thesis, and more details can be found in [143] and in the thesis by Jan Südbek [REF!]. Here, I consider only one case, following the original proposal [141]: $\delta_a = 0, \delta_b = -\gamma$:

$$\alpha_1 = 0, \quad \alpha_2 = -\arctan \frac{2\gamma^2}{\Omega^2}; \quad (3.173)$$

$$\beta_1 = \arctan \left[\frac{2\gamma\Omega}{\gamma^2 - \Omega^2} \right], \quad \beta_2 = \arctan \left[\frac{2\gamma\Omega}{2\gamma^2 - \Omega^2} \right]; \quad (3.174)$$

$$\cos[\beta_2(\Omega) - \beta_1(\Omega)] \cos[\alpha_1(\Omega) + \alpha_2(\Omega) - \zeta_a - \zeta_b] = \quad (3.175)$$

$$= \frac{2\gamma^4 + \gamma^2\Omega^2 + \Omega^4}{(\gamma^2 + \Omega^2)(4\gamma^4 + \Omega^4)} (\Omega^2 \cos(\zeta_a + \zeta_b) - 2\gamma^2 \sin(\zeta_a + \zeta_b)). \quad (3.176)$$

I consider two limiting cases: low frequency and high frequency, and show that as expected for frequency-dependent squeezing, at low frequencies the amplitude quadrature is squeezed, and at high frequencies the phase quadrature.

$$S_{yy}(0) = (P_a + P_b) \cosh 2r - 2\sqrt{P_a P_b} \sin(\zeta_a + \zeta_b) \sinh 2r; \quad (3.177)$$

$$S_{yy}(\Omega \gg \gamma) = (P_a + P_b) \cosh 2r + 2\sqrt{P_a P_b} \cos(\zeta_a + \zeta_b) \sinh 2r. \quad (3.178)$$

Assuming the equal powers of LOs, $P_a = P_b$, at high frequencies the noise is squeezed in phase quadrature, $\zeta_a = \zeta_b = \pi/2$: $S_{yy}(\Omega \gg \gamma) = P_a e^{-2r}$. At low frequency, the noise is squeezed in amplitude quadrature, $\zeta_a = 0, \zeta_b = \pi/2$: $S_{yy}(0) = P_a e^{-2r}$. In Fig. 3.12, I show how the spectrum of quantum noise depends on the homodyne angle.

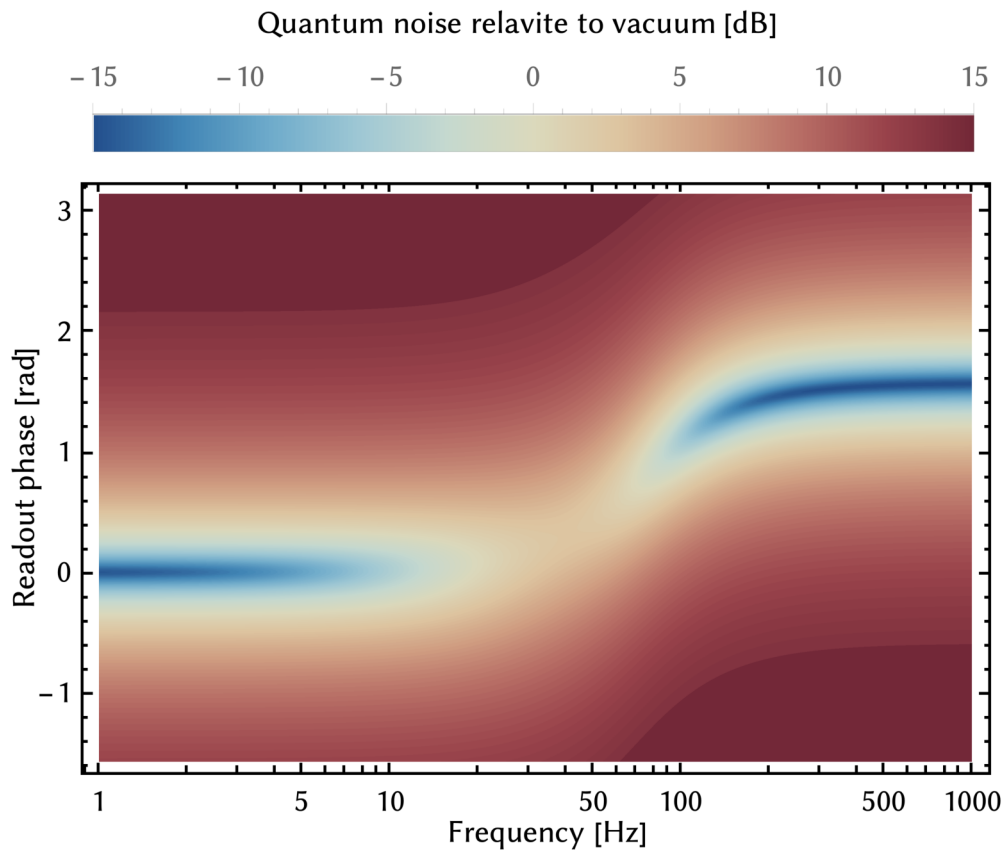


Fig. 3.12. Example of conditional frequency-dependent squeezing through Einstein–Podolsky–Rosen entanglement. Quantum noise is plotted as a function of signal frequency and readout angle. The color shows quantum noise measured on the bichromatic homodyne detector, relative to the shot noise level. Blue regions correspond to squeezed noise, red regions correspond to anti-squeezed noise. The frequency-dependence of the noise is demonstrated: at low frequencies it is squeezed in one quadrature (readout angle $\zeta_a = 0$), and at high frequencies it is squeezed in the orthogonal quadrature (readout angle $\zeta_a = \pi/2$). The correlations around the rotation frequency ~ 50 Hz are lost due to sub-optimal processing of the data, see [143] for details.

Proof-of-principle of a ring-cavity speedmeter

Quantum radiation pressure noise (QRPN) will be limiting Advanced LIGO at low frequency once it reaches its design sensitivity [10]. This noise can be suppressed (without increasing the shot noise) by using back-action evading techniques, such as variational readout or frequency-dependent squeezing. These approaches typically require sophisticated and costly high-quality filter cavities, as I discussed in Chapter 3.

There is an alternative approach: using quantum non-demolition (QND) measurements instead. As I introduce in Chapters 2,3, QRPN fundamentally arises due to the measurement process itself. In a Michelson interferometer light senses the position of the mirrors, and since the position does not commute with a measurement Hamiltonian: $[\hat{x}, \hat{H}] \sim [\hat{x}, \hat{p}] \neq 0$, this introduces a measurement back-action on the mirrors [34]. If it were possible to measure the value that does commute with the measurement Hamiltonian, it would not introduce back-action, and would thus be a QND measurement. For a free mass, such an observable is mirror's momentum. Unfortunately, direct measurement of momentum is very difficult, but it is possible to measure the velocity instead. Since the momentum and velocity for a free mass are connected by a simple relation $\hat{p} = m\hat{v}$, such a measurement is also QND measurement [35]. Velocity measurement is the basis for a *speedmeter* concept.

A speedmeter measures the change in displacement of the test mass $\hat{x}(t) - \hat{x}(t')$ over a time τ , and thus the average velocity $\hat{v}(t) = (\hat{x}(t) - \hat{x}(t'))\tau^{-1}$. For example, it can be achieved by sensing the displacement of a mirror from two different sides with the same beam that experiences the delay τ , see Fig. 4.1.

A quantum speedmeter for gravitational-wave detectors was first proposed by Braginsky and Khalili [119], and since then has been conceptualized in dif-

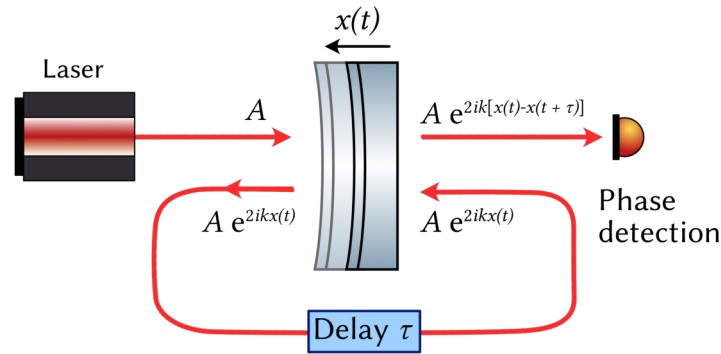


Fig. 4.1. The concept of a quantum speedmeter. The motion of the mirror is sensed by light field A from two sides with some delay τ . On the first reflection it acquires a phase $\exp 2ikx(t)$, and on the second a phase $\exp 2ikx(t + \tau)$. The signal on the phase-sensitive detector (e.g. a homodyne detector) is then proportional to $x(t) - x(t + \tau) = v(t)\tau^{-1}$. Since the light momentum transfer to the mirror is the same from both sides, the net radiation-pressure force is approximately zero. This feature makes quantum speedmeter useful for suppressing QRPN.

ferent topologies [121–126, 175, 176]. The characteristic optical transfer function of the speedmeter has been demonstrated [177]. However, to date, there has been no experimental demonstration of speedmeter sensing enhancement. The challenge in such demonstrations is not only reaching the quantum regime in an optomechanical system, but also proving the sensitivity enhancement from velocity measurements. Since most speedmeter topologies differ significantly from the position meter ones, such comparison might be challenging due to differences in experimental parameters.

In this chapter, I propose a new ring cavity topology that simultaneously and independently measures speed and position of a mechanical oscillator, which would allow to compare the sensitivities. Such optomechanical cavity has been investigated in a different context in [178–180]. I perform a table-top experiment directly comparing the position and velocity optical transfer function. I use a micro-mechanical oscillator to implement the sensing of the external force in this setup. This is the first step towards the direct comparison of the speed and position meter sensitivities. I further provide a detailed theoretical description of the setup, and outline the possible applications for it.

4.1 Quantum speedmeter

I start by introducing the concept of a quantum speedmeter in a toy example [35]. As in the Chapter 3, I start by writing the input-output relations for the quadratures of the light reflected off a mechanical oscillator, see Fig. 4.1.

This time, however, I consider a interaction that takes place twice with an opposite phase and time delay τ :

$$b^c(t) = a^c(t), \quad (4.1)$$

$$b^s(t) = a^s(t) + 2k_p A (x(t - \tau) - x(t)), \quad (4.2)$$

which can be converted into the frequency domain:

$$b^c(\Omega) = a^c(\Omega), \quad (4.3)$$

$$b^s(\Omega) = a^s(\Omega) - 2k_p A x(\Omega) (1 - e^{i\Omega\tau}) \approx a^s(\Omega) - 2ik_p A x(\Omega) \Omega\tau, \quad (4.4)$$

where I assumed the time delay to be small. Here, one can already see the characteristic property of the speedmeter: the output contains the displacement proportional to the frequency Ω , which is a consequence of the fact that velocity and position are connected by a Fourier transform as: $v(t) = \dot{x}(t) \rightarrow -ix(\Omega)\Omega$. Displacement $x(\Omega)$ has contribution from a signal force G , which we would like to measure, and radiation-pressure force F_{rp} , which contaminates the measurement:

$$x(\Omega) = \chi(\Omega)(G(\Omega) + F_{\text{rp}}(\Omega)), \quad (4.5)$$

where $\chi(\Omega)$ is the mechanical transfer function. For the case of a free mass it is connected to the mass M by $\chi(\Omega) = -(M\Omega^2)^{-1}$.

Radiation-pressure fluctuating force $F_{\text{rp}}(t)$ depends on the fluctuations in the amplitude quadrature of the light field and, since the light interacts with the mirror twice, it has two contributions:

$$F_{\text{rp}}(t) = \delta P(t)c^{-1} = 2\hbar k_p A (a^c(t - \tau) - a^c(t)) \quad (4.6)$$

$$F_{\text{rp}}(\Omega) \approx -2i\hbar k_p A a^c(\Omega)\Omega\tau. \quad (4.7)$$

When the light is sensed by a homodyne detector, it measures a quadrature ζ :

$$\begin{aligned}
y(\Omega) &= b^c(\Omega) \cos \zeta + b^s(\Omega) \sin \zeta = \\
&= a^c(\Omega) \cos \zeta + (a^s(\Omega) - 2ik_p A x(\Omega) \Omega \tau) \sin \zeta = \\
&= a^c(\Omega) \cos \zeta + a^s(\Omega) \sin \zeta - \\
&\quad - 2ik_p A \Omega \tau \chi(\Omega) (G(\Omega) - 2i\hbar k_p A a^c(\Omega) \Omega \tau) \sin \zeta. \tag{4.8}
\end{aligned}$$

The output signal can be normalized to the displacement:

$$\tilde{y}(\Omega) = -y(\Omega) \frac{1}{2ik_p A \Omega \tau \sin \zeta} = x_{\text{fl}}(\Omega) + \chi \Omega (G(\Omega) + F_{\text{rp}}(\Omega)), \tag{4.9}$$

where I introduced shot noise x_{fl} . Spectral densities of the shot noise x_{fl} , radiation-pressure noise F_{rp} and their cross-correlation can be found, assuming the input noise to be in a coherent state, i.e. $S_{a^c a^c} = S_{a^s a^s} = 1$, $S_{a^c a^s} = 0$:

$$S_{xx}(\Omega) = \frac{1}{4k_p^2 A^2 \Omega^2 \tau^2 \sin^2 \zeta}, \tag{4.10}$$

$$S_{FF}(\Omega) = 4\hbar^2 k_p^2 A^2 \Omega^2 \tau^2, \tag{4.11}$$

$$S_{xF}(\Omega) = -\hbar \cot \zeta. \tag{4.12}$$

Total noise spectral density normalized to displacement is:

$$\begin{aligned}
S_x(\Omega) &= S_{xx} - \frac{2\Re[S_{xF}(\Omega)]}{M\Omega^2} + \frac{S_{FF}(\Omega)}{M^2\Omega^4} = \\
&= \frac{1}{4k_p^2 A^2 \Omega^2 \tau^2 \sin^2 \zeta} + \frac{\hbar \cot \zeta}{M\Omega^2} + \frac{4\hbar^2 k_p^2 A^2 \Omega^2 \tau^2}{M^2\Omega^4} = \\
&= \frac{\hbar}{M\Omega^2} \left(\frac{cM}{4k_p P \tau^2 \sin \zeta} + \cot \zeta + \frac{4k_p P \tau^2}{Mc} \right) \tag{4.13}
\end{aligned}$$

where I define the optical power $P = \hbar k_p c A^2$. In a standard case the homodyne detector measures the phase quadrature of the light: $\zeta = \pi/2$, and no cross-correlation between the noises is present. In this case a spectral density follows the SQL:

$$S_x(\Omega) = \frac{\hbar}{M\Omega^2} \left(\frac{cM}{4k_p P \tau^2} + \frac{4k_p P \tau^2}{Mc} \right). \tag{4.14}$$

This sensitivity can be improved by using the cross-correlation between noises. With the optimal choice of frequency-*independent* homodyne angle

$$\cot \zeta = -\frac{4k_p P \tau^2}{Mc},$$

the sensitivity can reach any value below the SQL, only dependent on the available light power (or squeezed light):

$$S_x(\Omega) = \frac{\hbar c}{4k_p P \tau^2 \Omega^2}. \quad (4.15)$$

This is the power of the speedmeters: even without using quantum correlations, it naturally has a better sensitivity at low frequencies than the position meter, see Fig. 4.2. There is also no need for costly filter cavities for producing frequency-dependent squeezing (or variational readout) for surpassing the SQL. There are also downsides: experimental topology is more complicated than for the position meters and sensitivity is more fragile with respect to internal impurities that could destroy the correlations in the light between two measurements. Overall, the potential of the speedmeter is high, but it requires experimental effort to demonstrate the feasibility of this idea.

In the next section, I make a first step towards a table-top proof-of-principle demonstration of a speedmeter.

4.2 Optomechanical ring cavity as a speedmeter

I propose to implement the idea of a sequential measurement of the test mass' position by placing a movable mirror (a semi-transparent Si_3N_4 membrane) inside the optical ring cavity, see Fig. 4.3 The ring cavity is composed of three mirrors: one semi-transparent (incoupling) mirror and two highly reflective mirrors. The membrane is positioned inside, orthogonally to the beam propagation direction. The symmetry of the setup allows to separate the signal from the membrane into two output ports, which I refer to as *velocity* and *position* outputs from here on.

Upon entering the cavity, the beam can be reflected or transmitted through the membrane. The reflected beam can travel around the cavity and be again either

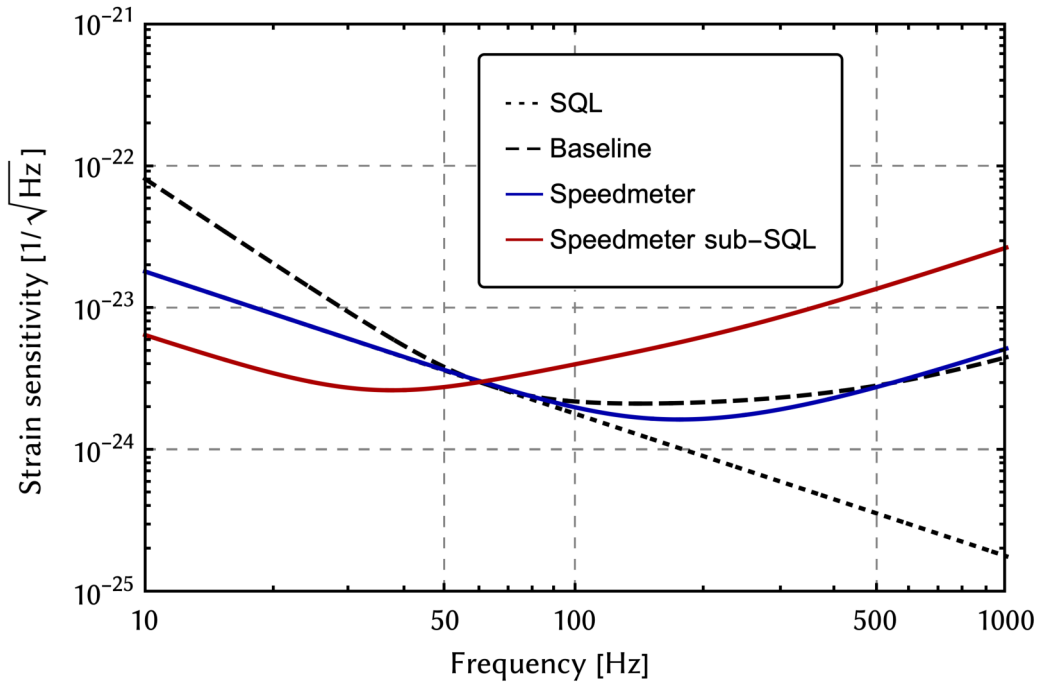


Fig. 4.2. Comparison between the total noise spectral densities of the speedmeter and position meter: (black dashed) the baseline interferometer with bandwidth $\gamma = 2\pi \times 500 \text{ s}^{-1}$; (solid blue) the Sagnac speedmeter without cross-correlation between quantum noises, and bandwidth $\gamma = 2^{2/3} \times 2\pi \times 100 \text{ s}^{-1}$; (solid red) the Sagnac speedmeter with the cross-correlation, with bandwidth $\gamma = 2\pi \times 100 \text{ s}^{-1}$, $\cot \zeta = 4$. Using the optimal cross-correlation allows to surpass the SQL at low frequencies. The SQL is in black dotted line. In all cases, optical power $I_0 = 840 \text{ kW}$ and no losses are taken into account.

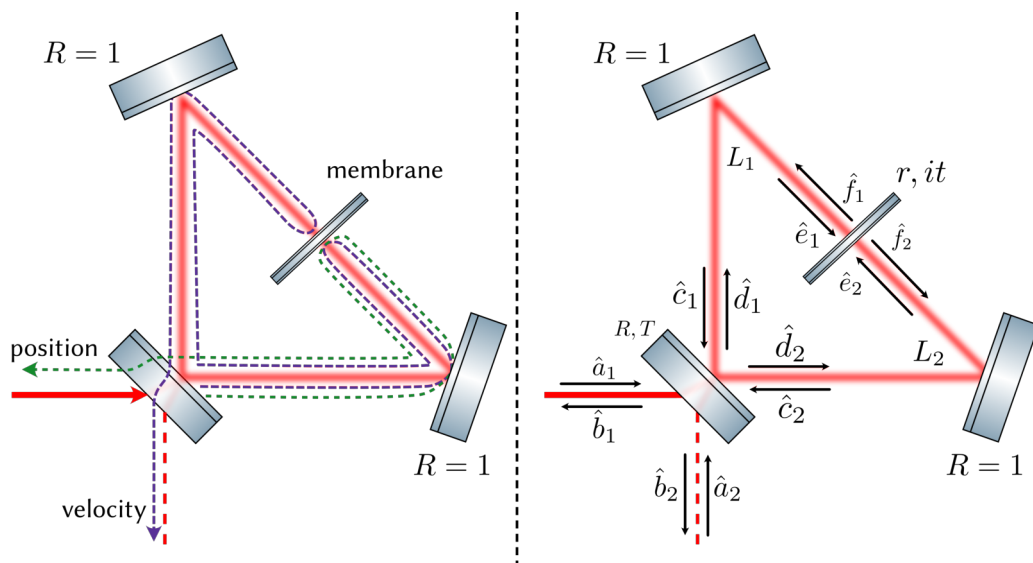


Fig. 4.3. Optomechanical ring cavity. (Left) conceptual representation. A movable reflective element (membrane) is placed inside a ring cavity. Only the incoupling mirror of the cavity is semi-transparent, the other two are highly reflective. There are two output ports: velocity and position. Velocity port contains no light power (it's dark), and only the information about the velocity of the membrane. (Right) the notation for the amplitudes of the light field in the ring cavity.

transmitted, or reflected. The beam that is reflected twice acquires the velocity information — in direct analogy with a thought experiment in Fig. 4.1. This beam exits through the velocity output port, together with the contributions from all even number of reflections. The port contains purely velocity information. The beam that is reflected an even amount of times is reflected directly back towards the incoming beam into the position output port. This beam contains a combined displacement information (more about it below).

Such an optomechanical ring cavity has several features: (i) it has a particular resonance structure, where the resonance normal mode is split into two by the membrane's reflectivity; (ii) the classical light power is fully reflected back into the input port; (iii) the second port remains dark, and only contains the velocity signal; (iv) the resonance condition does not depend on the position of the membrane: this setup features a new type of optomechanical coupling [68].

In the next sections, I explore in detail the properties of the ring cavity.

4.2.1 Input-output relations

I start by solving the input-output relations for the optical fields in the cavity in matrix form, and then study the properties of the solutions. Following the procedure described in Chapter 3, I define the propagation matrices for light fields in frequency domain, see Fig. 4.3:

$$\mathbb{R} = \begin{pmatrix} R & 0 \\ 0 & R \end{pmatrix} \quad \text{reflection matrix;} \quad (4.16)$$

$$\mathbb{T} = \begin{pmatrix} T & 0 \\ 0 & T \end{pmatrix} \quad \text{transmission matrix;} \quad (4.17)$$

$$\mathbb{M} = \begin{pmatrix} r & it \\ it & r \end{pmatrix} \quad \text{reflection/transmission of the membrane;} \quad (4.18)$$

$$\mathbb{P}(\Omega) = \begin{pmatrix} e^{i(k_p + \Omega/c)L_1} & 0 \\ 0 & e^{i(k_p + \Omega/c)L_2} \end{pmatrix} \quad \text{propagation of quantum fields;} \quad (4.19)$$

$$\mathbb{P}(0) = \begin{pmatrix} e^{ik_p L_1} & 0 \\ 0 & e^{ik_p L_2} \end{pmatrix} \quad \text{propagation of classical fields.} \quad (4.20)$$

Here k_p is the laser field wave vector, R is the amplitude reflectivity of the front mirror (I assume the other mirrors perfectly reflective), T is the amplitude transmissivity of the front mirror, r, t are the amplitude reflectivity and transmissivity of the membrane, $L_{1,2}$ are the distances from the front mirror to the membrane (clock and counterclockwise), Ω is the sideband frequency and c is the speed of light. In addition, I define some useful matrices:

$$\sigma_1 = \begin{pmatrix} 0 & 1 \\ 1 & 0 \end{pmatrix}, \quad \sigma_2 = \begin{pmatrix} 0 & -i \\ i & 0 \end{pmatrix}, \quad \sigma_3 = \begin{pmatrix} 1 & 0 \\ 0 & -1 \end{pmatrix}, \quad \mathbb{I} = \begin{pmatrix} 1 & 0 \\ 0 & 1 \end{pmatrix} \quad (4.21)$$

Classical field

First, it is useful to write the equations of motion for the classical fields (i.e. at frequency $\Omega = 0$). I combine two propagating fields into a single vector, represented by a bold letter, e.g.

$$\mathbf{B} = \begin{pmatrix} B_1 \\ B_2 \end{pmatrix}$$

In this notation the input-output equations are:

$$\mathbf{B} = -\mathbb{R}\sigma_1\mathbf{A} + \mathbb{T}\mathbf{C}, \quad (4.22)$$

$$\mathbf{C} = \mathbb{P}(0)\mathbf{F}, \quad (4.23)$$

$$\mathbf{F} = \mathbb{M}\mathbf{E}, \quad (4.24)$$

$$\mathbf{E} = \mathbb{P}(0)\mathbf{D}, \quad (4.25)$$

$$\mathbf{D} = \mathbb{R}\sigma_1\mathbf{C} + \mathbb{T}\mathbf{A}. \quad (4.26)$$

This set of equations can be brought to a single equation for the intra-cavity field \mathbf{C} :

$$\mathbf{C} = \mathbb{P}(0)\mathbb{M}\mathbb{P}(0) (\mathbb{R}\sigma_1\mathbf{C} + \mathbb{T}\mathbf{A}), \quad (4.27)$$

from which I obtain the input-output relation for the intra-cavity field:

$$\mathbf{C} = (\mathbb{I} - \mathbb{P}(0)\mathbb{M}\mathbb{P}(0)\mathbb{R}\sigma_1)^{-1} \mathbb{P}(0)\mathbb{M}\mathbb{P}(0)\mathbb{T}\mathbf{A} = \mathbb{K}(0)\mathbb{P}(0)\mathbb{M}\mathbb{P}(0)\mathbb{T}\mathbf{A}, \quad (4.28)$$

$$\mathbb{K}(0) = (\mathbb{I} - \mathbb{P}(0)\mathbb{M}\mathbb{P}(0)\mathbb{R}\sigma_1)^{-1}. \quad (4.29)$$

From this the outgoing field \mathbf{B} and field on the membrane \mathbf{E} are:

$$\mathbf{B} = (-\mathbb{R}\sigma_1 + \mathbb{T}\mathbb{K}(0)\mathbb{P}(0)\mathbb{M}\mathbb{P}(0)\mathbb{T}) \mathbf{A} \quad (4.30)$$

$$\mathbf{E} = \mathbb{P}(0) (\mathbb{R}\sigma_1\mathbb{K}(0)\mathbb{P}(0)\mathbb{M}\mathbb{P}(0) + \mathbb{I}) \mathbb{T}\mathbf{A}. \quad (4.31)$$

Quantum field

For the quantum field, it's necessary to keep the frequency dependence, and also consider that upon reflection off the membrane, the field picks up a phase modulation signal:

$$r \rightarrow r e^{2ikx} \approx r(1 + 2ik_p x(\Omega)).$$

Generally $k = k_p + \Omega/c$, but since I assume the displacement to be small, and frequency Ω to be small compared to the optical frequency, I keep only the zeroth order term k_p .

Quantum fields are considered as a first order perturbation on top of the classical signal: $\hat{A}(\Omega) = A + \hat{a}(\Omega)$. The field that picks up the signal upon reflection is approximated to the first order of smallness: $r\hat{E}(\Omega)e^{2ik(\Omega)\hat{x}(\Omega)} \approx rE + r\hat{e}(\Omega) + 2ik_p rE\hat{x}$. With these approximations, I write down the input-output relations for the quantum fields, omitting the hats over the quantum field vectors for brevity:

$$\mathbf{b}(\Omega) = -\mathbb{R}\sigma_1\mathbf{a}(\Omega) + \mathbb{T}\mathbf{c}(\Omega) \quad (4.32)$$

$$\mathbf{c}(\Omega) = \mathbb{P}(\Omega)\mathbf{f}(\Omega) \quad (4.33)$$

$$\mathbf{f}(\Omega) = \mathbb{M}\mathbf{e}(\Omega) + 2ik_p x(\Omega)r\sigma_3\mathbf{E} \quad (4.34)$$

$$\mathbf{e}(\Omega) = \mathbb{P}(\Omega)\mathbf{d}(\Omega) \quad (4.35)$$

$$\mathbf{d}(\Omega) = \mathbb{R}\sigma_1\mathbf{c}(\Omega) + \mathbb{T}\mathbf{a}(\Omega) \quad (4.36)$$

The solution to these equations for the intra-cavity field is:

$$\mathbf{c}(\Omega) = \mathbb{K}(\Omega)\mathbb{P}(\Omega)\mathbb{M}\mathbb{P}(\Omega)\mathbb{T}\mathbf{a}(\Omega) + 2ik_p x(\Omega)r\mathbb{K}(\Omega)\mathbb{P}(\Omega)\sigma_3\mathbf{E}, \quad (4.37)$$

$$\mathbb{K}(\Omega) = [\mathbb{I} - \mathbb{P}(\Omega)\mathbb{M}\mathbb{P}(\Omega)\mathbb{R}\sigma_1]^{-1} \quad (4.38)$$

The output field vector can also be obtained by solving the equations above:

$$\mathbf{b}(\Omega) = [-\mathbb{R}\sigma_1 + \mathbb{T}\mathbb{K}(\Omega)\mathbb{P}(\Omega)\mathbb{M}\mathbb{P}(\Omega)\mathbb{T}] \mathbf{a}(\Omega) + 2ik_p x(\Omega)r\mathbb{Y}(\Omega)\mathbf{A}, \quad (4.39)$$

$$\mathbb{Y}(\Omega) = \mathbb{T}\mathbb{K}(\Omega)\mathbb{P}(\Omega)\sigma_3\mathbb{P}(0) (\mathbb{R}\sigma_1\mathbb{K}(0)\mathbb{P}(0)\mathbb{M}\mathbb{P}(0) + \mathbb{I}) \mathbb{T}. \quad (4.40)$$

These equations are admittedly not convenient for studying the properties of the setup analytically, yet useful for generalized description and computer simulation. Further, I will write the solutions explicitly.

4.2.2 Ring-cavity resonance structure

The first unusual property of the ring cavity is its resonance structure. In order to study it, I start with input-output relations for the classical fields explicitly:

$$B_{1,2} = \frac{A_{2,1}}{\mathcal{D}(0)} \left[R \left(1 - e^{2ik_p L} \right) - it (R^2 + 1) e^{ik_p L} \right] - \frac{A_{1,2}}{\mathcal{D}(0)} r T^2 e^{2ik_p L_{1,2}} \quad (4.41)$$

where $L = L_1 + L_2$ is the total cavity length; and $\mathcal{D}(\Omega)$ is the cavity resonance factor:

$$\mathcal{D}(\Omega) = R^2 e^{2i(k_p + \Omega/c)L} + 2iRt e^{i(k_p + \Omega/c)L} - 1 \quad (4.42)$$

The resonance condition for the classical field corresponds to maximal enhancement of the intra-cavity field. This can be found as the minimum of the resonance factor $\mathcal{D}(0)$:

$$\frac{d|\mathcal{D}(0)|^2}{dk_p} = 0, \quad (4.43)$$

which gives the following resonance conditions for the frequency $\omega_c = k_p c$:

$$\omega_c = \begin{cases} \frac{c}{L} \arcsin \left(-t \frac{1+R^2}{2R} \right) \\ \frac{c}{L} \left(\pi - \arcsin \left(-t \frac{1+R^2}{2R} \right) \right). \end{cases} \quad (4.44)$$

Notice that there are two possible resonances, which depend on the reflectivity of the membrane, as shown in 4.4. Without the membrane, these two resonance modes are degenerate, and the membrane splits this degeneracy.

However, the part that makes this system unique is in the independence on the membrane's position. In order to understand this property, I consider the case of a

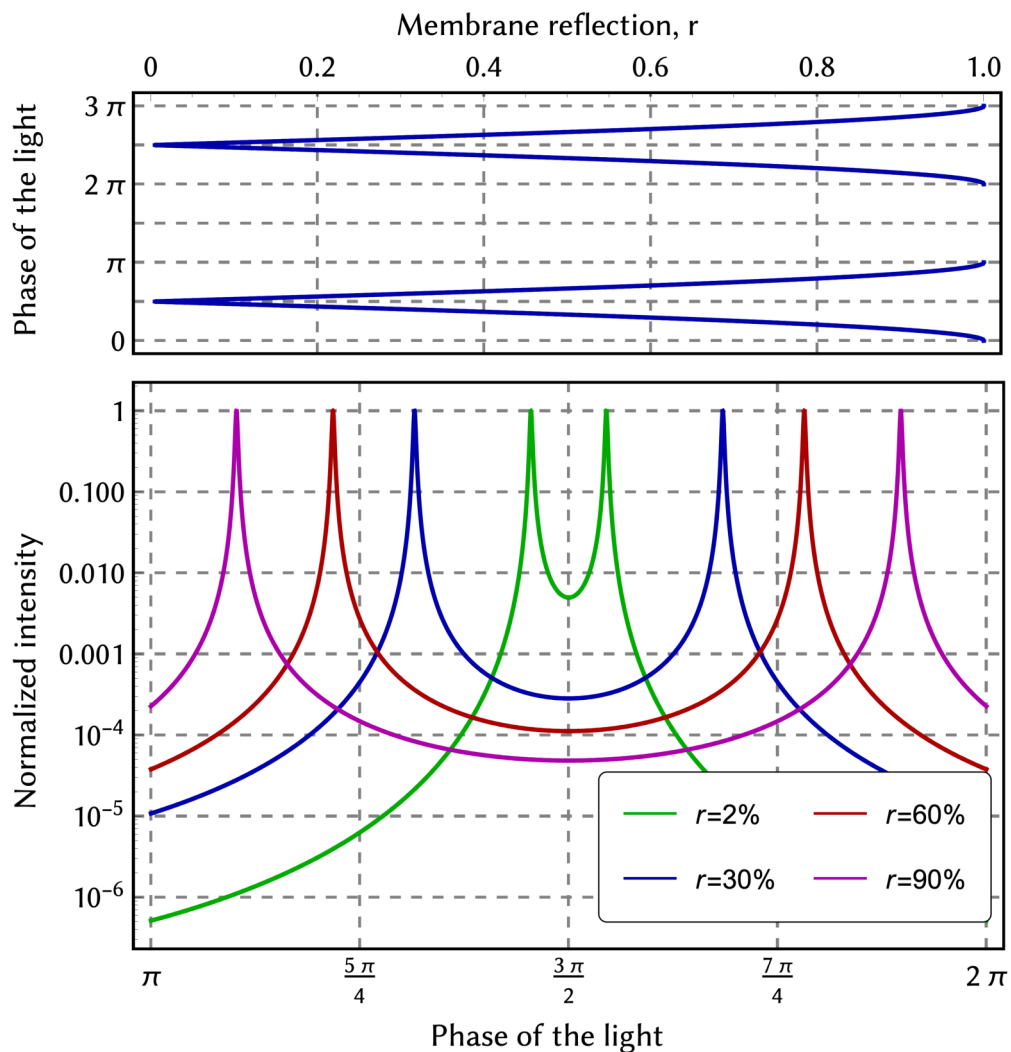


Fig. 4.4. Resonance structure of the ring cavity. Top: the resonance condition for the phase of the incoming light as a function of membrane reflection coefficient. Bottom: intensity of intra-cavity field normalized to its peak as a function of the phase of incoming light for different reflectivities of the membrane. Without a membrane, $r = 0$, the peaks are separated by one FSR (2π phase), which corresponds to the empty ring cavity. With a membrane the resonance splits into two, and the separation between the two modes increases with increased reflectivity. When the membrane is perfectly reflective, the peaks are equidistant again, corresponding to the Fabry-Perot cavity case.

perfectly reflective membrane. On resonance the standing wave is formed, much as in a Fabry-Perot cavity. However, the shift of the membrane does not cause the change of total length of the cavity, unlike the Fabry-Perot cavity. Therefore the resonance condition for the standing wave does not change either. This becomes important in the discussion of the optomechanical coupling below.

When the membrane's reflectivity is equal to zero, the resonance condition reproduces a usual ring cavity resonance with FSR c/L . Such a cavity maintains two possible modes: clockwise and counter-clockwise, which have the same resonant frequency – they are degenerate. Introducing a reflecting element couples clockwise and counter-clockwise modes, and the interference between them results in two new resonant modes (symmetric and anti-symmetric). These two new modes have a different resonance frequency, so the membrane reflectivity breaks the degeneracy of the ring cavity.

When the reflectivity of the input mirror is rather large, the resonance condition can be approximated as:

$$\cos k_{\pm}L \approx \pm r, \quad r = \cos \theta, \quad t = \sin \theta \quad (4.45)$$

$$\Delta\omega_c \equiv c(k_+ - k_-) \approx \frac{2c}{L} \arcsin r. \quad (4.46)$$

This mode splitting effect occurs also in other optomechanical systems, such as membrane-in-the-middle setups [181–185]. The unusual property in the ring cavity is that the splitting depends only on the reflectivity of the membrane, not its position.

4.2.3 Single mode approximation

The parameter regime for the system allows to use a single-mode approximation [35] to simplify the equations assuming: (i) the sideband (signal) frequency is much smaller than the cavity free spectral range $\Omega, \delta_a \ll c/L$, and (ii) the transmissivity T of the front mirror is small, so that I can make a Taylor expansion $R \approx 1 - T^2/2$. I define the linewidth of the system:

$$\gamma = \frac{cT^2}{2L} = \frac{T^2}{2\tau}, \quad (4.47)$$

where $\tau = L/c$ is the round-trip time, and write down the resonance factor:

$$\begin{aligned}\mathcal{D}(\Omega) &= -1 + 2itRe^{-i\theta}\left(1 + i\frac{\Omega L}{c}\right) + R^2e^{-2i\theta}\left(1 + 2i\frac{\Omega L}{c}\right) = \\ &= -2r\tau e^{-i\theta}(\gamma - i\Omega),\end{aligned}\tag{4.48}$$

where I applied the resonance condition in the single mode approximation:

$$e^{ik_p L} = r - it = e^{-i\theta}.$$

In the single mode approximation the velocity port remains dark for the classical field, i.e. the full power is reflected back to the position port (assuming the laser input only from one side: $A_2 = 0$):

$$B_1 = A_1\tag{4.49}$$

$$B_2 = 0\tag{4.50}$$

For the quantum fields, since the macroscopic position of the membrane does not affect the resonance of the system, I simplify the equations without loss of generality by assuming $L_1 = L_2 = L/2$. The output fields on the two ports can be represented as:

$$b_1 = b_{11}a_1 + b_{12}a_2 + b_{13}x,\tag{4.51}$$

$$b_2 = b_{21}a_1 + b_{22}a_2 + b_{23}x,\tag{4.52}$$

where the coefficient are computed from the matrices:

$$b_{11} = b_{22} = -\frac{1}{\mathcal{D}(\Omega)} r T^2 e^{i(k_p + \Omega/c)L}, \quad (4.53)$$

$$b_{12} = b_{21} = -\frac{1}{\mathcal{D}(\Omega)} \left(-R + it(1 + R^2) e^{i(k_p + \Omega/c)L} + R e^{2i(k_p + \Omega/c)L} \right), \quad (4.54)$$

$$b_{13} = \frac{2ik_p r T^2 A_1 e^{i(k_p + \Omega/2c)L}}{\mathcal{D}(0)\mathcal{D}(\Omega)} \times \left(1 - R e^{ik_p L} (it + ite^{i\Omega L/c} + R e^{i(k_p + \Omega/c)L}) \right), \quad (4.55)$$

$$b_{23} = \frac{2ik_p A_1 r^2 T^2 R e^{i(2k_p + \Omega/2c)L} (-1 + e^{i\Omega L/c})}{\mathcal{D}(0)\mathcal{D}(\Omega)}. \quad (4.56)$$

In the single mode approximation these relations simplify to:

$$b_{11}(\Omega) = b_{22}(\Omega) \approx \frac{\gamma}{\gamma - i\Omega}, \quad (4.57)$$

$$b_{12}(\Omega) = b_{21}(\Omega) \approx \frac{-i\Omega}{\gamma - i\Omega}, \quad (4.58)$$

$$b_{13}(\Omega) \approx \frac{2ik_p A_1 (\gamma - i\Omega/2)}{\gamma - i\Omega}, \quad (4.59)$$

$$b_{23}(\Omega) \approx i\Omega \frac{2ik_p A_1}{2(\gamma - i\Omega)}. \quad (4.60)$$

First notice the most important feature of the system: the signal on the velocity port $b_{23}(\Omega)$ is proportional only to frequency, which is the speedometer definition, since in the frequency domain: $v(t) = \dot{x}(t) \rightarrow v(\Omega) = -i\Omega x(\Omega)$. At low frequencies, where $\Omega \ll \gamma$, this signal is purely velocity. At high frequencies, the cavity bandwidth averages the signal, which becomes purely position signal (i.e. zeroth order in frequency): $b_{23}(\Omega \gg \gamma) \approx -ik_p A_1$. The position port contains a mixture of position and velocity signal:

$$b_{13}(\Omega) = 2ik_p A_1 \left(1 + \frac{i\Omega}{2(\gamma - i\Omega)} \right), \quad (4.61)$$

approaching purely position contribution for small and large frequencies (and only getting the mixture of velocity in the intermediate regime $\Omega \sim \gamma$). In my

experiment, the cavity linewidth was significantly larger than the measurement frequency, so the position port indeed contained almost only position signal.

The second important point to be seen in the equations is the optical transfer functions for the incoming fields $b_{11,12,21,22}$. It can be seen that the noise coupling from one port to another acquires a speedmeter scaling, and the noise reflected directly to the position port does not. This fact I will confirm experimentally.

In this section I demonstrated that the ring cavity indeed serves as a speedmeter. Moreover, it features two separate output ports that allow to measure velocity and position independently.

4.3 Full quantum noise sensitivity

4.3.1 Shot-noise limited sensitivity

Two-photon quadratures

In order to conveniently compute the spectral densities as measured with the homodyne detector, I transition to the two-photon quadratures, as described in the Chapter 3. Two-photon quadratures for a field $a(\omega_p \pm \Omega)$ are defined as following:

$$a^c(\Omega) = \frac{a(\omega_p + \Omega) + a^\dagger(\omega_p - \Omega)}{\sqrt{2}}, \quad a^s(\Omega) = \frac{a(\omega_p + \Omega) - a^\dagger(\omega_p - \Omega)}{i\sqrt{2}}$$

and the corresponding vector:

$$a = \begin{bmatrix} a^c \\ a^s \end{bmatrix}.$$

Expressed in terms of two-photon quadratures, the input-output relations 4.51 become:

$$b_1 = \mathcal{R}_1(\Omega) a_1 + \mathcal{R}_2(\Omega) a_2 + x \mathcal{M}_{1x}(\Omega) \mathcal{A}_1 + \Omega x \mathcal{M}_{1v}(\Omega) \mathcal{A}_1, \quad (4.62)$$

$$b_2 = \mathcal{R}_2(\Omega) a_1 + \mathcal{R}_1(\Omega) a_2 + \Omega x \mathcal{M}_{2v}(\Omega) \mathcal{A}_1, \quad (4.63)$$

where the transfer matrices are:

$$\mathcal{R}_1(\Omega) = \frac{\gamma}{\gamma - i\Omega} \mathbb{1}, \quad (4.64)$$

$$\mathcal{R}_2(\Omega) = \frac{-i\Omega}{\gamma - i\Omega} \mathbb{1}, \quad (4.65)$$

$$\mathcal{M}_{1x}(\Omega) = -\frac{ik_p\gamma}{\gamma - i\Omega} \sigma_2, \quad (4.66)$$

$$\mathcal{M}_{1v}(\Omega) = -\frac{ik_p}{2(\gamma - i\Omega)} \sigma_2, \quad (4.67)$$

$$\mathcal{M}_{2v}(\Omega) = \frac{k_p}{\gamma - i\Omega} \sigma_2. \quad (4.68)$$

Shot noise spectral density

The displacement signal from the ring cavity is measured with a homodyne detector with homodyne phase ζ :

$$y_{1,2} = \mathbf{H}_{1,2}^T \hat{b}_{1,2}, \quad \mathbf{H}_{1,2}^T = [\cos \zeta, \sin \zeta]^T. \quad (4.69)$$

In order to get the sensitivity, I want to normalize both outputs to the corresponding signal transfer function. The way to do it can be dividing by the pre-factor in front of x in Eqs. 4.69:

$$\tilde{y}_1 = \frac{y_1}{\mathbf{H}_1^T \mathcal{M}_{1x} \mathcal{A}_1 + \Omega \mathbf{H}_1^T \mathcal{M}_{1v} \mathcal{A}_1} = \mathcal{X}_1 + x, \quad (4.70)$$

$$\tilde{y}_2 = \frac{y_2}{\Omega \mathbf{H}_2^T \mathcal{M}_{2v} \mathcal{A}_1} = \mathcal{X}_2 + x, \quad (4.71)$$

where $\mathcal{X}_{1,2}$ are the quantum noise parts of the normalized output. Since the signal in a cavity tuned on resonance with incoming field is in the phase quadrature, I select $\zeta = \pi/2$, and also without loss of generality fix the phase of the incoming light such that

$$\mathcal{A}_1 = \sqrt{2A} \begin{bmatrix} 1 \\ 0 \end{bmatrix} = \sqrt{\frac{2I_{\text{in}}}{\hbar\omega_p}} \begin{bmatrix} 1 \\ 0 \end{bmatrix}. \quad (4.72)$$

	position meter	speedmeter
without cavity	$\frac{\hbar c^2}{4I_{\text{in}}\omega_p}$	$\frac{\hbar c^2}{4I_{\text{in}}\omega_p} \frac{1}{\Omega^2 \tau^2}$
ring cavity	$\approx \frac{\hbar c^2}{4I_{\text{in}}\omega_p}$	$\frac{\hbar c^2}{4I_{\text{in}}\omega_p} \frac{T^4}{\Omega^2 \tau^2}$
standard detector	$\frac{\hbar c^2}{4I_{\text{in}}\omega_p} \frac{T^4}{4}$	$\frac{\hbar c^2}{4I_{\text{in}}\omega_p} \frac{T^4}{4} \frac{T^4}{16\Omega^2 \tau^2}$

Tab. 4.1. Comparison between the shot-noise-limited sensitivities of different detectors. The columns represent speed or position measurement. The rows define the type of the detector: position and speedmeters without optical cavities, or a standard Michelson-Fabry-Perot position meter and a Sagnac speedmeter.

The spectral densities of noises $\mathcal{X}_{1,2}$ then are:

$$S_{\mathcal{X}_1} = \frac{\hbar c^2}{4I_{\text{in}}\omega_p} \frac{\gamma^2 + \Omega^2}{\gamma^2 + \Omega^2/4} \quad (4.73)$$

$$S_{\mathcal{X}_2} = \frac{\hbar c^2}{4I_{\text{in}}\omega_p} \frac{\gamma^2 + \Omega^2}{\Omega^2} \quad (4.74)$$

Comparison to other setups

It is interesting to compare the shot-noise-limited sensitivity of the ring cavity to other setups, see Table 4.1. In a standard speedmeter, optical cavities play several roles: they enhance the light power and signal, much like in a standard position meter, and also increase the effective delay $\tau \rightarrow \tau/T^2$, which benefits the sensitivity of a speedmeter. In the ring optomechanical cavity setup the cavity itself plays an unusual role: it does not enhance the signal proportionally to its finesse. Instead, the position signal has the same strength as for a free-standing perfectly reflective membrane. When the membrane has small reflectivity, a free-standing membrane would lose the signal proportionally to its transmission, but in a ring cavity that does not happen. In a ring cavity the signal adds from the many round trips such, that even for a very small reflectivity of the membrane, the output signal is not reduced compared to the signal from a perfectly reflective membrane. On the other hand, most of the signal gets coherently canceled due to

the resonance condition of the cavity, and only a small part due to the imbalance of powers on two sides of the membrane produces a signal. As a result, in the ring cavity the sensitivity does not depend on the reflectivity of the membrane, but also is not enhanced by a cavity resonance. For the velocity signal, the ring cavity also enhances the effective delay, in addition to reflectivity-independence, which makes the sensitivity significantly, $\sim T^4$ times better than the one of a free-standing membrane without cavity.

The light power inside the cavity is enhanced by a cavity finesse. However, when the two light fields of almost equal power interact with the membrane, the signal that is carried away is almost completely canceled by destructive interference between these beams. The setup is slightly asymmetric due to the semi-transparent front mirror – the light field on one side of the membrane is slightly reduced compared to other side, since part of it leaked to the outside through the front mirror. The small difference in powers equals the power that leaked out of the cavity. By energy conservation, the power that leaks out equals the input power. Since the powers on the two sides of the membrane are not equal, this imbalance translates into an imperfect cancellation of the signal – again, proportionally to the input light power. Therefore, for the position signal, it looks as if the light was directly reflected from the membrane without experiencing any cavity effects. As a result, both position and velocity sensitivities are $\sim T^4$ times worse than the ones of a standard position- or speedmeter, see Table 4.1. In the next sections I will discuss the necessary changes to the setup for achieving a sensitivity comparable to the standard GW detectors.

4.3.2 Radiation-pressure noise

The motion of the membrane is excited by thermal noise and by radiation-pressure noise. In order to find how large these noises are, I compute the radiation-pressure noise explicitly.

Each light field reflected off a membrane applies some force on it in the direction it impinges on it. In the ring cavity, there are two sides of the membrane, both subject to radiation pressure. This force causes a displacement of the membrane. As I discuss in Chapter 2, the radiation pressure noise is a manifestation of the measurement back-action applied by a meter (light) on the object (membrane).

It can be separated in two contributions: static force and corresponding shift of the membrane's position (if the light powers are unequal on two sides of the membrane), and noisy force, coming from quantum (or classical) fluctuations of the light field. The total force can be defined as a sum of all contributions:

$$F_{\text{rp}} = \sum \pm \mathcal{I}_i / c,$$

where \mathcal{I}_i is the intensity of i -th field falling on the oscillator, and the sign of intensity is defined by the direction of travel.

There are two equivalent ways of calculating the QRPN: using two-photon and sideband picture. *In the sideband picture:*

$$F_{\text{rp}} / \hbar k_p = \mathbf{E}^\dagger \sigma_3 \mathbf{e}(\omega_p + \Omega) + \mathbf{F}^\dagger \sigma_3 \mathbf{f}(\omega_p + \Omega) + \mathbf{E}^T \sigma_3 \mathbf{e}^\dagger(\omega_p - \Omega) + \mathbf{F}^T \sigma_3 \mathbf{f}^\dagger(\omega_p - \Omega) \quad (4.75)$$

In the two-photon picture:

$$F_{\text{rp}} / \hbar k_p = \mathcal{E}_1^T e_1(\Omega) - \mathcal{E}_2^T e_2(\Omega) + \mathcal{F}_1^T f_1(\Omega) - \mathcal{F}_2^T f_2(\Omega) \quad (4.76)$$

I use the two-photon picture, since it makes it easier to compute the spectral densities. I calculate the classical intra-cavity fields and simplify the denominator in a single-mode approximation, but keep the numerator unexpanded (it will be done at a later stage):

$$E_1 = -A_1 \frac{T e^{ik_p L/2} (1 - iT e^{ik_p L})}{\mathcal{D}(0)} = A_1 \frac{T e^{i\theta/2} (1 - it R e^{-i\theta})}{2r\tau\gamma} \quad (4.77)$$

$$E_2 = -A_1 \frac{r R T e^{3ik_p L/2}}{\mathcal{D}(0)} = A_1 \frac{r R T e^{-i\theta/2}}{2r\tau\gamma} \quad (4.78)$$

$$F_1 = rE_1 + itE_2 = A_1 \frac{r T e^{i\theta/2}}{2r\theta\gamma} \quad (4.79)$$

$$F_2 = rE_2 + itE_1 = A_1 \frac{T (ite^{i\theta/2} + R e^{-i\theta/2})}{2r\tau\gamma} \quad (4.80)$$

For quantum amplitudes, the equations in the sideband picture are:

$$e_1 = \frac{T e^{ikL/2}}{\mathcal{D}(\Omega)} \left(-a_1(1 - itRe^{ikL}) - a_2 r Re^{ikL} + 2ik_p r R \mathcal{G}_2(\Omega) x(\Omega) e^{ikL/2} \right) \quad (4.81)$$

$$e_2 = \frac{T e^{ikL/2}}{\mathcal{D}(\Omega)} \left(-a_2(1 - itRe^{ikL}) - a_1 r Re^{ikL} + 2ik_p r R \mathcal{G}_1(\Omega) x(\Omega) e^{ikL/2} \right) \quad (4.82)$$

$$\mathcal{G}_1(\Omega) = \frac{1}{T} \left((1 - itRe^{ikL}) E_1 - r R E_2 e^{ikL} \right) \quad (4.83)$$

$$\mathcal{G}_2(\Omega) = \frac{1}{T} \left(-(1 - itRe^{ikL}) E_2 + r R E_1 e^{ikL} \right) \quad (4.84)$$

$$f_1 = r e_1 + i t e_2 + 2ik_p x r E_1 \quad (4.85)$$

$$f_2 = r e_2 + i t e_1 - 2ik_p x r E_2 \quad (4.86)$$

The amplitudes of the fields depend on the position $x(\Omega)$, and therefore the QRPN has a dynamical (position-dependent) contribution. This contribution is called dynamical back-action or optical rigidity. First, I find the position-independent part of the QRPN, setting $x(\Omega) = 0$, and going to two-photon quadratures:

$$e_1 = \frac{T e^{i\Omega\tau/2}}{2r\tau(\gamma - i\Omega)} [\mathcal{P}_1(\Omega) a_1 + \mathcal{P}_2(\Omega) a_2], \quad (4.87)$$

$$e_2 = \frac{T e^{i\Omega\tau/2}}{2r\tau(\gamma - i\Omega)} [\mathcal{P}_1(\Omega) a_2 + \mathcal{P}_2(\Omega) a_1], \quad (4.88)$$

$$f_1 = r \mathbb{1} e_1 - i t \sigma_2 e_2 \quad (4.89)$$

$$f_2 = r \mathbb{1} e_2 - i t \sigma_2 e_1 \quad (4.90)$$

$$\mathcal{E}_1 = \frac{T}{2r\tau\gamma} \mathcal{P}_1(0) \mathcal{A}_1, \quad (4.91)$$

$$\mathcal{E}_2 = \frac{T}{2r\tau\gamma} \mathcal{P}_2(0) \mathcal{A}_1, \quad (4.92)$$

$$\mathcal{F}_1 = r \mathbb{1} \mathcal{E}_1 - i t \sigma_2 \mathcal{E}_2 \quad (4.93)$$

$$\mathcal{F}_2 = r \mathbb{1} \mathcal{E}_2 - i t \sigma_2 \mathcal{E}_1 \quad (4.94)$$

where I defined the frequency-dependent matrices:

$$\mathcal{P}_1 = \begin{bmatrix} \cos \frac{\theta}{2} - tRe^{i\Omega\tau} \sin \frac{\theta}{2} & -\sin \frac{\theta}{2} + tRe^{i\Omega\tau} \cos \frac{\theta}{2} \\ \sin \frac{\theta}{2} - tRe^{i\Omega\tau} \cos \frac{\theta}{2} & \cos \frac{\theta}{2} - tRe^{i\Omega\tau} \sin \frac{\theta}{2} \end{bmatrix} \quad (4.95)$$

$$\mathcal{P}_2 = rRe^{i\Omega\tau} \begin{bmatrix} \cos \frac{\theta}{2} & \sin \frac{\theta}{2} \\ -\sin \frac{\theta}{2} & \cos \frac{\theta}{2} \end{bmatrix} \quad (4.96)$$

Taking these into account, I compute the contributions to the QRPN from the reflected fields:

$$\begin{aligned} \mathcal{F}_1^T f_1 &= (r\mathcal{E}_1 - it\sigma_2\mathcal{E}_2)^T (r\mathbb{1}e_1 - it\sigma_2e_2) = \\ &= r^2\mathcal{E}_1^T e_1 + t^2\mathcal{E}_2^T e_2 + irt \left(\mathcal{E}_1^T \sigma_2 e_2 - \mathcal{E}_2^T \sigma_2 e_1 \right) \end{aligned} \quad (4.97)$$

$$\mathcal{F}_2^T f_2 = r^2\mathcal{E}_2^T e_2 + t^2\mathcal{E}_1^T e_1 + irt \left(\mathcal{E}_2^T \sigma_2 e_1 - \mathcal{E}_1^T \sigma_2 e_2 \right) \quad (4.98)$$

From this, the QRPN can be simplified:

$$F_{\text{rp}} = 2\hbar k_p \left(r^2 (\mathcal{E}_1^T e_1 - \mathcal{E}_2^T e_2) + irt (\mathcal{E}_1^T \sigma_2 e_2 - \mathcal{E}_2^T \sigma_2 e_1) \right), \quad (4.99)$$

Choosing the phase of the input field such, that $\mathcal{A}_1 = \{A, 0\}^T / \sqrt{2}$, I obtain the QRPN in the single mode approximation:

$$\begin{aligned} F_{\text{rp}}(\Omega) &= \frac{\hbar k_p A}{\sqrt{2}(\gamma - i\Omega)} \left[(r^2 - t^2) (2\gamma - i\Omega) a_1^c(\Omega) + irt\Omega a_1^s(\Omega) + \right. \\ &\quad \left. + (r^2 - t^2) \Omega a_2^c(\Omega) + irt (2\gamma - i\Omega) a_2^s(\Omega) \right]. \end{aligned} \quad (4.100)$$

The equations above allow to compute the spectral density of the QRPN:

$$S_{\text{rp}}(\Omega) = 2\gamma^2 \frac{\hbar\omega_p I_{\text{in}}}{c^2(\gamma^2 + \Omega^2)} + \Omega^2 \frac{\hbar\omega_p I_{\text{in}}}{c^2(\gamma^2 + \Omega^2)} = S_{\text{rp}}^x(\Omega) + S_{\text{rp}}^v(\Omega), \quad (4.101)$$

where $I_{\text{in}} = \frac{1}{2}\hbar k_p c A^2$ is the average optical power in the incoming beam. This spectral density has two contributions: position $S_{\text{rp}}^x(\Omega)$ and velocity $S_{\text{rp}}^v(\Omega)$. This corresponds to the two detection channels. Since every measurement produces a back action, the position port must have its contribution, as well as the velocity one.

However, the measurement outputs of these two channels can be optimally combined to evade the back-action, as it is done in variational readout approach, or in Chapter 5. Alternatively, if the two input light fields are entangled such, that $(r^2 - t^2)a_1^c = -irta_2^s$, the position-dependent part in Eq. 4.100 gets canceled. Finally, if $r = t$, it is sufficient to inject squeezed light to suppress a_2^s to achieve speedmeter sensitivity. These approaches require further study into their detailed implementation and feasibility.

Another important fact is that the QRPN in the ring cavity is significantly smaller than the noise in a conventional Fabry-Perot cavity:

$$S_{\text{rp,FP}}(\Omega) = \frac{4\hbar I_{\text{in}} \omega_p}{L^2(\gamma^2 + \Omega^2)}. \quad (4.102)$$

This is expected: since the shot noise is increased compared to the Fabry-Perot cavity, the radiation-pressure must be reduced to obey the Heisenberg uncertainty relation (for a minimum uncertainty state). Fundamentally, the origin of this reduction is exactly the symmetry of the setup that allows the velocity measurement: most of the radiation pressure is canceled coherently on the round trip. Only a small fraction of the signal that leaks through the front mirror, is not canceled.

Intra-cavity light field also depends on the position of the membrane, which causes a position-dependent part of the QRPN. From Eqs. 4.87, I obtain this position-dependent part in the single-mode approximation:

$$F_{\text{rp}}^x = \frac{4\omega_p I_{\text{in}} t}{cL\gamma} x = \mathcal{K}_{\text{os}} x, \quad (4.103)$$

where \mathcal{K}_{os} is the optical spring constant. The dynamics of the mirror is described by:

$$M\ddot{x}(t) + 2\gamma_m \dot{x}(t) + M\omega_m^2 x(t) = F_{\text{rp}}(t) + F_{\text{rp}}^x(t) + F_{\text{th}}(t) \quad (4.104)$$

where ω_m is the mechanical frequency, γ_m is the mechanical linewidth, M is membrane's mass, F_{th} is the random force caused by thermal fluctuations in the

membrane. Taking into account the change in dynamics due to the QRPN, the dynamics changes:

$$M\ddot{x}(t) + 2\gamma_m\dot{x}(t) + (M\omega_m^2 - \mathcal{K}_{os})x(t) = F_{rp}(t) + F_{th}(t). \quad (4.105)$$

Dynamical QRPN effectively introduces a shift to the mechanical frequency, thus its name – ”optical spring”. This optical spring is different from the optical spring arising in a Fabry-Perot cavity, where additionally to changing the frequency, the QRPN introduces additional damping or anti-damping. In a Fabry-Perot cavity optical spring arises only when the laser is detuned off the cavity’s resonance frequency. In the ring cavity the optical spring arises on resonance, and it only shifts the mechanical resonance frequency, without introducing any damping or anti-damping.

However, this optical spring is rather weak: for the experimental parameters of a ring cavity presented in the experimental section of this chapter, the shift due to the optical spring is on the order of 10 kHz to the mechanical frequency of 395 kHz.

4.3.3 Spectrum and discussion

The expressions obtained in the previous sections allow to plot the sensitivity of the ring cavity to the displacement, see Fig. 4.5. The expected sensitivity of the table-top setup is fully dominated by thermal noise, even at cryogenic temperatures. This is expected from the previous discussion: e.g. the sensitivity to the displacement in a ring cavity is analogous to a mirror without the cavity, which is too low to be limited by QRPN in any regime (that is why cavities are used in optomechanical devices in the first place). However, unlike in sensing a single mirror, the velocity signal is of the same magnitude as the position one. That, in principle, allows to directly compare two types of sensitivities in the same setup.

It is possible to enhance the sensitivity of the setup by placing a cavity around the membrane, see Fig. 4.6. In this case, the response would be enhanced and the sensitivity would become comparable to the standard Fabry-Perot based setups. This, however, requires careful tuning of all the phases in the cavity.

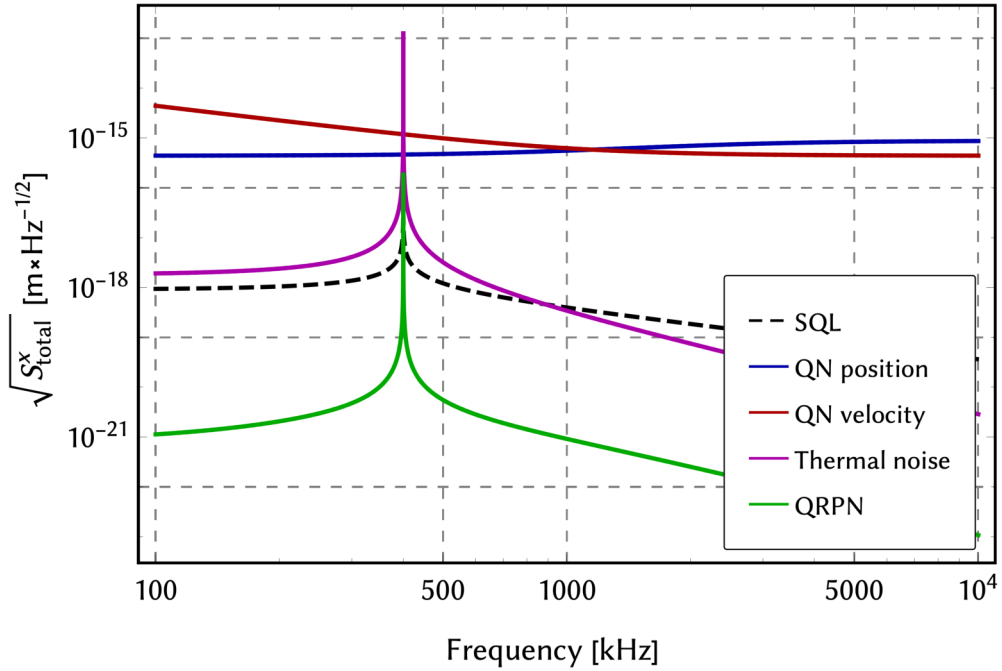


Fig. 4.5. Displacement sensitivity of the ring cavity on the position and velocity output ports. The quantum noise (QN) sensitivity is shown for position and velocity outputs. The speedometer scaling of the shot noise is visible at low frequencies. Thermal excitation of the fundamental mode is visible above the shot noise, and it is significantly above the QRPN. Only the fundamental mode is plotted in this plot (there are higher order mechanical modes, as I discuss in the next section). The parameters are listed in Table 4.2.

Another similar approach is to place signal and power recycling mirrors in the two ports of the cavity. This will enhance the signal and the light power, allowing to reach the QRPN-limited regime. It will, however, also require a very careful tuning of different lengths and control of the subsystems, which makes such an approach practically very challenging.

4.3.4 Towards large-scale design

The ring cavity topology offers interesting properties, that might be used for future gravitational-wave detectors. In particular, it would be possible to implement the ring-cavity type design directly in the current generation of GWOs. For that purpose the central beamsplitter has to be "turned" by 90 degrees to form a front

mirror that couples the two arms of the interferometer, see Fig 4.6. Such a detector would feature the full enhancement to the sensitivity from the arm cavities, and the speedmeter signal on the output of the detector.

However, there are difficulties associated with such a design. Firstly, some information leaks through the position port, and creates the position-dependent contribution to the QRPN, which spoils the speedmeter scaling. In order to cancel this contribution, an optimal combination of two measured outputs is required, as described in Chapter 5. Then, it is possible to achieve a full speedmeter sensitivity. The theoretical investigation of this scheme is currently underway.

Secondly, the dark (velocity) port contains not only a velocity signal from the differential motion of the mirrors, but also common motion noise, which contaminates the sensitivity, since it contains no GW signal. Usually in a standard Michelson interferometer, this common mode is canceled naturally. In the L-shaped detector, this is not the case, and special measures would have to be considered for avoiding the influence of this common mode contamination. This requires a separate analysis.

4.4 Optomechanical coupling

Ring cavities feature an unusual optomechanical coupling, one we call *coherent*. In this section I briefly overview this type of coupling and mention the consequences for the cavity optomechanical experiments. The results presented in this section were obtained in collaboration with X.Li, Y.Ma and Y.Chen, and were published in [68].

In the previous section I described the resonant structure of the ring cavity. The equations for the propagating fields were written in terms of clockwise and counterclockwise modes. These modes are the eigenmodes of a ring cavity without the membrane. However, when the membrane is placed inside, these modes are no longer resonant. The eigenmodes of the system have new resonant frequencies ω_{\pm} . These eigenmodes can be constructed out of clock- and counterclockwise modes $e_{1,2}$:

$$e_{\pm} = \frac{e_1 \pm e_2}{\sqrt{2}}. \quad (4.106)$$

We call the new eigenmode e_+ *symmetric*, and e_- – *anti-symmetric*.

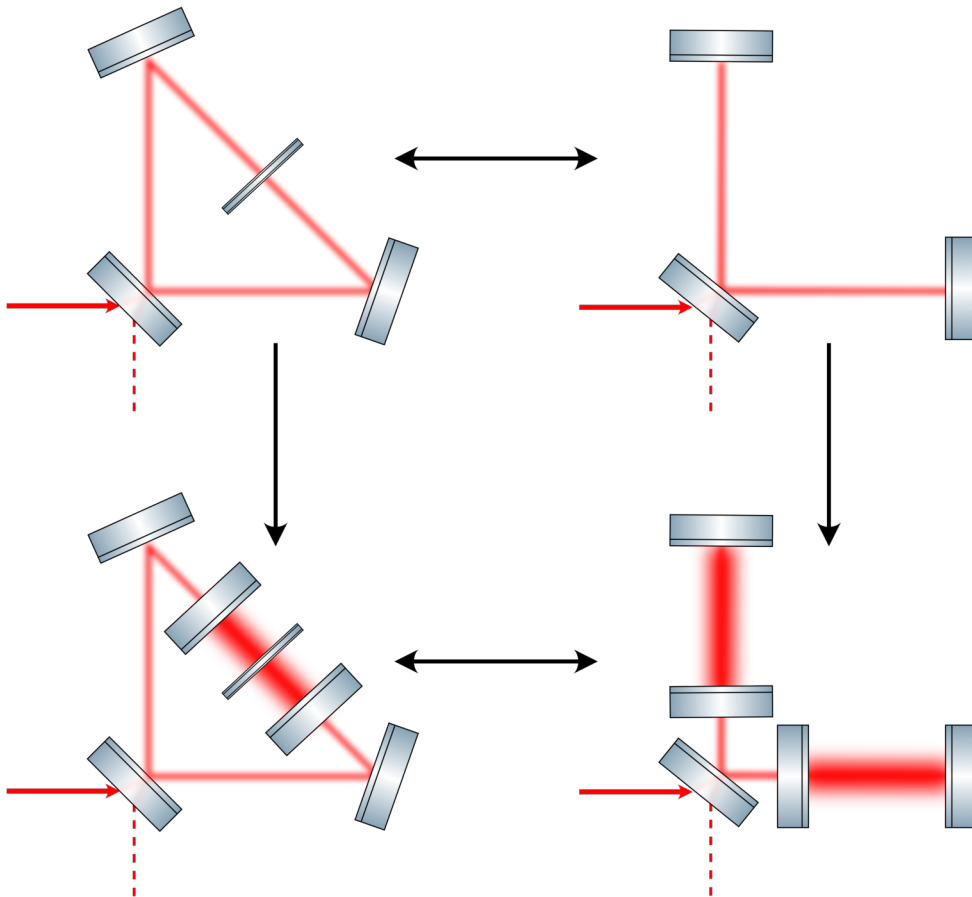


Fig. 4.6. A path towards ring-cavity-based GW detector. The ring cavity with a perfectly reflective membrane (top left) is invariant to the L-shaped cavity (top right). Placing a Fabry-Perot cavity around the membrane (bottom left) enhances the light power as well as the signal. So do the arm cavities in the L-shaped topology (bottom right). The resulting sensitivity is compatible with traditional speedmeter topologies (e.g. a Sagnac speedmeter).

The motion of the membrane introduces a phase shift on the modes $e_{1,2}$, see Eqs. 4.87. These modes can be re-written in terms of symmetric and anti-symmetric modes:

$$e_+ = -\frac{a_+ T e^{-i(\theta-\Omega\tau)/2} (e^{2i\theta} + R e^{i\Omega\tau})}{2r\tau e^{-i\theta} (\gamma - i\Omega)} - 2ik_p x \frac{E_- R e^{-i(2\theta-\Omega\tau)} (e^{2i\theta} + R e^{i\Omega\tau})}{\tau(\gamma - i\Omega)}, \quad (4.107)$$

$$e_- = -\frac{a_- T e^{i(3\theta+\Omega\tau)/2} (1 - R e^{i\Omega\tau})}{2r\tau e^{-i\theta} (\gamma - i\Omega)} - 2ik_p x \frac{E_+ R e^{i\Omega\tau} (1 - R e^{i\Omega\tau})}{\tau(\gamma - i\Omega)}. \quad (4.108)$$

In the single-mode approximation these equations are significantly simplified:

$$e_+ = -\frac{\sqrt{2}a_+ e^{-i\theta/2}}{\sqrt{\gamma\tau}} - \frac{i\sqrt{2}k_p x A_+ e^{-i\theta/2}}{\sqrt{\gamma\tau}}, \quad (4.109)$$

$$e_- = -\frac{\sqrt{2}a_- e^{i\theta/2} (\gamma - i\Omega)\tau}{2r\sqrt{\gamma\tau}} - \frac{i\sqrt{2}k_p x A_+ e^{-i\theta/2} (\gamma - i\Omega)}{\sqrt{\gamma\tau} \gamma}. \quad (4.110)$$

There are several important features that can be seen from these equations. First, mode e_+ is on resonance, and e_- is off resonance: $e_-(x=0) \sim e_+(x=0)\gamma\tau$, where $\gamma\tau \ll 1$. This is expected for the eignemodes of the system. Second, from Eq. 4.107 it follows, that for symmetric mode the displacement couples with anti-symmetric classical amplitude, and vice versa for the anti-symmetric. In other words, the displacement couples symmetric and anti-symmetric modes. This statement reflects the most important feature of the optomechanical interaction in the ring cavity: mechanical motion couples two eigenmodes of the system. In a general form, the dynamical coupling between the modes is [68]:

$$e_{\pm}(x) = \frac{e^{ik_p L/2}}{e^{-ik_p x} e_1 \pm e^{ik_p x} e_2}. \quad (4.111)$$

We call such optomechanical coupling *coherent*.

In general, in optomechanical systems, mechanical motion can affect different parameters of the system. The systems are usually classified based on this cou-

pling between the mechanical and optical degrees of freedom. In systems with *dispersive* coupling, mechanical motion changes the resonance frequency of the eigenmodes. In systems with *dissipative* coupling, mechanical motion changes the coupling rate of the eigenmodes to the environment. In a ring cavity, neither dispersive, nor dissipative coupling is present. Instead, mechanical motion re-distributes the energy between the two eigenmodes of the system. The optical part of the Hamiltonian of the ring cavity system explicitly shows that the modes themselves are changed with mechanical motion:

$$\hat{H} = \hbar\omega_+\hat{e}_+(x)^\dagger\hat{e}_+(x) + \hbar\omega_-\hat{e}_-(x)^\dagger\hat{e}_-(x) \approx \quad (4.112)$$

$$\approx \hbar\omega_+\hat{e}_+(0)^\dagger\hat{e}_+(0) + \hbar\omega_-\hat{e}_-(0)^\dagger\hat{e}_-(0) + 2i\Delta\omega(\hat{e}_-(0)^\dagger\hat{e}_+(0) - \text{h.c.}). \quad (4.113)$$

This equation directly shows how displacement x creates a photon in one mode and annihilates in another mode, thus enabling the energy exchange between the modes.

In [68] we developed a general framework for unambiguous classification of optomechanical couplings. This classification allows to identify the type of coupling, and predict the properties of the system based on that. In particular, coherent coupling allows enhanced laser cooling of mechanical oscillator to its motional ground state. The main property of coherent coupling – energy conversion between the modes of different frequencies, can allow new types of quantum optomechanical devices and frequency converters. Further research of different aspects of coherent coupling is underway. In the next section, I focus on the experimental investigation of the system as a speedmeter, towards the GW detection.

4.5 Experimental results

It is difficult to directly compare the sensitivity of most quantum speedmeter designs to a position meter, since their topology and optical parameters differ significantly. The ring cavity features two output ports, one containing the position signal, another one containing the velocity signal. All the parameters, such as cavity length, linewidth or light power, are the same for the speed and position outputs of the cavity. I propose this design for a direct comparison between the velocity and position sensitivity.

In this section I present the first steps towards this goal in a table-top ring cavity experiment. As I described in the theory section, it is not possible to reach the quantum-noise limited sensitivity at room temperature with feasible light powers. Therefore, the goal of the experiment was to demonstrate the speedometer-like classical sensitivity (i.e. not limited by quantum noise). This goal was achieved partially: I demonstrated the speedometer-type optical transfer function of the cavity, but the full sensitivity was not achievable due to fundamental limitations in the experimental setup. In this section, I describe the characterization of the optomechanical setup, show the experimental sensing of the external signal and explain the origins of the limitations on demonstrating the full sensitivity of the speedometer in this setup.

The experimental setup shown on Fig. 4.7 implemented the proposed ring cavity design with a micromechanical SiN membrane serving as a central mirror, see Fig. 4.8

4.5.1 Optical cavity

There were several practical considerations regarding the cavity design:

- Cavity waist size had to be smaller than the membrane size of $\sim 0.5\text{-}1$ mm.
- One of the mirrors had to be curved for the cavity to sustain a stable Gaussian mode. The angle of incidence on this mirror had to be as small as possible in order to minimize the ellipticity of the mode. This imposed some restrictions on the possible length of the cavity: given the size of the membrane, the membrane holder and positioner, the minimal length could be around 30 cm.
- One of the back mirrors had to be partially transparent for alignment purposes, but not too transparent to avoid significant signal leakage.
- The mirrors and membrane had to be adjustable in vacuum for proper alignment.

These requirements resulted in the design parameters in Table 4.2. The cavity length was optimized to minimize the effect of high-order optical modes on

Cavity parameters	
Length	39.1 cm
Front mirror power transmission	0.01
Back mirror power transmission	0.0007
Back mirror radius of curvature	25 cm
Back mirror angle of incidence	10.5°
Waist w_x	221 μm
Waist w_y	229 μm
Cavity linewidth peak 1	0.84 MHz
Cavity linewidth peak 2	0.95 MHz
Cavity resonance splitting	~53.5 MHz
Light power input	0.01 mW
Light power detection	100 μW
Membrane parameters	
Membrane reflectivity	4.6%
Membrane size	1 mm \times 1 mm
Membrane clipping	~0.002%
Membrane frequency	395.2 kHz
Membrane Q factor	4.6×10^5

Tab. 4.2. Main experimental parameters of the ring-cavity system.

the main resonance, see Fig. 4.9. The cavity spacer was designed by T.Sobottke during his master thesis. The cavity parameters were experimentally verified by measuring the linewidth of the cavity (with and without the membrane), see Fig. 4.10.

The laser was stabilized to the cavity resonance by the Pound-Drever-Hall technique [46, 47]. For that purpose a phase modulation sideband was reflected off the cavity, and the beat between the main field and the sideband was detected on a separate photodiode. After demodulation at the sideband frequency, the resulting error signal was fed back to the servo controller with appropriately designed integrators and filters, which produced a control signal for the piezoactuator acting on the length of a diode cavity in the laser. For the laser that was used in the experiment (EOM 1W NKT Photonics 15C BoostiK), I designed a special add-on for the existing servo design, which allowed to directly feed the output of the servo into the laser.

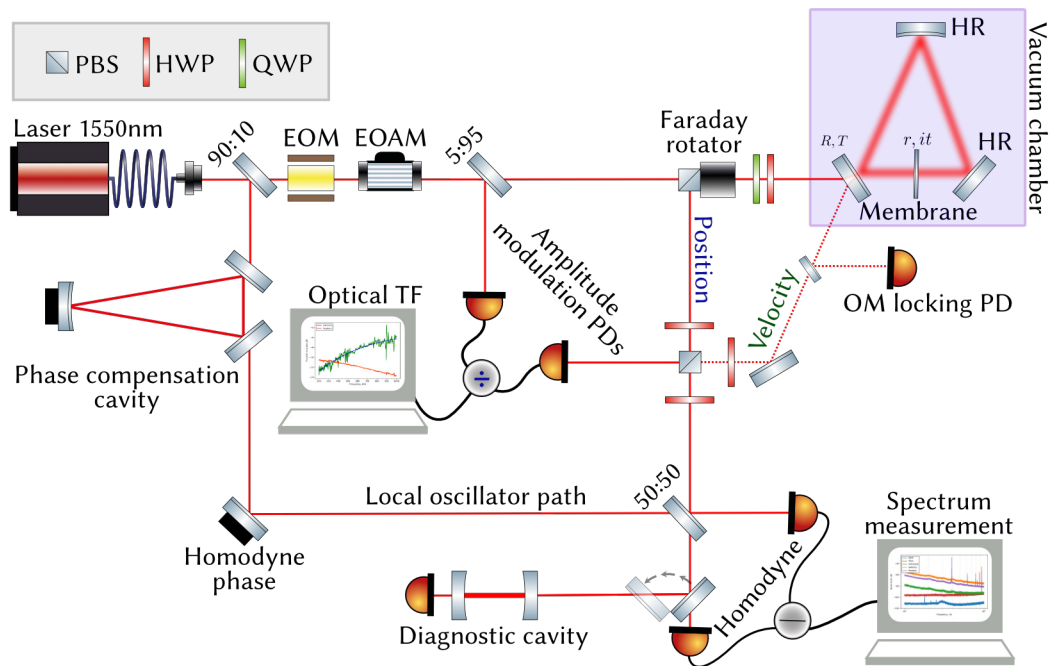


Fig. 4.7. Simplified setup of a ring-cavity experiment. The 1550 laser beam was split into two beams: signal and local oscillator. The local oscillator went through the phase compensation cavity, which reduced the phase noise, and also cleaned the spatial mode profile of the beam (see Sec. 4.5.3). The signal beam went through the electro-optic amplitude modulator (EOAM) that produced the sidebands that were detected in amplitude modulation PDs, and allowed to probe the optical transfer function (TF) of the ring cavity. The electro-optic modulator (EOM) in the signal path generated phase modulation sidebands that were used for the PDH stabilization of the laser to the cavity resonance: the beat between the sidebands and the main field was detected on the OM locking PD, which generated the error signal for the feedback loop to the laser frequency. The signal beam was injected into the optomechanical cavity, which was placed inside the vacuum chamber. The velocity port was almost dark, only a small fraction of the light power leaked into it, and it mainly contained the velocity signal from the membrane and classical noises. The signal in the position port went through the Faraday isolator and a PBS for separating it from the incoming beam. Then both position and velocity signals were overlapped on a PBS, which allowed to send either of two signals on the balanced homodyne detector. The signal was then overlapped with the local oscillator beam on a 50:50 beamsplitter. The good overlap between the beams was controlled by monitoring the matching of both optical modes, local oscillator and signal beams, to a separate diagnostic cavity. The spectrum of a differential signal between the two photodiodes of a homodyne detector was then observed.

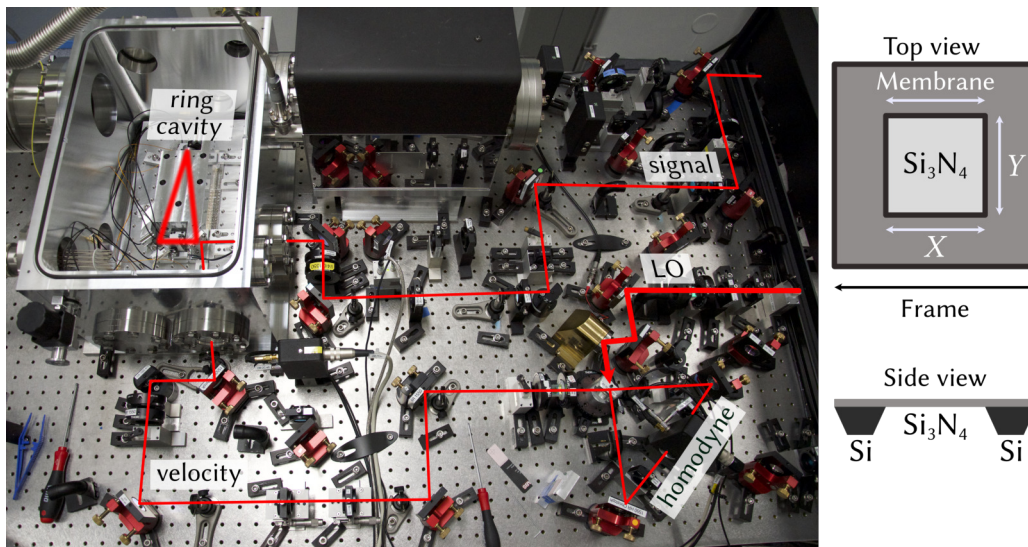


Fig. 4.8. The optomechanical ring-cavity experiment with a membrane in the laboratory. Left: a photograph of the experimental setup, with the laser beam drawn in red (in reality invisible at 1550 nm). An optomechanical ring cavity (top left) is placed inside the vacuum chamber. A signal beam propagates through the ring cavity. The velocity signal is then overlapped with the local oscillator (LO) beam and detected on a balanced homodyne detector. Right: a schematic of a silicon-nitride membrane made by Norcada.

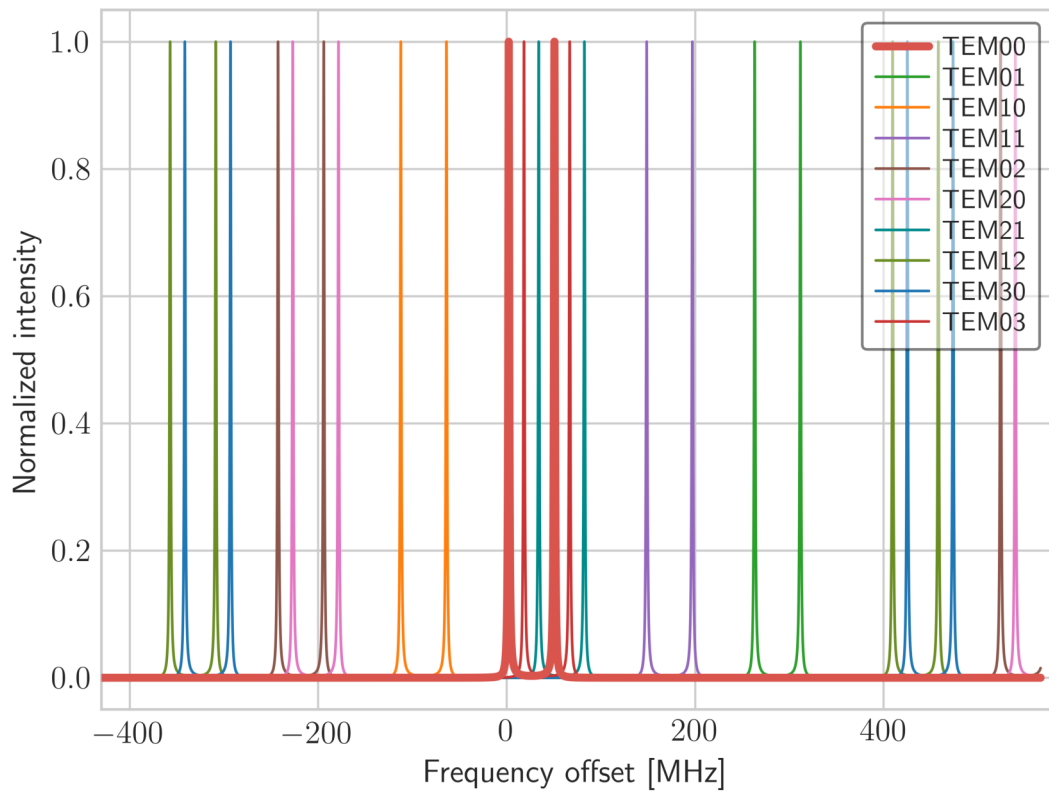


Fig. 4.9. Simulation of resonances of the higher order TEM modes in the ring cavity. The design length was selected such that there was a minimal overlap between the TEM00 modes and the higher order modes, such that only one became resonant at a selected frequency. All modes are normalized to their peak intensity.

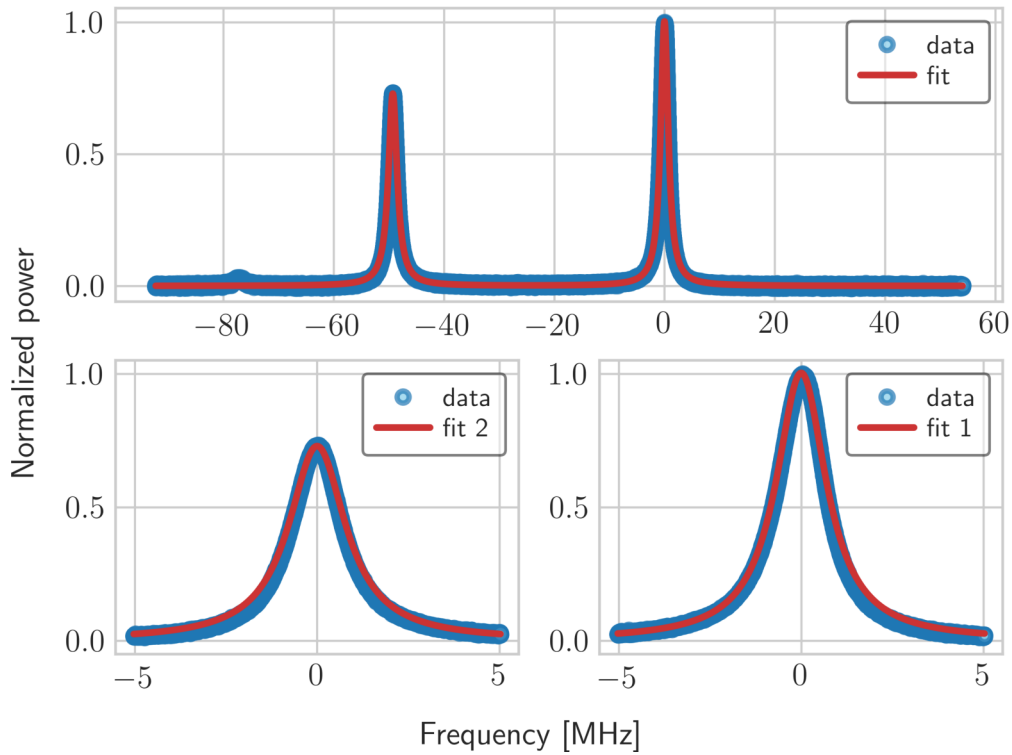


Fig. 4.10. Measurement of the ring-cavity linewidth and the mode splitting of the ring cavity with membrane. The frequency of the laser was scanned continuously, and the time trace of the power changes in the position port was recorded. The frequency scale was calibrated using a PDH signal. The power was normalized to the peak power of the larger peak. The parameters acquired from the fit: $\gamma_1 = 0.84$ MHz, $\gamma_2 = 0.95$ MHz, $\Delta\omega_c = 49.28$ MHz, $r = 3.9\%$. The experimentally measured linewidth matched the theoretical prediction of $\gamma = 0.84$ MHz, based on the mirrors' parameters. The power of one of the peaks differed from the other one due to a contribution of a higher-order optical mode that became degenerate with the TEM₀₀ mode, so the corresponding peak was higher, but also broader.

4.5.2 Membrane motion

The membrane was positioned inside the ring cavity close to the front mirror (since the macroscopic position of the membrane did not have an effect on the resonance structure). The whole cavity was placed inside a vacuum chamber with residual pressure of 10^{-7} mbar. The vacuum could be maintained with only the high-speed ion-getter pump. This minimized the coupling of acoustic noise to the cavity. The cavity was isolated from the vibrations of the table by two-stage passive isolation made of alternating layers of steel sheets and Viton feet. The optical table itself was floating on air-filled vibration isolation feet.

The position of the membrane could be adjusted by tilting the membrane holder and displacing the membrane along the optical axis. In the alignment procedure, the membrane was first positioned perpendicularly to the beam without the optical cavity (front mirror replaced by a transparent window) and the beam was centered well on the membrane by monitoring the transmission and reflection from the membrane on a CCD camera. Then, the front blank substrate was replaced by a 50:50 beamsplitter, allowing to roughly adjust the cavity around the membrane and get some interference on the output. In the next step, the front 50:50 beamsplitter was replaced by a highly reflective mirror, and the final alignment was performed with minimal adjustments to the incoming beam. The alignment was done by monitoring the photodiode and the CCD camera placed in transmission of one of the back mirrors. Finally, the membrane was slightly tilted by a motorized holder to the position of maximal reflection (by monitoring the mode splitting distance).

When the cavity was brought to resonance, most of the light power was reflected directly back to the position port. Only a small fraction of power went into the velocity port (due to the non-perfectly reflective back mirror). The signal in the position port was then separated from the incoming field with the help of a Faraday rotator and a PBS.

The signal from the resonating ring cavity was sent to a balanced homodyne detector, from two ports: position and velocity. These two signals were overlapped on a PBS, allowing to switch between detecting one or another without changing the alignment by blocking one path and adjusting the polarization with a half-wave plate. This PBS also allowed to adjust the light power to match the signal

strength in both ports (since position port has most of the input power, it has to be reduced significantly). The homodyne was adjusted to achieve good visibility and mode overlap (although it was not critical for the experiment), with the use of an additional diagnostic cavity. The phase of the local oscillator was actively stabilized to the phase quadrature, where the membrane signal reaches maximal strength.

A typical measured spectrum is presented in Fig.4.11. This measurement was largely limited by the laser phase noise (more about it below). The membrane motion was produced by thermal Brownian noise exciting the resonance frequencies of the membrane. For a square membrane, these frequencies for the mode (m,n) are:

$$f_{m,n} = \sqrt{\frac{T}{4\rho}} \sqrt{\frac{m^2}{X^2} + \frac{n^2}{Y^2}}, \quad (4.114)$$

where $T = 800 \times 10^6$ Pa is the stress of the membrane, $\rho \sim 2.7$ kg/m³ is the mass density, and (X, Y) are the dimensions of the membrane, see Fig. 4.8. In the experimental data, the fundamental mode f_{00} at 395 kHz is well visible, together with the higher-order modes at (622, 625, 789, 879, 886) kHz.

In order to characterize the membrane, I performed ring-down measurements. For this measurement, a small piezoactuator was attached to the membrane holder, and the membrane was excited at its resonance frequency by applying a sinusoidal voltage to the piezo. After the oscillation stabilized on a certain level, I switched off the voltage and recorded the time trace of a ringdown of a membrane motion. It is convenient to automate the measurement procedure by generating a square signal on the signal generator with a period of several seconds, trigger the spectrum analyzer on the downslope of the signal (with small time shift to the past in order to capture the flat region), and then set it to average. The spectrum analyzer should be operating in the zero span mode precisely at the resonance frequency of the membrane. By repeating this measurement 100 times, I acquired an averaged trace, presented in Fig. 4.12. From this trace I computed the quality factor of the membrane by fitting an exponential ringdown to the data:

$$X(t) = X(t_0)e^{-\omega_m(t-t_0)Q^{-1}} \quad \Rightarrow \quad Q = \frac{10\omega_m(t-t_0)}{(X_{\text{dB}}(t_0) - X_{\text{dB}}(t)) \log 10} \quad (4.115)$$

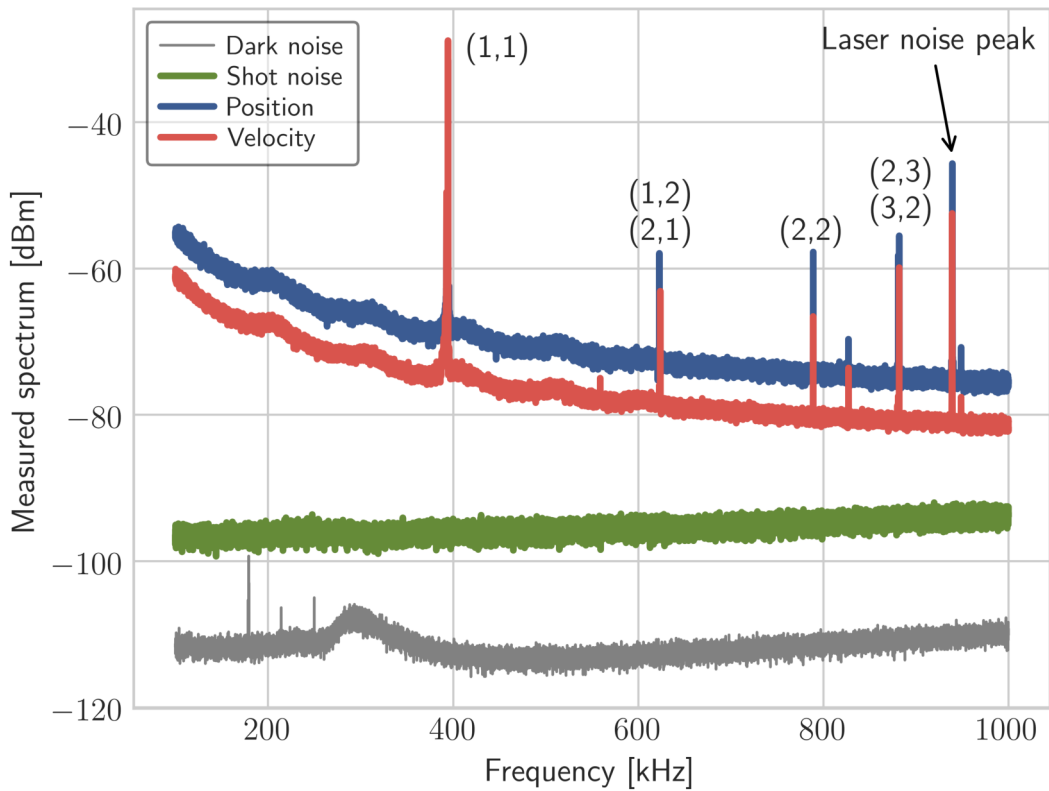


Fig. 4.11. Spectral density of noise and membrane motion. The membrane peaks were produced by thermal motion of the membrane. The fundamental (1,1) mode is at 395 kHz. The higher order modes at higher frequencies fit the expected frequencies. The measurement was limited by the phase noise of the laser, which was much higher than the shot noise.

The resulting quality factor is $Q \sim 4.6 \times 10^5$, which is typical for this type of membrane [186].

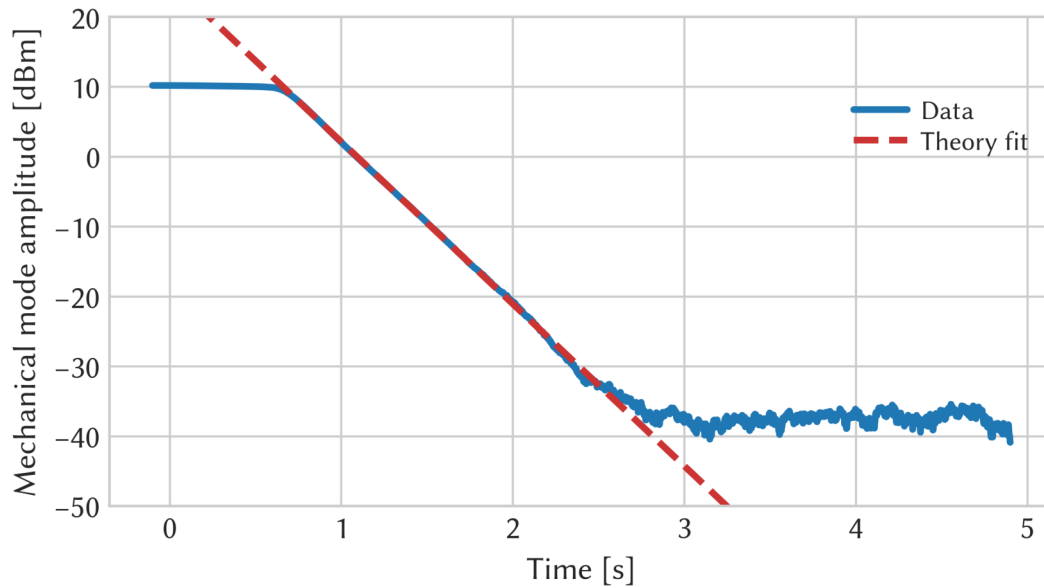


Fig. 4.12. Ringdown measurement of the quality factor of the membrane’s fundamental mode. The membrane motion was measured without a cavity, i.e. the front mirror of the cavity was replaced by a blank substrate, and the reflection off the membrane was sent directly to the homodyne detector. The membrane was then excited at the resonance frequency of 395 kHz, and the time trace of its motion was recorded. When the excitation was removed, the motion ringed down at the membrane’s damping rate, which was fitted and a quality factor of 4.6×10^5 was computed after multiple repetitions of the measurement.

4.5.3 Laser noises

Classical laser noises were the main sensitivity limitation in the current setup, mainly laser phase noise. The laser source was not perfectly monochromatic, and also had various fluctuations and imperfections that lead to classical power and frequency (phase) fluctuations. These fluctuations came in addition to the quantum noises in phase and amplitude quadratures that I considered so far.

Amplitude noise

I measured the amplitude noise of the laser by splitting the light field into two parts with equal power, and sending them on two identical photodiodes, see Fig. 4.13. The photodiodes measured the amplitude fluctuations in the laser field that had contributions both from quantum shot noise and classical amplitude noise. After that, I added and subtracted the voltages from these photodiodes. Since the classical noise was correlated, and quantum shot noise was not, the subtracted part contained only shot noise, and the added part contained both shot and amplitude noises. Thus subtracting the two spectra gave only the contribution of the amplitude noise.

The amplitude noise can be considered as a small modulation $a(t)$ on the classical field with average intensity \bar{I}_0 and variance $\Delta^2 I$:

$$I(t) = I_0(t)(1 + a(t)), \quad (4.116)$$

$$\Delta^2 I(t) = \Delta^2 I_0(t) + \bar{I}_0^2 \Delta^2 a(t) = \bar{I}_0 + \bar{I}_0^2 \Delta^2 a(t). \quad (4.117)$$

The contributions from shot noise $\Delta^2 I_0 = \bar{I}_0$ and amplitude noise $\bar{I}_0^2 \Delta^2 a(t)$ scale differently with light intensity I_0 , which makes it possible to distinguish between the two by measuring the spectrum scaling with power. For example, when the light power is doubled, the shot noise is increased by 3 dB, and the amplitude noise – by 6 dB.

This was demonstrated experimentally in Fig. 4.14, where the amplitude noise was measured by subtracting the shot noise (subtracted voltage spectrum) from total noise (added voltage spectrum). Since real electronic devices had their own transfer functions, which were frequency-dependent, in order to obtain the real spectrum of the amplitude noise, I also accounted for these transfer functions

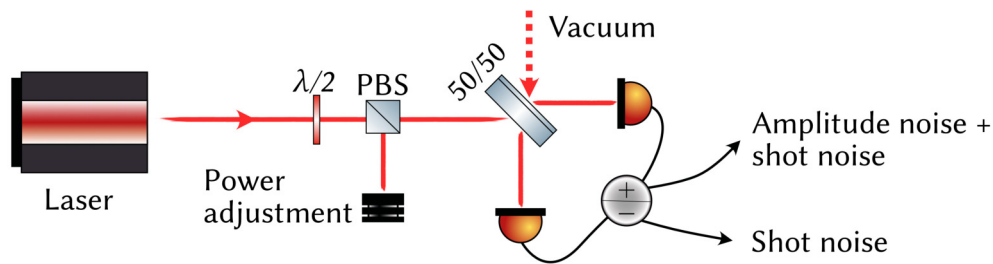


Fig. 4.13. The setup used for measuring laser amplitude noise. Laser was split into two beams on a 50:50 beamsplitter, and the outputs were sent on the photodiodes. Added photocurrents resulted in a sum of amplitude and shot noise, subtracted photocurrents contain only the shot noise. Subtracting two spectra allowed to retrieve the amplitude noise spectrum.

of two photodiodes and an adder/subtractor electronic box. This measurement demonstrated that in terms of amplitude noise the laser was sufficiently good for the purposes of my experiment: it was shot-noise limited in the frequency range of interest (300-600 kHz) for 1 mW of light power. Since the typical powers in the signal beam were on the order of tens of μW , amplitude noise had virtually no contribution to the sensitivity.

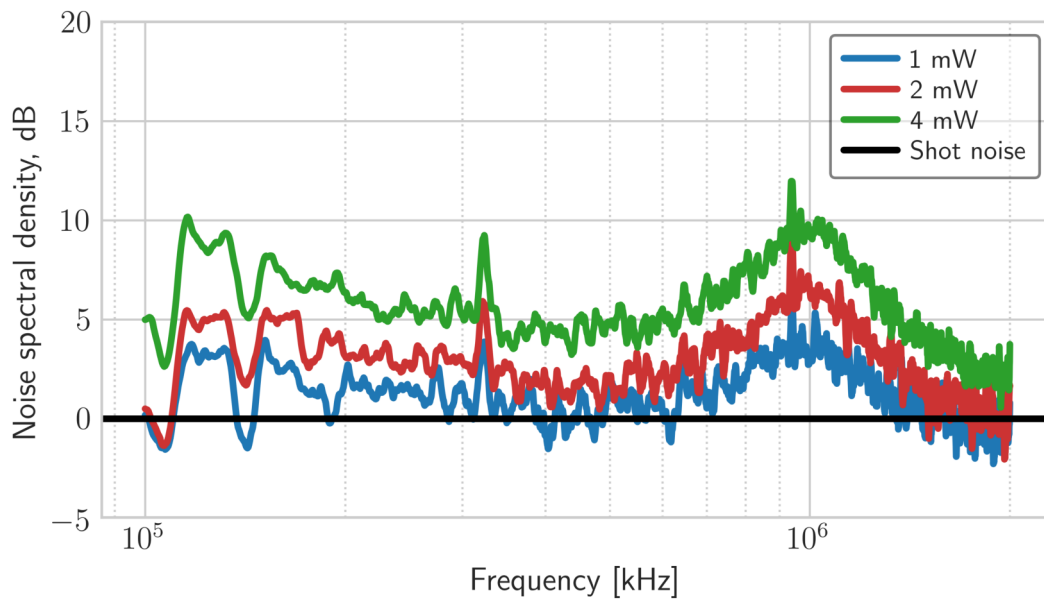


Fig. 4.14. Amplitude noise of the laser measured at frequencies of interest for the experiment. The sum of amplitude and shot noise was measured with two photodiodes, whose voltages were added and subtracted. The latter part contained only the shot noise, since the correlated amplitude noise was subtracted. This measured shot noise could then be subtracted from the total noise, thus inferring only the amplitude noise contribution. The noise was normalized to the shot noise level, and the scaling of the ratio with optical power was demonstrated. At 1 mW the amplitude noise and shot noise had roughly equal amplitudes. For the light powers in the signal (less than 100 μ W) the amplitude noise had virtually no contribution to sensitivity.

Phase noise

Laser phase noise is often a limiting factor in laser cavity experiments. As I discuss in detail in Chapter 3, phase noise in homodyne detection becomes relevant when the signal and local oscillator paths are not balanced in length. In usual cavity-based experiments, this imbalance is either rather small to have a significant effect from the phase noise at frequencies of interest, or it can be compensated by adding another cavity that compensates the path length difference.

In the ring cavity, the complicated resonance structure complicates mitigation of the phase noise. In order to compensate the phase delay in such a cavity, one needs to place exactly the same cavity in the local oscillator path. Usually it is possible to make the cavities very similar in optical properties. However, in the ring cavity, also the membrane reflectivity should exactly match the reflectivity of the membrane in the compensation cavity. Since all membranes are slightly different in their shape and thickness, they never have the same reflectivity.

This effect is shown in Fig. 4.15, where I compared the transfer functions and simulated frequency noise in the cases without a compensating cavity in LO path, and with a compensating cavity, but with imperfect match in membrane reflectivity. The effect is basically such that the phase noise had significant coupling even with minimal imbalance. Therefore, such compensation cavity was not implemented in the experiment. Instead, a usual mode-cleaner cavity without a membrane was used as a compensation cavity.

I measured the phase noise by transmitting the beam through a mode-cleaner cavity offset from its resonance condition, see Fig. 4.16, and also in an imbalanced Mach-Zehnder interferometer, confirming that the noise that was limiting the experiment was indeed the phase noise of the laser.

The investigation of the phase noise in my experiment confirmed the empirical evidence for difficult balancing of the optical paths for phase noise reduction. Due to special features of the setup, it was not possible to passively cancel phase noise by introducing compensation cavities in the local oscillator beam. A potential solution to this problem was the realization of an active stabilization of the laser for suppressing the phase noise. However, this remained the task for future upgrades to the setup.

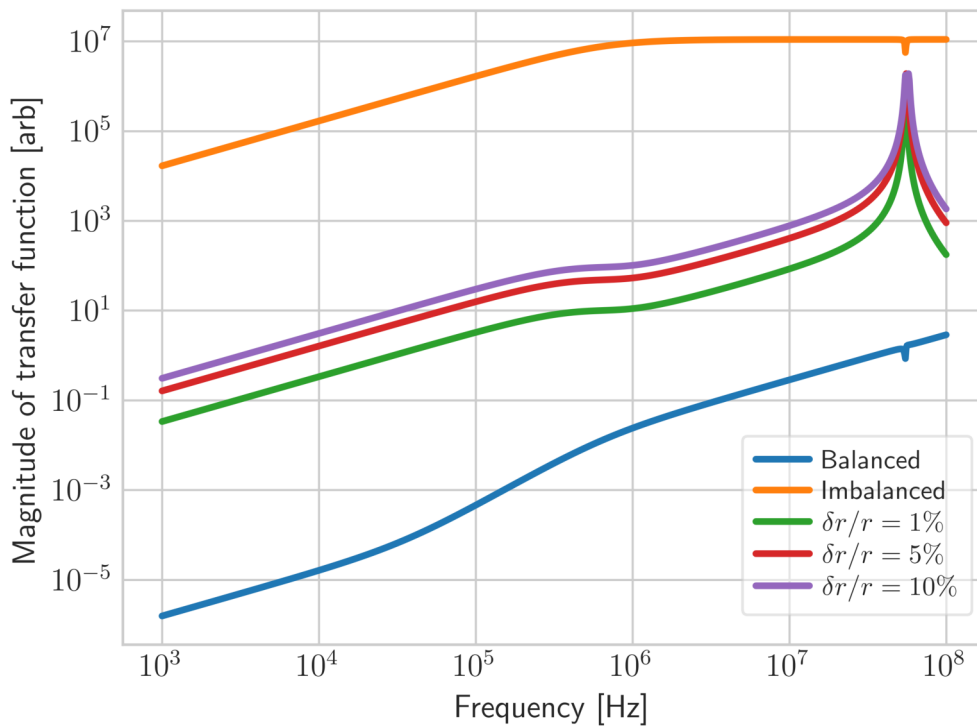


Fig. 4.15. Transfer function for the laser frequency noise in different cases: imbalanced – without compensation cavity in LO path, balanced – with identical cavity in LO path, various plots for a cavity in LO path with membrane whose reflectivity differs from the main cavity by $\delta r = r_{LO} - r$. This demonstrates that only a perfectly matched cavity allows for a sufficient cancellation of the frequency noise. The peaks at ~ 50 MHz correspond to the second resonance of the optomechanical cavity, where the phase delay acquires an additional contribution. This is high above all mechanical peaks that I am interested in.

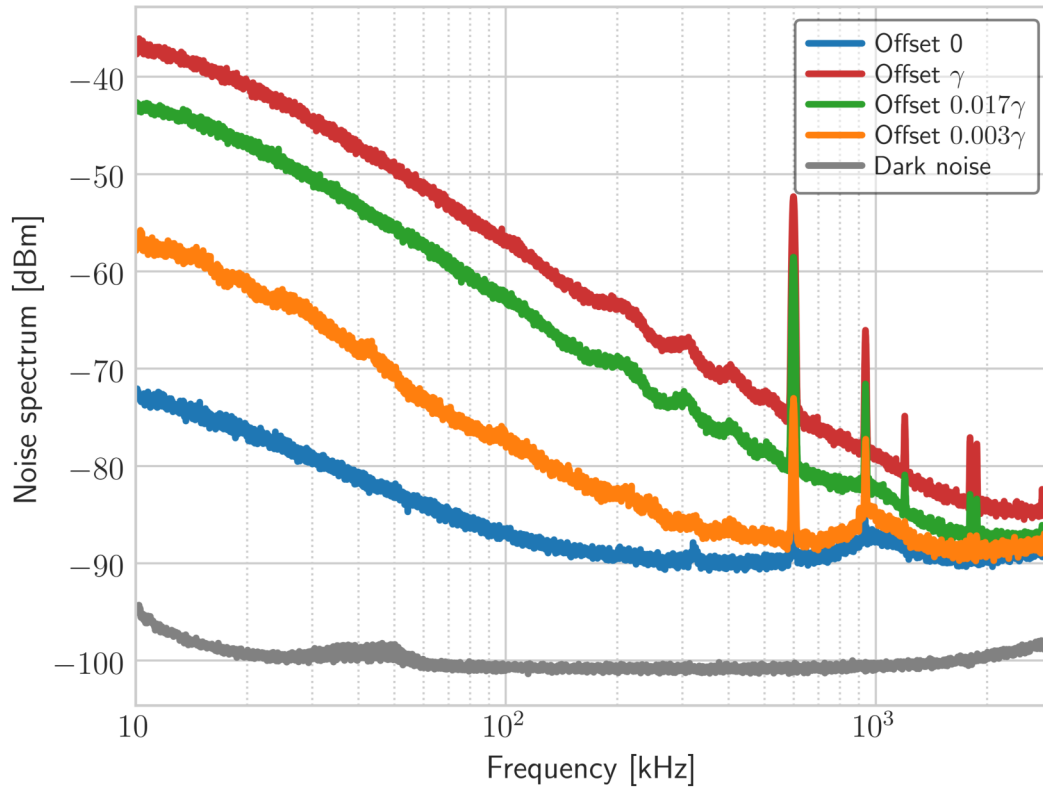


Fig. 4.16. Laser frequency noise measurement. The noise was measured in transmission through a filter cavity detuned from its resonance. Frequency fluctuations were converted into amplitude fluctuations and were detected on the photodiode. Depending on the offset, the magnitude of the effect changed. The characteristic ripples in between 100 – 500 kHz (that were not the membrane peaks) were visible, as in the spectrum measured on the homodyne detection in Fig. 4.11. The laser noise peaks were seen at ~ 900 kHz, that were also identified on the membrane spectrum in Fig. 4.11. This measurement method did not allow for a calibrated measurement of the frequency noise, but allowed to confirm the origin of the limitation of the sensitivity.

4.5.4 Speedmeter signatures

Optical transfer function

In the course of the experiment, I demonstrated the speedmeter optical transfer function. For that, I generated an amplitude modulation sideband with an EOAM, split it on a beamsplitter, detected one part on a broadband photodiode, and sent the second part into the ring cavity, see Fig. 4.7. The sideband traveled through the cavity, partially into the position, partially into the velocity port. I then measured the amplitude of the sideband on another photodiode. The setup allowed for switching the position and velocity signals by blocking paths and adjusting polarizations. I ensured the two signals to have the same light power by adjusting the power with waveplates and PBSs. The ratio between the signals on two photodiodes gave the optical transfer function at the modulation frequency. This frequency was swept and the broadband optical transfer function recorded both for position and velocity signals. The procedure was repeated 10 times (as long as the setup remained stable) and the signal was averaged. The resulting optical transfer function is shown in Fig. 4.17. It demonstrates a clear difference between the velocity and position signals in frequency scaling. While the speed signal had a small contribution of the position signal (due to imperfectly reflective back mirror in the cavity), it still remained significantly different from the position signal. This measurement validated the ring cavity setup as a speedmeter setup.

Signal transfer function

In order to validate the possibility of enhanced sensing, it was necessary to demonstrate the measurement of an external signal with a mechanical oscillator. This point became an unexpected difficulty in the experiment. The initial idea was to measure the response of the membrane to the external force (mechanical or optical) at frequencies above the mechanical resonance, where the membrane response could be approximated by the free mass response. In this regime, the distinction between the velocity and position signals was expected to be most pronounced, as I showed in the theory sections of this chapter. However, in the course of the measurement it turned out that the initial analysis did not take into account the higher order mechanical modes of the membrane.

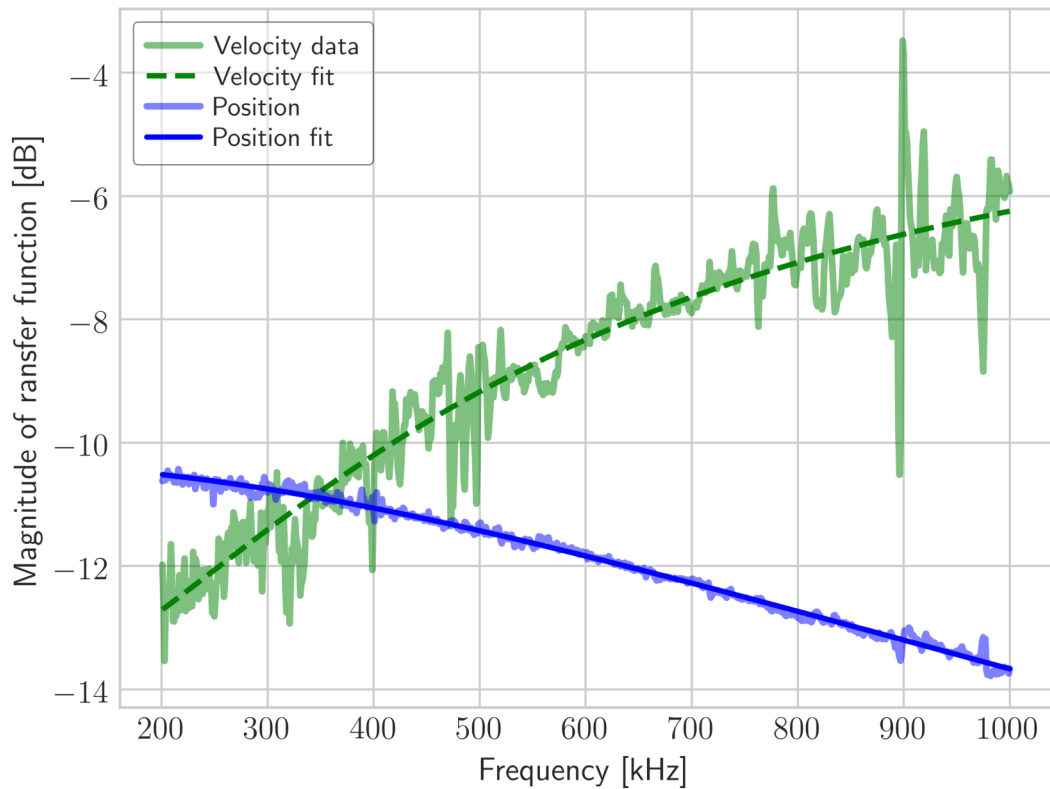


Fig. 4.17. Measurement of the optical transfer function of the ring cavity on the position and velocity ports. The transfer function is measured by observing the change in the amplitude modulation sidebands imprinted on the light fields as they go through the ring cavity. The frequency scaling of the position and velocity port is clearly different and matches well with the theoretical expectations. The fit of the theory gives an optical linewidth of ~ 900 kHz, which approximately matches the independently measured value.

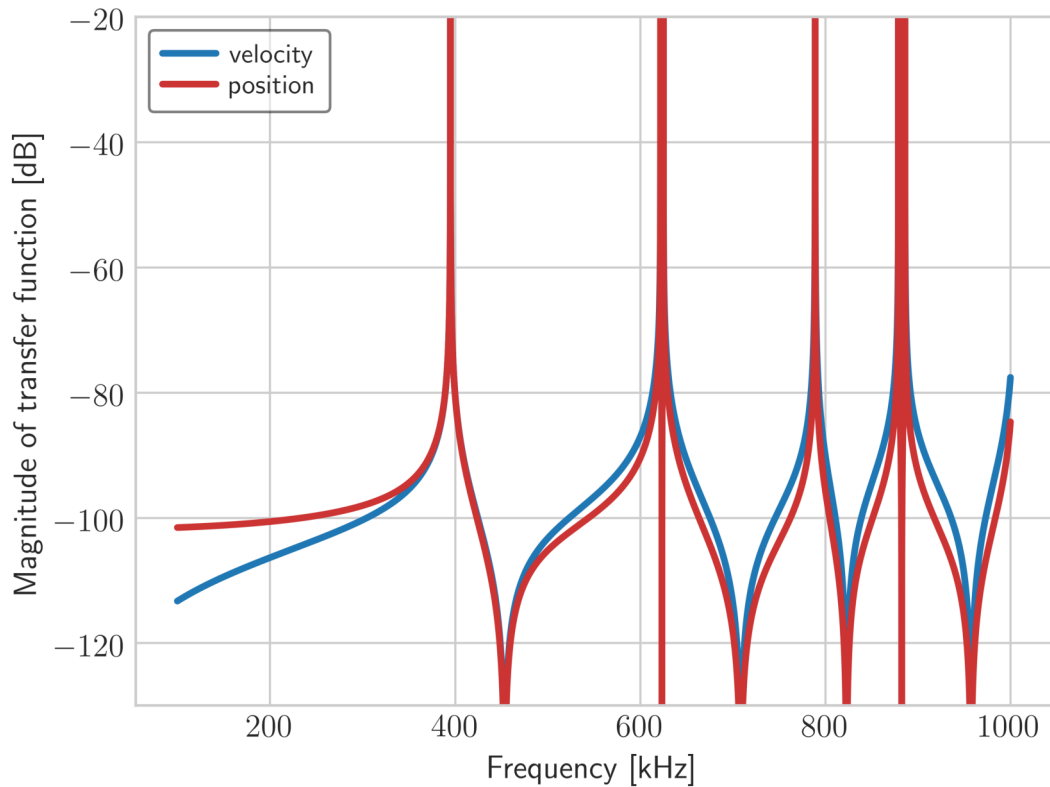


Fig. 4.18. Theoretical calculation of the signal transfer function for an external force acting on the membrane as seen on the homodyne detector. The transfer functions are normalized to their corresponding peak values. The free-mass regime above the resonance of the fundamental mode is spoiled by the interaction with the next high-order mode, which makes the observation of difference between the velocity and position response unfeasible in that frequency regime. The real difference in scaling is only observable below the first resonance at low frequencies. Its observation requires, however, a high sensitivity, in particular, low laser frequency noise at frequencies between 100-300 kHz.

As I show in Fig. 4.18, the measured difference between the velocity and position response was expected to be very small - on the order of few dB, and the frequency scaling barely differed. This prevented observing the speedmeter sensitivity above the mechanical resonance frequency. It could still be possible to measure the speedmeter response below the mechanical frequency, although it would require a significant improvement to the sensitivity of the setup, mainly by reducing the phase noise of the laser, which is the direction of future research.

Despite that, I demonstrated the sensing of the external signal on the membrane by acting on it with a piezoactuator and observing the optical signal from the membrane motion on the homodyne detector both in velocity and position ports. Changing the frequency of the signal allowed to sweep across the mechanical resonance and take a full response to the external signal. As expected, no difference in frequency scaling between the velocity and position signals was visible, see Fig. 4.19. However, the signal strength was smaller in the velocity signal, as predicted by theory in Eq. (4.57). The shape of the experimental data differed from the theory prediction due to the effects of the low-frequency vibrational excitations of the holder of the membrane, and the transfer function of electronics and piezoactuators that were not included in the model.

In this section I demonstrated that although the direct demonstration of the speedmeter sensitivity was not possible in my experiment due to various limitations of both technical and fundamental nature, it was still possible to observe some speedmeter features in the ring cavity. I observed the optical transfer function and reduction in the membrane response, which I found to be in good agreement with the theory.

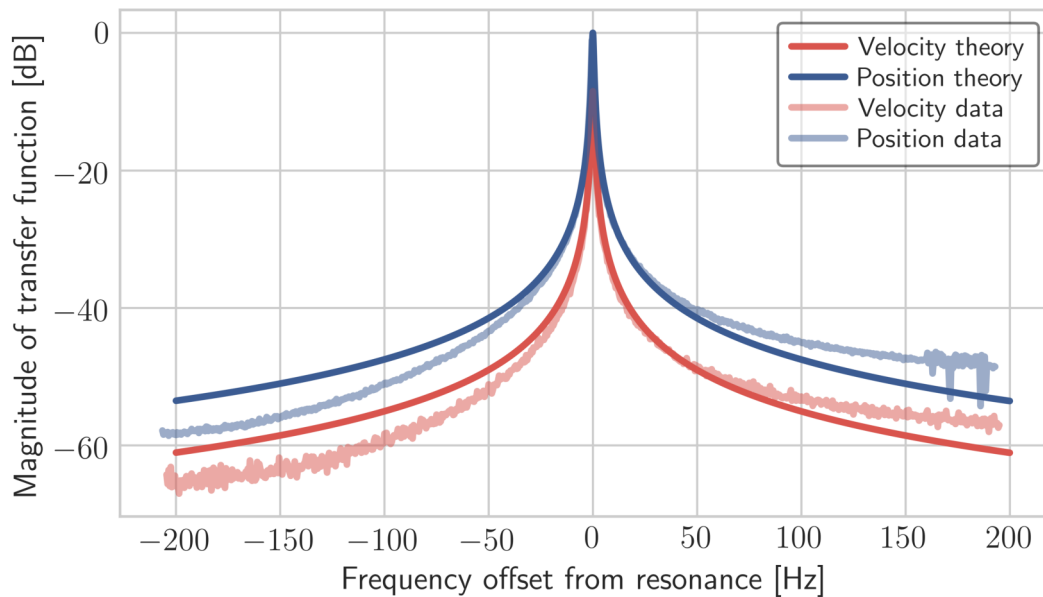


Fig. 4.19. Signal transfer function for external excitation on the membrane as seen on the homodyne detector: theory and experiment. The experimental curves differ slightly from theory on the slopes of the peaks due to the unmodeled effects of low-frequency vibrational excitation from the holder of the membrane and electronic transfer functions. The overall difference in magnitude between two ports corresponds to the expected difference in signal transfer function $\sim \gamma^2/\Omega^2 \sim 8$ dB. Note that the theory curve is not fitted to data, but plotted as an approximated model with independently estimated parameters of the system from Table 4.2.

4.6 Conclusion

An optomechanical ring cavity is a new and interesting optomechanical setup. On the one hand, it features unusual optomechanical properties, such as coherent optomechanical coupling. On the other hand, it can work as a test-bed for the speedometer, allowing to directly compare velocity and position measurements.

The table-top realization in my experiment came with several experimental challenges, which prevented me from observing speedometer sensitivity, but still allowed to see some of the features predicted by the theoretical description. I observed mode splitting and independence of the resonance frequency on the sensitivity, compared the position and velocity transfer functions, and measured the external signal on the membrane in both position and velocity ports.

In order to achieve the table-top speedometer sensitivity it is necessary to use a different low-frequency mechanical oscillator that has a significantly broad frequency range where it acts as a free mass, and where the velocity signal can be observed. This would require active laser frequency stabilization for suppressing the phase noise. Alternatively, it could be possible to design a membrane that features a broader frequency range where the motion can be approximated by the free mass motion. Either way, this remains a direction for future research.

Ultimately, the ring cavity has potential applications in both optomechanics and gravitational-wave detection.

Theoretical analysis of paired carriers for tailoring sensitivity

Quantum radiation-pressure noise will become the limiting factor in the sensitivity of future gravitational-wave detectors at low frequencies. There are many approaches to reducing this noise either by frequency-dependent squeezing, or by QND measurements. One particular type of a QND measurement – measurement of test masses velocity instead of position – has already been introduced in the previous chapter. This speedometer approach promises a significant enhancement to the sensitivity, yet it requires substantial changes to the topology of the detectors. While it is promising for the detectors yet to be built, such as the Einstein Telescope, turning existing interferometers into a speedometer might be challenging. Such approaches exist, but in this chapter I will present another concept, that takes advantage of quantum entanglement between two light fields that interact with the same test mass through radiation pressure.

This allows to create a speedometer-like sensitivity with minimal adjustments to the general topology of the detector, but with some changes to the core optics. This *paired carriers* approach has several other advantages: it enhances the sensitivity gain from increasing light power and/or squeezing injection; it allows to flexibly tailor the sensitivity and probe specific frequencies with very high precision.

The paired carriers approach relies on creating entanglement between two light fields using dynamical back-action in a detuned interferometer, with subsequent optimal processing of the detected signals.

In this chapter I discuss the concept in detail, provide the theoretical framework for computing the sensitivities, and demonstrate possible enhancements to the sensitivity. The results in this chapter were published in [69], the numerical

optimization was performed in collaboration with N.Voronchev using the software written by him; theoretical analysis

5.1 Optical spring in gravitational-wave detectors

In a standard interferometer that does not use non-classical states of light, the best achievable sensitivity is given by a standard quantum limit (SQL). It is not possible to overcome this limit by merely increasing the light power, and instead some kind of non-classical light is required. Therefore, the SQL is often used as a benchmark for quantum-noise reduction schemes. For example, a quantum speedmeter would allow to follow the SQL in a broad frequency band, and even overcome it with appropriate signal readout.

One of the approaches to reducing quantum noise in GW detectors is modification of the test masses' dynamics by means of the *optical spring* effect which arises in detuned interferometers [129, 187, 188]. Optical springs convert GW detectors test masses into harmonic oscillators with eigenfrequencies within the detection band, which makes them very sensitive to a signal around this frequency. Rigorously speaking, this approach does not allow to overcome the SQL, but instead reduces the SQL itself around the eigenfrequency [35]. Unfortunately, optical springs allow to improve the sensitivity only in a limited frequency band, while substantially degrading it at other frequencies.

The optical spring approach was further developed in [189, 190], where it was proposed to use two optical carriers, which create two optical springs of the opposite signs. Provided the appropriate power, detuning and bandwidth of the carriers, the total effect of the double optical spring can be described as a *negative optical inertia*. It cancels the positive inertia of the test masses, thus increasing their response to gravitational waves and correspondingly reducing the SQL within a broad band from zero frequency to some upper frequency, limited by the available optical power. Unfortunately, estimates show that for the Advanced LIGO, this upper frequency is equal to only ~ 50 Hz, and scales very slowly (as $I_c^{1/3}$) with the circulating optical power I_c [190].

In the articles [131, 191] the double-carrier configuration was proposed as a mean to create a dynamically stable optical spring. It is known that, depending

on the detuning sign, a single carrier creates either positive rigidity accompanied by negative damping, or negative rigidity with positive damping. Both cases lead to unstable dynamics of the detector. However, by combining two carriers with different powers and detunings, it is possible to implement a stable configuration with positive total rigidity and positive total damping. The scheme considered in [131] is shown in Fig. 5.1. In essence, it is the standard Michelson/Fabry-Pérot topology of the second generation GW detectors, but with two light sources, which either have to have orthogonal polarizations, or have to be separated by one or more FSRs of the interferometer, in order to avoid interference between them. Each of the two output beams is supposed to be measured by its own homodyne detector, and their output signals are combined with the optimal weight functions. In addition, the so called *annihilation* regime was considered in [131], which uses the two carriers with equal power and opposite detunings; as a result, the optical springs created by these two carriers completely cancel each other.

On first glance this annihilation regime does not look useful: the optical spring is created with one beam, and canceled with the second beam. However, the two beams acting on the same mirror become entangled via radiation-pressure force, which introduces correlations between two beams. It is then possible to measure the two beams independently, and predict the outcome of one measurement based on the other, in the EPR style, as in the example of EPR-based frequency-dependent squeezing [141, 143, 144] I described in Chapter 3. Optimal processing of the signal from the two beams allows to cancel a significant part of the back-action, effectively creating a speedmeter-like quantum noise.

In the following, we consider the implementation of this scheme for current generation of GWOs, like the Advanced LIGO [10]. In particular, we suppose, that the total circulating optical power of all carriers is limited to 840 kW, which corresponds to the normalized power $J = (2\pi \times 100)^3 \text{ s}^{-3}$, with the notation for this chapter given in Table 5.1

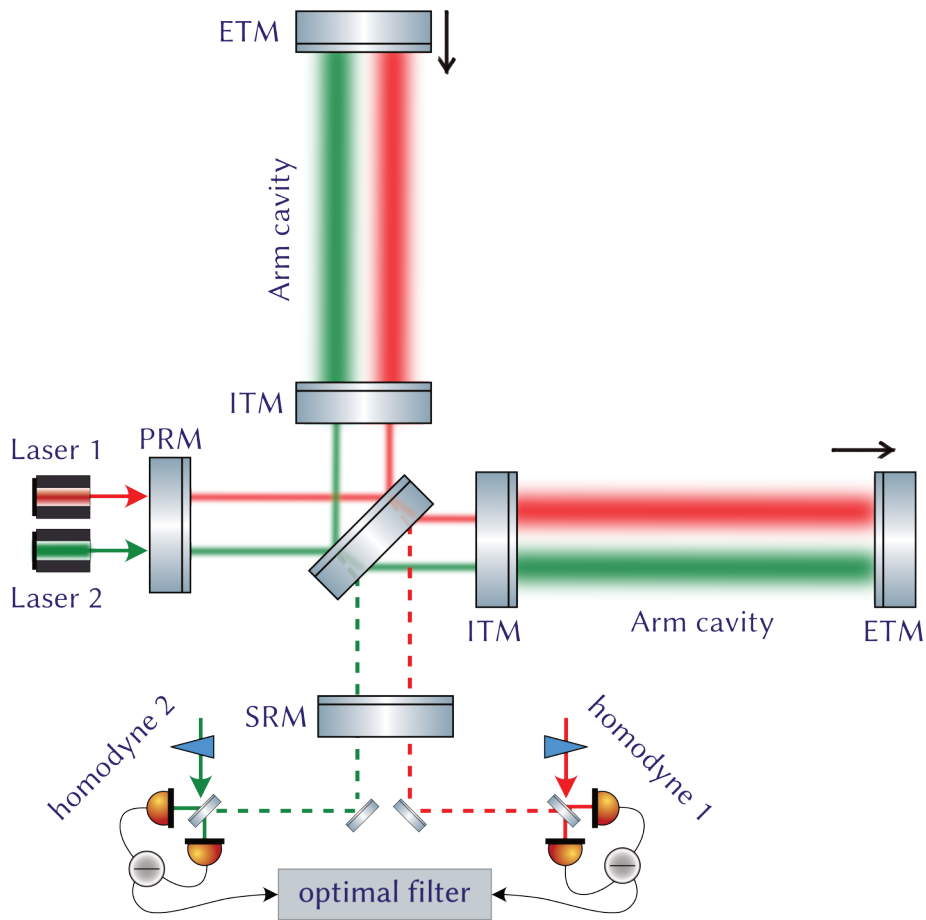


Fig. 5.1. Gravitational-wave detector with paired carriers. Two independent light fields of different frequency or polarization get entangled with each other through optomechanical interaction with the test masses. The two fields are detected on two separate homodyne detectors, and the outputs of the detectors are processed with an optimal filter. The correlations between the light fields allow to reduce the impact of QRPN on the sensitivity.

Quantity	Description
c	Speed of light
\hbar	Reduced Plank constants
$M = 40 \text{ kg}$	Mass of each of the arm cavities mirrors
$L = 4 \text{ km}$	Length of the interferometer arm cavities
$\omega_p = 2\pi c / 1.064 \mu\text{m}$	Optical pump frequency
ω_0	Resonance frequency of the interferometer
γ	Half-bandwidth of the interferometer
$\delta = \omega_p - \omega_0$	Detuning
$\Gamma = \sqrt{\gamma^2 + \delta^2}$	Effective half-bandwidth
$\beta = \arctan \frac{\delta}{\gamma}$	Normalized detuning
Ω	Audio sideband frequency of the GW signal
I_c	Optical power circulating in the arm cavities
$J = \frac{4\omega_p I_c}{MLc}$	Normalized optical power
ζ	Homodyne angle
e^{2r}	Squeezing power
θ	Squeezing angle
η	Unified quantum efficiency

Tab. 5.1. Main notations used in this chapter.

5.2 Quantum noise in position meter and speedometer

Quantum noise in a gravitational-wave detector can be generally described by individual contributions of shot, radiation-pressure and their cross-correlation noises, as it was discussed in Chapter 3:

$$S_{\text{sum}}(\Omega) = \frac{8}{L^2} \left[S_{xx}(\Omega) - \frac{2\Re[S_{xF}(\Omega)]}{M\Omega^2} + \frac{S_{FF}(\Omega)}{M^2\Omega^4} \right], \quad (5.1)$$

where $S_{xx}(\Omega)$, $S_{FF}(\Omega)$, and $S_{xF}(\Omega)$ are, respectively, spectral densities of the shot noise, the radiation pressure noise, and the cross-correlation spectral density of these two noises, which obey the following uncertainty relation:

$$S_{xx}(\Omega)S_{FF}(\Omega) - |S_{xF}(\Omega)|^2 = \frac{\hbar^2}{4\eta(\Omega)}, \quad (5.2)$$

where $\eta \leq 1$ is the quantum efficiency of the detector, which takes into account both the optical losses and the photodetector quantum efficiency. For simplicity, we will assume the ideal case of $\eta = 1$ in the rest of this section, although in general they can have a significant impact on the proposed approach, as on any other approach taking advantage of quantum correlations.

In the standard case shot noise and the radiation pressure noise are uncorrelated: $S_{xF}(\Omega) = 0$. In this case the minimum of total spectral density (5.1) is achieved at the free mass SQL:

$$S_{\text{SQL}}(\Omega) = \frac{8\hbar}{L^2 M \Omega^2} \quad (5.3)$$

As I showed in Chapter 3, the total spectral density of such a detector:

$$S_{\text{sum}}(\Omega) = \frac{S_{\text{SQL}}(\Omega)}{2} \left[\frac{1}{\mathcal{K}_{\text{PM}}(\Omega)} + \mathcal{K}_{\text{PM}}(\Omega) \right], \quad (5.4)$$

where

$$\mathcal{K}_{\text{PM}}(\Omega) = \frac{2J\gamma}{\Omega^2(\gamma^2 + \Omega^2)} \quad (5.5)$$

is the optomechanical coupling factor of the position meter [112]. This spectral density (5.4) reaches the SQL only at one frequency Ω_0 which satisfies the following equation:

$$\Omega_0^2(\gamma^2 + \Omega_0^2) = 2J\gamma, \quad (5.6)$$

and goes above the SQL at all other frequencies. The detector with such sensitivity is referred to as a *baseline detector*, with the particular case of $J = (2\pi \times 100)^3 \text{ s}^{-3}$ and $\gamma = 2\pi \times 500 \text{ s}^{-1}$, corresponding to the design values for the Advanced LIGO [10].

In the general case of $S_{xF} \neq 0$, as I discussed in Chapter 3, the minimum of (5.1) is not bounded by the SQL, and instead follows the QCRB:

$$S_{\text{opt}}(\Omega) = \frac{2\hbar^2}{L^2 S_{FF}(\Omega)}, \quad (5.7)$$

$$S_{xF}(\Omega) = \frac{S_{FF}(\Omega)}{M\Omega^2}. \quad (5.8)$$

The sensitivity in this case can be increased by increasing the radiation-pressure noise (e.g. by increasing light power or injecting squeezed light), as required by the QCRB. The structure of equation (5.8) suggests that this equation can be fulfilled in a broad band by making either S_{FF} or S_{xF} frequency dependent. These two options correspond to two methods of overcoming the SQL considered as the most probable candidates for implementation in the third generation GW detectors. The first one, proposed in the work [112], is based on use of additional *filter cavities*, which allow to create the frequency-dependent cross-correlation of the quantum noises.

The second method which is more relevant for our consideration, the so-called “quantum speedmeter”, was first proposed as semi-*gedanken* scheme in [192] and later developed into two realistic interferometer topologies (based on the Sagnac interferometer and on the ordinary Michelson one, but with an additional *sloshing cavity*) in papers [121, 176, 193–195]. This scheme is sensitive to the velocity of test masses, instead of their displacement (hence the designation “speedmeter”).

This corresponds to the following characteristic frequency dependencies of the quantum noise spectral densities:

$$S_{xx}(\Omega) = \frac{S_{vv}}{\Omega^2}, \quad S_{FF}(\Omega) = \Omega^2 S_{pp}, \quad (5.9)$$

where S_{vv} , S_{pp} are spectral densities of the velocity measurement noise and the momentum perturbation noise, respectively. Note that in the quantum speedmeter scheme, the effective coupling of the test mass with the meter is proportional to its velocity v ; therefore its momentum $p \neq mv$ and $S_{pp} \neq m^2 S_{vv}$. Within the bandwidth of the interferometer, $\Omega < \gamma$, these spectral densities can be considered as frequency independent ones, which allows to fulfill condition 5.8 in a broad band by measuring a proper homodyne angle, without using filter cavities.

The explicit equation for the total quantum noise spectral density of the speedmeter is the following [35]:

$$S_{\text{sum}}(\Omega) = \frac{S_{\text{SQL}}(\Omega)}{2} \left[\frac{1}{\mathcal{K}_{\text{SM}}(\Omega) \sin^2 \zeta} - 2 \cot \zeta + \mathcal{K}_{\text{SM}}(\Omega) \right], \quad (5.10)$$

where the optomechanical coupling factor of the speedmeter \mathcal{K}_{SM} is equal to

$$\mathcal{K}_{\text{SM}}(\Omega) = \frac{4J\gamma}{(\gamma^2 + \Omega^2)^2} \quad (5.11a)$$

for the Sagnac-type speedmeter and

$$\mathcal{K}_{\text{SM}}(\Omega) = \frac{4J\gamma}{4\gamma^4 + \Omega^4} \quad (5.11b)$$

for the speedmeter realized by using an additional sloshing cavity (only the low-frequency optimized case is shown for brevity, and refer to Ref. [121] for more details). Note that in both cases (in contrast with \mathcal{K}_{PM}), this factor does not depend on Ω in the asymptotic case of $\Omega \ll \gamma$.

Therefore, if the shot noise and the radiation pressure noise are not correlated, that is $\zeta = \pi/2$, then the low-frequency optimization of the optomechanical coupling that minimizes the spectral density:

$$\mathcal{K}_{\text{SM}}(0) = 1 \Rightarrow J = \frac{\gamma^3}{4} \quad (5.12)$$

gives the total noise spectral density that asymptotically follows the SQL within the interferometer bandwidth. In particular, in the Sagnac speedmeter case, it is equal to

$$S_{\text{sum}}(\Omega) = \frac{S_{\text{SQL}}(\Omega)}{2} \left[\frac{\gamma^4}{(\gamma^2 + \Omega^2)^2} + \frac{(\gamma^2 + \Omega^2)^2}{\gamma^4} \right]. \quad (5.13)$$

In contrast, using the quantum noise cross correlation at low frequencies by choosing:

$$\cot \zeta = \mathcal{K}_{\text{SM}}(0) = \frac{4J}{\gamma^3} \quad (5.14)$$

gives the total noise spectral density below the SQL within the interferometer bandwidth:

$$S_{\text{sum}}(\Omega) = \frac{S_{\text{SQL}}(\Omega)}{2\mathcal{K}_{\text{SM}}(\Omega)} \left\{ 1 + [\mathcal{K}_{\text{SM}}(0) - \mathcal{K}_{\text{SM}}(\Omega)]^2 \right\}. \quad (5.15)$$

These two scenarios are illustrated in Fig. 5.2, where the spectral densities (5.4, 5.13, 5.15) are plotted for some characteristic values of γ and J .

5.2.1 General equations for the quantum noise of a position meter

In a general case, the sensitivity of a Michelson interferometer with arbitrary squeezing input and arbitrarily detuned from its resonance (which causes optical rigidity), can be expressed as (derivation of these equations can be found in [35]):

$$S_{\text{sum}}(\Omega) = \frac{8}{L^2} \left[S_{xx}(\Omega) + 2\Re[\chi_{\text{eff}}^*(\Omega)S_{xF}(\Omega)] + |\chi_{\text{eff}}(\Omega)|^2 S_{FF}(\Omega) \right], \quad (5.16)$$

where the mechanical susceptibility of a free mass $\chi(\Omega) = [-M\Omega^2]^{-1}$ can be modified by the optical rigidity $K(\Omega)$:

$$\chi_{\text{eff}}(\Omega) = [K(\Omega) + \chi^{-1}(\Omega)]^{-1} = [K(\Omega) - M\Omega^2]^{-1} \quad (5.17)$$

$$K(\Omega) = \frac{MJ\delta}{\mathcal{D}(\Omega)}, \quad (5.18)$$

$$\mathcal{D}(\Omega) = (\gamma - i\Omega)^2 + \delta^2, \quad \Gamma = \sqrt{\gamma^2 + \delta^2}. \quad (5.19)$$

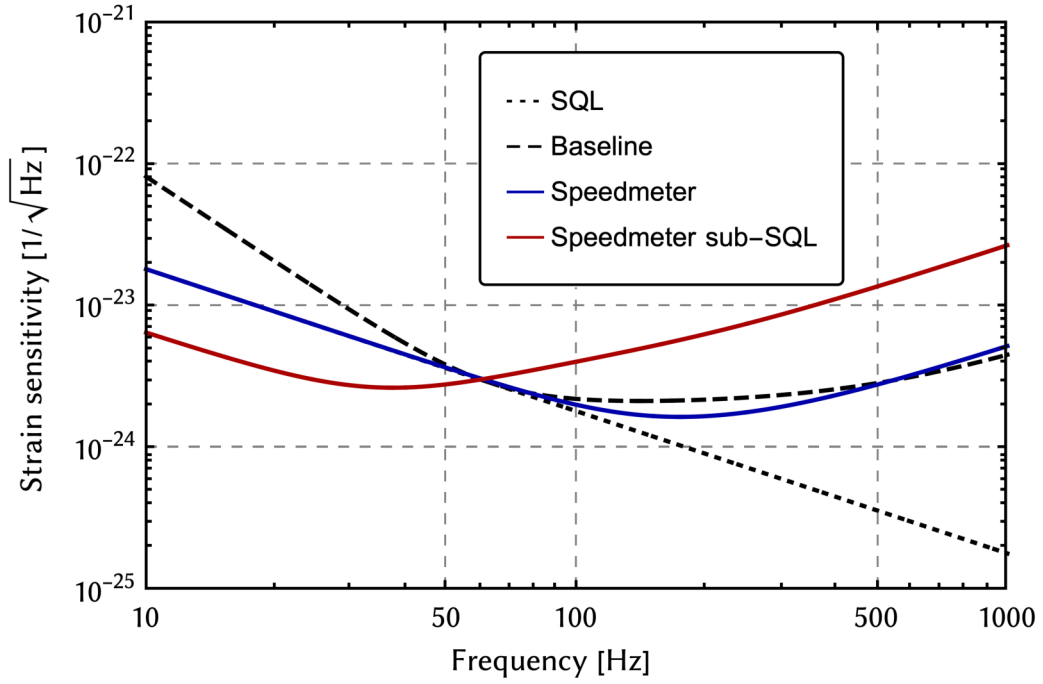


Fig. 5.2. Comparison between the total noise spectral densities of speedmeter and position meter: (black dashed) the baseline interferometer with bandwidth $\gamma = 2\pi \times 500 \text{ s}^{-1}$ [Eq. (5.4)]; (solid blue) the Sagnac speedmeter without cross-correlation between quantum noises, and bandwidth $\gamma = 2^{2/3} \times 2\pi \times 100 \text{ s}^{-1}$ [Eq. (5.13)]; (solid red) the Sagnac speedmeter with the cross-correlation, with bandwidth $\gamma = 2\pi \times 100 \text{ s}^{-1}$, $\cot \zeta = 4$, [Eq. (5.15)]. The SQL is in black dotted line [Eq. (5.3)]. In all cases, $J = (2\pi \times 100)^3 \text{ s}^{-3}$ and $\eta = 1$ (no losses).

The individual contributions to the spectral density take the form:

$$S_{xx} = \frac{\hbar}{4MJ\gamma} \frac{1}{\Gamma^2 \sin^2(\zeta - \beta) + \Omega^2 \sin^2 \zeta} \times \left[Q_c^2(\Omega) e^{2r} + Q_s^2(\Omega) e^{-2r} + \frac{1-\eta}{\eta} |\mathcal{D}(\Omega)|^2 \right], \quad (5.20)$$

$$S_{FF} = \frac{\hbar MJ\gamma}{|\mathcal{D}(\Omega)|^2} \left[|P_c(\Omega)|^2 e^{2r} + |P_s(\Omega)|^2 e^{-2r} \right], \quad (5.21)$$

$$S_{xF} = \frac{\hbar}{2\mathcal{D}^*(\Omega)} \frac{Q_c(\Omega) P_c(\Omega) e^{2r} + Q_s(\Omega) P_s(\Omega) e^{-2r}}{\Gamma \sin(\zeta - \beta) - i\Omega \sin \zeta}, \quad (5.22)$$

where we defined the homodyne angle ζ , squeezing phase θ and effective detuning phase $\beta = \arctan \delta/\gamma$, and introduced the effective parameters:

$$Q_c(\Omega) = \Gamma^2 \cos(2\beta + \theta - \zeta) + \Omega^2 \cos(\theta - \zeta), \quad (5.23a)$$

$$Q_s(\Omega) = -\Gamma^2 \sin(2\beta + \theta - \zeta) - \Omega^2 \sin(\theta - \zeta), \quad (5.23b)$$

$$P_c(\Omega) = \Gamma \cos(\theta + \beta) + i\Omega \cos \theta, \quad (5.23c)$$

$$P_s(\Omega) = -\Gamma \sin(\theta + \beta) - i\Omega \sin \theta. \quad (5.23d)$$

In the next section we present how the complicated frequency dependence in these spectral densities can result in a speedmeter-like spectral densities.

5.3 Multi-carrier shaping of quantum noise

In a general case of an arbitrary detuning δ and homodyne angle ζ , the quantum noise spectral densities of the ordinary Michelson/Fabry-Pérot interferometer have sophisticated frequency dependencies, see Eqs. (5.20). Here for us the important regime would be when

$$\left| \frac{\sin(\zeta - \beta)}{\sin \zeta} \right| \Gamma \ll \Omega \ll \Gamma. \quad (5.24)$$

In this regime, the shot noise spectral density has a speedmeter-like frequency dependence:

$$S_{xx}(\Omega) \propto \frac{1}{\Omega^2}. \quad (5.25)$$

However, frequency dependencies of the other two spectral densities are improper: $S_{FF}(\Omega) \propto \Omega^0$ instead of $S_{FF}(\Omega) \propto \Omega^2$ and $S_{xF}(\Omega) \propto 1/\Omega$ instead of $S_{xF}(\Omega) \propto \Omega^0$. Moreover, while the quantum speedmeter requires the free mass dynamics, in the detuned interferometer the dynamics of the test masses is modified by the optical rigidity [196]. Therefore, the frequency dependence (5.25) by itself does not allow to realize the speedmeter-type total quantum noise. It is possible though to use quantum entanglement between multiple carriers created by the radiation-pressure noise, and use quantum correlations between the carriers to conditionally cancel the unwanted parts of QRPN and achieve the desired speedmeter-like sensitivity.

5.3.1 Conditional measurement of a multi-channel detector

In this section, we describe the ways to use several channels (measurement devices) all coupled to the same movable mirror. The interaction with the mirror entangles different channels, and for each channel separately worsens the sensitivity. However, when they are combined in an optimal way, the total sensitivity can be increased.

Consider a system consisting of N linear meters measuring position x of a test mass. Each of the meters is described by its measurement noise \hat{x}_j and back action (radiation-pressure) noise \hat{F}_j ($i = 1..N$), with the spectral densities $S_{xx}^{(j)}$, $S_{FF}^{(j)}$, $S_{xF}^{(j)}$. The test object is described by its mechanical susceptibility function

$$\chi(\Omega) = \frac{1}{D(\Omega)}, \quad (5.26)$$

with the possible dynamic back action of the meters (the optical springs) included into it.

In Fourier representation, outputs of these meters are equal to

$$\mathcal{G}_j(\Omega) = G(\Omega) + D(\Omega)\hat{x}_j(\Omega) + \sum_{j=1}^N \hat{F}_j(\Omega), \quad (5.27)$$

where G is the signal force. The combined output is equal to

$$\mathcal{G}(\Omega) = \sum_{j=1}^N \alpha_j(\Omega) \mathcal{G}_j(\Omega) = G(\Omega) + \hat{F}_{\text{sum}}(\Omega), \quad (5.28)$$

where $\alpha_j(\Omega)$ are weight functions satisfying the normalization condition

$$\sum_{j=1}^N \alpha_j(\Omega) = 1 \quad (5.29)$$

and

$$\hat{F}_{\text{sum}}(\Omega) = \sum_{j=1}^N [D(\Omega) \alpha_j(\Omega) \hat{x}_j(\Omega) + \hat{F}_j(\Omega)] \quad (5.30)$$

is the total effective noise force with the spectral density being equal to

$$S_{\text{sum}}^F(\Omega) = \sum_{j=1}^N \left\{ |D(\Omega)|^2 |\alpha_j(\Omega)|^2 S_{xx}^{(j)}(\Omega) + 2\Re [D(\Omega) \alpha_j(\Omega) S_{xF}^{(j)}(\Omega)] + S_{FF}^{(j)}(\Omega) \right\}. \quad (5.31)$$

Using the vector notation, Eqs. (5.29, 5.31) can be rewritten as follows:

$$\mathbf{A}^\dagger(\Omega) \mathbf{1} = 1, \quad (5.32)$$

$$S_{\text{sum}}^F(\Omega) = |D(\Omega)|^2 \mathbf{A}^\dagger \mathbf{S}_{xx}(\Omega) \mathbf{A}(\Omega) + 2\Re [D(\Omega) \mathbf{A}^\dagger(\Omega) \mathbf{S}_{xF}(\Omega)] + \sum_{j=1}^N S_{FF}^{(j)}(\Omega), \quad (5.33)$$

where we defined vectors and matrices:

$$\mathbf{A}^\dagger(\Omega) = \left(\alpha_1(\Omega) \quad \dots \quad \alpha_N(\Omega) \right), \quad (5.34)$$

$$\mathbf{1} = (1 \dots 1)^\top, \quad (5.35)$$

$$\mathbf{S}_{xF}(\Omega) = \begin{pmatrix} S_{xF}^{(1)}(\Omega) \\ \vdots \\ S_{xF}^{(N)}(\Omega) \end{pmatrix}, \quad (5.36)$$

$$\mathbf{S}_{xx} = \begin{pmatrix} S_{xx}^{(1)}(\Omega) & & \mathbf{0} \\ & \ddots & \\ \mathbf{0} & & S_{xx}^{(N)}(\Omega) \end{pmatrix}. \quad (5.37)$$

With account of condition (5.32), the minimum of (5.33) can be found by taking a derivative with respect to the gain vector and solving the Lagrange equation:

$$\frac{\partial (S_{\text{sum}}^F + \lambda[\mathbf{1} - \mathbf{A}^\dagger(\Omega)\mathbf{1}])}{\partial \mathbf{A}^\dagger(\Omega)} = 0. \quad (5.38)$$

The solution to this equation:

$$\mathbf{A}^\dagger(\Omega) = -\frac{\lambda \mathbf{1}^\dagger + D^*(\Omega) \mathbf{S}_{xF}^\dagger(\Omega)}{|D(\Omega)|^2} \mathbf{S}_{xx}^{-1}(\Omega), \quad (5.39)$$

$$\lambda = -\frac{|D(\Omega)|^2 + D^*(\Omega) \mathbf{S}_{xF}^\dagger(\Omega) \mathbf{S}_{xx}^{-1}(\Omega) \mathbf{1}}{\mathbf{1}^\dagger \mathbf{S}_{xx}^{-1}(\Omega) \mathbf{1}} \quad (5.40)$$

This allows to define the individual weight coefficients as:

$$\alpha_j(\Omega) = \frac{1}{S_{xx}^{(j)}(\Omega)} \left\{ S_{xx}^{\text{eff}}(\Omega) + \frac{[S_{xF}^{\text{eff}}(\Omega) - S_{xF}^{(j)}(\Omega)]^*}{D(\Omega)} \right\} \quad (5.41)$$

where I introduced the effective noise spectral densities:

$$S_{xx}^{\text{eff}}(\Omega) = \left[\sum_{j=1}^N \frac{1}{S_{xx}^{(j)}(\Omega)} \right]^{-1}, \quad (5.42)$$

$$S_{FF}^{\text{eff}}(\Omega) = \sum_{j=1}^N \left[S_{FF}^{(j)}(\Omega) - \frac{|S_{xF}^{(j)}(\Omega)|^2}{S_{xx}^{(j)}(\Omega)} \right] + \frac{|S_{xF}^{\text{eff}}(\Omega)|^2}{S_{xx}^{\text{eff}}(\Omega)}, \quad (5.43)$$

$$S_{xF}^{\text{eff}}(\Omega) = S_{xx}^{\text{eff}}(\Omega) \sum_{j=1}^N \frac{S_{xF}^{(j)}(\Omega)}{S_{xx}^{(j)}(\Omega)}. \quad (5.44)$$

Taking this all into account, the total spectral density can be expressed in terms of these effective spectral densities:

$$S_{\text{sum}}^F(\Omega) = |D(\Omega)|^2 S_{xx}^{\text{eff}}(\Omega) + 2\Re [D(\Omega) S_{xF}^{\text{eff}}(\Omega)] + S_{FF}^{\text{eff}}(\Omega). \quad (5.45)$$

This optimization procedure is used to compute spectral densities in the next section, but in principle the same concept (with the same outcome for the optimal filter) can be used for any other entangled light fields, see e.g. the EPR-based frequency-dependent squeezing, see Chapter 3 for details.

5.3.2 Speedmeter-like sensitivity in Michelson-Fabry-Perot interferometer

Although for an ordinary detector the cross-correlation in the noises and the optical spring prevent from achieving the speedmeter-like sensitivity, both can be canceled using the annihilation regime discussed in [131]. Note that S_{xx} is an even function of δ , ζ , θ ; S_{xF} is an odd function of these three parameters; and

K is an odd function of δ [see Eqs. (5.20, 5.18)]. Therefore two carriers with the following parameters:

$$J_1 = J_2, \quad (5.46a)$$

$$r_1 = r_2, \quad (5.46b)$$

$$\Gamma_1 = \Gamma_2, \quad (5.46c)$$

$$\beta_1 = -\beta_2, \quad (5.46d)$$

$$\zeta_1 = -\zeta_2, \quad (5.46e)$$

$$\theta_1 = -\theta_2 \quad (5.46f)$$

(the *antisymmetric* carriers) create an effective position meter with canceled optical spring and with the quantum noise spectral densities equal to [see Eqs. (5.42)]

$$S_{xx}^{\text{eff}}(\Omega) = \frac{S_{xx}(\Omega)}{2}, \quad (5.47a)$$

$$S_{FF}^{\text{eff}}(\Omega) = \eta(\Omega) \frac{\hbar^2}{4S_{xx}^{\text{eff}}(\Omega)} + 2[1 - \eta(\Omega)]S_{FF}(\Omega), \quad (5.47b)$$

$$S_{xF}^{\text{eff}}(\Omega) = 0. \quad (5.47c)$$

where S_{xx} , S_{FF} describe the individual carriers.

The first (major) term of the back action noise spectral density (5.47b), being proportional to Ω^2 , has the proper speedmeter-like frequency dependence. The second one (originating from the optical losses) has the ordinary position meter spectral dependence ((5.20)), which degrades the effect of the described regime.

It is worth noting that the effective back action noise is smaller, than that just the sum of back action noises of the individual carriers, $S_{FF}^{\text{eff}} < 2S_{FF}$. This means that the effective back action noise actually is a *conditional* one, that is, it describes only the residual noise remaining after subtraction of the part known to the observer due to the cross-correlation of the shot noise and the radiation pressure noise. While the residual cross-correlation (5.47b) is canceled, the weight functions for the individual output signals depend on the cross-correlation spectral densities of the individual carriers, see Eq. (5.41).

Examples of the resulting total quantum noise spectral densities, based on the simplified analytical optimization procedure, described in App. A.3.2, are

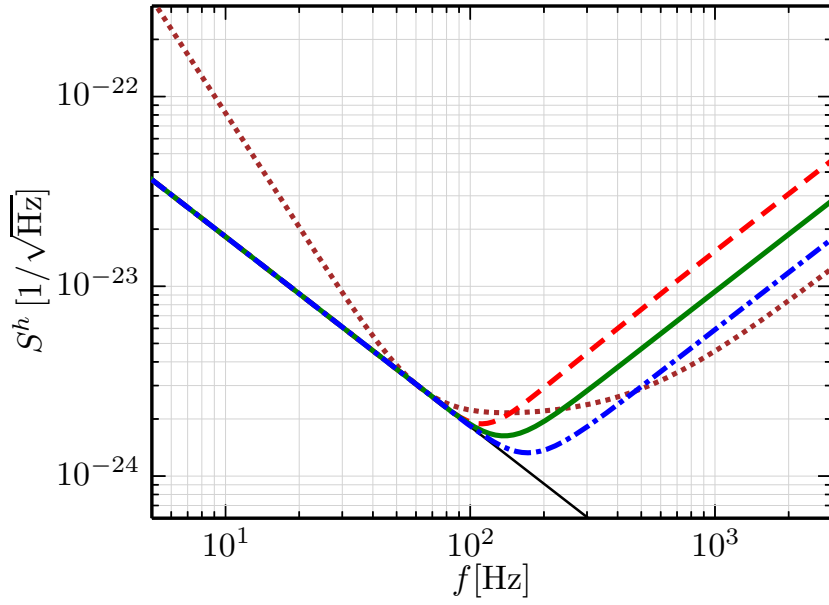


Fig. 5.3. Plots of the total quantum noise spectral density in the double antisymmetric carriers regime without squeezing (dashes), with 6 db squeezing (solid), and with 12 db squeezing (dash-dots). The parameters Γ , ζ , β , and θ are given by Eqs. (A.116), (A.109), and Table A.1, respectively. Dots: the baseline interferometer (5.4), at $\gamma = 2\pi \times 500 \text{ s}^{-1}$ (dots). Thin solid line: the SQL (5.3). In all cases, $J = (2\pi \times 100)^3 \text{ s}^{-3}$ and $\eta = 1$ (no losses).

shown in Fig. 5.3. Comparison of Figs. 5.2 and 5.3 shows (assuming the Advanced LIGO parameters), that the double-carrier Michelson/Fabry-Pérot interferometer can provide the sensitivity comparable with the one of the simplified Sagnac interferometer with uncorrelated quantum noises described by Eq. (5.13).

One interesting feature of the paired carrier detector is the unusual dependence of the quantum noise on the circulating optical power and the squeezing power. Similar to the ordinary single-carrier Michelson/Fabry-Pérot interferometer case and to the quantum speedmeter one, the high-frequency noise spectral density decreases with the power and the squeezing increase, albeit the dependence is different: $(I_c e^r)^{-4/3}$ [see Eq. (A.121)] instead of $(I_c e^{2r})^{-1}$. On contrary to these cases, the low-frequency noise, after the proper adjustment of the parameters Γ , ζ , β , and θ , does not change at all. Therefore, the paired-carriers detector does not require the frequency-dependent squeezing or the variational readout to take full advantage of the stronger optical power and/or squeezing.

5.3.3 Combining multiple detectors in one

A pair of carrier forms an effectively independent detector. It is thus possible to combine two pairs in a xylophone configuration: one pair is tuned such that it increases the sensitivity at low frequency, the other one – at high frequency. The effective spectral density of each carrier reaches its minimum at frequency $\Omega_0 \propto \Gamma$ [see Eq. (A.114)]. The width of this minimum depends on β and the squeezing power e^{2r} , see App. A.3.2. Varying parameters of the pairs, it is possible to flexibly shape the resulting total quantum noise spectral density, described by Eqs. (5.1, 5.42).

In particular, the high-frequency sensitivity of the antisymmetric double carrier regime can be improved by adding one or more additional pair(s) of carriers tuned to higher frequencies Ω_0 . For a fixed total power in the carriers, the total power in each carrier would have to be reduced, which degrades the individual sensitivity. However, the optimal sensitivity of a xylophon is nonetheless increased.

An example of the configuration with two pairs of antisymmetric carriers (four carriers total, with the optical power evenly distributed among them) is shown in Fig. 5.4. Parameters of the low-frequency component are calculated using the same optimization procedure, that was used for the previous example

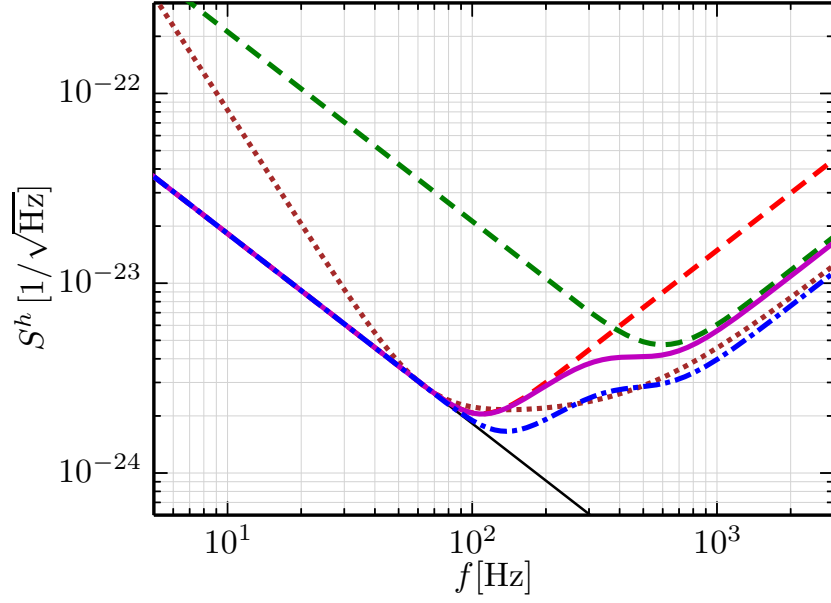


Fig. 5.4. Plots of the total quantum noise spectral densities of the xylophone configuration with two pairs of antisymmetric carriers with 6 db (solid magenta) and with 12 db (dash-dotted blue) squeezing. The values of Γ are given by Eq. (A.116) the low-frequency pair and Eq. (A.123) with $\Omega_0 = 2\pi \times 600$ Hz for the high-frequency pair. The parameters ζ , β , and θ are given by Eq. (A.109), and Table A.1, respectively. The optical power is distributed evenly between the all carriers. Dashed red and green: the total quantum noise spectral densities of the individual pairs. Dotted red: the baseline interferometer (5.4), at $\gamma = 2\pi \times 500$ s⁻¹. Solid black: the SQL (5.3). In all cases, the total circulating optical power corresponds to $J = (2\pi \times 100)^3$ s⁻³ and $\eta = 1$ (no losses).

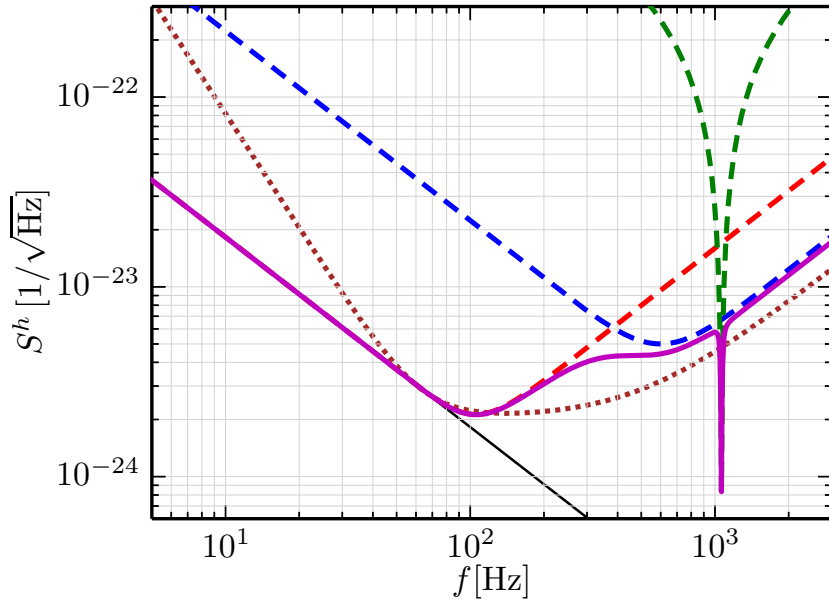


Fig. 5.5. Total sensitivity of triple-paired detector optimized for a pulsar J0034-0534. Solid magenta: total quantum noise spectral densities of the xylophone configuration with two broadband pairs of antisymmetric carriers, with the parameters defined in the same way as in Fig. 5.4, and one additional narrow-band pair with $\Gamma = 4\pi \times 532.7 \text{ s}^{-1}$ (the double frequency of the pulsar J0034-0534), $\beta = \pi/2 - 0.002$, $\theta = \pi/2$. The optical power is distributed among the all carriers as 45%:45%:10%, and 6 db squeezing is used for all carriers. Dashes: the total quantum noise spectral densities of the individual pairs. Dots: the baseline interferometer (5.4), at $\gamma = 2\pi \times 500 \text{ s}^{-1}$ (dots). Thin solid line: the SQL (5.3). In all cases, the total circulating optical power corresponds to $J = (2\pi \times 100)^3 \text{ s}^{-3}$ and $\eta = 1$ (no losses).

(see App. A.3.2). For the high-frequency pair, another procedure was used, see App. A.3.2, which does not take into consideration the radiation pressure noise, which in this case is negligibly small, but takes into account instead, that the minimum of the shot noise spectral density has to correspond to some given frequency Ω_0 .

The total noise spectral density of the higher-frequency pair in this case scales with the optical power and with the squeezing power as $(I_c e^r)^{-1}$ (a bit weaker, than for a single pair).

The xylophone configuration can also be used to create “on demand” some special features of the quantum noise spectral density, for example, narrow-

band minima at some given frequencies, associated with the known pulsars. This possibility is demonstrated in Fig. 5.5, where the total quantum noise of a configuration with three antisymmetric pairs is shown. The parameters of the first two (broadband) pairs are optimized in the same way as described above. However, 10% of the total optical power is relocated to the third narrow band pair. Parameters of this pair are calculated using the optimization procedure described in App. A.3.2. As an example of millisecond pulsars, we have chosen J0034-0534 [197], which has the rotation frequency $f_0 \approx 532.7$ Hz and therefore presumably radiates near-monochromatic gravitation waves at frequency $2f_0 \approx 1065.4$ Hz.

5.4 Discussion

The paired carrier approach to the detector design allows to flexibly shape the sensitivity of the detector. At low frequency it results in a speedometer-like quantum noise, following the SQL closely. Additional pairs of carriers allow to increase the detection bandwidth or create high sensitivity at particular frequencies, where we expect to see some signal. These additional pairs do not disturb the low-frequency sensitivity, since they are added coherently in a xylophon configuration.

Another feature of the approach is that a simple brute-force increase of the circulating optical power and/or the squeezing power improves high-frequency sensitivity the multi-carrier scheme without degradation of the low-frequency one. In the “ordinary” single-carrier Michelson interferometer, increase of the circulating optical power and/or the squeezing improve the high-frequency sensitivity, but degrades the low-frequency one due to increased radiation-pressure noise. Using frequency-dependent squeezing [111, 113] in an ordinary interferometer allow to avoid this degradation, but in this case increase of the circulating power has to be supplemented by the proportional increase of the squeezing in order to keep the low-frequency sensitivity unchanged. In a realistic setup both schemes promise similar overall sensitivity gain, but paired carrier approach is more focused on the low-frequency band dominated by the radiation pressure noise and provides almost no gain at high frequencies. Both share the same main shortcoming, namely, the vulnerability to the optical losses, which is a general

feature of methods for overcoming the SQL based on the quantum noise cross-correlation (which includes, in particular, all the filter cavities based schemes, as well as the quantum speedmeter [35]).

Unlike the speedmeter topologies [121, 176, 194, 195], paired carriers allow only to reach the SQL in a broad band, but overcome it, since there's no residual cross-correlation. However, practically the gain that the speedmeter configuration can achieve below the SQL is rather limited currently by technical noises, most notably, the mirrors coating and the suspension thermal noise, and the gravity gradient noise), while introducing cross-correlation noticeably increases the shot (high-frequency) noise, see Fig. 5.2. In the paired carrier it is possible to relax to some extent the anti-symmetry condition (5.46) by removing constrains for the homodyne and squeezing angles ζ and θ , it is possible to create the residual cross-correlation S_{xF} and overcome the SQL in some frequency band, see Fig. 5.6. The details of the numerical optimization, and parameters can be found in [69].

The proposed approach is rather challenging experimentally: it requires at least two carriers, both of them detuned off resonance by a value set with high precision. These carriers have to be spatially separated on the output and sent to separate homodyne detectors. For a single pair, this separation can be implemented by using two orthogonal polarizations for the two carriers, as it was proposed in the initial paper [131]. In the case of two and more pairs, the output beams can be separated by means of short (table-top scale) filter cavities. Such cavity would result in additional loss $1 - \eta_f = \frac{A_f}{T_f + A_f}$, where T_f is the input mirror power transmissivity, and A_f are losses per round trip, $A_f \sim 10^{-5}$, the resulting quantum inefficiency can be on the order of 10^{-2} . This results in an estimation for the half-bandwidth of such a cavity:

$$\gamma_f = \frac{cA_f}{4l_f(1 - \eta_f)} \sim 2\pi \times 10 \text{ kHz}, \quad (5.48)$$

given the length $l_f = 1$ m. If frequency separation between the carriers exceed 100 kHz, which roughly corresponds to three free spectral ranges of the Advanced LIGO interferometer, then this bandwidth gives the separation efficiency better than 99%. In order to implement different values of the interferometer bandwidth γ for different pairs of carriers, the optical outputs can be equipped by the additional

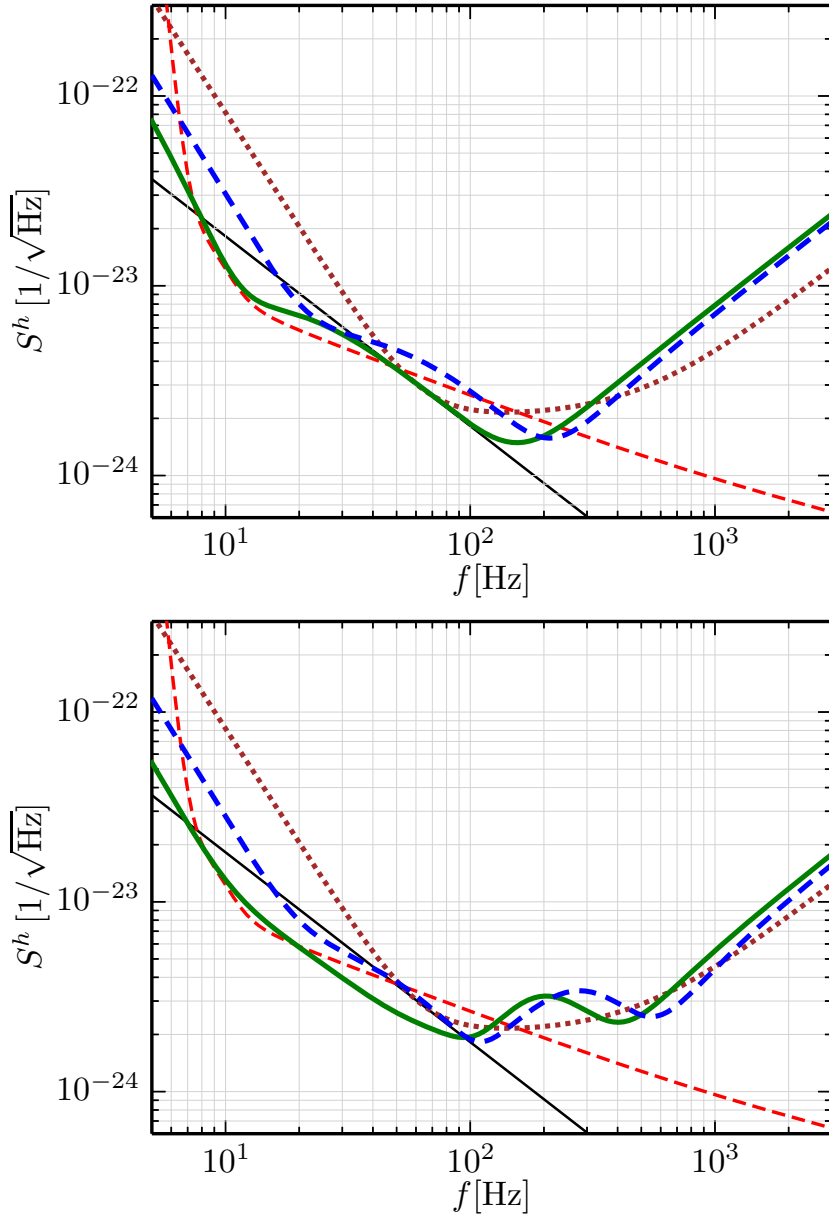


Fig. 5.6. Numerically optimized quantum noise spectral densities for one (top) and two (bottom) pairs of carriers, with $\eta = 1$ (solid) and $\eta = 0.95$ (dashes). The corresponding optimal parameters are listed in Table II in [69]. In all cases, the total circulating optical power corresponds to $J = (2\pi \times 100)^3 \text{ s}^{-3}$ and 6 dB squeezing is used for all carriers. Dashes: the total quantum noise spectral densities of the individual pairs. Dots: the baseline interferometer (5.4), at $\gamma = 2\pi \times 500 \text{ s}^{-1}$ (dots). Thin solid line: the SQL (5.3). Thin dashed line: total technical noise, based on Advanced LIGO design.

signal recycling mirrors, which either supplement the main signal recycling mirror or completely replace it.

These challenges motivate further research into the practical implementation of paired carriers in future gravitational wave-detector. In particular, of interest are a combination with another approach taking advantage of entangled light [141, 143, 144], and a combination with quantum expander, as presented in Chapter 8.

First demonstration of beating the standard sensitivity-bandwidth limit with internal squeezing

Quantum noises are always present in any quantum metrological device. In particular, measurement noise and measurement back-action noise limit the sensitivity of these devices. As I discussed in previous chapters, it can be avoided by back-action evading measurements or QND techniques. Measurement noise is a more fundamental limit to sensitivity. Nevertheless, it can be squeezed.

In cavity-based devices, such as gravitational-wave detectors, not only the maximal sensitivity is important, but also the frequency bandwidth in which the detector is most sensitive. In this chapter, I introduce the standard sensitivity-bandwidth limit (SSBL) on the sensitivity of a cavity-based detector. This limit cannot be overcome without using nonclassical states of light. I introduce the concept of internal squeezing, and discuss how it allows to beat the standard sensitivity-bandwidth limit of a single-cavity detector. I present the experimental demonstration of beating this limit by 36%.

Although in this chapter I talk about single-cavity detectors, this discussion can be extended to a more general case of cavity-enhanced systems with multiple cavities, such as gravitational-wave detectors.

The results of this chapter were published in [70]. The experiment was performed in collaboration with Lisa Kleybolte using the squeezed-light experimental setup built by her and homodyne detector provided by Stefan Ast.

6.1 Introduction

As discussed in Chapter 1, according to the Heisenberg uncertainty principle, one has to increase the uncertainty in the light's amplitude quadrature in order to improve the measurement sensitivity by decreasing the uncertainty in the light's phase quadrature. Since energy is needed to increase the uncertainty, the sensitivity limit of an interferometer is set by the optical energy inside the cavity [34, 151]. In a more general case of arbitrary signal waveforms, this consideration leads to the Quantum Cramer-Rao Bound (QCRB) for the estimation of signals in Gaussian quantum noise: at each signal frequency, the maximal phase sensitivity is inversely proportional to the fluctuations in the amplitude quadrature at the same frequency [153, 154], as I discussed in Chapter 2.

Based on the QCRB, first of all, the concept of enhancing the sensitivity with optical cavities can be understood. Both amplitude and phase quadratures resonate inside the cavity and have their uncertainties amplified within the bandwidth of the resonance, and attenuated at other frequencies. In the case of a coherent input field and a simple Fabry-Perot cavity the state remains coherent inside the cavity. The standard sensitivity-bandwidth limit is defined as the maximum product of a peak sensitivity \mathcal{S} and a detection bandwidth \mathcal{B} , that can be achieved using coherent states of light and a given light power P_c inside the cavity [155]: $\mathcal{S} \times \mathcal{B} \leq 8\pi P_c / (\hbar \lambda L)$, where λ is the optical wavelength, L is the cavity length and \hbar is the reduced Plank constant.

We discuss three different strategies for improving the sensitivity of a cavity-enhanced detector beyond the SSBL, see Fig. 6.1. The first approach is based on the *white-light cavity* effect [133, 198–201]. It broadens the cavity resonance without changing the finesse, increasing the amplitude fluctuations in a broader frequency band. As a result, the variance of amplitude quadrature inside the cavity increases above the vacuum uncertainty, and so does the sensitivity-bandwidth product. It was proposed recently that the white-light cavity effect can be achieved by using an anomalously dispersive medium inside the cavity [135–137, 202].

The second approach is called *external squeezing*. In this case, the uncertainty of the optical field that is injected into the cavity is squeezed below the vacuum level in the phase quadrature, without influencing the signal enhancement due to the optical cavity [40–42, 44, 45, 66, 67]. The bandwidth remains unchanged, and

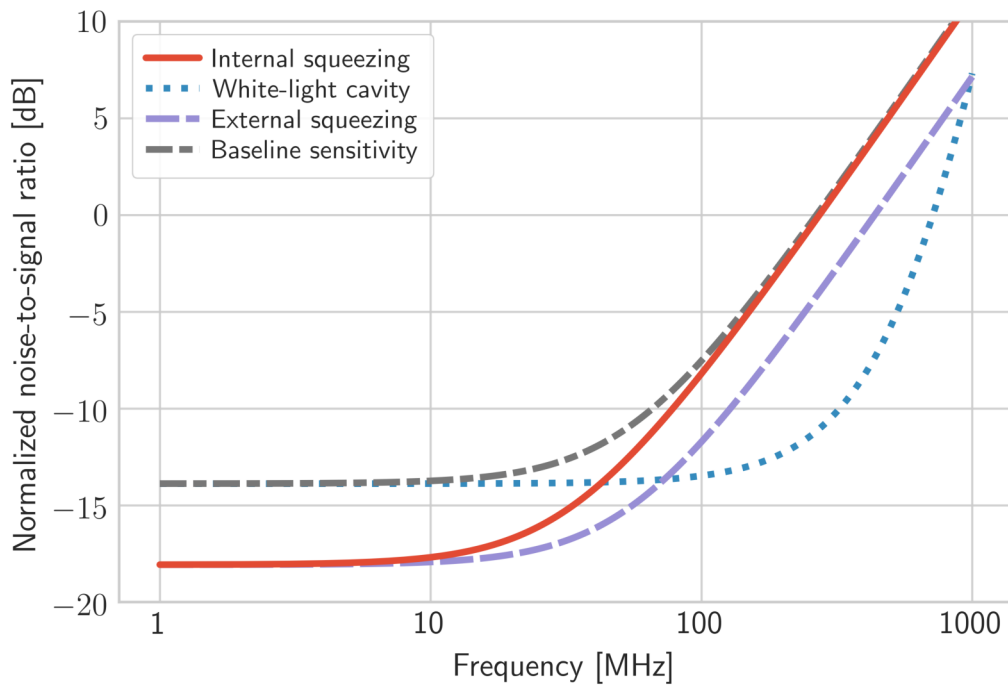


Fig. 6.1. Three different approaches to improving the sensitivity (noise-to-signal ratio) of a baseline detector (gray) beyond the SSBL. Internal squeezing approach (red) generates squeezed states inside the detector cavity. The sensitivity is increased maximally at low frequencies, and remains unchanged at high frequencies outside the cavity’s linewidth. External squeezing approach (violet) generates quantum squeezed states outside the cavity. The sensitivity is enhanced in a broad band. White-light cavity approach (blue) increases the cavity linewidth with negative dispersion medium inside the cavity. The sensitivity is enhanced at high frequencies.

hence the standard sensitivity-bandwidth limit is surpassed due to the increased peak signal-to-noise ratio.

The third approach is *internal squeezing* [203–205]. Here, squeezed states of light are produced inside the detector’s cavity, for instance using an optical parametric amplifier. In contrast to external squeezing, in this approach, the phase quadrature squeezing happens mainly inside the optical cavity linewidth and affects both the noise and the signal. The amplitude quadrature uncertainty is correspondingly increased above the vacuum level, and in accordance with the QCRB, the sensitivity increases: the noise is squeezed more than the signal is deamplified. The detection bandwidth narrows in this case, but the peak sensitivity is increased even more strongly, which allows the standard sensitivity-bandwidth limit to be surpassed.

In the following sections I provide the theoretical background for calculating the effect of internal squeezing on the sensitivity-bandwidth product, and then describe the experiment we performed to demonstrate the ability to surpass the standard-sensitivity bandwidth limit.

6.1.1 Energetic quantum limit

In order to measure a small change in the light phase produced by an external classical force, it is necessary to reduce the phase fluctuations in the light field. According to the Heisenberg uncertainty principle, that requires increasing the energy fluctuations, as I discussed in Chapter 2. In fact, the argument has to be reversed: energy defines the resource available for storing the information. Heisenberg uncertainty relation ensures that it leads to increased resolution in phase [34]. Therefore, in order to increase the signal-to-noise ratio (SNR), it is necessary to increase the energy fluctuations, or in other words the fluctuations of amplitude quadrature of the light field.

This statement is known as the Energetic Quantum Limit [151]. To express this statement mathematically, we define the measured spectrum as

$$S_{\text{total}}(\Omega) = S_n(\Omega) + |T(\Omega)|^2 |x(\Omega)|^2, \quad (6.1)$$

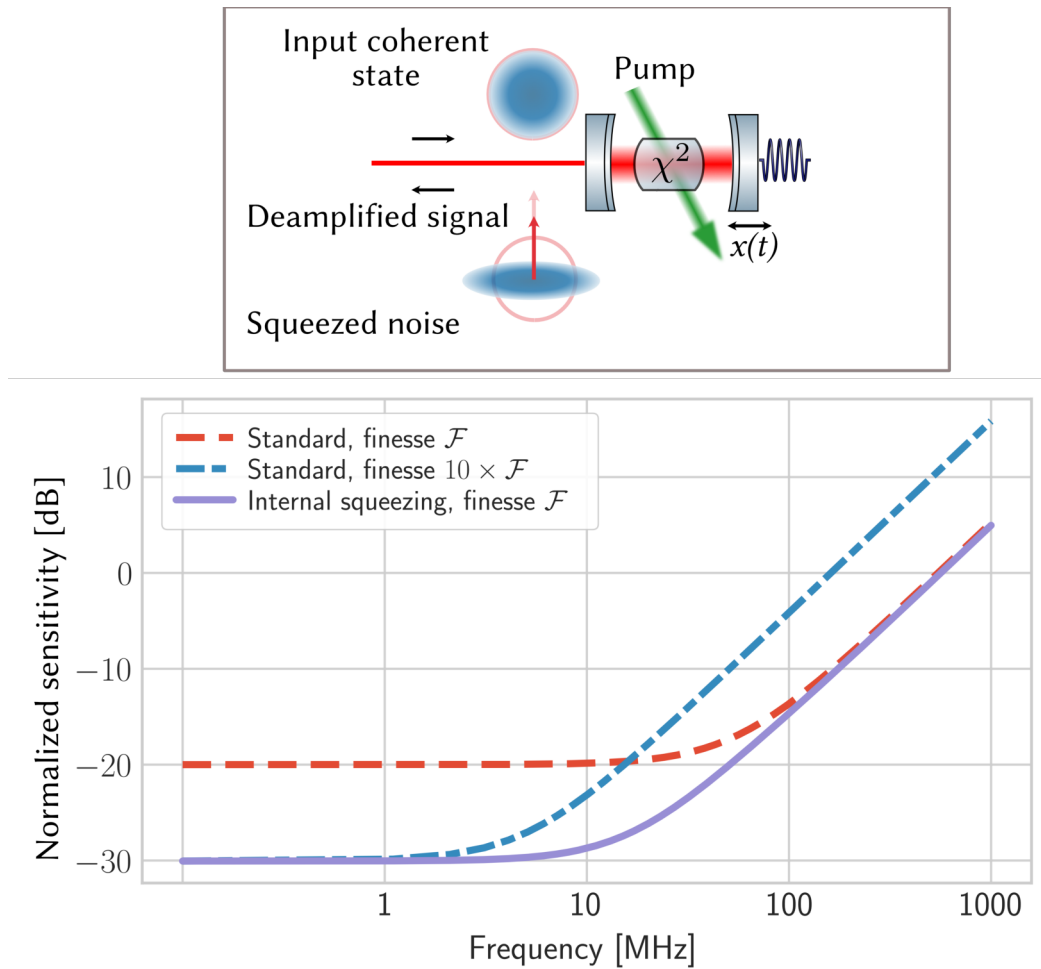


Fig. 6.2. Internal squeezing approach to cavity-enhanced quantum metrology. Top: a concept of internal squeezing. The phase quadrature of the input coherent light field is squeezed inside the cavity, deamplifying the signal at the same time. Signal deamplification is smaller than the noise reduction by squeezing, so the sensitivity increases. An increased amplitude quadrature, according to the QCRB, leads to the enhancement of the sensitivity-bandwidth product beyond the SSBL. Bottom: sensitivity enhancement by internal squeezing. The three curves show the quantum measurement noise of a cavity-based detector with the same coherent light power in its arms, normalized to a phase signal optical transfer function. The peak sensitivity \mathcal{S} is defined as the inverse of the minimum of the curves; the bandwidth \mathcal{B} is the frequency at which the noise rises by 3 dB above its minimal value. The standard sensitivity-bandwidth product remains constant for a given coherent light power inside the cavity: to increase the peak sensitivity by 10 dB, the finesse \mathcal{F} has to be increased by a factor of 10, thus the bandwidth decreases by the same amount (compare red dashed and blue dashed-dotted curves). When the sensitivity enhanced with internal squeezing (violet solid curve) the bandwidth is larger than the one of a classical detector with increased finesse (blue dot dashed).

where $S_n(\Omega)$ is shot-noise, $x(\Omega)$ is a classical signal, and $T(\Omega)$ is the transfer function of the signal through the cavity to the detector. Then, according to the Energetic Quantum Limit, the integrated SNR, assuming a signal equal to unity $x(\Omega) = 1$, is limited by:

$$\rho \equiv \int_0^{\omega_{\text{FSR}}} \frac{|T(\Omega)|^2}{S_n(\Omega)} \frac{d\Omega}{2\pi} \leq \frac{\omega_0 P_c L}{\hbar c} V_{PP}, \quad (6.2)$$

where V_{PP} is the variance of the amplitude quadrature of the light, c is the speed of light, ω_0 is the carrier light angular frequency and ω_{FSR} is the free spectral range of the cavity. Here, the equal sign stands for the quantum-noise limited case without optical loss. For an optical cavity the amplitude quadrature fluctuations have to be high inside the cavity, as that is where the transfer of information to the light field occurs.

For optical cavities, the SNR has a Lorentzian profile. Therefore, it is possible to define the peak sensitivity \mathcal{S} as the SNR at zero frequency, and its bandwidth \mathcal{B} as the half width at half maximum. In this case, the integrated SNR by definition is equal to the sensitivity-bandwidth product: $\rho = \mathcal{S} \times \mathcal{B}$. For the coherent field, $V_{PP} = 1$, the sensitivity-bandwidth product is limited by $\mathcal{S} \times \mathcal{B} = \omega_0 P_c L V_{PP} (\hbar c)^{-1} = \omega_0 P_c L (\hbar c)^{-1}$. This limit that is achievable with coherent light we call the SSBL.

We mentioned three different ways of increasing the quantum fluctuations of the amplitude quadrature inside the detector. Leaving aside the white-light cavity approach, here, we compare internal and external squeezing. In the case of external squeezing, the increase in the SNR is proportional to the amount of injected squeezing at all frequencies, provided that the bandwidth of external squeezing is large compared to the detector's bandwidth. Consequently, detection bandwidth remains unaffected. In the case of internal squeezing, the parametric amplification reduces the phase quadrature of the light and amplifies the amplitude quadrature. The phase quadrature sidebands are suppressed mostly inside the cavity bandwidth, and there is little deamplification outside the cavity bandwidth. As a result, the bandwidth of the optical transfer function is increased, both for signal and quantum noise. However, the bandwidth of the SNR is reduced, since both the signal and the squeezed quantum noise become closer to the coherent level (more about it below). Another way of seeing that is the following: internal

squeezing increases the SNR inside the cavity optical linewidth, but not outside, therefore the detection bandwidth is effectively decreased, see Fig. 6.2. As the bandwidth is reduced, in order the Energetic Quantum Limit to be satisfied, it is necessary that the SNR is increased more, than the bandwidth is reduced, which is what we observe in the presented experiment. At the same time, when comparing the internal squeezing with a classical detector of the same peak sensitivity, internal squeezing results in a broader bandwidth, as dictated by the increase in the sensitivity-bandwidth product, see Fig. 6.2.

6.2 Theoretical calculation

We consider the propagation of a signal through a Fabry-Perot cavity with a nonlinear crystal inside, see Fig. 6.3. Pumping the crystal with light of the doubled frequency leads to optical parametric amplification of the cavity mode. The highest squeeze factor inside the cavity is achieved around cavity resonance and is limited to 6 dB. At this level, the threshold for optical parametric oscillation is reached, and the amplified amplitude quadrature becomes unstable and causes lasing [168, 169]. However, the squeeze factor outside the cavity is not fundamentally limited, due to destructive interference between the incoming vacuum field and outgoing squeezing [206]. The signal, on the contrary, originates from the inside of the cavity, and does not experience this such interference. Therefore, the deamplification in the signal remains limited to 6 dB. The resulting difference between noise squeezing and signal deamplification constitutes the gain in the signal-to-noise ratio (SNR), which represents the sensitivity of the detector. On the other hand, the bandwidth gets reduced, as the internal squeezing increases the sensitivity only inside the cavity linewidth, and leaves it unchanged outside. Despite this, the sensitivity-bandwidth product is enhanced, according to the QCRB, as we amplify the amplitude quadrature fluctuations inside the cavity.

In order to compute this, we start by writing down the input-output relations, as prescribed in Chapter 3. While it's often more convenient to use matrix form of input-output relations, in this Chapter I explicitly go through the derivation, since the system allows for a methodological demonstration. The procedure is standard, but one needs to keep in mind several key points: i) the signal appears

field, E is the mean amplitude of the light field inside the detector, $t_{c,b}$, $r_{c,b}$ are the amplitude transmissivity and reflectivity of coupling and back mirrors, such that $r_{c,b}^2 + t_{c,b}^2 = 1$, r_{det} is the detection loss, r_{int} is the intra-cavity loss without the coupling and the back mirrors; $r_{\text{det,int}}^2 + t_{\text{det,int}}^2 = 1$. This set of equations can be solved for the detected fields $d_{x,y}$:

$$d_x(\Omega) = \frac{t_{\text{det}}}{e^{-2q} - e^{2i\Omega\tau} r_c r_b t_{\text{int}}} \left(v_x(\Omega) \left(-r_c e^{-2q} + r_b r_{\text{int}}^2 e^{2i\Omega\tau} \right) + n_x^c(\Omega) t_c t_b t_{\text{int}} e^{-q} e^{i\Omega\tau} + n_x^{\text{int}}(\Omega) t_c r_{\text{int}} e^{-2q} \right) + r_{\text{det}} n_x^{\text{ext}}(\Omega), \quad (6.5)$$

$$d_y(\Omega) = \frac{t_{\text{det}}}{e^{2q} - e^{2i\Omega\tau} r_c r_b t_{\text{int}}} \times \left(2ik_p E x(\Omega) t_c t_{\text{int}} e^q e^{i\Omega\tau} + v_y(\Omega) \left(-r_c e^{2q} + r_b t_{\text{int}} e^{2i\Omega\tau} \right) + n_y^c(\Omega) t_c t_b t_{\text{int}} e^q e^{i\Omega\tau} + n_y^{\text{int}}(\Omega) t_c r_{\text{int}} e^{2q} \right) + r_{\text{det}} n_y^{\text{ext}}(\Omega). \quad (6.6)$$

The spectrum of the noise $a(\Omega)$ is defined as:

$$S_a(\Omega) \delta(\Omega - \Omega') = \frac{1}{2} \langle a(\Omega) a(\Omega') + a(\Omega') a(\Omega) \rangle. \quad (6.7)$$

Assuming that all noises in the system are uncorrelated (as they are quantum vacuum fluctuations), we find the spectral density of the detected noise in the signal quadrature:

$$S_n(\Omega) = 1 - \frac{t_c^2 t_{\text{det}}^2 t_{\text{int}}^2 (1 - e^{-2q})(1 + e^{-2q} r_b^2)}{1 + r_c^2 r_b^2 t_{\text{int}}^2 e^{-4q} - 2r_c r_b t_{\text{int}} e^{-2q} \cos 2\Omega\tau}. \quad (6.8)$$

The transfer function of the signal $x(\Omega)$ through the optical cavity to the detector is:

$$T(\Omega) = 2ik_p E \frac{t_c t_{\text{det}} t_{\text{int}} e^q e^{i\Omega\tau}}{e^{2q} - e^{2i\Omega\tau} r_c r_b t_{\text{int}}}, \quad (6.9)$$

and it's spectral shape:

$$|T(\Omega)|^2 = \frac{8\pi P_c}{\hbar\lambda c} \frac{e^{-2q} t_c^2 t_{\text{det}}^2 t_{\text{int}}^2}{1 + r_c^2 r_b^2 t_{\text{int}}^2 e^{-4q} - 2r_c r_b t_{\text{int}} e^{-2q} \cos 2\Omega\tau}, \quad (6.10)$$

where $P_c = \hbar k_p c |E|^2$ is the light power inside the cavity, and λ is the carrier wavelength.

6.2.1 Optical parametric oscillation threshold

The squeezing value cannot be arbitrary large inside the cavity, as at some pump power the cavity will become unstable and initiate lasing. We can find the stability criterion from the equation for the amplitude quadrature inside the cavity to be:

$$b_x = \frac{v_x(\Omega)r_b t_c t_{\text{int}} e^{2q} e^{2i\Omega\tau} + n_x^c(\Omega)t_b e^q e^{i\Omega\tau} + n_x^{\text{int}}(\Omega)r_{\text{int}}}{1 - r_c r_b t_{\text{int}} e^{2q} e^{2i\Omega\tau}}. \quad (6.11)$$

The threshold value represents the condition, at which the gain becomes larger than the total loss: leaking through the coupler transmission and the round trip loss. This condition is defined by setting the denominator equal to zero, and is reached when

$$e^{2q} = \frac{1}{r_c r_b t_{\text{int}}}. \quad (6.12)$$

It is straightforward to see from Eq.(6.8) that at the threshold parametric gain, without detection loss, the noise is fully suppressed on resonance: $S_n(0) = 0$, which corresponds to infinite squeezing. At the same time, the signal is only reduced by a factor of 4 in this limit. As expected, the SNR is increased.

6.2.2 Maximal squeeze factor inside the cavity

It is well-known that there is a limitation to the amount of squeezing (and signal deamplification) inside the cavity [168, 169]. Since this limitation on the signal deamplification is crucial for our consideration — the difference between the signal and noise behavior allows to increase the SNR — I demonstrate this limitation explicitly.

Inside the cavity, the squeezing spectrum of the phase quadrature is (in the assumption of the sideband frequency being much smaller than the cavity FSR):

$$S^{\text{in}}(\Omega) = \frac{r_c^2 r_{\text{int}}^2 + t_c^2 + r_c^2 t_b^2 t_{\text{int}}^2 e^{-2q} + t_c^2 r_b^2 r_{\text{int}}^2 t_{\text{int}}^2 e^{-4q}}{(1 - r_c r_b t_{\text{int}}^2 e^{-2q})^2 + 4e^{-2q} r_c r_b t_{\text{int}}^2 \Omega^2 \tau^2}. \quad (6.13)$$

At the threshold, in the limiting case $r_{f,b} \rightarrow 1$, $r_{\text{int}} \rightarrow 0$, the amount of squeezing approaches

$$S^{\text{in}}(0)/S^{\text{in}}(0)_{q=0} \rightarrow \frac{1}{4}, \quad (6.14)$$

which is what we call the 6 dB squeezing limit. On the other hand, in some literature one can find 3 dB as the intra-cavity limit for squeezing. This limit refers to the maximal reduction in the noise variance of the cavity mode. Indeed, by integrating the spectrum (6.13) over the full frequency range and applying the same limits one finds the value of 1/2 as a limit.

6.2.3 Single-mode approximation

The expression for the spectral density (6.8) and signal transfer function (6.10) can be simplified by making the standard single-mode approximation. The amplitude transmissivities of the coupling and the back mirrors, as well as the internal loss, are much smaller than unity, and we can approximate correspondingly $r_{c,b} \approx 1 - t_{c,b}^2/2$ and $t_{\text{int}} \approx 1 - r_{\text{int}}^2/2$; the squeezing factor q is much smaller than unity, so we can approximate $e^q \approx 1 + q$; the frequency of interest is much smaller than the FSR of the cavity $\Omega \ll 1/2\tau$, which enables us to make a Taylor expansion: $\cos \Omega\tau \approx 1 - \Omega^2\tau^2/2$.

We define three quantities that influence the cavity bandwidth: cavity decay rate through the coupling mirror, squeezing rate and the round-trip optical loss rate, correspondingly:

$$\gamma_c = \frac{ct_c^2}{4L}, \quad \gamma_s = \frac{qc}{L}, \quad \gamma_l = \frac{cl^2}{4L}, \quad (6.15)$$

where $l^2 = r_{\text{int}}^2 + t_b^2$ is the total loss inside the cavity. We can define the common bandwidth for the noise and signal transfer functions: $\Gamma = \gamma_c + \gamma_s + \gamma_l$.

Taking into account the single-mode approximation, and the newly defined bandwidth contributions, we can simplify Eqs.(6.8), (6.10) to

$$S_n(\Omega) \approx 1 - \frac{4\gamma_c\gamma_s}{\Gamma^2 + \Omega^2}\eta, \quad (6.16)$$

$$|T(\Omega)|^2 \approx \frac{8\pi P_c}{\hbar\lambda L} \frac{\gamma_c\eta}{\Gamma^2 + \Omega^2}, \quad (6.17)$$

where $\eta = 1 - t_{\text{det}}^2$ is the detection efficiency. The ratio between these quantities constitutes the signal-to-noise ratio

$$\frac{|T(\Omega)|^2}{S_n(\Omega)} = \frac{8\pi P_c}{\hbar\lambda L} \frac{\gamma_c \eta}{\Gamma^2 - 4\gamma_c \gamma_s \eta + \Omega^2}. \quad (6.18)$$

It's peak value $\mathcal{S} \equiv |T(0)|^2/S_n(0)$ and bandwidth \mathcal{B} are given by

$$\mathcal{S} = \frac{8\pi P_c}{\hbar\lambda L} \frac{\gamma_c \eta}{\mathcal{B}^2}, \quad (6.19)$$

$$\mathcal{B} = \sqrt{\Gamma^2 - 4\gamma_c \gamma_s \eta}. \quad (6.20)$$

The sensitivity-bandwidth product naturally emerges from computing the integrated sensitivity:

$$\rho = \int_0^{\omega_{\text{FSR}}} \frac{|T(\Omega)|^2}{S_n(\Omega)} d\Omega \approx \mathcal{S} \times \mathcal{B}, \quad (6.21)$$

where ω_{FSR} is a free spectral range of the cavity.

The standard sensitivity-bandwidth limit is defined for the absence of internal squeezing and internal loss (i.e. $\gamma_{s,l} = 0$):

$$(\mathcal{S} \times \mathcal{B})_{\gamma_s=0} = \frac{8\pi P_c}{\hbar\lambda L} \quad (6.22)$$

The internal squeezing enhances the sensitivity-bandwidth product beyond the standard limit by:

$$(\mathcal{S} \times \mathcal{B})/(\mathcal{S} \times \mathcal{B})_{\gamma_s=0} = \frac{\gamma_c + \gamma_l}{\mathcal{B}}. \quad (6.23)$$

In a more general case, when the single-mode approximation is not valid (like in our experiment), a better way to demonstrate the enhancement is to compute the integrated sensitivity ρ directly from Eqs. (6.8), (6.10).

6.3 Experimental demonstration

6.3.1 Experimental setup

In our proof-of-principle experiment, the signal was generated by injecting a phase modulated field from the back of the Fabry-Perot cavity with the optical

parametric amplifier inside. In terms of signal detection and observation of the internal squeezing effect, this approach was viewed as a one-to-one analogy to a detector with a movable end mirror sensitive to the external force. The advantage of our approach was that it allowed for signal generation in a broad frequency band, which was necessary to observe the change in the detection bandwidth.

The experimental setup, shown in Fig. 6.4 consisted of a second harmonic generation cavity (SHG), producing 775 nm light for optical-parametric amplification of the longitudinal resonance at 1550 nm of our internal squeezing cavity (ISC). The cavity had an optical length of $L = 3.69$ cm, an optical linewidth (half-width at half maximum) of $\gamma_c \sim 2\pi \times 54$ MHz, and contained a periodically poled KTP (PPKTP) crystal [106]. A control field at 1550 nm with a phase-modulation signal imprinted on it was injected from the highly reflective back side of the ISC. The signal was produced by the broadband fiber electro-optical modulator (EOM). The cavity length was stabilized via the Pound-Drever-Hall (PDH) locking technique [46, 47]. The ISC had two locking modes — with and without the pump light. When the measurements with squeezing were taken, the cavity length was stabilized with 775 nm light, while the 1550 nm control field was used to stabilize the squeezing angle in the phase quadrature. When the measurements without squeezing were taken, the 775 nm pump was turned off, and the cavity length was stabilized with the 1550 nm control field. Between consecutive measurements, the system was out of lock, and had to be brought to the optimal working point for the new measurement, which caused some variations in data. The signal with and without squeezing was detected with a high-efficiency broadband homodyne detector with a bandwidth of ~ 800 MHz and dark noise clearance of ~ 13 dB in the frequency range of interest from 10 to 200 MHz. The homodyne detector had an electrical high-pass, which prevented it from detecting squeezing at very low frequencies. The maximal squeezing observed was around 6.8 dB below shot noise level. The full spectrum is shown in Fig. 6.5. The main limitation to the squeezing level came from the detection efficiency, which was estimated to be 82-86% for different measurement sets. The total detection loss had contributions from the quantum efficiency of the photodiodes in the homodyne detector, mode mismatch between the local oscillator beam and the squeezed mode, and propagation losses in various optical elements.

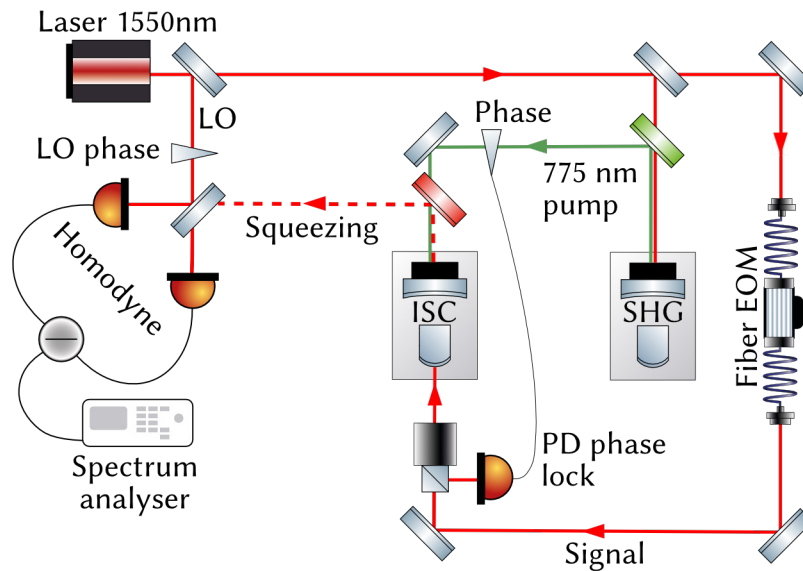


Fig. 6.4. Experimental setup — The internal squeezing cavity (ISC) was resonant for both the fundamental wavelength 1550 nm and the second harmonic wavelength 775 nm used for pumping the nonlinear crystal. The pump was generated in a second harmonic generation (SHG) cavity. Through the highly reflective back mirror, a beam at 1550 nm was injected, carrying a phase modulation signal between 5.5 to 151 MHz and phase modulation sidebands at 54 MHz for Pound-Drever-Hall (PDH) cavity length stabilization (not shown in the picture), both generated by the fiber EOM. The output signal, consisting of squeezed light and the deamplified signal sideband, was detected on a balanced homodyne detector using 2.8 mW local oscillator (LO) power, with an overall detection efficiency of $\sim 85\%$. The phase of the local oscillator was actively stabilized to the phase quadrature and the phase of the pump was stabilized to produce squeezing in this quadrature.

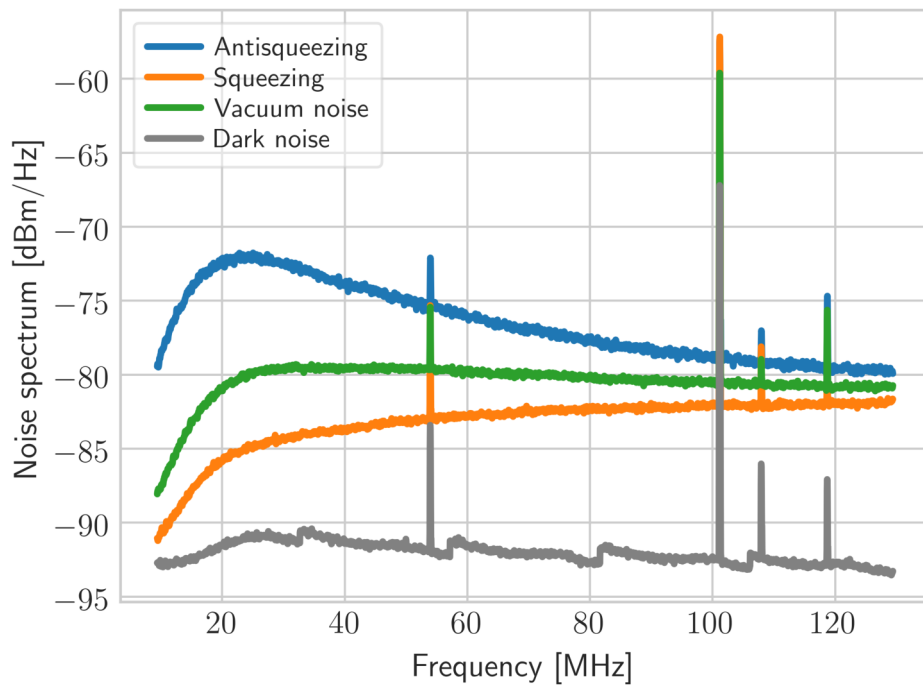


Fig. 6.5. Noise spectral densities measured on the homodyne detector: squeezing (orange), anti-squeezing (blue), vacuum (green) and dark (grey) noises. The reduction below 20 MHz was due to the high-pass in the homodyne circuit board. Peaks at 53, 101, 108, 119 MHz were electronic pickups from the environment, in particular from frequency generators used to produce control signals. Jumps in the dark noise around 34, 58, 82, 106 MHz were due to the spectrum analyzer sampling.

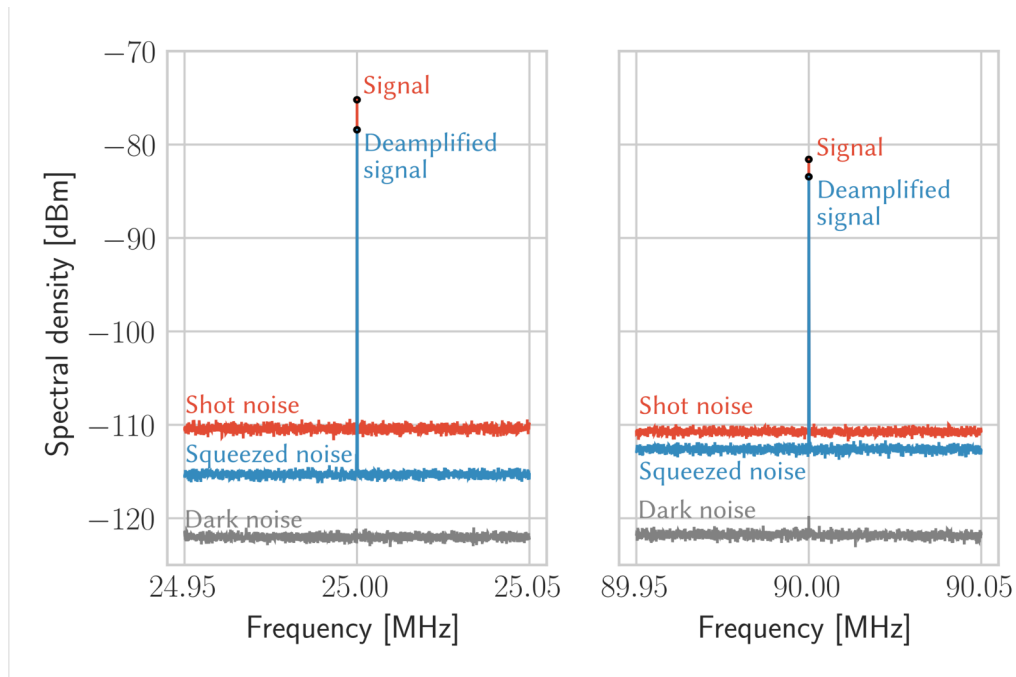


Fig. 6.6. Example of experimental data. Signal and shot noise were measured on the homodyne detector. When the pump of the ISC was switched on, the quantum noise was squeezed and the signal was deamplified. At low frequencies, within ISCs' bandwidth (left plot), squeezing and deamplification were stronger than at high frequencies outside the bandwidth (right plot). The dark noise of the homodyne detector was not limiting the measurement precision.

Measured noise suppression was compared to the signal deamplification. We created a phase modulation signal at different frequencies. At each frequency, we detected the signal together with the noise on the homodyne detector, in two regimes: with the optical parametric amplification being on and off. The noise was detected over a narrow frequency band around the signal frequency, see Fig. 6.6, and then averaged over this band to obtain an estimate of the squeezing level for this signal frequency. This allowed us to observe how the signal got deamplified and the noise got squeezed. The combined spectra with signal can be seen in Fig. 6.7.

From the squeezing spectrum, we estimated the experimental parameters: squeezing factor q , transmissivity of the coupling mirror t_c , internal loss l^2 and detection efficiency η . The fitted upper bound on the internal loss, $l^2 \leq 2300$ ppm, resulted in a round-trip loss bandwidth of $\gamma_l \leq 2\pi \times 743$ kHz $\ll \gamma_c$. This value

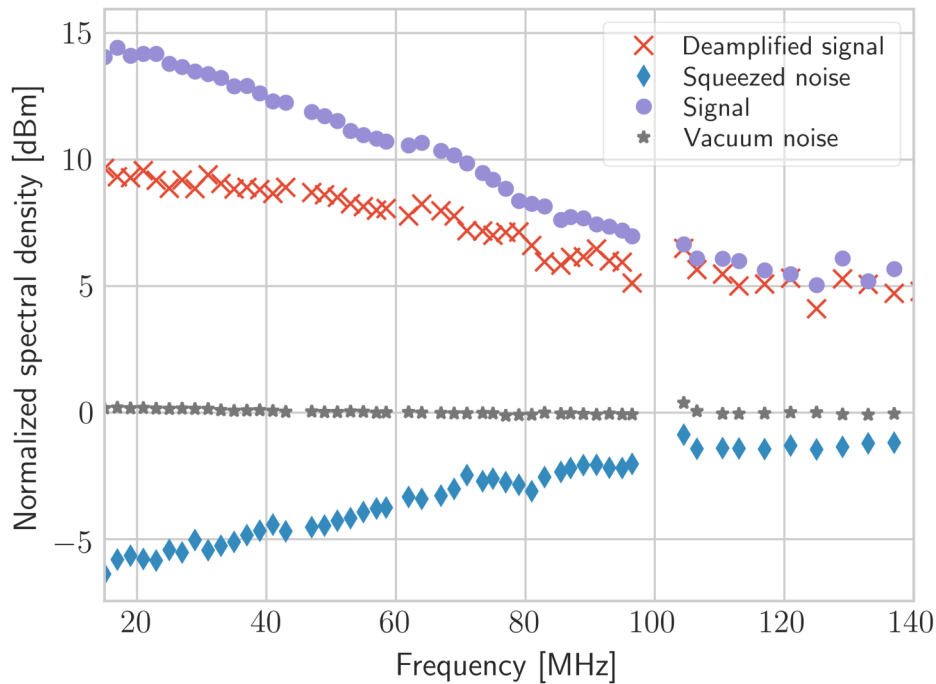


Fig. 6.7. Signal and noise measurements. Every point corresponds to a set of data as in Fig. 6.6, and was normalized to the vacuum noise level and the electrical transfer functions, with subtracted dark noise. The signal was suppressed at high frequencies due to the cavity bandwidth, which was the origin of the sensitivity-bandwidth limit. When the ISC generated squeezing, it also deamplified the signal, but the signal deamplification was weaker than the noise suppression, which allowed to gain in the SNR. The gain was strong at low frequencies within ISC bandwidth, and reduced at high frequencies.

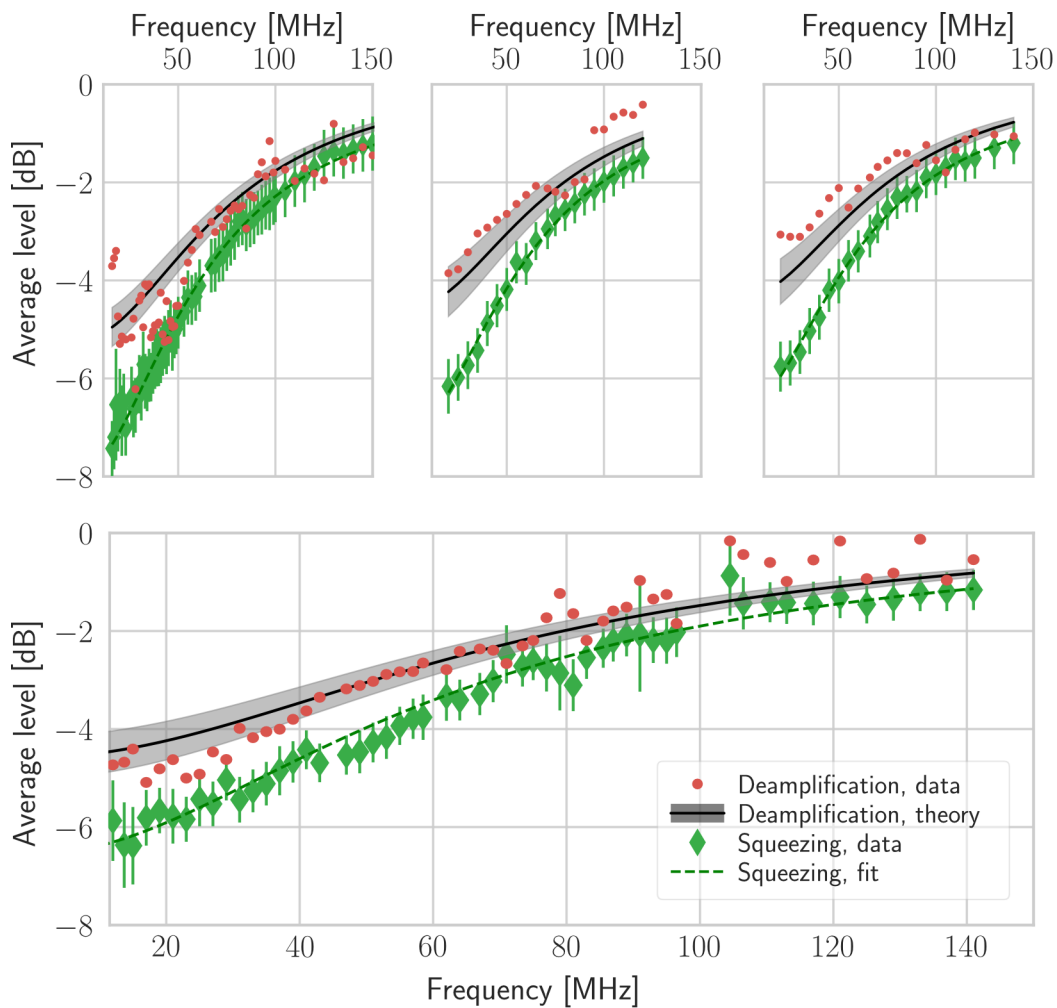


Fig. 6.8. Beating the standard sensitivity-bandwidth limit with internal squeezing. In the plots, we demonstrate the increase in the signal-to-noise ratio for different total quantum efficiencies of $\eta = 0.86, 0.85, 0.84, 0.82$. The squeezing data (green rhombus) was fit with a theoretical curve (green dashed line), and the parameters of the system were estimated from the fit. The signal deamplification is represented by the red dots. It is compared to the results of the theoretical modeling (black solid line) with parameters obtained from the squeezing measurement, where the gray area represents the confidence interval based on the estimation error. The difference between the two data sets directly demonstrates the increase in the SNR, corresponding to enhancements of (36%, 33%, 31%, 26%) in the sensitivity-bandwidth product beyond the standard limit, depending on the detection efficiency η . The data for signal deamplification suffered from instabilities in the setup (since every point required re-locking the setup twice) and only after optimizing the setup and exchanging the homodyne detector electronics the last data set (bottom plot) was more stable at a price of reduced efficiency. This data set was selected for the publication [70].

was consistent with the previously measured absorption of a PPKTP crystal [207], and the manufacturer-specified transmissivity of the back mirror ($t_b^2 = 0.05\%$ at 1550 nm) and bound on the anti-reflective coating of the crystal ($r^2 < 0.1\%$). The coupling mirror transmissivity of $t_c^2 = 15\%$ at 1550 nm was confirmed by an independent measurement of the cavity finesse. The detection loss estimation was also bounded within 1% of the estimated value by comparing squeezing and anti-squeezing spectra [106, 107]. We used these estimated parameters to calculate the expected theoretical spectrum of the signal deamplification and compared it with the measured values. The details on the experimental setup for squeezed-light generation can be found in the thesis of Lisa Kleybolte [208].

Fig. 6.8 compares noise squeezing with signal deamplification for different detection efficiencies. The difference between the squeezing and deamplification curves directly represents the gain in the SNR at a given frequency. We collected four data sets. First, three with one homodyne detector, which had slightly higher detection efficiency, but was prone to electronic instabilities caused by control signals. As a result, the data had more spread. For the final set of data, we used another homodyne detector with better stability but slightly lower detection efficiency. For this set, we found the theory to be in good agreement with the experimental data, lying within the confidence interval obtained from the parameter estimation error. We ascribe the observed discrepancies to the electronic resonances in the homodyne circuitry and wires that were not taken into account in the theoretical analysis.

The experimentally achieved enhancement factors (36%, 33%, 31%, 26%) represented four different overall detection efficiencies $\eta = 0.86, 0.85, 0.84, 0.82$.

6.3.2 Data analysis

Unlike squeezing spectrum, the data for signal deamplification had a rather significant spread. It was also difficult to collect sufficient statistics on the signal strength, since every measurement would require a time-consuming re-locking the system. As a result, every data point for the signal was a single random sample out of statistical distribution for the fluctuating signal strength. Inferring any experimental parameters, like the SNR, by fitting the theory curve into data would yield highly uncertain results. Instead, our approach was to use the independently

estimated parameters of the system, to plot the theoretical prediction for what the signal deamplification should be, and to compare the experimental data with this prediction. Most of the parameters could be measured independently, except for the internal gain and internal loss values. To obtain these values, we used the fit of measured squeezing spectrum with these two parameters as fitting parameters. Squeezing was more stable and reproducible, and allowed to compute an average level and a standard deviation for values around every signal frequency. We collected this statistics and then propagated the errors from parameter estimation to the theoretical model for the signal deamplification. This allowed to compute the confidence intervals for the model, and see that the experimental data was within these intervals.

The full procedure went as follows. First, the data in a small frequency span of 100 kHz around every signal frequency was processed for removing any spurious spikes higher than 3σ above the average in a small running window. The dark noise was subtracted and data was normalized to the resolution bandwidth. Then, the signal was corrected for the EOM transfer function to ensure that the signal strength was equal for every frequency. The signal level was obtained as the peak point, and the noise level as the average of the noise over the small range around the peak. While, in general, due to the cavity bandwidth, the noise has a slope and such estimate could be biased, the frequency span of choice (100 kHz) was much smaller than the bandwidth of the ISC (~ 60 MHz), so the effect was negligible. The average value of squeezed shot noise (S) after subtracting the dark noise (D) and normalizing to vacuum noise (V) and its variance is:

$$S_v = \frac{S - D}{V - D}, \quad (6.24)$$

$$\begin{aligned} \Delta^2 S_v = & (V - D)^{-2} \Delta^2 S + S_v^2 (V - D)^{-2} \Delta^2 V + \\ & + (S_v - 1)^2 (V - D)^{-2} \Delta^2 D + \\ & + 2(S_v - 1)(V - D)^{-2} \text{cov}(D, S) - \\ & - 2S_v(S_v - 1)(V - D)^{-2} \text{cov}(D, V), \end{aligned} \quad (6.25)$$

where $\Delta^2 S$, $\Delta^2 V$, $\Delta^2 D$ are the experimental variances of not-normalized shot, vacuum and dark noises, and $\text{cov}(D, S)$, $\text{cov}(D, V)$ are the covariances between the corresponding noise traces. For every measurement frequency, the corresponding

average values and variances were calculated and used for fitting the theoretical squeezing curve into this data using the least squares algorithm. From the fit, the values of front mirror transmissivity, single-pass gain, internal losses and detection losses were obtained.

The theoretical prediction for the signal was based on the best-fit parameter set obtained from the squeezing values. In order to account for estimation and measurement uncertainties, the most credible region for the signal was computed by performing a Monte-Carlo simulation [209]. For that purpose, at every frequency, a random value for the squeezing level was sampled from a normal distribution centered around the average, with the variance being the sum of the residuals from the fit and the measured variance (6.24). For the new set of generated data a new fit was computed, with a new set of parameters. The process was repeated 1000 times, resulting in a distribution for a set of parameters. This distribution was averaged, and the standard deviations for every parameter was calculated. Then these average parameters were used to compute the theoretical predictions, and the standard deviations allowed to set the confidence interval for this prediction. The confidence interval was computed by performing the bounded optimization for the squeezing and signal shapes to obtain the minimal and maximal possible curves given the parameters' standard deviations as bounds.

As a result, I obtained a theoretical prediction for the signal deamplification that was based solely on the parameters from the squeezing fit. This prediction was independent of the quality of the signal data, which varied due to the instabilities in the system and the necessity to re-lock it for every measurement, which resulted in unavoidable drifts. Despite that, the data mostly fell within the confidence intervals for the theoretical prediction.

Finally, the enhancement factor to the sensitivity-bandwidth product was computed by numerically integrating the signal-to-noise ratios (and comparing it to the sensitivity-bandwidth product as obtained from fit parameters).

6.4 Discussion and outlook

In summary, this chapter serves as the introduction to internal squeezing approach to quantum metrology. QCRB and the energetic quantum limit allow to

gain a new intuition into the ways of achieving a better sensitivity. The insight about the necessity to increase the amplitude fluctuations on the mirrors is especially useful: it allows to approach the experimental design from a different perspective. For the cavity-enhanced detectors, the sensitivity-bandwidth product provides a convenient value to judge the possible enhancement to the sensitivity. It also provides a unified view of three different non-classical concepts for improving the quantum measurement noise limited sensitivity of cavity-enhanced laser interferometers. All of them can be seen as concepts of beating the standard sensitivity-bandwidth limit, which is unsurpassable without using quantum states of light. Two of these concepts: “white-light cavity” and “external squeezing”, have been investigated intensively in recent years for the improvement of gravitational-wave detectors [134, 202, 206]. The third concept, “internal squeezing”, is investigated here, theoretically as well as experimentally, and also with the intention of improving gravitational-wave detectors. We presented the first experimental demonstration of beating the standard sensitivity-bandwidth limit with internal squeezing.

The most mature quantum enhancement concept is external squeezing, and it is already implemented in all gravitational-wave detectors [41, 44, 45]. Since it avoids any deamplification of the signal and squeezes shot noise in a broadband way, it provides larger improvement to the sensitivity-bandwidth product than the internal squeezing does. However, external squeezing is more sensitive to intra-cavity losses than internal squeezing. This can be understood in the limiting case when the cavity’s round trip loss equals the coupler’s transmissivity. In this case, the cavity is impedance matched for external squeezing and no squeezing gets reflected off the coupling mirror. By contrast, in the internal squeezing case, only half of the squeezing produced inside the cavity is lost through the back mirror. The other half is coupled out through the front mirror, resulting in a maximal measurable squeeze factor of 3 dB. I discuss the consequences of that for quantum limits in the next chapter.

The consideration presented in this Chapter focused on a detector based on a single cavity. This approach can be generalized for a cavity-enhanced laser interferometer. In particular, quantum noises in a gravitational-wave detector, which is tuned to a *signal-recycling* (narrow-band) mode, can be described by the equations for a single cavity [196]. Therefore the results of this section can be

considered as a proof-of-principle for such signal-recycled detector. Currently the detectors operate in a *signal-extraction* (broadband) mode, which results in a different effect of internal squeezing. I compare the two cases in details in Chapter 8. From a practical perspective, when implementing the internal squeezing concept in gravitational-wave detectors, the nonlinear crystal would have to be placed in the dark output port, between the central beamsplitter and the signal-extraction mirror [210]. More details about the implementation of the internal squeezing are discussed in Chapters 8,9.

Ultimately, internal squeezing serves as a tool that allows to take advantage of the quantum noise, and it works best in combination with external squeezing, as I show in the next chapters.

Analysis of compensation of quantum decoherence with internal squeezing

Quantum states of light are very fragile, and even a small amount of decoherence can significantly reduce the effect they have on a system. In optics the main source of decoherence is optical loss, leading to a fraction of the quantum state being lost and replaced by vacuum. While modern metrological devices benefit from the best optical components, they are never devoid of some loss. For squeezed light, this loss directly leads to a reduced suppression in the shot noise of the laser.

It was theorized by Miao *et al.* [211] that while QCRB is the ultimate limit on measurement precision, there exists another limit, caused by quantum decoherence. In this chapter, I build up on this work, and show that internal squeezing allows to surpass this proposed limit. Instead, I show that there exists another lower limit, and make a connection to the previously established limit by Miao *et al.* I demonstrate how the optimal choice of internal gain allows to compensate part of the decoherence.

Optical loss can occur in several places: inside the detector's cavity, which I call *internal* loss; on the path from the cavity to the photodetectors, including the photodetection inefficiency, which I call *detection* loss; in the case of additionally injected external squeezing — *injection* loss, which destroys the purity of the injected state. I make an argument that internal loss is most fundamental and defines the ultimate limit to the sensitivity. Detection loss, on the other hand, can be mostly compensated by appropriate optimization of the internal gain. The notion of optimal internal gain was proposed in [70, 71], and here I study it in more detail. Counter-intuitively, I show that in some cases it is optimal not to

squeeze the noise inside, but to amplify it instead. At first glance, this defies the QCRB logic, but I show that in fact there is no contradiction.

The discussion in this chapter goes beyond purely methodological study of the quantum limits, and allows to re-think the approach to the experimental design of cavity-enhanced metrological devices. In particular, many devices that use weakly nonlinear materials in their cavities (such as whispering-gallery-mode resonators [212–214]) and have large losses that prevent them from using external squeezing efficiently, can benefit even from weak internal squeezing for increasing the sensitivity.

7.1 Quantum limit from decoherence

7.1.1 Physical picture

I start with presenting an physical argument for the existence of an optimal internal squeeze factor. The optimal point in internal squeezing exists for every combination of experimental parameters, and this point can be well below the threshold value.

Consider the following simple argument. The maximal detectable squeeze factor is bounded by the amount of optical loss. The loss of squeezing can be seen as mixing with vacuum [215]. Therefore, above a certain value, the increase in squeezing is not detectable any more. However, the signal deamplification is independent of the detection loss, and has weaker dependence on the internal loss. Therefore, increasing the internal gain above a certain level deamplifies the signal, but does not suppress the shot noise further (since it is limited by loss). As a result, above this level the signal-to-noise ratio drops. This level corresponds to the optimal internal squeezing. It is also useful to look at this level from a different perspective.

Consider the example of detecting some signal G embedded in squeezed vacuum with a squeeze factor r . The detected signal and noise includes the effect of detection efficiency η :

$$S = \eta(e^{-2r} + G^2) + 1 - \eta, \quad (7.1)$$

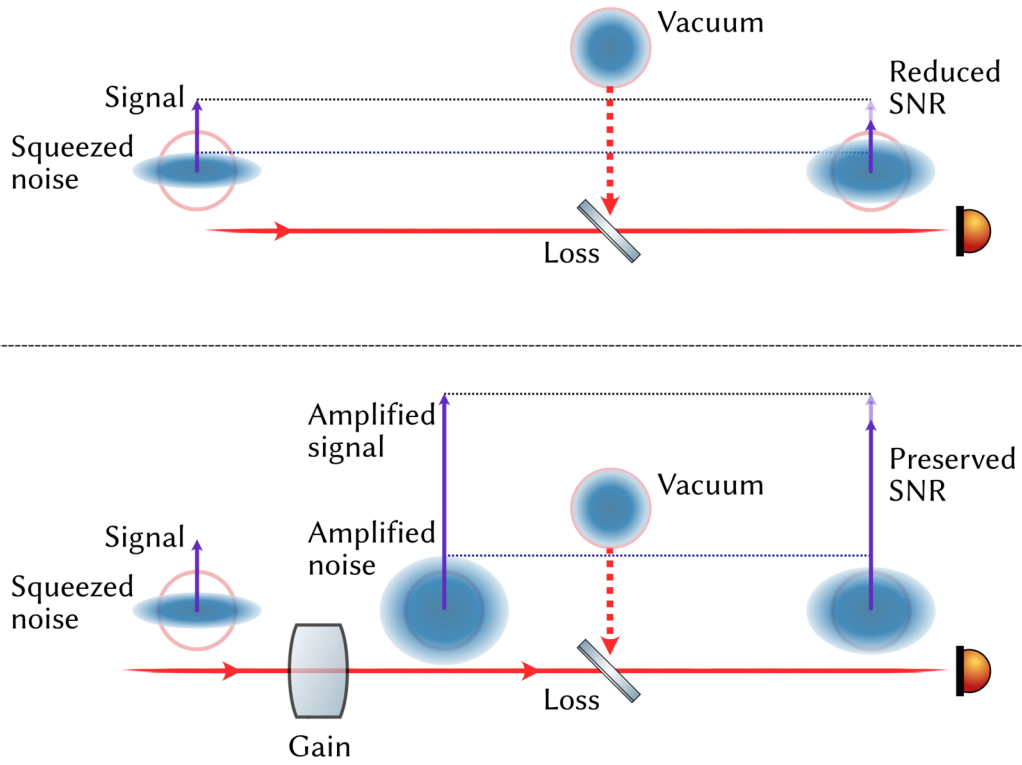


Fig. 7.1. Illustration of optical loss as a cause of reduced SNR and the way to compensate for it. Top: squeezed noise and a signal experience optical loss. The signal is reduced, the noise is increased due to mixing with vacuum. As a result, the SNR is reduced. Bottom: parametric gain amplifies both the signal and the noise above the vacuum uncertainty level. Both of them are affected by optical loss in the same way, since mixing with vacuum does not have a significant effect on the noise. As a result, the SNR is preserved.

such that the SNR is reduced due to the vacuum noise destroying the correlations in squeezed vacuum: $\text{SNR} = \eta (1 - \eta(1 - e^{-2r}))^{-1}$. It was proposed by Caves [66] and recently re-investigated experimentally [216] that the detection loss can be mitigated by parametric amplification of the signal and noise before detection. The idea of this approach is to amplify both the signal and the noise by the same amount before it experiences loss, such that the resulting noise is much above vacuum uncertainty, and the loss does not affect it significantly. Consider the same signal as above, but now with an additional amplification of the signal and noise by a factor e^q :

$$S_q = \eta(e^{-2r} + G^2)e^{2q} + 1 - \eta, \quad (7.2)$$

The SNR is given by $\text{SNR} = \eta e^{2q} (1 - \eta(1 - e^{-2r} e^{2q}))^{-1}$. Without amplification, $q = 0$, in the limit of large squeezing, $e^{-2r} \approx 0$, the SNR is limited to $\text{SNR}_{q=0} \leq \eta(1 - \eta)^{-1}$. When the amplification is moderate, $q = r$, the SNR scales linearly with loss and amplification: $\text{SNR}_{q=r} = \eta e^{2r}$. When the amplification is large, $q \rightarrow \infty$, the SNR becomes independent on the loss: $\text{SNR}_{q \rightarrow \infty} = e^{2r}$, and only benefits from initial squeezing.

This parametric amplification generally does not have to occur outside the detector. In fact, if the external squeezing is injected into the detector, internal squeezing can serve as such parametric amplifier for avoiding the detection loss. There is a subtle point there, because the internal squeezing, unlike the original proposal, operates in the loop of the optical cavity, and acts on the signal and external squeezing differently. However, I will exploit exactly this concept to derive the new decoherence-induced quantum limit, updating the results of Miao *et al.* [211].

7.1.2 Computing the decoherence-induced limit

In order to compute the new decoherence-induced limit, I start with the model of internal squeezing described in the previous chapter, in Eqs. (6.10),(6.8). I proceed to apply the single-mode approximation as in Chapter 6.2.3, but write the equations in a slightly different notation, in order to more directly compare the results to [211]: $\epsilon_{\text{int}} = r_{\text{int}}^2$, $\epsilon_{\text{ext}} = r_{\text{det}}^2$, $t_b = 0$, $T_c = t_c^2$. For the demonstration purposes I limit the analysis here to the case of a tuned cavity, while it's straightforward

to generalize it to the detuned case without adding substantially new physical insights. I assume the external squeezing is injected into the cavity, with the spectral density $S_{vv} = e^{2q_{\text{input}}}$. With these assumptions, I obtain the noise spectral density:

$$S_n(\Omega) = 1 - \frac{16qT_c(1 - \epsilon_{\text{ext}})}{(4q + T_c + \epsilon_{\text{int}})^2 + 16\Omega^2\tau^2} - \frac{(1 - e^{-2q_{\text{input}}})(1 - \epsilon_{\text{ext}})((4q - T_c + \epsilon_{\text{int}})^2 + 16\Omega^2\tau^2)}{(4q + T_c + \epsilon_{\text{int}})^2 + 16\Omega^2\tau^2} \quad (7.3)$$

and the signal transfer function:

$$|T(\Omega)|^2 = \frac{8\pi P_c}{\hbar\lambda c} \frac{4T_c(1 - \epsilon_{\text{ext}})}{(4q + T_c + \epsilon_{\text{int}})^2 + 16\Omega^2\tau^2} \quad (7.4)$$

For simplicity, I first consider a low-frequency case: $\Omega \approx 0$, and compute different limiting cases and which limits they lead to. First I compute the QCRB, which is a lossless case, $\epsilon_{\text{int}} = 0$, $\epsilon_{\text{ext}} = 0$:

$$S_{hh}^{\text{QCRB}} = \frac{\hbar c^2}{32P_c\omega_0 L^2} \frac{e^{-2q_{\text{input}}}(T_c - 4q)^2}{4T_c}, \quad (7.5)$$

where I normalized the sensitivity to the GW strain $h_0 = x/L$. Notably, in the lossless case the sensitivity becomes unlimited, $S_{xx}^{\text{QCRB}} = 0$, at the parametric threshold: $q = T_c/4$.

Clearly, optical losses will prevent from achieving the QCRB. It is therefore possible to compute the new limit S_{hh}^ϵ , induced by the losses. One way of doing it is to follow Miao *et al.* [211] and assume that this this limit will be additive to the QCRB, i.e. $S_{hh}^{\text{min}} \approx S_{hh}^{\text{QCRB}} + S_{hh}^\epsilon$. However, this approximation does not hold in all experimental settings. In order to account for a broader range of experimental parameters, it is useful to directly minimize the full spectral density S_{hh} and then compare it to the QCRB. I show below that choosing the optimal internal gain allows to surpass the limit S_{hh}^ϵ .

First, I consider several limiting cases for the internal squeezing at threshold regime: $q_{\text{th}} = (T_c + \epsilon_{\text{int}})/4$. It is important that unlike Miao *et al.* [211], I don't assume the smallness of external loss η_{ext} and also keep the possibility of the front mirror's transmission to be on the same order as internal loss (thus the threshold

is slightly different). I compute the sensitivity limits in the two ultimate cases: without input squeezing, and with infinite input squeezing:

$$S_{hh}^\epsilon(q_{\text{input}} = 0) = \frac{\hbar c^2}{32P_c \omega_0 L^2} \frac{1}{1 - \epsilon_{\text{ext}}} \left(T_c \epsilon_{\text{ext}} + \epsilon_{\text{int}} + \frac{\epsilon_{\text{int}}^2}{4T_c} \right), \quad (7.6)$$

$$S_{hh}^\epsilon(q_{\text{input}} \rightarrow \infty) \rightarrow \frac{\hbar c^2}{32P_c \omega_0 L^2} \frac{1}{1 - \epsilon_{\text{ext}}} \left(T_c \epsilon_{\text{ext}} + \epsilon_{\text{int}} + \frac{\epsilon_{\text{ext}} \epsilon_{\text{int}}^2}{4T_c} \right). \quad (7.7)$$

Notice, that in the case of small detection loss I recover the limit in [211]. The limit with infinite input squeezing is strictly lower than the limit without input squeezing (notice the factor $\epsilon_{\text{ext}} < 1$ in front of the last term in the equation above).

For future comparison it is also useful to consider the case without internal squeezing, $q = 0$:

$$S_{hh}^\epsilon(q = 0, q_{\text{input}} = 0) = \frac{\hbar c^2}{32P_c \omega_0 L^2} \frac{1}{1 - \epsilon_{\text{ext}}} \times \left(\frac{T_c}{4} \epsilon_{\text{ext}} + \frac{1}{2} \epsilon_{\text{int}} + \frac{\epsilon_{\text{int}}^2}{4T_c} \right), \quad (7.8)$$

$$S_{hh}^\epsilon(q = 0, q_{\text{input}} \rightarrow \infty) \rightarrow \frac{\hbar c^2}{32P_c \omega_0 L^2} \frac{1}{1 - \epsilon_{\text{ext}}} \times \left(\frac{T_c}{4} \epsilon_{\text{ext}} + \frac{2 - \epsilon_{\text{ext}}}{2} \epsilon_{\text{int}} + \frac{\epsilon_{\text{ext}} \epsilon_{\text{int}}^2}{4T_c} \right). \quad (7.9)$$

It is interesting to note that in the case without internal squeezing the limit is 4 times lower than in the case with at-threshold internal squeezing. This occurs due to 6 dB of signal deamplification in the case of internal squeezing at threshold. This does not mean that internal squeezing is not useful, since it does lower the QCRB, and thus the total sensitivity S_{hh}^{min} .

However, the maximal benefit to the sensitivity can be obtained by optimizing the total sensitivity S_{hh} with respect to the internal gain. The optimal internal gain q_{opt} allows to reach the optimal sensitivity, which becomes a new sensitivity limit:

$$S_{hh}^{\text{opt}} = \frac{\hbar c^2}{32P_c \omega_0 L^2} \left(\frac{T_c \epsilon_{\text{ext}}}{1 + \epsilon_{\text{ext}} (e^{2q_{\text{input}}} - 1)} + \epsilon_{\text{int}} \right). \quad (7.10)$$

In the absence of external squeezing I achieve:

$$S_{hh}^{\text{opt}}(q_{\text{input}} = 0) = \frac{\hbar c^2}{32P_c \omega_0 L^2} (T_c \epsilon_{\text{ext}} + \epsilon_{\text{int}}) \quad (7.11)$$

which looks like the limit in [211], but it has no assumptions on the detection loss. Notice, that in this case the QCRB is not zero, since the internal squeezer operates below threshold. There's no sense in which it's useful to split this sensitivity into two contributions like $S_{hh}^{\text{opt}} = S_{hh}^{\text{QCRB}} + S_{hh}^{\epsilon}$.

Finally I can compute the ultimate limit for infinite squeezing:

$$S_{hh}^{\text{opt}}(q_{\text{input}} \rightarrow \infty) \rightarrow \frac{\hbar c^2}{32P_c \omega_0 L^2} \epsilon_{\text{int}}. \quad (7.12)$$

This is the ultimate limit to the sensitivity, and it can be significantly lower than S_{hh}^{ϵ} . There are several important conclusions I draw from this section:

- The ultimate limit on the sensitivity is defined only by internal loss;
- This limit is strictly below the previously reported S_{hh}^{ϵ} ;
- In this consideration the input state considered to be pure, *i.e.* there's no injection loss.

In the next section I discuss the physical nature of the new limit, and connect it to the intuitive picture I developed before.

7.2 Optimal gain

It is instructional to see how the optimal internal squeezing depends on the parameters of the system:

$$q_{\text{opt}} \approx \frac{1}{4} \left(-\epsilon_{\text{int}} + T_c \left(1 - \frac{2e^{q_{\text{input}}} \epsilon_{\text{ext}}}{\cosh q_{\text{input}} + (1 - 2\epsilon_{\text{ext}} - 2\epsilon_{\text{int}}) \sinh q_{\text{input}}} \right) \right) \quad (7.13)$$

In the limiting case of infinite input squeezing, where the new limit is achieved, the optimal internal gain is exactly opposite to the threshold value: $q_{\text{opt}} \rightarrow -q_{\text{th}} = -(T_c + \epsilon_{\text{ext}})/4$. This connects to the intuitive picture I presented above. In order

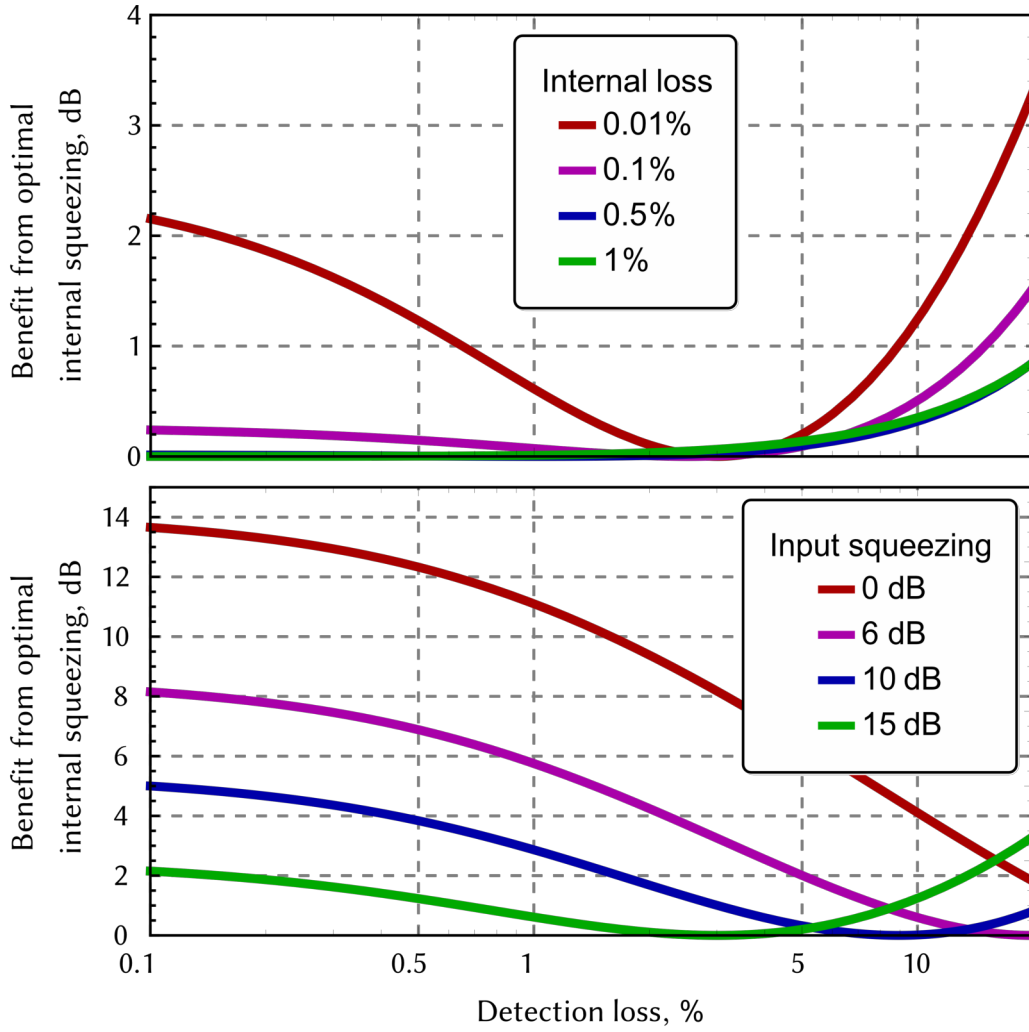


Fig. 7.2. Relative improvement from optimizing the internal squeezing compared to the case without internal squeezing. Top: relative improvement compared as a function of detection loss for different levels of internal loss, for 15 dB external squeezing. Bottom: relative improvement as a function of detection loss for different levels of input squeezing, for $\epsilon_{\text{int}} = 0.001$. For all plots $T_c = 0.01$, $\Omega = 0$.

to avoid the detection loss, one can amplify the signal together with the noise right before the detection, keeping the signal-to-noise ratio intact. Here, internal squeezing acts to fulfill this condition.

In the other case without input squeezing, the optimal gain is:

$$q_{\text{opt}}(q_{\text{input}} = 0) = \frac{1}{4} (T_c (1 - 2\epsilon_{\text{ext}}) - \epsilon_{\text{int}}) = q_{\text{th}} - \frac{1}{2} (T_c \epsilon_{\text{ext}} + \epsilon_{\text{int}}), \quad (7.14)$$

which is clearly below the threshold, but is still above zero for as long as the approximation used for calculation is valid (i.e. relatively small loss and transmissivity). In this case the purpose of internal squeezing is to generate as much squeezing as possible, at the same time keeping the deamplification of the signal as low as possible, given the losses in the system (which connects to the intuitive picture from the previous section).

When input squeezing is nonzero, the optimal internal squeezing reflects a combination of detection loss mitigation and balancing the signal deamplification.

Having gained this insight into the nature of the internal squeezing effect on the sensitivity limit, I explain the relation of the new limit to the QCRB. As I discuss in Chapter 2, the ultimate limit — QCRB — depends on the interaction Hamiltonian between the light and the probe. This Hamiltonian is defined by the properties of light and test mass at the point of interaction. Therefore the state of light would affect the QCRB, but anything that happens upon the detection would not. From this point of view it becomes clear why internal loss sets the ultimate limit, and the detection loss can be avoided. Internal loss destroys the correlations that directly enter the interaction Hamiltonian, and thus has an effect on the QCRB. Detection loss reflects an imperfection in our measurement protocol and thus our inability to reach the QCRB. Internal squeezing cannot have a significant effect on the internal loss (although it does squeeze the vacuum that entered with internal loss on each round trip, but only slightly so), so the main effect it can have is the Caves' parametric amplification for avoiding the detection loss. It might seem counter-intuitive that the optimal internal gain can be full amplification of the phase quadrature, which should reduce the amplitude quadrature, going against the QCRB statement. However, it's important to remember, that the maximal deamplification (in amplitude quadrature in this case) reaches 6 dB inside the cavity, and when the injected squeezing is infinite, it would produce infinite anti-squeezing to the amplitude quadrature, thus fulfilling the requirement for lowering the QCRB.

7.2.1 Benefit of internal squeezing in numbers

First, I demonstrate the benefit of internal squeezing compared to the case without internal squeezing in Fig. 7.2. One can see that the benefit is higher for lower input

squeezing: because then internal squeezing works to generate more squeezing. For higher input squeezing the benefit increases with increased detection loss, since then internal squeezing works to compensate detection loss. Internal loss defines the sensitivity limit, so the higher it is, the smaller is the benefit from internal squeezing. There also exists a detection loss value for which it's optimal not to squeeze internally, since the introduced signal deamplification exactly cancels a potential benefit.

Now, when it's clear that internal squeezing in most cases is beneficial, in Fig. 7.3 I compare it to the limit in [211], *i.e.* with internal squeezing at threshold. As expected from the equations, when the detection loss is small, the effect is negligible (since internal squeezing works best when there is detection loss to compensate). However, as the detection loss and input squeezing increase, the benefit increases, and at the same time it requires less squeezing, quickly transitioning into the amplification regime (negative values for q). For example, already for a detection loss of around 5% (which is smaller than the current loss in gravitational-wave detectors) it becomes optimal to amplify inside (for 15 dB of input squeezing).

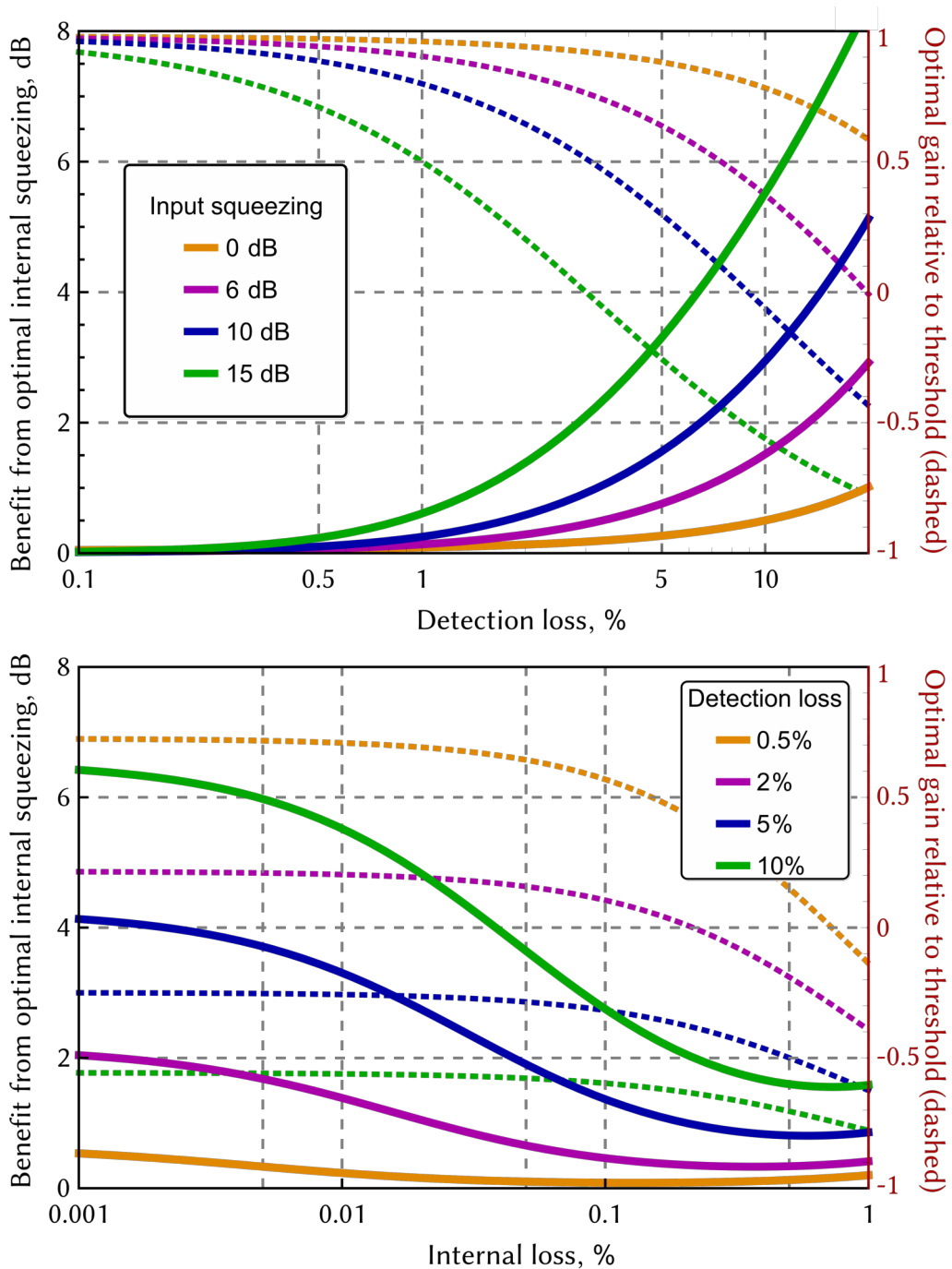


Fig. 7.3. Relative improvement from optimizing the internal squeezing compared to the case of internal squeezing at threshold: the improvement $S_{hh}^{opt}/S_{hh}^\epsilon$ (solid), and the corresponding optimal internal gain relative to the threshold q_{opt}/q_{th} (dashed). (Top) relative improvement as a function of detection loss for different levels of input squeezing, for $\epsilon_{int} = 0.001$; (bottom) relative improvement as a function of internal loss for different levels of detection loss, for 15 dB external squeezing. Internal gain is optimized to squeezing for low losses, but for high losses switches to parametric amplification regime (values below zero). For all plots $T_c = 0.01$, $\Omega = 0$.

7.3 Frequency dependence

In the previous Sections I considered only the effect of internal squeezing on the peak sensitivity. In general, as I explained in the previous Chapter, it is important to also consider the detection bandwidth, and the sensitivity-bandwidth product as a generic measure. Internal squeezing reduces the effective bandwidth of the system, and the higher the squeezing is, the smaller is the bandwidth. However, since the peak sensitivity increases faster, the overall sensitivity-bandwidth product increases too.

In Fig. 7.4, I show the gain in the SNR relative to the case without internal squeezing, and the corresponding reduction in the squeezer's bandwidth, when no input squeezing is present. As in the previous Section, here the clear optimum point is reached for every experimentally detected squeezing level (which in turn corresponds to the internal gain). This theoretical prediction is compared to the experimental values I obtained in the experiment described in Chapter 6.

When input squeezing is added, internal squeezing acts in different ways depending on the loss level, as described in the previous Section. The bandwidth is always smaller than in the case without internal squeezing, but its dependence on the losses is nontrivial. In Fig. 7.5, I show the enhancement relative to the case with input squeezing, demonstrating that the sensitivity can be always enhanced, despite the reduction in bandwidth. I also show the enhancement relative to the SSBL, demonstrating that although the main contribution comes from the input squeezing, internal squeezing helps to gain sensitivity. In this case the bandwidth can also be enhanced in some parameter regimes, due to nontrivial dependence of the bandwidth on losses and squeezing levels.

The reason for input squeezing to have higher contribution to the overall sensitivity gain is the deamplification of the signal due to internal squeezing. Consider the noise suppression of 10 dB both in the case of input and internal squeezing. Input squeezing would result in 10 dB of increased sensitivity. Internal squeezing (at threshold) would result only in 4 dB increase. However, the key difference is the behavior with loss. Ultimately the best sensitivity is given by the optimal combination of input and internal squeezing.

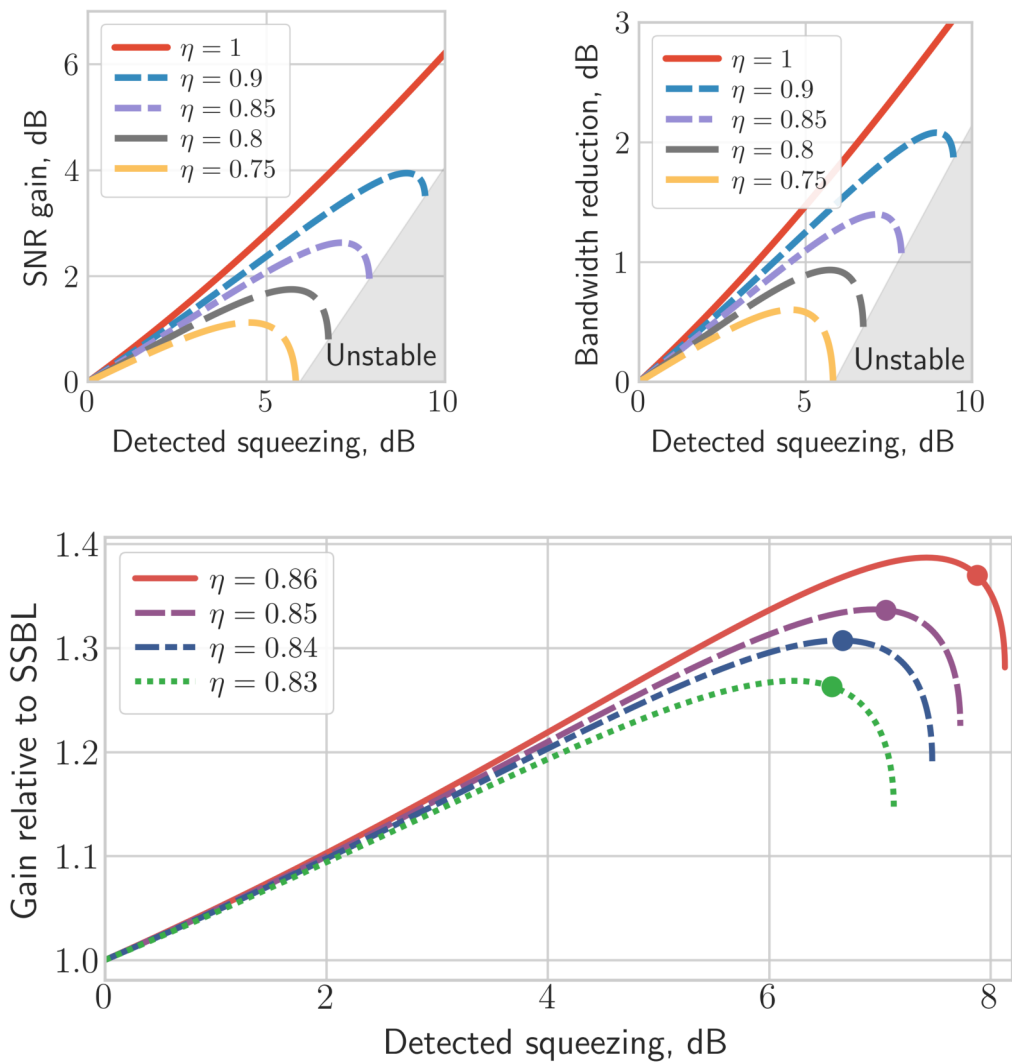


Fig. 7.4. Dependence of the gain in the signal-to-noise ratio (top left) and the reduction in the bandwidth (top right) on the detected squeeze factor. Different plots represent the influence of the detection loss on the enhancement. The existence of an optimal squeezing is demonstrated. The shaded region represents the parametric gains for which the intra-cavity field becomes unstable. (Bottom) the gain in the sensitivity-bandwidth product as a function of detected squeezing for different values of experimental loss factors with experimental points from Chapter 6 (dots on theoretical lines).

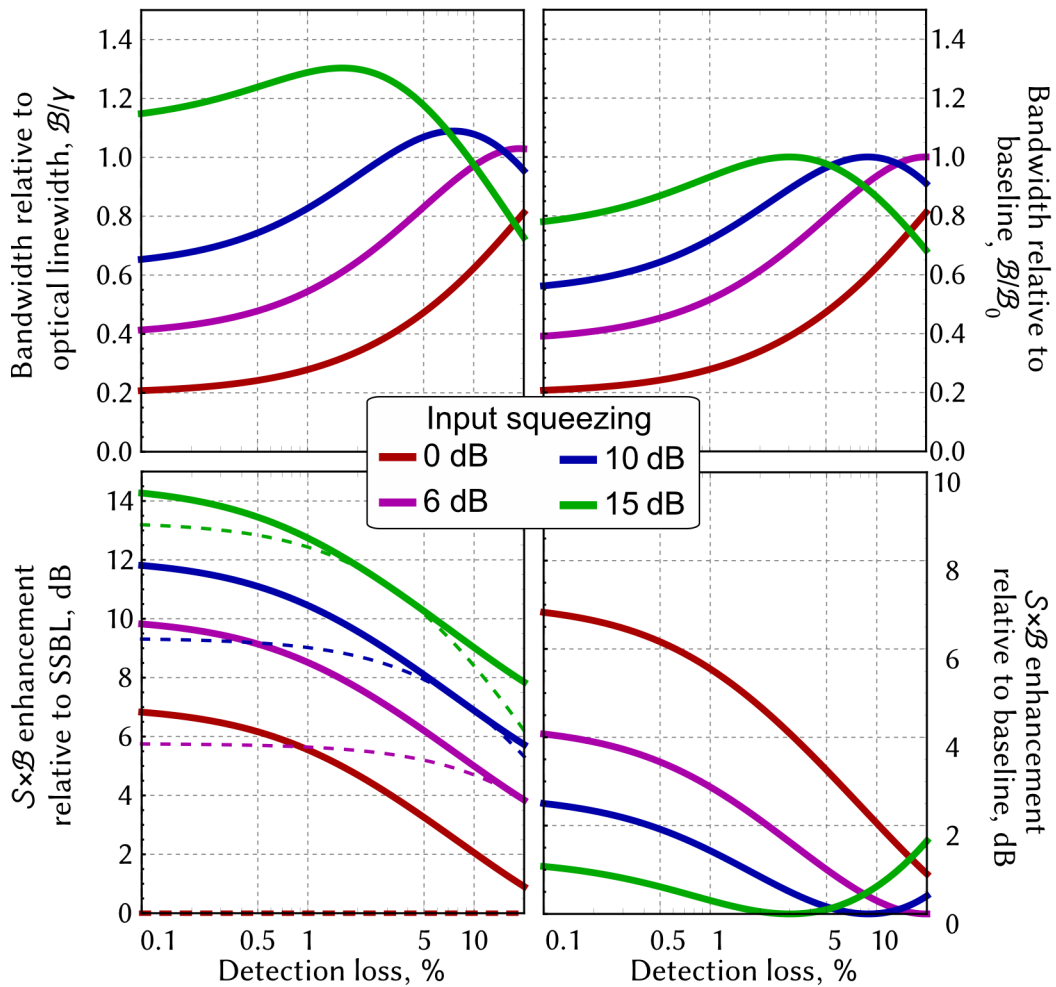


Fig. 7.5. Effect of optimal internal squeezing on the detection bandwidth (top) and the sensitivity-bandwidth product $S \times \mathcal{B}$. Left: the changes relative to the standard interferometer without internal or external squeezing. Right: the changes relative to the baseline interferometer without internal squeezing. The optimal internal squeezing is different for different parameters, and influences the bandwidth differently. The sensitivity-bandwidth product is enhanced always except for a single specific value of detection loss. Bottom left: the solid line is a combination of optimal internal squeezing with input squeezing, dashed line is only input squeezing. Input squeezing provides the main contribution to the enhancement, internal squeezing helps to suppress the detection losses. For all plots $T_c = 0.01$, $\epsilon_{\text{int}} = 0.0001$.

7.3.1 Injection loss and additional amplification

Finally, in order to complete the consideration, I provide the expression for the sensitivity including the injection loss for input squeezing. This expression also takes into account an additional Caves-style amplifier before the detection. Such three-stage squeezing scheme (input, internal, output) would yield the best sensitivity with any combination of losses.

In order to include the injection loss ϵ_{input} , I add a loss term when computing the spectral density, *i.e.* $\langle v_y, v_y \rangle = e^{2q_{\text{input}}} (1 - \epsilon_{\text{input}}) + \epsilon_{\text{input}}$. The output amplification would be represented as a linear gain $e^{q_{\text{out}}}$ just before the detection loss term.

The resulting sensitivity with optimized internal gain (in the single-mode approximation):

$$S_{hh}^{\text{opt}}(\Omega) = \frac{T_c \epsilon_{\text{det}} (e^{-2q_{\text{input}}} (1 - \epsilon_{\text{input}}) + \epsilon_{\text{input}})}{e^{2q_{\text{out}}} (1 - \epsilon_{\text{det}}) (e^{-2q_{\text{input}}} (1 - \epsilon_{\text{input}}) + \epsilon_{\text{input}}) + 1} + \epsilon_{\text{int}} + \frac{4\Omega^2 \tau^2}{T_c (1 - \epsilon_{\text{det}})} \left\{ e^{-2q_{\text{out}}} \epsilon_{\text{det}} + e^{-2q_{\text{input}}} (1 - \epsilon_{\text{det}}) \left[1 - (1 - e^{2q_{\text{input}}}) \epsilon_{\text{input}} \right] \right\}. \quad (7.15)$$

It is interesting to consider limiting cases here as well. In the limit of infinite input squeezing (at zero frequency):

$$S_{hh}^{\text{opt}}(\Omega = 0, q_{\text{input}} \rightarrow \infty) \rightarrow \frac{T_c \epsilon_{\text{det}} \epsilon_{\text{input}}}{\epsilon_{\text{det}} + e^{2r_{\text{out}}} \epsilon_{\text{input}} (1 - \epsilon_{\text{det}})} + \epsilon_{\text{int}}. \quad (7.16)$$

Without output amplification ($r_{\text{out}}=0$), the limit is dependent on the injection loss. From the QCRB point of view, it's rather clear: the injected state is no longer pure, and that impurity contributes to the interaction Hamiltonian. The internal squeezing is unable to compensate that effect, since it has to find the optimum between countering detection and internal loss. Therefore, an additional term turns to zero both when the injection loss is zero (then internal squeezing compensates detection loss), and detection loss is zero (then internal squeezing compensates injection loss).

Interestingly, in the limiting case of infinite output amplification, the result is independent on the input squeezing $q_{\text{out}} \rightarrow \infty$:

$$S_{hh}^{\text{opt}}(\Omega = 0, q_{\text{out}} \rightarrow \infty) \rightarrow \epsilon_{\text{int}}, \quad q_{\text{opt}} = (T_c - \epsilon_{\text{int}})/4. \quad (7.17)$$

This result is clear: the detection loss is fully compensated by output amplification, and internal squeezing can be used to create maximal squeezing (taking into account balance between signal deamplification and internal loss).

7.4 Discussion

In this chapter I explore the potential of internal squeezing for compensating decoherence in quantum metrological devices. I show that the previously reported limit [211] can be surpassed by using the optimal choice of internal gain. This gain depends on the parameters of the system, and in some cases can be set to amplifying the phase quadrature, instead of squeezing it. In general, internal squeezing is in the unique position of being able to improve the sensitivity in two directions: either by maximizing the SNR directly, when the loss is small, or by amplifying the signal together with the noise in order to avoid large detection losses. The optimal spectral density I compute in Eq. 7.15 takes into account all major sources of loss and frequency dependent cavity response.

I show that the best sensitivity with finite squeezing levels can be achieved when three parametric processes are involved: input, internal, and output squeezing. The choice of implementing them, however, relies on interplay between the anticipated benefit (which for some parameters can be marginal), and experimental complexity. Some of the technical issues have not yet been taken into account here: i) the loss introduced by placing the crystal inside the detector; ii) the loss of introducing an output amplifier; iii) the detection loss was assumed to occur after the parametric amplifier, but in reality it would be split into two contributions — before and after; iv) all the issues of control. These are the directions of future studies.

The analysis as presented here is readily applicable to quantum-metrological devices that are not limited by QRPN at low frequencies, and whose principle schemes can be reduced to a single cavity. Especially the cavities that naturally have nonlinear materials in them (such as on-chip devices [217, 218] or whispering-gallery-mode sensors [147, 150, 219]). For these devices squeezing injection might be challenging, and the readout is often subject to losses. Then internal squeezing can become a useful tool for achieving quantum improvement to the sensitivity.

In GWD, however, large squeezing at low frequency will lead to increased QRPN, thus degrading the sensitivity instead of increasing it. QRPN can be avoided or suppressed by increasing the mass of the mirrors, but in general the design of the detector with internal squeezing would require a separate analysis. In particular, the technical details of implementing the crystal inside the detector have not been considered here. In the next chapter I discuss the realistic design of a detector with internal squeezing, where it plays a different role: the combination of specific tuning of the detector and internal squeezing can expand the detection bandwidth without affecting the low-frequency sensitivity. In the next Chapter, I also go into much more technical details of placing the crystal inside the detector.

Proposal for quantum expansion of detection bandwidth

The issue of detector *bandwidth* becomes crucial in the era of multi-messenger astronomy [3]. The information about physics of extremal nuclear matter is hidden in waveforms of gravitational waves radiated from the post-merger remnants of binary neutron star systems [220]. Obtaining this information is important for unraveling the physics of compact astrophysical objects - the engines that drive gamma-ray bursts, the origin of heavy elements and possible modifications to general relativity [221, 222]. These waveforms have typical frequencies above 1 kHz, where the sensitivity of current observatories degrades due to limited bandwidth.

Over the past 20 years the challenge of increasing the bandwidth without changing the peak sensitivity at low frequencies has become one of the cornerstones for the design of future gravitational-wave detectors [133, 198]. Previous concepts involved unstable optomechanical or atomic systems in the so-called “negative dispersion” operation [134–137, 202].

In this chapter I present a new concept of expanding the detection bandwidth based on the internal squeezing approach, see Fig. 8.1. In addition to internal squeezing, quantum expander utilized the coupled-cavity structure of the GWD. Due to the optical coupling between the cavities, the quantum uncertainty at high frequencies gets squeezed such that it compensates the reduction in signal enhancement due to the cavity linewidth, see Fig. 8.2 At low frequencies neither signal nor quantum noise change, which maintains the existing sensitivity, which is optimized for observing the pre-merger stages of binary coalescence. This approach is fully compatible with other enhancements to the detector de-

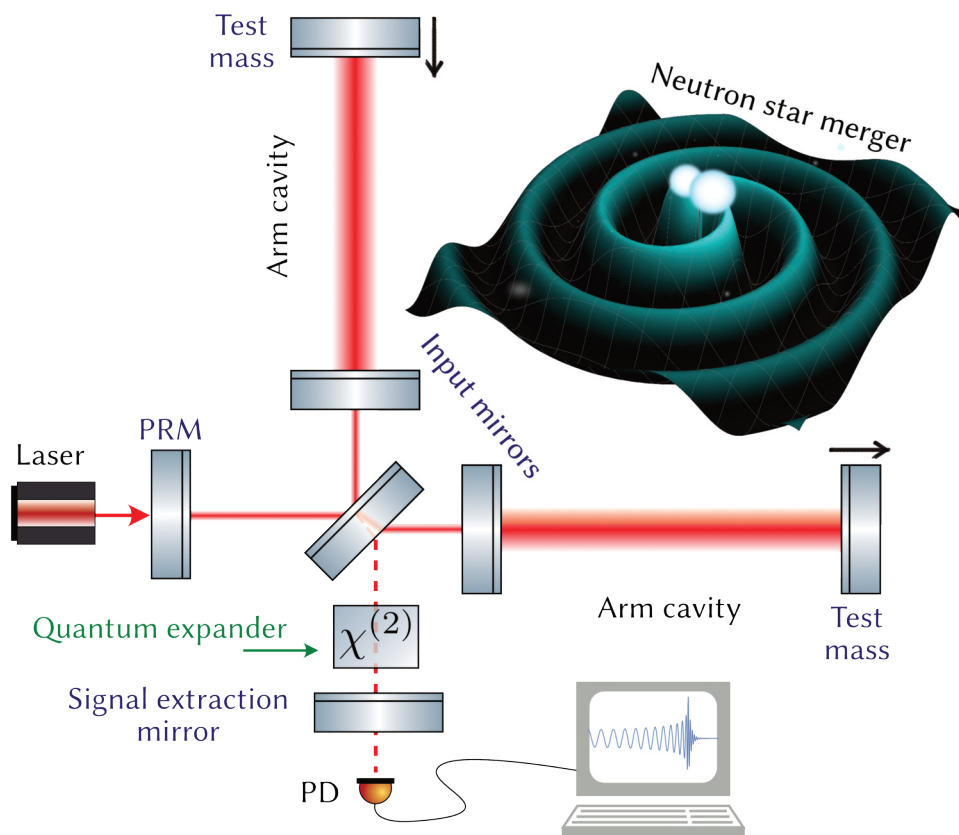


Fig. 8.1. Conceptual representation of the GW observatory with our quantum expander. The relative change in the distance between the central beamsplitter and the test masses due to a gravitational wave is measured on the signal port with a photodiode PD. Optical cavities in the arms are used to enhance the light power and the signal. Additional mirrors independently enhance the signal (signal extraction mirror) and power (power recycling mirror, PRM). We add a nonlinear $\chi^{(2)}$ crystal into the signal extraction cavity, formed by the SE mirror and input mirrors, which creates internally squeezed light field to boost the high-frequency sensitivity and expand the detection bandwidth.

sign, such as injection of frequency-dependent squeezed light or variational readout [35, 112, 223, 224].

Placing an optical parametric amplifier inside the detector has been considered for other purposes before, i.e. for increasing the low-frequency [70] or mid-

frequency [72, 203, 205] sensitivity, yet all-optical quantum expansion of bandwidth has never been proposed so far. The results presented in this chapter are published in [71].

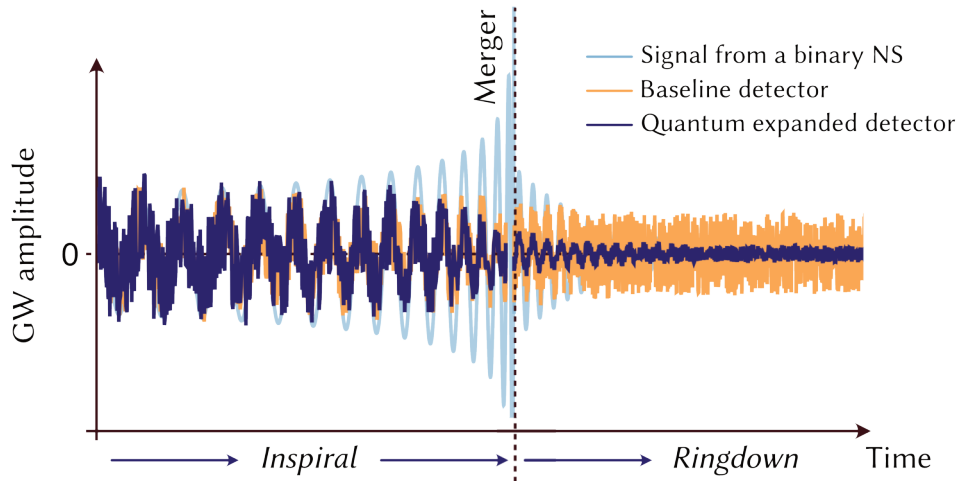


Fig. 8.2. Simulated signal from a binary neutron star coalescence (pale blue). The signal is well resolved at low frequencies for the inspiral stage. After the merger, the ringdown oscillations produce high-frequency GWs, which could not be resolved by the baseline detector due to the cavities' linewidth (orange). Quantum expander (dark blue) allows to resolve the ringdown oscillations by suppressing the quantum noise at high frequencies.

8.1 Quantum expander concept

8.1.1 Hamiltonian of the Quantum Expander

With respect to the quantum noise and the signal, the interferometer topology can be conceptually represented by a simpler system of two coupled cavities [196]: the arm cavity with optical mode \hat{a} , and the signal-extraction cavity, formed by the front mirror of the arm cavity and the signal-extraction mirror, with optical mode \hat{a}_q , see Fig. 8.4A. The two modes are coupled through the partially reflective front mirror of the arm cavity, with a coupling frequency ω_s , which depends on the front mirror's reflectivity. For illustrative purposes we limit the

discussion to the interaction of these two modes, while the complete description should include the modes of the next longitudinal resonances of the arm cavity, separated by one free spectral range. In this approximation the system can be described by the standard Hamiltonian for coupled harmonic oscillators: $\hat{H}/\hbar = \omega_0 \hat{a}^\dagger \hat{a} + \omega_0 \hat{a}_q^\dagger \hat{a}_q + \omega_s (\hat{a}_q^\dagger \hat{a} + \hat{a}^\dagger \hat{a}_q)$. If the system is continuously excited at one of the normal frequencies, $\omega_0 \pm \omega_s$, the excitation energy is equally split between the two modes \hat{a} and \hat{a}_q . However, when one of the modes (e.g. \hat{a}_q) is continuously excited at ω_0 , the complete energy gets redistributed into the other mode (e.g. \hat{a}). In this way when mode \hat{a}_q is open to the environment and driven by the incoming zero-point fluctuation, its noise components are strongly suppressed at sideband frequencies $\omega_0 \pm \Omega$, $\Omega \ll \omega_s$, and all the energy at these frequencies goes into the arm cavity mode \hat{a} . For large values of Ω , the noise becomes resonant inside the SE cavity as well, reaching its resonance maximum at ω_s , as can be seen of Fig. 8.4B. It is this particular resonant structure of the coupled system that we take advantage of for boosting the sensitivity of the detector at high frequencies as follows.

We propose to place an optical parametric amplifier, e.g. a $\chi^{(2)}$ nonlinear crystal, inside the SE cavity. The parametric process will amplify the fluctuations in one quadrature of the mode \hat{a}_q , and suppress the fluctuations in its conjugate counterpart. Depending on the sideband frequency Ω , the amplification strength varies due to the presence of the coupled cavity structure. At frequencies around ω_0 , the excitation of mode \hat{a}_q is suppressed, so the parametric process is inefficient, and almost no squeezing is produced. At the same time, the SE cavity is resonant for higher frequencies $\Omega \sim \omega_s$, so the crystal produces a high squeeze factor. The suppression of shot noise at the frequencies $0 \ll \Omega \ll \omega_s$ happens exactly at the same rate as the reduction in the signal amplification due to the detector bandwidth, see Fig. 8.4C. The two processes compensate each other, and the signal-to-noise ratio remains constant, thus the bandwidth is expanded, see Fig. 8.4D.

The quantum expansion effect can be demonstrated in more detail by formulating a complete Hamiltonian of the model two-mode system:

$$\hat{H} = \hat{H}_0 + \hat{H}_{\text{int}} + \hat{H}_\gamma + \hat{H}_x - F_{\text{GW}}x; \quad (8.1)$$

$$\hat{H}_0 = \hbar\omega_0\hat{a}^\dagger\hat{a} + \hbar\omega_0\hat{a}_q^\dagger\hat{a}_q; \quad (8.2)$$

$$\hat{H}_{\text{int}} = \hbar\omega_s\hat{a}_q^\dagger\hat{a} + \frac{1}{2}\hbar\kappa\beta e^{-2i\omega_0 t}\hat{a}_q^\dagger\hat{a}_q^\dagger e^{i\phi} + h.c.; \quad (8.3)$$

$$\hat{H}_\gamma = i\hbar\sqrt{2\gamma} \int_{-\infty}^{\infty} \left(\hat{a}_q^\dagger(\omega)\hat{a}_{\text{in}}(\omega) - \hat{a}_{\text{in}}^\dagger(\omega)\hat{a}_q(\omega) \right) d\omega; \quad (8.4)$$

$$\hat{H}_x = -\hat{F}_{\text{rp}}\hat{x} = -\hbar G_0\hat{a}^\dagger\hat{a}\hat{x}, \quad (8.5)$$

where \hat{a}, \hat{a}_q are the arm cavity and SE cavity modes, and ω_0 is their natural resonance frequency; $\omega_s = c\sqrt{T_{\text{ITM}}}/(4L_{\text{SE}}L_{\text{arm}})$ is the coupling rate between two cavities, T_{ITM} is the transmission of the front mirror of the arm cavity, $L_{\text{SE}}, L_{\text{arm}}$ are the lengths of the signal extraction and arm cavity, respectively; $\gamma = cT_{\text{SE}}/(4L_{\text{SE}})$ is the coupling rate of the SE mode to the continuum of input modes \hat{a}_{in} ; x is the displacement of the test mass partially in reaction to the gravitational-wave tidal force F_{GW} ; the mirror motion x is coupled via the radiation-pressure force \hat{F}_{rp} to the cavity mode with strength $G_0 = \omega_0/L_{\text{arm}}$; κ is the coupling strength due to a crystal nonlinearity under a second harmonic pump field with amplitude β and phase ϕ . The pump field is assumed to be classical and its depletion is neglected. Quantum expansion affects only the high frequency sensitivity, which is dominated by shot noise. This justifies us to ignore in this simple model the effects of the quantum radiation pressure on the dynamics of the test mass, effectively assuming infinite mass of the mirrors. The displacement of the mirrors x in this approximation is caused only by the GW strain $h_0 = x/L_{\text{arm}}$. Also note that the expression for the coupling frequency ω_s only applies when $\omega_s \ll \omega_{\text{FSR}} \equiv c/(2L_{\text{arm}})$, and modifies when the neighboring longitudinal resonances of the arm cavity are taken into account.

Equations of motion

The light field in the coupled system can be expressed in terms of the input fields by solving the Hamiltonian above.

We obtain the Langevin equations of motion for the cavity modes in the frame rotating at ω_0 and expand the quantum amplitudes into a sum of large classical amplitude and small quantum fluctuation, $\hat{a} \rightarrow A + \hat{a}$:

$$\dot{\hat{a}} = -i\omega_s \hat{a}_q + iGh_0; \quad (8.6)$$

$$\dot{\hat{a}}_q = -i\omega_s \hat{a} - \gamma \hat{a}_q + \sqrt{2\gamma} a_{\text{in}} - i\chi \hat{a}_s^\dagger e^{i\phi}; \quad (8.7)$$

$$\dot{\hat{a}}_{\text{out}} = -\hat{a}_{\text{in}} + \sqrt{2\gamma} \hat{a}_q. \quad (8.8)$$

where we defined an effective coupling strength of GW strain to the light field $G = \sqrt{2P_c L_{\text{arm}} \omega_0 / (\hbar c)}$, and optical power inside the arm cavity $P_c = \hbar \omega_0 \bar{a}$, with \bar{a} being an average amplitude of the mode \hat{a} ; and the effective parametric gain $\chi = \kappa \beta$,

As we are interested in the spectral properties of the system, we transform into a Fourier domain: $\dot{\hat{a}}(t) \rightarrow -i\Omega \hat{a}(\Omega)$. The outgoing light is measured by a homodyne detector, which measures the quadratures of the light, that are defined as:

$$\hat{a}^{(1)} = \frac{\hat{a}(\Omega) + \hat{a}^\dagger(-\Omega)}{\sqrt{2}}, \quad \hat{a}^{(2)} = \frac{\hat{a}(\Omega) - \hat{a}^\dagger(-\Omega)}{i\sqrt{2}} \quad (8.9)$$

We obtain the input-output relations for the two quadratures by solving Eqs. (8.6):

$$\begin{aligned} \hat{a}_{\text{out}}^{(1)}(\Omega) &= \hat{a}_{\text{in}}^{(1)}(\Omega) \frac{(\gamma - \chi)\Omega + i(\Omega^2 - \omega_s^2)}{(\gamma + \chi)\Omega - i(\Omega^2 - \omega_s^2)} + \\ &+ h_0(\Omega) \frac{2iG\sqrt{\gamma}\omega_s}{(\gamma + \chi)\Omega - i(\Omega^2 - \omega_s^2)}, \end{aligned} \quad (8.10)$$

$$\begin{aligned} \hat{a}_q^{(2)}(\Omega) &= \hat{a}_{\text{in}}^{(2)}(\Omega) \frac{\sqrt{2\gamma}\Omega}{(\gamma + \chi)\Omega - i(\Omega^2 - \omega_s^2)} + \\ &+ h_0(\Omega) \frac{iG\omega_s}{(\gamma + \chi)\Omega - i(\Omega^2 - \omega_s^2)}, \end{aligned} \quad (8.11)$$

$$\hat{a}^{(1)}(\Omega) = \hat{a}_{\text{in}}^{(2)}(\Omega) \frac{i\sqrt{2\gamma}\omega_s}{(\gamma - \chi)\Omega - i(\Omega^2 - \omega_s^2)}, \quad (8.12)$$

The phase of the pump field was chosen such that the parametric process squeezes the signal quadrature inside the SE cavity, i.e. $\phi = \pi/2$. Several features can be seen in these equations. First, when we remove the crystal (i.e. $\chi = 0$) in the typical operational range of GW observatories $\Omega \ll \omega_s$, the input-output

relation Eq.(6) reduces to the standard one for a baseline GWO [196, 225], with the detection bandwidth given by: $\gamma_{\text{baseline}} = \omega_s^2/\gamma = cT_{\text{ITM}}/(T_{\text{SE}}L_{\text{arm}})$. Second, the noise term in Eq.(7) is strongly suppressed at zero sideband frequency, as we described above in the example with two coupled modes: $\hat{a}_q^{(2)}(0) = h(0)G/\omega_s$, therefore virtually no squeezing is produced at low frequencies. The noise on the output in Eq.(6) at low frequencies is defined by the vacuum field reflected directly off the signal extraction mirror. Third, when the sideband frequency matches the normal mode frequency, $\Omega = \omega_s$, the signal mode takes the form: $\hat{a}_{\text{out}}^{(1)}(\omega_s) = \hat{a}_{\text{in}}^{(1)}(\gamma - \chi)/(\gamma + \chi) + 2ih_0(\omega_s)G\sqrt{\gamma}/(\gamma + \chi)$. This equation shows that for a parametric gain close to the threshold ($\chi \rightarrow \gamma$), the noise term becomes almost infinitely squeezed [43], but signal gets deamplified at most by a factor of 2. Despite the signal deamplification, ideally the SNR in this case can become infinite, as we show below by computing the sensitivity of the quantum-expanded observatory.

8.1.2 Input-output relations

We can derive the same input-output relations as in Eq. 8.10, but based on a more rigorous input-output formalism, as used in previous chapters. For simplicity in this section we ignore the effects of quantum radiation pressure noise and optical losses. These will be included in the full transfer matrix description in Section 8.2.1. We follow the standard procedure for the fields, as in the previous chapters.

We make several simplifications to the notation: as we are primarily interested in the phase quadrature, we will omit index (*s*) in equations below; we also omit the hats on the operators for brevity, although all the fields are quantized; we consider only the noise fields in the frequency domain, so we don't write that in the equations explicitly: e.g. $\hat{a}^{(s)}(\Omega) \rightarrow a$.

The signal we consider is a phase modulation on the light field induced by motion of the mirror with infinite mass caused by an external force. This modulation adds a phase shift on the light reflected off the movable mirror: $E_{\text{refl}} = E_{\text{in}}e^{2ikx(\Omega)} \approx E_{\text{in}}(1 + 2ik_p x(\Omega))$, where k_p is the light's wave vector, $E_{\text{refl, in}}$ are the amplitudes of the reflected and incident light fields, and $x(\Omega)$ is a small mirror

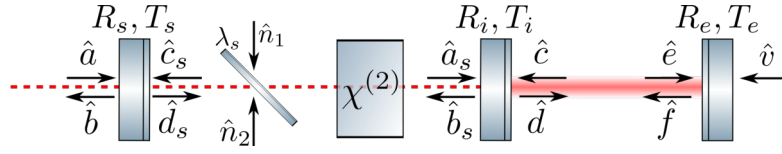


Fig. 8.3. Quantum fields in the model of a two-cavity system. $R_{s,i,e}$, $T_{s,i,e}$ are the amplitude reflectivities and transmissivities of the signal extraction, input and end test mirrors correspondingly; a beam-splitter with power reflectivity λ_s represents a source of intra-cavity loss, which causes vacuum noises $\hat{n}_{1,2}$ to enter the system.

displacement. The signal appears only in the equations for the phase quadrature of the light field.

We model the parametric amplification process as a simple linear amplification of amplitude quadrature of the light by some factor e^q , without considering the effects of the parametric pump and the finite size of a crystal. In the full model in section 5 we also will introduce the possibility to tune the amplification quadrature. With this in mind we start with writing down the steady-state input-output relations [165, 166] for the quantum fluctuations of the phase quadrature of the light field, for the cavity cavity model depicted of Fig. 8.3. We choose the arm cavity to be tuned on resonance, so that for $\Omega = 0$ it has the maximal light power inside.

$$d_s = T_s a + R_s c_s, \quad (8.13)$$

$$a_s = d_s e^{-q} e^{i\varphi} e^{i\Omega\tau_{SE}}, \quad (8.14)$$

$$b_s = T_i c + R_i a_s, \quad (8.15)$$

$$c = d e^{2i\Omega\tau_{arm}} + 2ik_p E x e^{i\Omega\tau_{arm}}, \quad (8.16)$$

$$b_s = -R_i a_s + T_i c, \quad (8.17)$$

$$c_s = b_s e^{-q} e^{i\varphi} e^{i\Omega\tau_{SE}}, \quad (8.18)$$

$$b = -R_s a + T_s c_s, \quad (8.19)$$

where $R_{i,s} = \sqrt{R_{ITM,SE}}$, $T_{i,s} = \sqrt{T_{ITM,SE}}$ are the amplitude reflectivity and transmissivity of input test mirror and signal-extraction mirror; q is an amplification factor on the single pass through the crystal; $\tau_{arm,SE} = L_{arm,SE}/c$ is the single trip time in arm cavity of length L_{arm} and signal extraction cavity of length L_{SE} , with c being

the speed of light; $\varphi = -\pi/2$ is the tuning of the SE cavity with respect to the arm cavity; x is a small displacement of the end mirror due to the GW signal, E is the large classical amplitude of field inside the arm cavity and k_p is the wave vector of the carrier light field.

We find a solution to these equation, splitting the output b into the noise part b_n and signal X_{out} : $b = b_n + X_{\text{out}}$.

$$\begin{aligned} b_n &= \mathcal{R}_a(\Omega)a(\Omega) = \\ &= -\frac{e^{2i\varphi} e^{2i\Omega\tau_{\text{SE}}} (e^{2i\Omega\tau_{\text{arm}}} - R_i) + e^{2q} (e^{2i\Omega\tau_{\text{arm}}} R_i - 1)}{e^{2q} (e^{2i\Omega\tau_{\text{arm}}} R_i - 1) + e^{2i\varphi} e^{2i\Omega\tau_{\text{SE}}} (e^{2i\Omega\tau_{\text{arm}}} - R_i) R_s} a(\Omega), \end{aligned} \quad (8.20)$$

$$\begin{aligned} X_{\text{out}} &= \mathcal{T}(\Omega)x(\Omega) = \\ &= \frac{2ik_p E e^{i\varphi} e^{i\Omega\tau_{\text{SE}}} e^{i\Omega\tau_{\text{arm}}} e^q T_i T_s}{e^{2q} (e^{2i\Omega\tau_{\text{arm}}} R_i - 1) + e^{2i\varphi} e^{2i\Omega\tau_{\text{SE}}} (e^{2i\Omega\tau_{\text{arm}}} - R_i) R_s} L_{\text{arm}} h_0(\Omega), \end{aligned} \quad (8.21)$$

where $\mathcal{R}_a(\Omega)$, $\mathcal{T}(\Omega)$ are the noise and signal optical transfer functions correspondingly.

We can obtain an intuitive expression for these functions by doing a single-mode approximation. We assume $\Omega\tau_{\text{arm}} \ll 1$, $\Omega\tau_{\text{SE}} \ll 1$, so $e^{i\Omega\tau_{\text{arm,SE}}} \approx 1 + i\Omega\tau_{\text{arm,SE}}$; and $T_{i,s} \ll 1$, so $R_i \approx 1 - T_i^2/2 = 1 - 2\gamma_{\text{arm}}\tau_{\text{arm}}$, $R_s \approx 1 - T_s^2/2 = 1 - 2\gamma\tau_{\text{arm}}$, where γ_{arm} , γ are the arm cavity and the signal-extraction cavity linewidth, respectively; a single-pass optical gain is small: $q \ll 1$, so $e^q \approx 1 + q = 1 + \chi\tau_{\text{SE}}$, where χ is an effective parametric gain.

With these approximations, Eqs. 8.20 can be simplified to

$$\mathcal{R}_a(\Omega) = \frac{(\gamma - \chi)\Omega + i(\Omega^2 - \omega_s^2)}{(\gamma + \chi)\Omega - i(\Omega^2 - \omega_s^2)} \quad (8.22)$$

$$\mathcal{T}(\Omega) = -\frac{4ik_p L_{\text{arm}} E}{\sqrt{\tau_{\text{arm}}}} \frac{\sqrt{\gamma}\omega_s}{(\gamma + \chi)\Omega - i(\Omega^2 - \omega_s^2)}, \quad (8.23)$$

where we defined a sloshing frequency $\omega_s = c\sqrt{T_i^2/(4L_{\text{SE}}L_{\text{arm}})}$. Based on these equations, we derive the Hamiltonian of the system in Sec. 8.1.1.

We would like to point out the limits of this approximation: it is valid only until sloshing and signal frequencies are much smaller than the free spectral range of the arm cavity: $\Omega, \omega_s \ll c/L_{\text{arm}}$. This condition sets a limit on the transmissivity of the ITM: $T_i^2 \ll L_{\text{SE}}/L_{\text{arm}}$. This restricts the applicability of the derived equations

to a detector with a relatively short arm length (e.g. Advanced LIGO), while a longer detector (as baseline GWO considered in Table 8.1) would require a more sophisticated expression with the higher FSR of the arm cavity taken into account. The assumption of a small transmission of the SE mirror is often not valid in real designs, which would lead to additional contributions in the noise spectrum.

Sensitivity spectrum

The noise spectral density of the GWO with quantum expander, normalized to the unity of strain h , can be obtained from Eqs. 8.22. The spectral density of the output noise $\hat{a}_{\text{out}}^{(c)}(\Omega)$ is:

$$S_{\text{out}}(\Omega) = S_{\text{in}}(\Omega)|\mathcal{R}_a(\Omega)|^2, \quad (8.24)$$

where $S_{\text{in}}(\Omega)$ is the spectral density of incoming light field, which we assume here to be vacuum: $S_{\text{in}}(\Omega) = 1$. When internal squeezing suppresses: $\phi = -\pi/2$, we obtain the following noise spectral density

$$S_{\text{out}}(\Omega) = 1 - \frac{4\gamma\chi\Omega^2}{(\gamma + \chi)^2\Omega^2 + (\Omega^2 - \omega_s^2)^2} \quad (8.25)$$

and signal transfer function:

$$|\mathcal{T}(\Omega)|^2 = \frac{4G^2\gamma\omega_s^2}{(\gamma + \chi)^2\Omega^2 + (\Omega^2 - \omega_s^2)^2}. \quad (8.26)$$

The sensitivity is given by the noise-to-signal ratio: $S_h(\Omega) = \frac{S_{\text{out}}(\Omega)}{|\mathcal{T}(\Omega)|^2}$. Typical GW signal has a relatively low-frequency, and the SE bandwidth is very large, so the sensitivity can be approximated for $\Omega \ll \omega_s \ll \gamma$.

$$\begin{aligned} S_h(\Omega) &= \frac{\hbar c}{8\omega_0 L_{\text{arm}} P_c} \frac{(\Omega^2 - \omega_s^2)^2 + (\gamma - \chi)^2 \Omega^2}{\gamma \omega_s^2} \approx \\ &\approx \frac{\hbar c}{8\omega_0 L_{\text{arm}} P_c} \frac{\gamma_q^2 + \Omega^2}{\gamma \omega_s^2} (\gamma - \chi)^2, \end{aligned} \quad (8.27)$$

with the new detection bandwidth defined as $\gamma_q = \omega_s^2/(\gamma - \chi)$. Without the quantum expansion, $\chi = 0$, the baseline sensitivity decreases with the frequency increase, limited by the detector's bandwidth $\gamma_{\text{baseline}} = \omega_s^2/\gamma$:

$$\begin{aligned} S_h^{\text{baseline}}(\Omega) &= \frac{\hbar c}{8\omega_0 L_{\text{arm}} P_c} \frac{(\Omega^2 - \omega_s^2)^2 + \gamma^2 \Omega^2}{\gamma \omega_s^2} \approx \\ &\approx \frac{\hbar c}{8\omega_0 L_{\text{arm}} P_c} \frac{\gamma_{\text{baseline}}^2 + \Omega^2}{\gamma \omega_s^2} \gamma^2. \end{aligned} \quad (8.28)$$

The detection bandwidth γ_q can ideally be expanded infinitely (in the single-mode approximation) by a factor of $\gamma/(\gamma - \chi) \rightarrow \infty$ when squeezing approaches the threshold point $\chi = \gamma$. At this point the sensitivity is given by

$$S_h(\Omega) = \frac{\hbar c}{8\omega_0 L_{\text{arm}} P_c} \frac{\omega_s^2}{\gamma}, \quad (8.29)$$

which is approximately frequency independent under $\Omega \ll \omega_s$, as a result of expanded bandwidth γ_q . In reality, even in the lossless case, the bandwidth is still limited by the next longitudinal resonance of the arm cavity, and the detector's reduced response when the detector's arm length is comparable to the gravitational wavelength.

The effect of the quantum expander is shown of Fig. 8.4C,D. The main properties of the concept are seen there:

- At frequencies around γ_{baseline} (i.e. 500 Hz) reduction in noise has exactly the same slope as reduction in signal due to cavity bandwidth. As a result, the SNR in that region remains flat, which is the effect of expanded bandwidth.
- The noise is maximally squeezed at ω_s , and there the SNR in the ideal case increases to infinity (there, as I show in the next section, QCRB turns to zero).
- At low frequencies the noise is almost unchanged. This makes quantum expander compatible with back-action evasion, such as variational readout or frequency-dependent squeezing.
- Above ω_s the next longitudinal resonance of the arm cavity starts to play a role, which reduces the sensitivity.

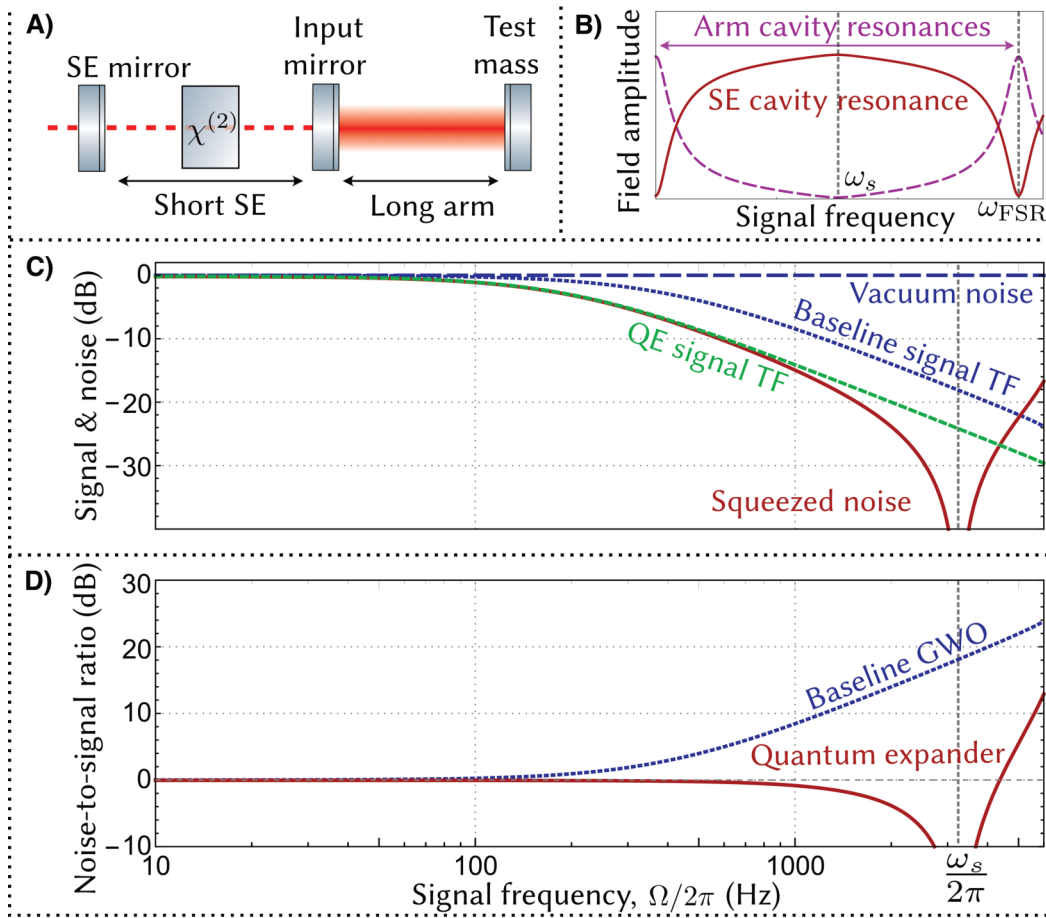


Fig. 8.4. Concept of the quantum expander. A) Model system of two coupled cavities, arm and signal extraction (SE), with nonlinear crystal inside SE cavity; B) resonance enhancement of the SE mode (solid red) at frequencies close to ω_s and suppression at low frequencies, with two longitudinal resonances of the arm cavity (dashed magenta) separated by a free spectral range (ω_{FSR}); C) suppression of the shot noise at high frequency by the quantum expander (red) compared to the vacuum level (blue), in comparison to the scaling of the signal transfer function (TF) due to the cavity linewidth with quantum expander (green) and without (blue), where the signal is suppressed by 6 dB due to the parametric process; D) noise-to-signal ratio for the detector with quantum expander (red) and without (blue). On C) the quantum expander noise squeezing has exactly the same scaling as signal reduction due to the cavity bandwidth, so the bandwidth of the signal-to-noise ratio is expanded, as seen on D).

It is important to point out the limits of the approximations used in this section: they valid only until coupling and signal frequencies are much smaller than the free spectral range of the arm cavity: $\Omega, \omega_s \ll \omega_{\text{FSR}} \equiv c/2L_{\text{arm}}$. This condition sets a limit on the transmissivity of the ITM: $T_i^2 \ll L_{\text{SE}}/L_{\text{arm}}$, which means the derived simplified equations are applicable only to a detector with a relatively short arm length (e.g. Advanced LIGO). A longer detector (such as the baseline GW chosen as a reference in the Figures (2-4)) would require a more sophisticated expression with the higher longitudinal resonances of the arm cavity taken into account. The assumption of a small transmission of the SE mirror is often not valid in real designs, which would lead to additional contributions in the noise spectrum. I perform the full analysis that avoids these limitations in the Appendix.

Quantum Cramer-Rao Bound

The sensitivity of any gravitational-wave observatory is ultimately limited by its quantum Cramer-Rao bound (QCRB) $S_h^{\text{QCRB}}(\Omega)$ [154]. The conditions for reaching its quantum Cramer-Rao bound are that (i) the quantum radiation pressure noise is evaded, and (ii) the upper and lower optical sidebands generated by the GW are equal in amplitude [154]. Naturally, there is also a typical requirement of absence of optical decoherence and technical noises. The quantum expander configuration does not affect the QRPN, and allows to satisfy condition (i) at low frequency by well-known back-action evading techniques (e.g. variational readout, see the Discussion below). We prove that the condition (ii) is satisfied by directly computing the QCRB in the case of GW detectors is defined as follows [154]:

$$S_h^{\text{QCRB}}(\Omega) = \frac{\hbar^2}{2L_{\text{arm}}^2 S_{FF}(\Omega)} = \frac{\hbar c}{4\omega_0 L_{\text{arm}} P_c} \frac{1}{S_{aa}(\Omega)}, \quad (8.30)$$

where $S_{FF}(\Omega)$ is the single-sided spectrum of the radiation-pressure force \hat{F}_{rp} , and $S_{aa}(\Omega)$ is the noise spectrum of the arm cavity field, which one can compute from Eq. 9:

$$S_{aa}(\Omega) = \frac{2\gamma\omega_s^2}{(\gamma - \chi)^2\Omega^2 + (\Omega^2 - \omega_s^2)^2} \quad (8.31)$$

Therefore the limit on the sensitivity is given by the QCRB in the following form:

$$S_h^{\text{QCRB}}(\Omega) = \frac{\hbar c}{4\omega_0 L_{\text{arm}} P_c} \frac{(\Omega^2 - \omega_s^2)^2 + (\gamma - \chi)^2 \Omega^2}{2\gamma \omega_s^2}, \quad (8.32)$$

which is identical to the Eq. 8.27. The sensitivity becomes unbounded (QCRB turns to zero) at the parametric threshold $\chi = \gamma$ at frequency $\Omega = \omega_s$.

This calculation demonstrates that the quantum expander strongly reduces the QCRB at high frequencies compared to the baseline GWO, and that the expanded detector does reach its lowered QCRB (in case of the typical assumption of zero photon loss).

8.2 The quantum expander in realistic GW detectors

Quantum-expanded signal extraction will further reduce the shot noise at high frequencies, without affecting the established improvement factor from external squeezing. The quantum noise at *low* frequencies (QRPN) will remain unchanged. This differs our approach from other designs targeting the high-frequency sensitivity [64, 225, 226]. The QRPN can be suppressed independently using already developed approaches using frequency dependent squeezing, variational readout or quantum non-demolition measurements [35, 112, 223, 224].

In this section I explore various aspects of implementing the quantum expander in a real GWO.

8.2.1 Full derivation of the spectral density

In the previous sections we did several approximations, which are not applicable to a real GWO. In particular, we did not consider QRPN, losses, next longitudinal resonances, and the frequency response of a detector to GW. I perform a full calculation in the Appendix A, using a transfer matrix approach. I choose a baseline observatory design that is independent on any specific proposed design, as ET or CE, with the parameters given in Table 8.1, except for the reference we choose a case without injected squeezing (we call this case semi-classical,

since it's limited by quantum noise, but does not use quantum techniques to overcome it). The resulting effect of the quantum expander on such baseline GW observatory is shown in Fig. 8.5. In order to highlight the possibility to combine the quantum expander with back-action evading techniques, I demonstrate the effect of a variational readout at low frequencies. Variational readout makes use of filter cavities on the output of the detector to rotate the detection quadrature in a frequency-dependent way such, that the back-action noise has no contribution to the observed sensitivity (it is in the orthogonal quadrature) [112]. Since quantum expansion has virtually no effect on quantum correlations at low frequency, variational readout can be applied without modifications.

The code used to produce this figure, which includes all the relevant effects, can be found in [227].

8.2.2 Optical loss

Non-classical light is sensitive to decoherence, i.e. to optical loss, which destroys the inherent quantum correlations [215]. Losses occur inside the detector as well as on the readout, and have multiple contributions. Any squeezed light application as well as QRPN suppression technique is limited by optical loss, and the proposed scheme is not an exception. The quantum expander relies on squeezing operation inside the interferometer to compensate the decrease in the signal amplification due to the finite cavity linewidth. The higher the squeeze factor is, the more it is susceptible to optical loss. The effect of different readout loss is shown on Fig. 8.5.

All observatories of the current generation are already operating with external-squeezing injection. When the quantum expander is combined with external-squeezing injection, the overall squeeze factor at high frequencies increases further. This imposes a strict requirements on reducing the optical losses. The losses occur inside the detector: inside the arm cavity, and inside the SE cavity; as well as on the readout train: from the SE mirror to the detector. The external squeezing additionally suffers from the injection loss (which can be partially mitigated by squeezing higher-order optical modes [54]). On Fig.8.6 we show the contribution of different sources of loss as a function of frequency. We note that the detection loss and loss inside the SE cavity are the most important

parameter	description	Baseline GWO	AdvLIGO
λ	optical wavelength	1550nm	1064nm
$P_{\text{arm}} = P_c/2$	arm cavity light power	4MW	840kW
L_{arm}	arm cavity length	20 km	4 km
m	mirror mass	200 kg	40 kg
L_{SE}	SE cavity length	56m	56m
T_i	input mirror power transmission	0.07	0.014
T_s	SE mirror power transmission	0.35	0.35
T_e	end mirror power transmission	5ppm	5ppm
e^{2r}	external squeezing	10 dB	—
λ_s	loss inside SE cavity	1500ppm	1000ppm
η	detection efficiency	99%	~85%

Tab. 8.1. Set of parameters of the proposed detector. In order to plot the spectral densities in the paper we use the following set of parameters of some baseline GW observatory, without choosing a specific design from many possibilities of a 3-G topologies. We note that our double-cavity model uses effective parameters. In order to use this model for the Michelson topology, an effective light power inside the arm cavity has to be used: $P_c = 2P_{\text{arm}}$, where P_{arm} is the power inside the arms of the Michelson topology [196]

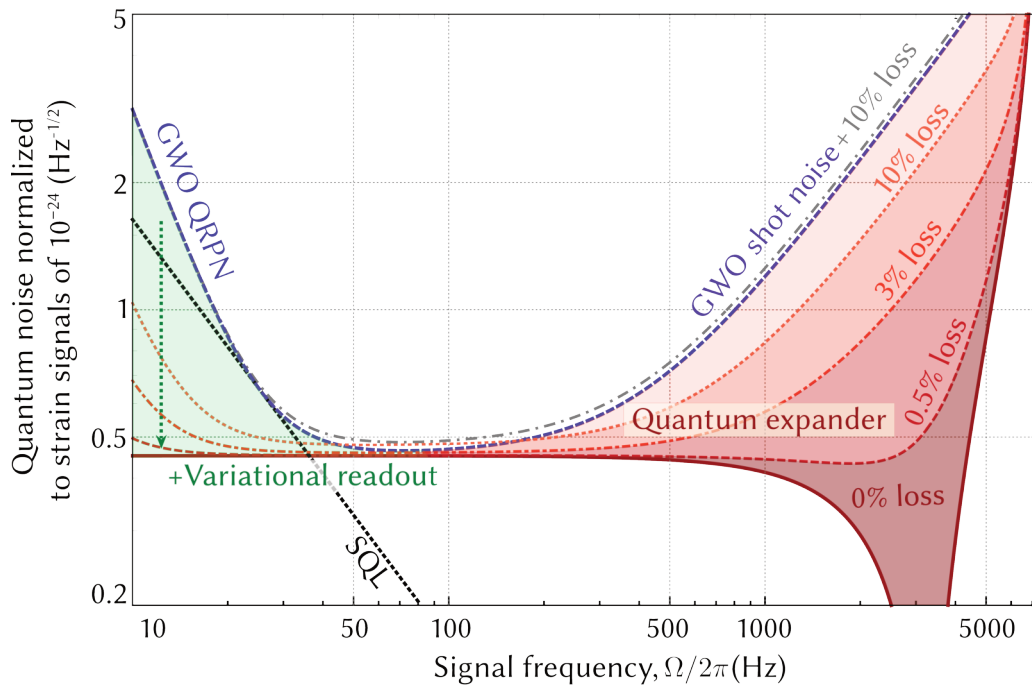


Fig. 8.5. Effect of the quantum expander on the detector’s sensitivity to gravitational-wave strain $S_h(f)$, in combination with variational readout [112]. The bandwidth of the semiclassical Gravitational Wave Observatory (GWO, blue dashed line) is expanded by squeezing operation inside the detector at high frequencies (solid red line, red shading). The effect deteriorates once quantum decoherence due to optical loss is introduced (different shades of red for quantum expander, gray dot-dashed line for semiclassical GWO). At low frequencies quantum noise remains unaffected by quantum expansion, and allows to use the variational readout (green shading) to evade the quantum radiation-pressure noise (QRPN). The efficiency of the variational readout is also affected by the optical loss, which leads to the loss of correlations between the two quadratures of the light field, resulting in the reduction in the sensitivity at low frequencies, as shown by dashed red lines. The boundary where the QRPN becomes equal to the shot noise at different light powers, know as the Standard Quantum Limit (SQL) is plotted in black dots. The parameters used for plotting are based on the benchmark parameter set for the 3d generation of GWOs: optical wavelength $\lambda = 1550$ nm; light power inside the arm cavity $P_c = 4$ MW; arm cavity length $L_{\text{arm}} = 20$ km; SE cavity length $L_{\text{SE}} = 56$ m; mirror mass $m = 200$ kg; input mirror power transmission $T_{\text{ITM}} = 0.07$; SE mirror power transmission $T_{\text{SE}} = 0.35$.

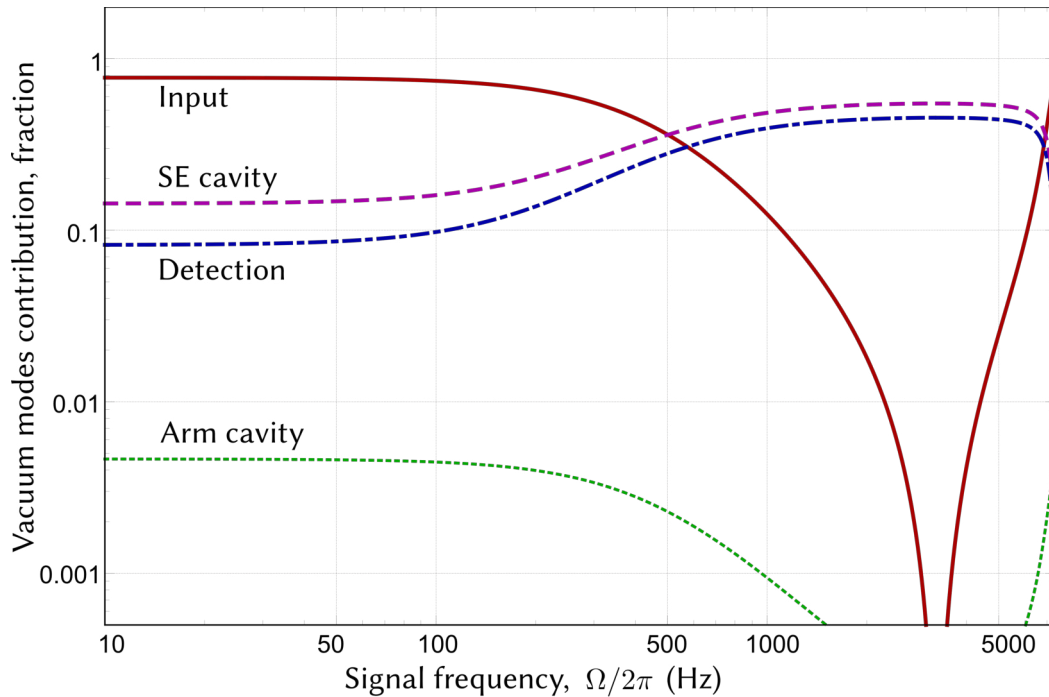


Fig. 8.6. Relative contribution of different vacuum modes to the overall sensitivity of the detector at different frequencies. Input (solid red) vacuum mode defines the main sensitivity level, and the rest come from the various sources of loss: loss inside the SE cavity (dashed magenta), detection loss (dot-dashed blue) and arm cavity loss (dotted green). The parameters are taken according to Table 8.1: internal loss is 1500 ppm single-trip, detection loss is 1%, transmission of the end mirror is 100 ppm (increased relative to Table 8.1 to emphasize the smallness of its influence on the sensitivity)

contributions. In the current generation of GWOs, the optical readout loss is on the order of 10% [228], and in next observatory generation 3–5% might be achievable [229]. There might be a way to mitigate this loss by parametric amplification before detection, as I discussed in Chapter 7. The only source of detection loss that cannot be mitigated by such amplification is the loss in the Faraday isolator used for injecting external squeezing. We assume this to be a limitation in the detection loss, which corresponds to the 0.5% [229] mentioned in the main text.

Internal loss will be increased due to the additional optical surfaces of the nonlinear crystal and the absorption of the crystal. While the actual contribution

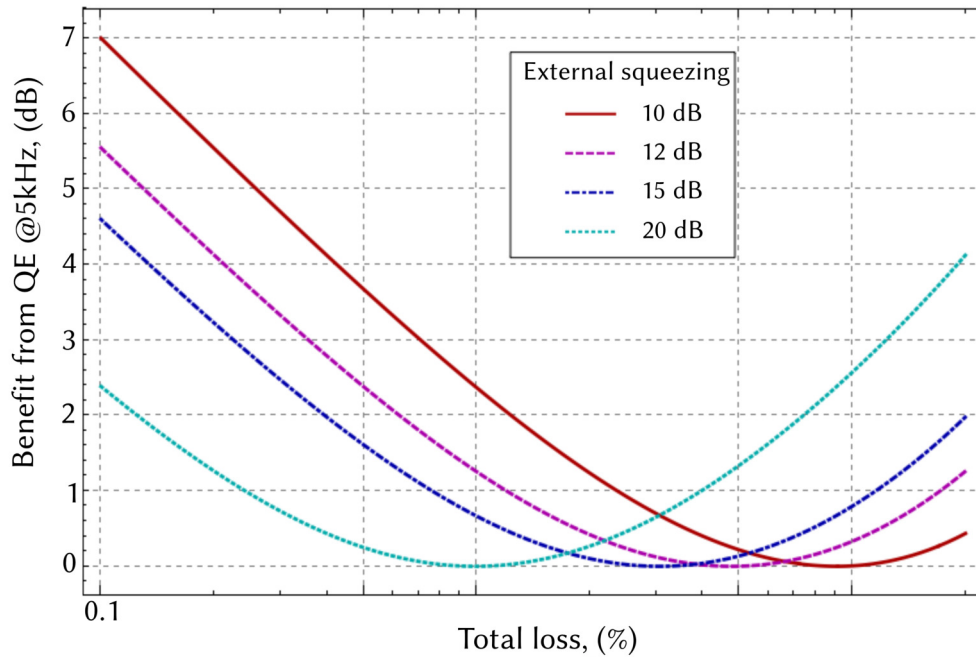


Fig. 8.7. An improvement in the sensitivity of the detector by quantum expander, relative to the detector with external squeezing injection, depending on the amount of total loss (internal and readout). The higher is the external squeezing, the more stringent is the loss requirement for being able to benefit from using the quantum expander. The sensitivity depends in a non-trivial way on the losses, which is reflected in the benefit from QE shown on the figure.

to the loss from such a crystal requires a separate investigation, we give an estimate based on the squeezing cavity design for the table-top experiments. If the PPKTP crystal is used, its absorption is ~ 100 ppm per cm depending on wavelength [207]; the surfaces of the crystal will have to be coated with anti-reflecting coating to minimize the scattering loss. We estimate that the current standard technology can bring this added loss on the level of 200–500 ppm in single-pass.

We would like to emphasize, that not every configuration of the GWO will be able to get a significant benefit from quantum expansion when the external squeezing is in use. Depending on the amount of loss, and amount of external squeezing injected, the benefit will vary. The reason is an additional de-amplification of the signal in the quantum expander — the same effect that we discuss in detail

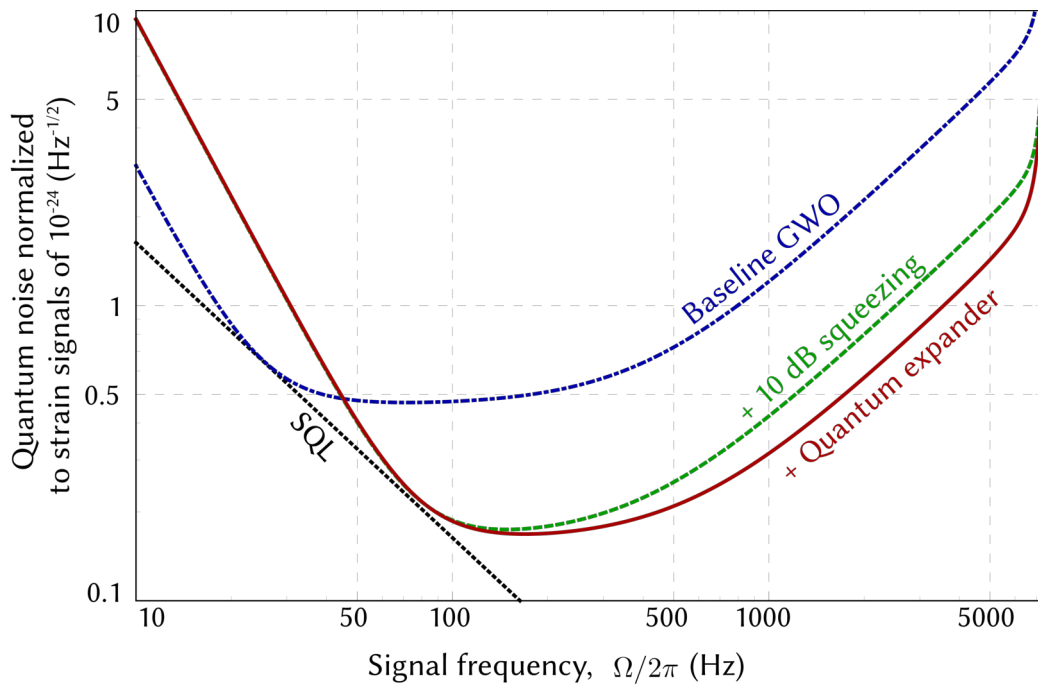


Fig. 8.8. An example of sensitivity improvement in a particular design of a detector with 1% of total loss and 10 dB external squeezing injection, the parameters are given in Table 8.1.

in Chapters 67. When the loss is high, the squeezing of the noise by quantum expander in addition to external squeezing might be not significant. However, the parametric process inside the detector reduces the signal, hence the signal-to-noise ratio might even become reduced compared to the detector without quantum expander, if the sub-optimal parametric gain is chosen. There always exists an optimal gain, for which the benefit is maximal. If the loss is high, it might be optimal to amplify the signal (and anti-squeeze the noise), similar to the Caves' amplification discussed above. We demonstrate possible improvements to the sensitivity in Fig. 8.7. We note, that this specific design is based on the benchmark parameters adopted by the LIGO-Virgo Collaboration, as presented in Table 8.1, and corresponds to the sensitivity as given in Fig. 8.8. In reality, the benefit from quantum expansion can be increased by optimizing the optical design (e.g. SE cavity length and mirrors' reflectivities). The optimized sensitivity given by the quantum expander is a topic of future studies.

8.2.3 Crystal inside the observatory

There are several issues to be taken into account with placing the crystal inside the SE cavity.

First, the size of crystal itself has to be large enough so that the optical beam does not clip on the edges of the crystal. Currently the diameter of the beam inside the SE cavity is $\sim 2\text{cm}$ [10], with the focal point outside the SE cavity. For comparison, as size of typical PPKTP crystal used in the squeezed light generation is $1\times 2\text{ mm}$ [207]. The crystal can be custom-made, or other nonlinear material can be used. Further, the beam can be focused inside the SE crystal by changing the curvatures of the mirrors of SE cavity, without using additional optics.

Second, the absorption and scattering in the crystal are generally an important issue due to possible heating. However, as in this design the detector operates at the dark port condition, there is no bright carrier field.

Third, the crystal has to be pumped with the frequency doubled parametric pump, which requires additional optical elements that would deliver the pump beam to the crystal and ensure the match between modes of the pump and the main beam. This can be done in multiple ways. As the wavelength of the pump is so different from the fundamental wavelength, it is possible to coat optical elements with different coatings, such that an additional cavity is formed by the SEM and ITM for the pump [70, 72]. Alternatively, the pump can be brought in by replacing the steering mirrors in the SE cavity with dichroic mirrors, transmissive for the frequency doubled pump. In any case, no additional optics inside the main interferometer would be required.

In conclusion, while a non-linear crystal inside the interferometer is technologically challenging, we do not foresee fundamental problems, and expect our proposal for quantum expansion to motivate the future research and development work in this direction.

8.3 Astrophysical analysis

Currently all GW observatories maximize the signal-to-noise ratio at frequencies around 100 Hz, where signals of compact binary inspirals can be observed. Merger and post-merger signals from binary neutron stars are expected to be at

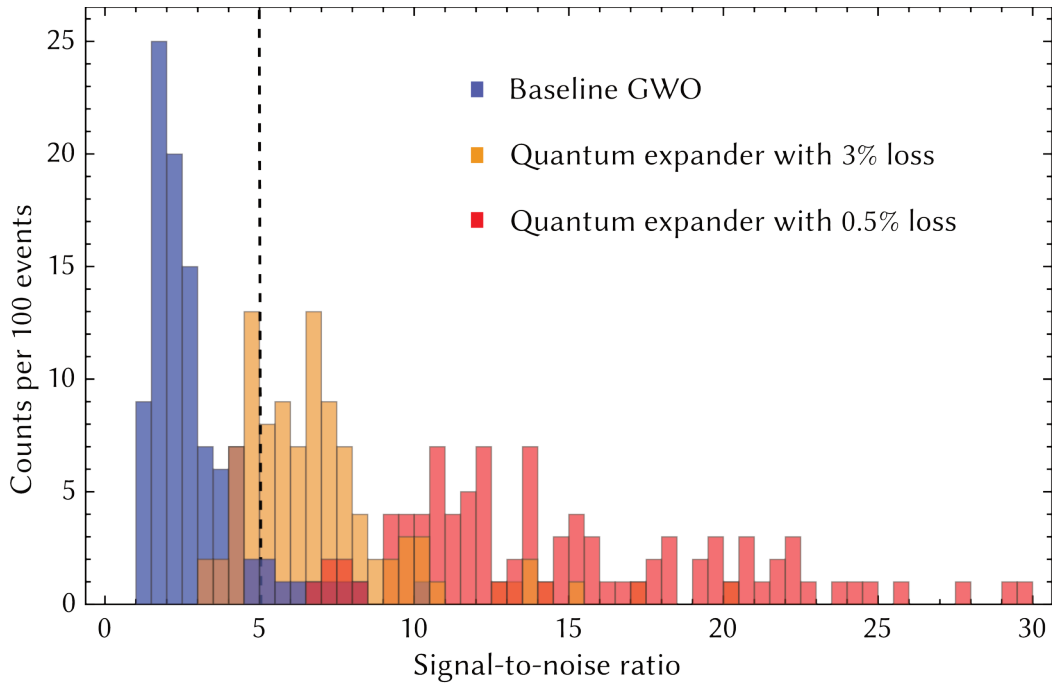


Fig. 8.9. Histogram for signal-to-noise ratio of the loudest event for 100 realizations in the Monte-Carlo simulation. Blue bins represent the SNR of our baseline gravitational wave observatory. Orange and red bins are associated with the quantum expander with total loss around 3% and 0.5%, respectively. The black dashed line indicates a detection threshold (SNR = 5). We used the equation of state in [230, 231] and the binary merger rate is taken to be $R = 1.54 \text{Mpc}^{-3} \text{Myr}^{-1}$. The mass distribution for each neutron star in the binary is taken to be Gaussian centered around $1.33 M_{\odot}$.

frequencies around 1-3 kHz, where the sensitivity of the detectors significantly deteriorates due to the detection bandwidth.

Quantum expansion of the detection bandwidth allows to increase the sensitivity exactly at these frequencies, as shown in Fig. 8.5. In order to illustrate the potential of the quantum expander, we compute the SNR of a particular model of the post-merger signal [230, 231]. The method we used here follows the estimation procedure as described in [64, 232]. We perform a Monte Carlo simulation based on the following assumptions: first, the mass of each individual neutron star in a binary system follows an independent Gaussian distribution centered at $1.33 M_{\odot}$ with variance $0.09 M_{\odot}$. The distributions of angular sky position, inclination and polarization angles, and the initial phase of the source are

assumed to be flat. The searching range is assumed to be 1 Gpc and the event rate is taken to be $\approx 1 \text{ Mpc}^{-3} \text{ Myr}^{-1}$. Second, the post-merger waveform is assumed to be a parametrized damped oscillation, which depends on the equation of state of a neutron star, and in frequency domain it is given by the equation:

$$h(f) = \frac{50 \text{ Mpc}}{\pi d} h_p \frac{Q(2f_p Q \cos \phi_0 - (f_p - 2ifQ) \sin \phi_0)}{f_p^2 - 4if f_p Q - 4Q^2(f^2 - f_p^2)}, \quad (8.33)$$

where d is the source distance, h_p is the peak value of the wave amplitude, Q is the quality factor of the post-merger oscillation, ϕ_0, f_p are the initial phase and the peak frequency of the waveform, respectively. Among them, h_p, Q, f_p are parametrized by fitting with the results generated by numerical simulation [233] and they depend on the choice of equation of states. In the illustrative examples here, we make use of a relatively stiffer equation of state proposed in [234], where $Q = 23.3, h_p \approx 5 \times 10^{-22}$, and the peak frequency is given by:

$$f_p = 1 \text{ kHz} \left(\frac{m_1 + m_2}{M_\odot} \right) \left[a_2 \left(\frac{R}{1 \text{ km}} \right)^2 + a_1 \frac{R}{1 \text{ km}} + a_0 \right], \quad (8.34)$$

where $R = 14.42 \text{ km}$ is the radius of each neutron star, and $m_{1,2}$ are their masses. The parameters a_2, a_1, a_0 take the value of 5.503, $-0.5495, 0.0157$, respectively [234]. We define the signal to noise ratio as:

$$\text{SNR} = \int_{f_{\min}}^{f_{\max}} df \frac{|h(f)|^2}{S_{hh}(f)}, \quad (8.35)$$

where we take the integration range to be $f_{\min} = 1000 \text{ Hz}, f_{\max} = 4000 \text{ Hz}$. We run 100 Monte-Carlo realizations each with 1000 samples, corresponds to one-year observation. We exclude the binaries with total mass larger than $3.45 M_\odot$ since they will collapse into a black hole in a very short period of time, less than one period of post-merger oscillation. For each different interferometer parameter set, we selected out the loudest event in each Monte-Carlo realization and set $\text{SNR} = 5$ as a threshold signal-to-noise ratio.

We demonstrate the improvement in detection rates on the histogram in Fig. 8.9: from 9% chance to have a single loud event surpassing the detection threshold

after a full-year data acquisition in a baseline GWO, to roughly 76% and almost 100% for quantum-expanded detectors with 3% and 0.5% optical loss, respectively.

8.4 Different tuning of cavities in GW detectors

The quantum expander is an extension of internal squeezing approach discussed in Chapter 6. Depending on the tuning of the cavities in the detector, a crystal acts to produce internal squeezing or quantum expansion. In this section, I provide an overview of the physical picture behind these two regimes, and the connection between them. I provide an explanation of the resonance structure of the detector.

As I discuss above, for the differential mode the detector can be modeled as a system of two optical cavities: short signal extraction (SE) cavity and long arm cavities. The assumption of the short length for SE cavity allows to ignore the effects of its linewidth on the optical fields, assuming the cavity to introduce only a constant phase shift, dependent on the tuning. Often the SE cavity is treated as a compound mirror with an effective reflectivity, and it was proven in the scaling law theorem [196] that the quantum noises of such system have the same properties as of a full interferometer. However this approach, while being convenient for mathematical models, hides some important physical effects.

For the further explanation we have to define the phase convention we're going to work in. First consider the SE cavity alone, without the arm cavity. We define that inside the SE cavity the reflection off SEM picks up zero phase shift, and the reflection off ITM - phase shift of π , changing the sign. Then for the SE cavity the resonance condition is satisfied on the single trip from SEM to ITM light acquires the phase shift of $\pi/2$. In this case the field inside the cavity reaches maximal value and the effective reflectivity of the whole cavity for the incoming light is minimal. In the opposite case, when the cavity is off resonance (zero phase shift on a single pass), the reflectivity of the cavity is maximal.

When the arm cavity is added, the situation changes. In our phase convention when the arm cavity is on resonance, the field reflected off ITM now has zero phase shift (at resonance frequency). That means, that the resonance condition for the SE cavity changes: now the single pass phase of $\pi/2$ corresponds to the anti-resonant case, when the field inside the cavity is minimal. However, the effective

reflectivity of the SE cavity remains low, which often is taken as a signature of a "resonant" behavior, and that might lead to a confusion. The effect is due to the fundamentally two-mode nature of the system. As the sideband frequency increases, the arm cavity goes off resonance, and the reflection phase on the ITM changes, thus bringing SE on resonance, when the arm cavity is completely non resonant. If the SE is initially tuned to be on resonance together with the arm cavity, they both will go off resonance with increasing sideband frequency.

Correspondingly there are two tuning regimes of the gravitational wave detector. The first one is narrow-band, when the SE cavity is tuned on resonance with zero phase shift, and effective reflectivity of SE cavity is high, leading to a narrow bandwidth and high sensitivity of the detector. The second tuning is broadband, when the SE cavity is off resonance, and its effective reflectivity is lower, leading to a broader bandwidth but reduced sensitivity.

Now, if we add a nonlinear crystal inside the SE cavity, the effect will differ for these two tunings. The broadband case I discussed in the current Chapter: squeezing will be produced only at high frequency, thus resulting in the expanded bandwidth. The narrowband case corresponds to a single-cavity case, where the squeezing is produced at low frequencies, as it was considered in Chapter 6.

The general expressions for the signal and noise that are valid for any tuning were derived in Eq. 8.20. Making a single-mode approximation for the arm cavity (but not for the SE cavity) and assuming the SE cavity to be short, ($\tau_{SE}=0$), these relations take a form:

$$\mathcal{R}(\Omega) = \frac{\gamma_{\text{arm}}(e^{2i\phi} - R_{\text{SE}}e^{2q}) + i\Omega(e^{2i\phi} + R_{\text{SE}}e^{2q})}{\gamma_{\text{arm}}(e^{2q} - R_{\text{SE}}e^{2i\phi}) - i\Omega(R_{\text{SE}}e^{2i\phi} + e^{2q})} \quad (8.36)$$

$$\mathcal{T}(\Omega) = -\frac{4ik_p E e^{i\phi} e^q \sqrt{\gamma_{\text{arm}} \tau_{\text{arm}} T_{\text{SE}}}}{\gamma_{\text{arm}}(e^{2q} - R_{\text{SE}}e^{2i\phi}) - i\Omega(R_{\text{SE}}e^{2i\phi} + e^{2q})}. \quad (8.37)$$

Since we are mainly interested in two tunings, we can compute the sensitivity for these two cases:

$$S_h(\Omega)|_{\phi=\frac{\pi}{2}, 0} = \frac{\hbar c}{8\omega_0 L_{\text{arm}} P_c} \frac{\gamma_{\text{arm}}^2 (1 \pm e^{2q} R_{\text{SE}})^2 + \Omega^2 (1 \mp e^{2q} R_{\text{SE}})^2}{4e^{2q} T_{\text{SE}}^2 \gamma_{\text{arm}} \tau_{\text{arm}}}, \quad (8.38)$$

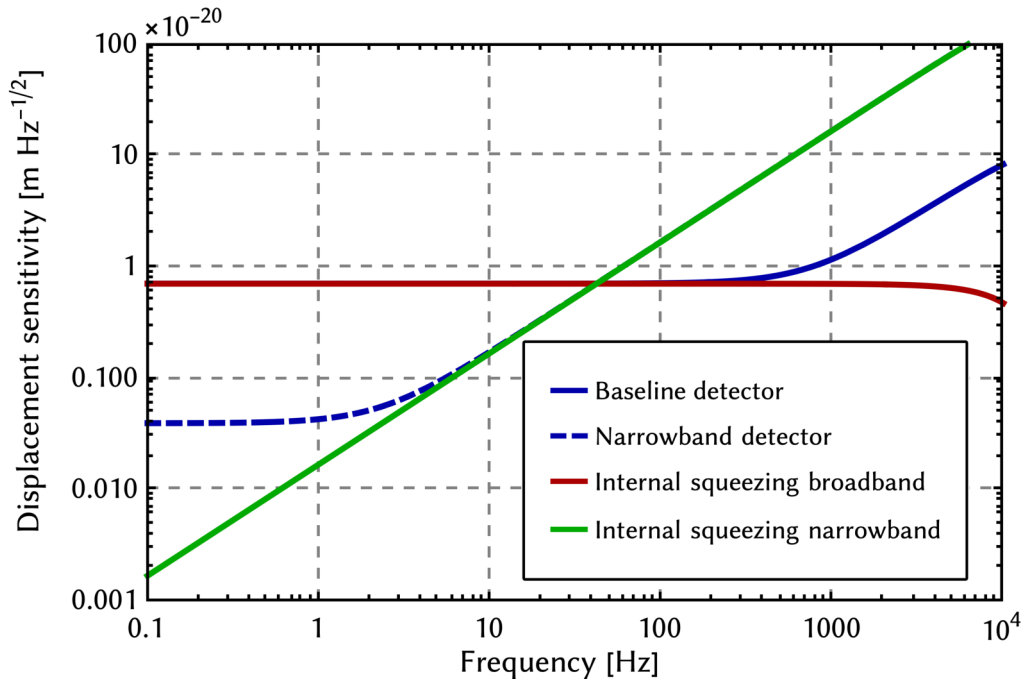


Fig. 8.10. Two tunings of the GW detector with internal squeezing. In a narrowband detector, internal squeezing increases sensitivity at low frequencies, increasing the peak sensitivity. In a broadband detector, internal squeezing increases the sensitivity at high frequencies, expanding the detection bandwidth.

and we can define the detector bandwidth as half width at half maximum of the SNR $S_h^{-1}(\Omega)$:

$$\gamma_q|_{\phi=\frac{\pi}{2},0} = \gamma_{\text{arm}} \frac{1 \pm e^{2q} R_{\text{SE}}}{1 \mp e^{2q} R_{\text{SE}}}. \quad (8.39)$$

One can see, that in the absence of internal squeezing $q = 0$, tuning the detector to $\phi = \pi/2$ achieves a broadband regime: $\gamma|_{\phi=\pi/2} \approx \gamma_{\text{arm}}(1 - R_s) \equiv \gamma_{\text{baseline}} > \gamma_{\text{arm}}$. The opposite tuning, $\phi = 0$, is indeed narrowband: $\gamma|_{\phi=0} \approx \gamma_{\text{arm}}(1 - R_s) < \gamma_{\text{arm}}$. This effect is enhanced in the presence of internal squeezing, $q > 0$: in broadband case $\gamma \xrightarrow{q \rightarrow q_{\text{th}}} \infty$, and in narrowband case $\gamma \xrightarrow{q \rightarrow q_{\text{th}}} 0$. The comparison of the two sensitivities in Fig. 8.10 highlights the effect of reduced bandwidth for the narrowband detector and expanded bandwidth for the broadband one.

From the perspective of the SSBL, both cases achieve the same enhancement to the sensitivity-bandwidth product but by different means: one case enhances the bandwidth, the other - peak sensitivity, at a price of reduced bandwidth. For

this sensitivity-bandwidth product in both broadband and narrowband the same value can be obtained at threshold:

$$\int_0^\infty \frac{1}{S_{xx}(\Omega)} \frac{d\Omega}{2\pi} = \frac{e^{2q} T_{SE}^2 \tau}{e^{4q} R_{SE}^2 - 1} \xrightarrow{q \rightarrow q_{th}} \infty. \quad (8.40)$$

This, according to the QCRB, tells us that the sensitivity-bandwidth product can be infinite, thus either the peak sensitivity or the bandwidth can be increased compared to the classical case. I show this explicitly by calculating the bandwidth γ of the signal-to-noise ratio as a function of SR tuning ϕ :

$$\gamma = \gamma_{arm} \frac{\sqrt{(1 + e^{4q} R_{SE}^2)^2 - 4e^{4q} R_{SE}^2 \cos 4\phi - 2e^{2q} R_{SE} \sin 2\phi}}{1 + e^{4q} R_{SE}^2 + 2e^{2q} R_{SE} \cos 2\phi}. \quad (8.41)$$

In the limiting case of internal gain at parametric oscillation threshold, $e^{2q} = 1/R_{SE}$, I obtain the expressions for the bandwidth and the gain in peak sensitivity compared to the case without internal squeezing, $\mathcal{G} = S_{xx}^{q=0}(0)/S_{xx}(0)$:

$$\gamma = \gamma_{arm} (\sqrt{2} - 1) \tan \phi, \quad (8.42)$$

$$\mathcal{G} = \frac{1 + R_{SE}^2 - 2R_{SE} \cos 2\phi}{4R_{SE} \sin^2 \phi}. \quad (8.43)$$

In the broadband tuning case the bandwidth becomes infinite: $\gamma \xrightarrow{\phi \rightarrow \pi/2} \infty$, while the peak sensitivity remains almost unchanged $\mathcal{G} \xrightarrow{\phi \rightarrow \pi/2} 4R_{SE}/(1 + R_{SE})^2 \approx 1$. In the narrow-band tuning case bandwidth approaches zero, and peak sensitivity approaches infinity.

8.5 Conclusion and outlook

The ‘quantum expander’ takes advantage of the coupled cavity structure of the GW detector and the internal squeezing approach for increasing the high-frequency sensitivity without affecting the low-frequency one. Using quantum expander for a selected model GW observatory will allow to significantly increase the detection rates for the neutron-star mergers, and enhance the SNR for post-

merger oscillation of the formed object. In the previous chapters I showed how internal squeezing can help to increase the peak sensitivity and overcome decoherence, and here I generalized the discussion to include a particular resonance structure of the detectors. I showed how internal squeezing in a form of quantum expander can be established as a practical approach for increasing the sensitivity of gravitational-wave detectors. When the concept is applied to a specific detector, the parameters have to be optimized to reach the best sensitivity. In some parameter regimes one has to find a balance between the practical complexity of implementing quantum expansion and achievable enhancement in sensitivity.

The analysis performed in this chapter (and presented in full in the Appendix A), considers the most general configuration of a GWO, which includes practically all relevant effects of quantum noise, and can be used to compute the sensitivities for any parameter combination (losses, detunings, squeezing, etc.). Applying this model to find a practical design of a future GW based on quantum expander is currently underway.

While in this chapter the discussion is focused on the gravitational-wave detection, the same concept can be implemented in different context of quantum metrology. There it would serve as an environment engineering approach, which engineers the coupling between the cavity and the environment by creating the multi-resonance structure and adding parametric amplification there. This would be the direction of future research.

In the next chapter I will explore the ways how internal squeezing can help to broad the sensitivity in a different — *dynamical* — way by enhancing the optomechanical interaction.

Theoretical investigation of an optical spring enhancement via internal squeezing

Back-action evading and QND techniques, such as speedometer approaches discussed in Chapters 4,5, allow to increase the sensitivity at low frequencies and thus detect binary objects at earlier stages of their evolution. The quantum expander increases the bandwidth of the detector towards higher frequencies, which allows to better observe the late stages of evolution (merger and post-merger).

In this chapter, I present an approach, which focuses on enhancing the sensitivity in the middle frequency range (between 20 and 200 Hz). This approach is also based on internal squeezing, and takes advantage of optomechanical interaction between the light and the test masses to enhance the sensitivity at a specific frequency. This frequency can then be shifted by tuning the phase of the pump field, such that it follows the GW signal. Such dynamical tuning would allow to significantly enhance the sensitivity for signals of special interest (e.g. from neutron star mergers). The advantage of this approach is that it allows to operate the detector in quantum expansion mode most of the time, and only switch to dynamical tuning when an extraordinary signal is detected.

In this chapter I focus on the effects of radiation-pressure on the sensitivity, and how internal squeezing can affect them. Unlike the previous chapters, where the SE cavity was tuned exactly on (or exactly off) resonance, in this chapter I consider an arbitrary tuning of the cavity, which results in additional optical and optomechanical resonances. The results of this chapter were partially published in [72].

9.1 The optical spring in GW detectors

Electromagnetic dynamical back-action was first observed in radio-frequency systems, and its existence predicted for optical Fabry-Perot cavities by Braginsky and his colleagues more than 50 years ago [89, 171]. 33 years later, Braginsky and co-workers made the first proposal of using the dynamical back-action to improve the sensitivity of laser-interferometric gravitational-wave detector [127]. The new scheme was called ‘optical bar’, since the light’s radiation pressure force rigidly connects two far separated mirrors, which are suspended as pendula but quasi-free otherwise. This way, a gravitational-wave signal is transformed into an acceleration of mirrors with respect to the local frame. The interferometric topologies that are considered in [127] as well as in related work [235] are different from the Michelson topology having a balanced beamsplitter, and were not experimentally realized so far. Recently, a more practical design was proposed [236]. The second proposal was made in 2002 by Buonanno and Chen [129] and was called ‘optical spring’. It targets the sensitivity improvement of Michelson-type gravitational-wave detectors having a signal-recycling (SR) cavity [237, 238] or signal-extraction (SE) cavity, also called resonant-sideband extraction [210, 239]. For the purpose of utilizing the optical spring in a Michelson interferometer operated on dark output port, these cavities need to be detuned from carrier light resonance. If the frequency of the carrier light is blue-detuned with respect to the cavity, the lower sidebands of phase modulations that are produced by gravitational waves and that are matching the detuning frequency get optically enhanced while the corresponding upper sidebands are suppressed. Due to energy conservation, the mechanical (pendulum) motion of the suspended mirror is enhanced [37, 240]. The overall process corresponds to optomechanical parametric amplification and results in optical heating of the mechanical motion, i.e. the opposite of optical cooling [241]. The radiation pressure of the light not only results in an optomechanical parametric amplification of the pendulum motion but also in an additional (optical) spring constant that increases the pendulum resonance frequency from typically 1 Hz to an optomechanical resonance of up to about 100 Hz. Around this frequency the mechanical response of the GW detector is significantly enhanced and its sensitivity improved. The frequency of the optomechanical resonance depends on the detuning and the optical power inside

the arms of the detector. To further exploit the optical spring, it was proposed to dynamically change the detuning by moving the SE mirror in order to follow expected chirps of GW signals [242, 243]. The optical spring was observed in several experiments [37, 191, 244–253]. The gravitational-wave detectors GEO 600 [254], Advanced LIGO [10], Advanced Virgo [12], and KAGRA [255] use either SR or SE cavities, but so far have not yet employed the optical spring for a sensitivity enhancement due to the requirement of additional control techniques.

The conventional scheme for producing the optical spring does not use any additional parametric amplification of purely optical kind. Recent work, however, proposed complementing the SE cavity with optical-parametric amplification [205] to allow for shifting up further the optomechanical resonance frequency without increasing the light power in the arms.

In this work we extend the consideration in [205] and analyze a more general situation, in which not only the parametric gain is varied but also the angle of the amplified quadrature amplitude. The parametric gain relates to the *intensity* of the second-harmonic pump field, whereas the angle relates to its *phase*. In particular the last parameter can be quickly changed providing a new degree of freedom for realizing dynamical detuning of the optical spring properties. We consider the internal quantum noise squeezing that is accompanied with the optical-parametric amplification together with the one from the optomechanical parametric amplification and derive spectral densities. Furthermore, we propose utilizing the second-harmonic pump field to implement a ‘local readout’ of the motion of the arm cavity input test masses (ITMs) [256], see Fig. 9.1. The local readout mitigates the unwanted effect of the optical spring, which is the rigid connection of the ITMs with their respective end test mass (ETM) at frequencies below the optical spring and a corresponding sensitivity loss at these frequencies.

9.2 The optomechanical system

Both optical and optomechanical parametric amplification can be described in a similar way by their effect on the light field. Both result in a consecutive rotation of quadratures (determined by the phase of the pump for optical amplification and by the detuning of the SE cavity for the optomechanical one), squeezing

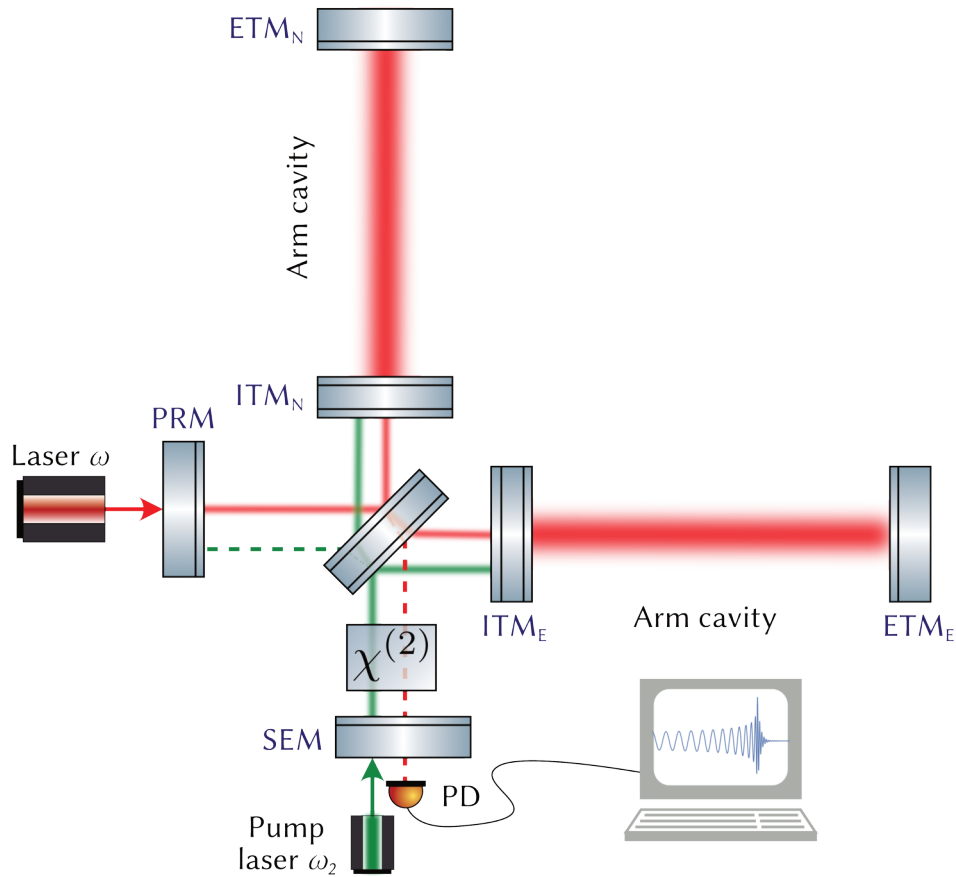


Fig. 9.1. Schematic diagram of a GW detector proposed here. On top of the Advanced LIGO topology, consisting of arm resonators, a power-recycling mirror (PRM) and a signal-extraction mirror (SEM), a second-order nonlinear ($\chi^{(2)}$) crystal is placed in the SE cavity. The main carrier light at optical frequency ω is blue-detuned with respect to this cavity, but resonating in the arm cavities as well as in PR cavity. The second-order nonlinear crystal is pumped with a light field at frequency $\omega_2 = 2\omega$ resulting in optical-parametric amplification (OPA) of light at ω , including its quantum uncertainty. The pump field (displaced for better visibility) is also used to measure the differential motion of the ITMs. The two different wavelengths can be separated easily with dichroic beamsplitters (not shown). ITM_{N,E}: input test mass in north and east arm, respectively. ETM_{N,E}: end test mass.

(optical and ponderomotive correspondingly) and rotation again [35, 130]. Thus the optical spring can be created by both types of parametric amplification,

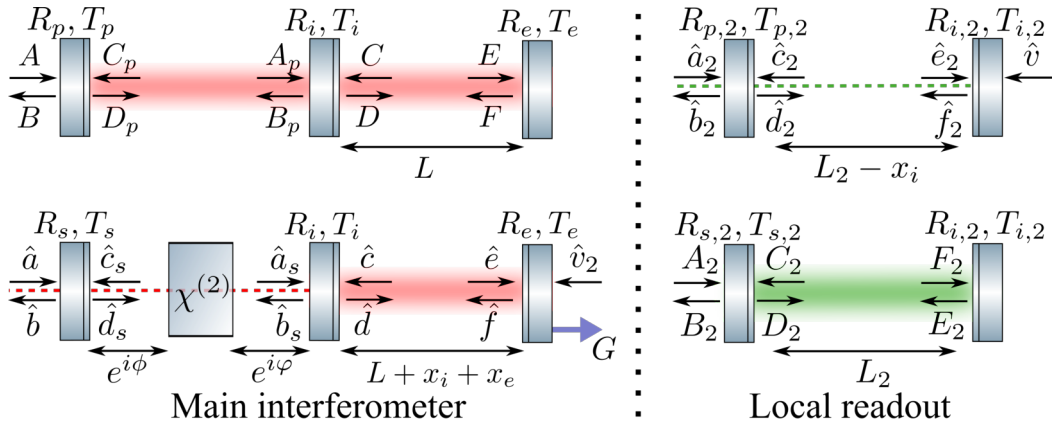


Fig. 9.2. Notations of the optical fields for the PR cavity together with the common mode of the arm cavities at ω (top left), for the SE cavity together with the differential mode of the arm cavities at ω (bottom left), and respective parts of the interferometer in Fig. 9.1 at ω_2 , which belongs to the local readout (top and bottom right). Operators are annihilation operators and denote complex amplitudes including their uncertainties. Capital letters A to F denote complex amplitudes whose uncertainties are irrelevant. Subscript ‘s’: signal extraction; ‘p’: power recycling; ‘i’: input to arm cavity; ‘e’: end of arm cavity; ‘2’: optical frequency ω_2 . R, T : amplitude reflectivity and transmissivity of mirrors. L is the average length of the arm resonators, L_2 is the relevant average length of the local read out, and $x_{i,e}$ represent their dynamical parts due to differential test mass motion. ϕ and φ are additional phases accumulated by the light field inside the SE cavity due to the cavity detuning. The gravitational-wave signal (‘G’) corresponds to a differential change of the arm length L .

and they can also be combined to achieve a higher flexibility. In this section I derive explicitly the optical spring in the case of additional optical-parametric amplification inside the SE cavity and show the effect of the squeeze angle on it.

We use an effective picture, where the interferometer is split into two separate cavity systems, coupled only via the displacement of the test mass mirrors [196]. The first cavity system (Fig. 9.2, top left) corresponds to the common mode, whose modulation as well as its uncertainty are irrelevant for the signal-to-noise-ratio of a gravitational-wave signal in the differential mode. It is thus fully described by the classical carrier fields at frequency ω . The second cavity system corresponds to the differential mode at ω and requires a quantized description (Fig. 9.2, bottom left), as we considered in the previous Chapter 8 In this Chapter I also explicitly

consider the pump field at ω_2 in the calculation. We propose to use the pump not only for the parametric process, but also for measuring the differential motion of the ITMs (local readout). For this purpose the pump is organized into a short Michelson interferometer, formed by ITMs in Fig. 9.1. Quantum fields for this system are defined in Fig. 9.2 (right). This part of the interferometer is considered in Section 9.2.1. The first mirrors of the main interferometer cavities (Fig. 9.2, left) are the power recycling (PRM) and signal extraction (SEM) correspondingly, and the middle (input, i) and the end (e) mirrors are combinations of ITM and ETM. Then the differential motion of four mirrors can be defined as the motion of input and end mirrors in the effective cavity picture:

$$\hat{x}_-(\Omega) = \left(x_{\text{ITM}}^{(E)}(\Omega) + x_{\text{ETM}}^{(E)}(\Omega) \right) - \left(x_{\text{ITM}}^{(N)}(\Omega) + x_{\text{ETM}}^{(N)}(\Omega) \right) = x_i(\Omega) + x_e(\Omega). \quad (9.1)$$

Relative to the beamsplitter only the far mirrors are accelerated due to the gravitational wave force G , as the input mirrors are so close to the beamsplitter that the effect can be neglected. In addition, all mirrors are accelerated by the light's radiation pressure force $F_{(i,e,2)}^{\text{ba}}$, which is proportional to the power of the light shining on the mirror and which we call back-action.

$$\hat{x}_i(\Omega) = \chi_i(\Omega) [F_i^{\text{ba}} - F_2^{\text{ba}}], \quad (9.2)$$

$$\hat{x}_e(\Omega) = \chi_e(\Omega) [F_e^{\text{ba}} + G], \quad (9.3)$$

where $\chi_{i,e} = [-m\Omega^2]^{-1}$ are mechanical susceptibilities of the input and end mirrors, that we assume here to be identical quasi-free masses of mass m . The input mirror is driven by two different optical forces, due to the additional back-action F_2^{ba} from the second harmonic pump field.

When the cavity is detuned from resonance, the back-action force has a position-dependent dynamical part, causing the optical spring effect. We thus split the force into two contributions – the fluctuating part due to the quantum uncertainty of the light's amplitude quadrature, and the optical spring force $F^{\text{ba}} = F^{fl}(\Omega) - \mathcal{K}(\Omega)x(\Omega)$, where $\mathcal{K}(\Omega)$ is the optical spring constant, also called *optical rigidity*.

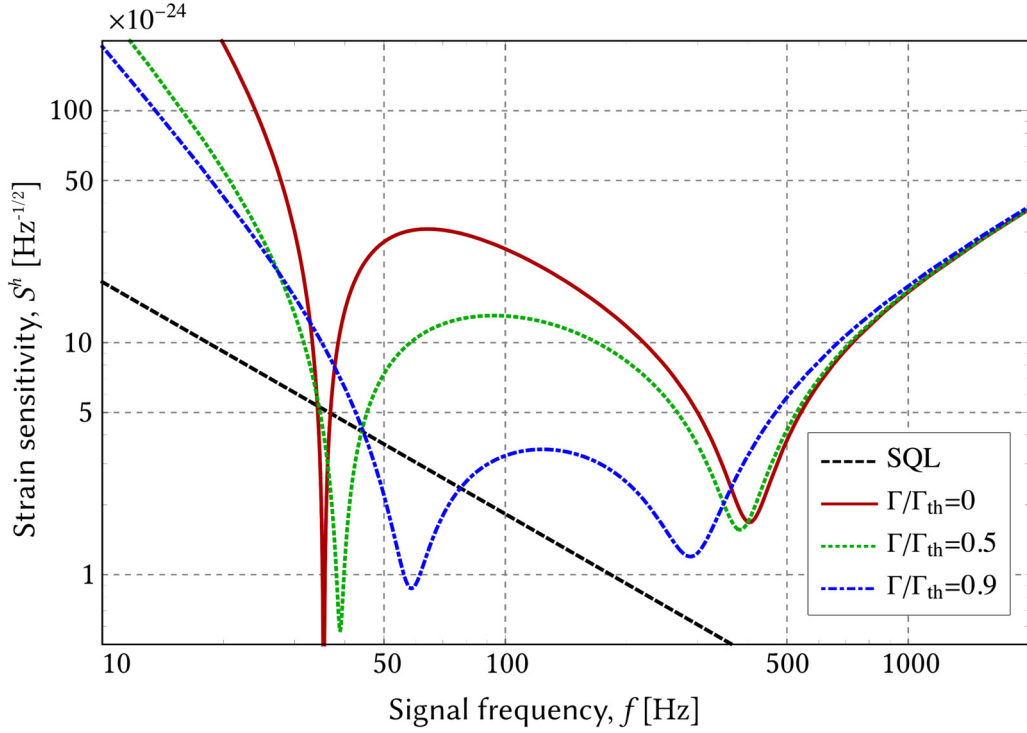


Fig. 9.3. Example of tuning of the sensitivity by changing the strength of intra-cavity amplification. Three plots correspond to three different values of gain, with $\delta/2\pi = 580$ Hz and amplification phase $\theta = 0$. This shows the enhancement of the optical spring with parametric amplification (i.e. the shift of optomechanical resonance to higher frequency.) The parameters of the system are: $I_c = 840$ kW, $T_i = T_s = 0.18$, $L = 4000$ m.

We calculate the optical rigidity in the single-mode approximation, where the back-action on the input and end mirrors are identical, yielding

$$F_{i,e}^{\text{ba}}(\Omega) = F_{fl}(\Omega) - \mathcal{K}(\Omega)x_-(\Omega). \quad (9.4)$$

The single-mode approximation [35], as discussed in the previous chapters, further involves (i) the sideband frequency and the arm cavity detuning being much smaller than the cavity free spectral range $\Omega, \delta_a \ll c/L$, with L being the arm cavity length, and c the speed of light, and (ii) the transmissivity $T_{i,e}$ of mirrors being small, so that we can make a Taylor expansion $R_{i,e} \approx 1 - T_{i,e}^2/2$. The single-mode approximation enables us to introduce an effective linewidth γ and the

detuning of the SE cavity δ_s as well as the normalized optical parametric gain (per cavity round trip) Γ in the following way (see details in the Appendix A)

$$\gamma = \frac{\gamma_a T_s}{D_0}, \quad (9.5)$$

$$\delta_s = \frac{2\gamma_a R_s}{D_0} (\cosh 2q \cos 2\phi \sin 2\varphi + \sin 2\phi \cos 2\varphi), \quad (9.6)$$

$$\Gamma = \frac{2\gamma_a R_s \sinh 2q \cos 2\phi}{D_0}, \quad \text{with} \quad (9.7)$$

$$D_0 = 1 + 2R_s (\cosh 2q \cos 2\phi \cos 2\varphi - \sin 2\phi \sin 2\varphi) + R_s^2, \quad (9.8)$$

where $\gamma_a = c(T_i^2 + T_e^2)/(4L)$ is the linewidth of the arm cavity, ϕ and φ are additional phases accumulated by the light field inside the SE cavity due to the cavity detuning and q is a squeeze factor on the single pass through the optical-parametric amplifier.

We find that the optical parametric gain Γ influences the total detuning of the interferometer δ_{eff} as well as the light power associated with the optical spring J_{eff}

$$\delta_{\text{eff}} = \sqrt{\delta^2 - \Gamma^2}, \quad (9.9)$$

$$J_{\text{eff}} = J \delta_{\text{eff}}^{-1} (\delta - \Gamma \sin 2\theta), \quad (9.10)$$

where $\delta = \delta_a + \delta_s$ with δ_a the arm cavity detuning, θ is the phase of the optical-parametric amplification (the squeeze angle), and $J = 4\omega I_c/(mcL)$ the normalized optical power with I_c being the power circulating in the arm cavities.

Given these definitions the optical rigidity $\mathcal{K}(\Omega)$ is found to be

$$\mathcal{K}(\Omega) = \frac{mJ(\delta - \Gamma \sin 2\theta)}{(\gamma - i\Omega)^2 + \delta^2 - \Gamma^2} = \frac{mJ_{\text{eff}}\delta_{\text{eff}}}{(\gamma - i\Omega)^2 + \delta_{\text{eff}}^2}. \quad (9.11)$$

The optical spring is enhanced by optical-parametric amplifier, as we show on in Fig. 9.4 and has several important properties.

First, the maximal enhancement of the optical spring due to the internal squeezing is achieved if $\theta = -\pi/4$ (for $\delta > 0$) yielding $J < J_{\text{eff}} \propto J e^{2q}$. In this case, for instance, 3 dB of intra-cavity squeezing modifies the optical spring in the same way as doubling the optical power.

Second, using Routh-Hurwitz' criterion [257] one can show, that the system is always unstable, in the same way the optical spring without internal squeezing is [129, 196, 258]. The mechanical system can be stabilized via active feedback [129]. The optical-parametric process leads to an additional stability condition that has to be satisfied: $\Gamma^2 < \Gamma_{\text{th}}^2 = \gamma^2 + \delta^2$, which is a threshold for optical-parametric instability.

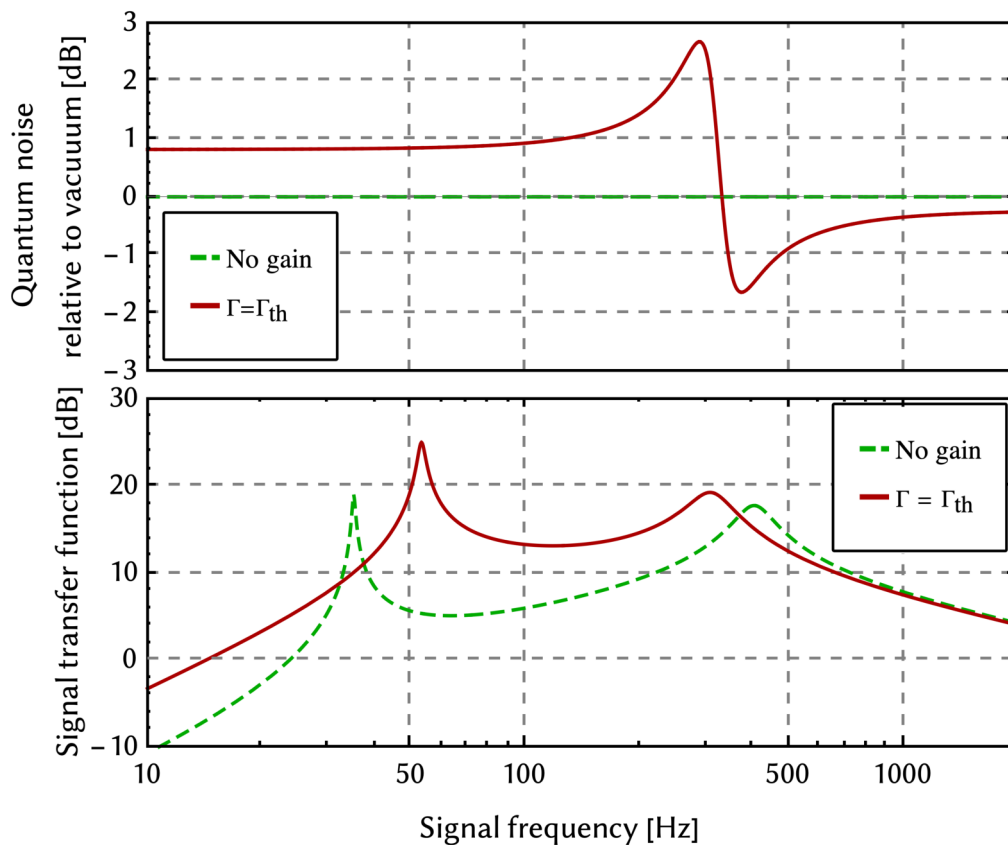


Fig. 9.4. Signal enhancement by optical spring amplification. Noise (top) and signal transfer function (bottom) behave differently when the gain is on (solid red) and off (dashed green). The signal is amplified significantly, yet the noise is increased as well, although only slightly. This demonstrates that the main effect on sensitivity is due to the optomechanical interaction (i.e. optical spring), and not noise squeezing. The parameters of the system are: $\delta/2\pi = 580$ Hz, $\theta = 0$, $I_c = 840$ kW, $T_i = T_s = 0.18$, $L = 4000$ m.

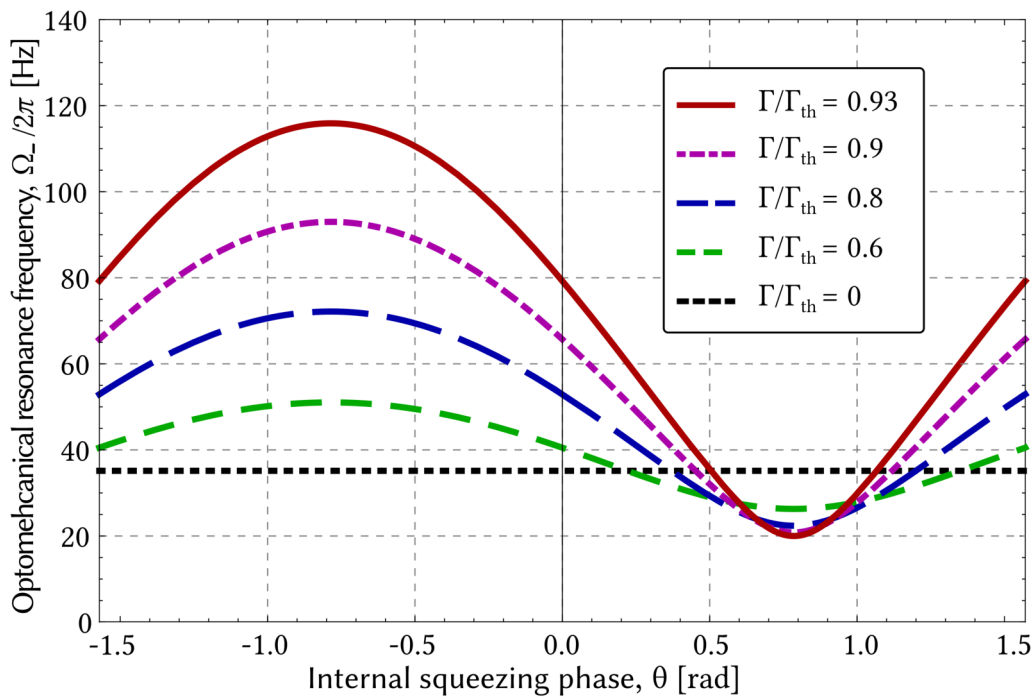


Fig. 9.5. Optomechanical frequency $\Omega_-/2\pi$ as a function of squeeze angle θ for different values of parametric gain Γ relative to the threshold value Γ_{th} . The parameters of the system are: $\delta/2\pi = 580$ Hz, $I_c = 840$ kW, $T_i = T_s = 0.18$, $L = 4000$ m.

Third, internal squeezing changes the dynamics and stability of the system. The characteristic equation for the optomechanical motion is

$$\Omega^4 + 2i\Omega^3\gamma + \Omega^2(\Gamma^2 - \gamma^2 - \delta^2) + J(\delta - \Gamma \sin 2\theta) = 0. \quad (9.12)$$

The resonances can be found in the perturbative way by expanding the roots of Eq. (9.12) in powers of γ . Then zeroth order of expansion gives two positive roots:

$$\Omega_{\pm}^{(0)} = \sqrt{\frac{\delta_{\text{eff}}^2}{2} \pm \sqrt{\frac{\delta_{\text{eff}}^4}{4} - J_{\text{eff}}\delta_{\text{eff}}}}, \quad (9.13)$$

where $\Omega_{-}^{(0)}$ corresponds to the shifted mechanical resonance, and $\Omega_{+}^{(0)}$ to the optical resonance. In the absence of optomechanical coupling, $J_{\text{eff}} = 0$, mechanical resonance is at zero, which corresponds to our assumption of having quasi-free masses, and $\Omega_{+}^{(0)} = \delta_{\text{eff}} = \sqrt{\delta^2 - \Gamma^2}$.

Notice how in this case quantum expansion appears naturally from selecting a broadband tuning $\phi = \pi/2$, $\varphi = 0$, $\cosh 2q = 0.5(1 + R_s^2)R_s^{-1}$: $D_0 \rightarrow 0$, $\gamma \rightarrow \infty$.

With increased effective power the mechanical resonance shifts to higher frequencies, and the optical one gets reduced, until, within the approximation used, these resonances become equal at the critical power $J_{\text{eff}}^{(c)} = \delta_{\text{eff}}^3/4$ [128]. Note that the absence of optomechanical coupling ($J_{\text{eff}} = 0$) can be due to zero power ($J = 0$) or if the condition $\Gamma \sin 2\theta = \delta$ holds. Generally, the effective power can be changed by tuning the squeeze angle, without affecting neither light power nor squeeze factor, see Fig. 9.5.

We propose thus to use this feature for *dynamical tuning* of the interferometer response to the GW signal. This way the mechanical resonance is changing adaptively to match the chirp GW signal, see Fig. 9.6. Tuning of the squeeze angle can be done in a straightforward way by tuning the phase of the second harmonic pump, e.g. by transmission through a fast electro-optical modulator. We note that the tuning speed is ultimately limited by the decay rate of the pump light's cavity.

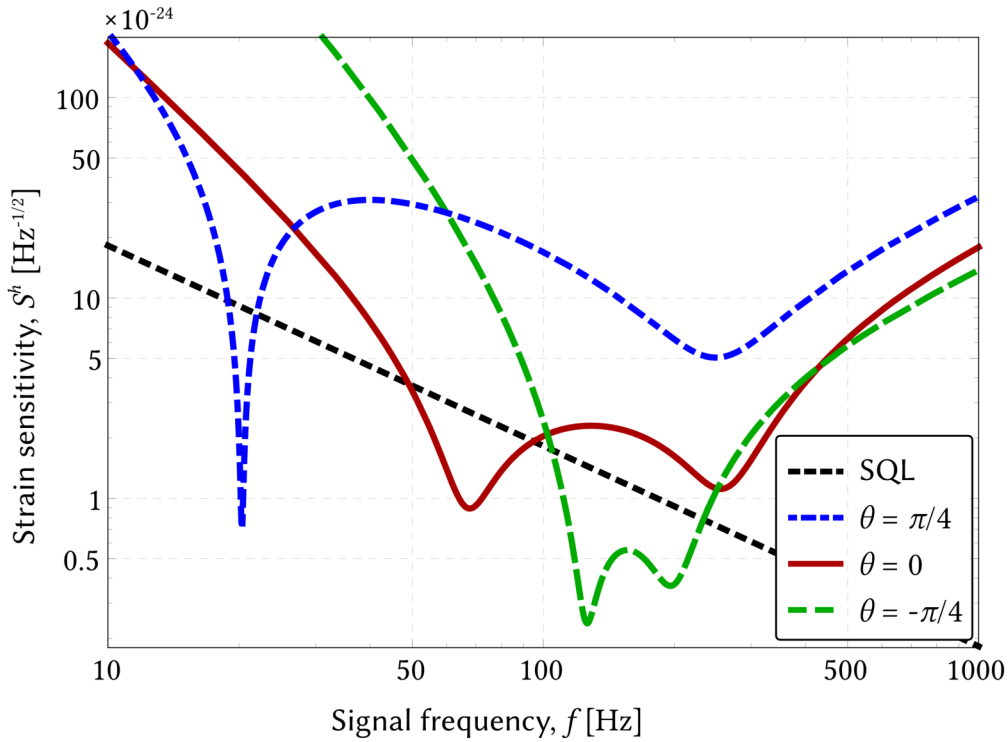


Fig. 9.6. Example of tuning of the sensitivity by changing only the squeeze angle of the intra-cavity amplifier. Three plots correspond to three different values of the angle, with $\delta/2\pi = 580$ Hz and $\Gamma/\Gamma_{\text{th}} = 0.93$. They demonstrate the possibility to engineer the optical spring by changing only the squeeze angle. Note that the generally poor sensitivity at low frequencies can be improved by an additional local read out of the differential motion of the near test masses [256]. The parameters of the system are: $I_c = 840$ kW, $T_i = T_s = 0.18$, $L = 4000$ m.

9.2.1 Sensing the radiation-pressure noise on input test masses

The optical spring can be efficiently combined with the *local readout* [256]. The idea of the local readout is based on that of the *optical bar*, proposed by Braginsky and co-authors. At frequencies below the optomechanical resonance, the ITMs and ETMs are connected in a rigid way via dynamical backaction. For this reason, at these low frequencies, the motion of the ETMs due to a gravitational wave causes an identical motion of the ITMs, which reduces the sensitivity at these frequencies. The idea behind the local readout is to measure the motion of the

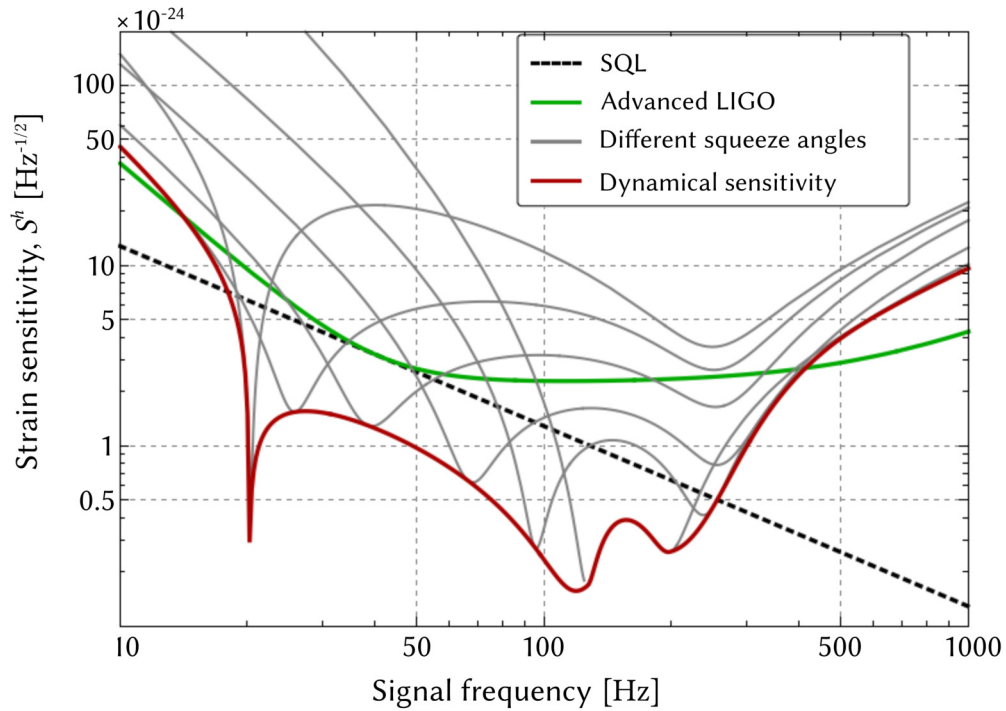


Fig. 9.7. Dynamical tuning of the sensitivity by changing only the squeeze angle of the intra-cavity amplifier. Grey plots correspond to different tuning angles, as the interferometer follows the GW signal. The red plot is a cumulative curve representing the maximal sensitivity over the whole dynamical tuning procedure. The parameters of the system are: $\delta/2\pi = 580$ Hz, $\Gamma/\Gamma_{\text{th}} = 0.93$, $I_c = 840$ kW, $T_i = T_s = 0.18$, $L = 4000$ m.

ITMs locally and to use this information in the data processing. This way the sensitivity can be greatly improved at low frequencies. Here we propose to use the second harmonic pump of the OPA to sense the local motion of the ITM. In this case the dark port of a second small Michelson interferometer, formed by ITMs, coincide with the bright port of the main interferometer, see Fig. 9.1 and 9.2. Both outputs have to be measured with balanced homodyne detectors with an optimal homodyne angle, and then combined in an optimal way. For the local readout it is important to take the motion of the central beamsplitter into account, as the arm length of the small interferometer is rather short and arm cavities are not used.

Using the second harmonic pump instead of a nearby wavelength [256] most

likely eases the fabrication of the optical components that are part of both interferometers. The large wavelength separation allows to manufacture a highly reflective optical coating on the ITMs for the local readout beam, while keeping a moderate transmissivity for the main beam to allow for over-coupling of the input light. The detection of the two beams can be done independently in efficient way, by separating the beams with dichroic beamsplitters, which avoids using polarization optics or filter cavities, as proposed in [256]. The particular design of the local readout and resulting sensitivity is a direction of future research.

9.3 Summary and outlook

In this chapter I analyze the optical spring that is created by the ‘conventional’ optomechanical parametric amplification inside a detuned cavity in combination with intra-cavity optical parametric amplification (OPA). Modifying the spectral density of the *conventional* optical-spring GW detector requires modifying the light power in the interferometer arms and/or changing the length of the signal recycling/signal extraction cavity. In this chapter I show how the same modification is achieved for the *OPA-enhanced* optical spring by changing the power of the OPA pump light and/or by changing the phase of the pump light. This opens a possibility for a more flexible tuning of the detector in-operation, since all the associated control is performed on the pump field independently on the main field. In particular, a dynamical tuning of the sensitivity in response to the GW signal can be performed in order to achieve the highest resolution at every signal frequency.

Such dynamical tuning would have certain practical limitations: the phase adjustment speed is limited by decay time of the optical cavities, and the detector has to be actively stabilized (since the optical spring is inherently unstable) dynamically with changing frequency. This excludes the possibility to use dynamical tuning for fast sweeping signals from binary black holes. However, the signal from neutron star merger usually remains at low frequencies for minutes, time potentially sufficient for dynamical tuning.

With this the overall concept of a broadband detector with internal squeezing is completed: at low frequency, quantum noise is suppressed with back-action

evading techniques (variational readout, frequency-dependent squeezing or speed-meter topology) and local readout, which allows to detect signals well before the merger; at mid-frequency range between ~ 20 Hz and ~ 200 Hz the dynamical tuning is switched on when suitable signal arrives; once the signal reaches higher frequencies, the dynamical tuning won't be fast enough (and strong enough), so the detector is switched in the quantum expander mode, that allows to observe the merger and post-merger signals. Note, that the dynamical sensitivity as presented in Fig. 9.7 uses physical detuning, and not only parametric phase, to achieve the optical spring. Therefore, this example is not easily transferred into quantum expansion mode (which requires a tuned detector). However, it is possible to create the optical spring only by changing the internal squeezing phase, but the resulting sensitivity requires further analysis.

The proposed parametric amplification can find its application in other designs too. In particular, Einstein Telescope design currently features two detectors - low frequency, and high frequency, where the former operates with low-power light and optical spring. The low light power for this design is critical, since the detector is planned to be cooled down to cryogenic temperatures for reducing thermal noises, and high light power would cause an absorption-induced heating. In this configuration an intra-cavity parametric amplifier would allow to reduce the light power without sacrificing the optical spring enhancement. Moreover, currently it is planned to use cost-intensive filter cavities for frequency-dependent squeezing that would suppress QRPN at low frequency. However, since the noise margin between the QRPN and technical noises is relatively small, a comparable enhancement might be achievable with local readout. This requires further investigation.

Finally, the pump field as the second carrier field might also be interesting for other schemes such as the double optical spring [131] or multi-carrier configurations [132, 190, 259], such as the one described in Chapter 5.

This work extends both aspects of the optical bar, the optical spring as well as the local readout, towards gravitational-wave detectors with intra-cavity parametric amplification, and shows that such an approach allows versatile engineering of GW detector sensitivities.

Conclusion and outlook

Quantum noise has been long thought to be the burden of gravitational-wave detection, limiting the sensitivity of the observatories almost at all signal frequencies. In this thesis I make an argument that it can become a useful tool that allows to increase the sensitivity in different ways at different frequencies. Such increase relies on the extensive use of quantum correlations: either between the two light fields of different frequencies, like in Chapter 5, or between the two cavity modes, like in Chapter 8, or between the light and the mechanical oscillator, like in Chapter 9. I present a conceptual vision of a gravitational-wave detector that operates with several quantum extensions, allowing to flexibly tune the sensitivity of the detector to match the specific scientific goal. Such detectors use quantum correlations for reducing quantum radiation-pressure noise at low frequencies, and allow to see the signals from binary inspirals at early stages of their evolution. These low-frequency signals not only give more precise information about the parameters of the binary system, but also allow to locate the source on the sky with increased precision. Providing this localization in advance to the electromagnetic observatories can allow them to observe the merger in electromagnetic diapason. Such a detector follows the signal sweeping through the detection band, and dynamically adjusts the frequency at which it is most sensitive. This can be achieved by taking advantage of the optomechanical interaction between the light and the test masses, amplified by a nonlinear crystal placed inside the detector. Finally, when the binary merges, radiating high-frequency gravitational waves, the detector is switched into the quantum expander mode, where the sensitivity at high frequency is increased with quantum squeezed light, generated by the nonlinear crystal inside the detector.

This vision for a future detector is based on several approaches, that I study in detail in this thesis. Every one of these approaches needs to be extended into a

practical configuration and tested experimentally. Therefore I hope this to serve as an inspiration for future research in these directions.

As the first step towards this goal, I investigate the details of quantum limits on the sensitivity of the detectors. These limits arise due to the interaction between the light and the test masses. One of them is the standard quantum limit (SQL), which originates in the balance between the quantum radiation-pressure noise and quantum shot noise. This limit can be surpassed by using quantum correlations and evading the radiation-pressure noise. I propose and investigate experimentally the optomechanical ring cavity setup, designed to evade the radiation-pressure noise by measuring the velocity of the mechanical oscillator. This novel setup has interesting optomechanical properties, which are partially studied by us in [68]. Much more remains to be studied, including the possible extensions to the setup, that would allow to reach quantum-noise-limited sensitivity, and possible applications of the ring cavity for gravitational-wave detection. The experiment, in order to demonstrate the velocity measurements of mechanical motion, will need further increase in sensitivity, in particular, reduction in classical phase noise, in order.

The other approach to reducing the quantum radiation pressure relies on quantum entanglement between the two light fields. This entanglement is created by an optomechanical interaction between these fields and test masses. With special combination of parameters, dubbed "paired carriers" regime, it can be possible to cancel a significant part of the radiation-pressure noise.

Once the SQL is surpassed, the sensitivity still remains bounded by the quantum Cramer-Rao bound. This bound cannot be surpassed, but can be lowered by employing quantum correlations. One approach to creating these correlations is to generate them directly inside the detector's cavities. I study the *internal squeezing* approach in different regimes. I show how it allows to increase the sensitivity in different frequency ranges, and expand the detection bandwidth. I make the emphasis on the role of optical loss that destroys quantum correlations and prevents from achieving high enhancements to the sensitivity. I propose how internal squeezing can be used to compensate for some part of these losses. I derive a new quantum bound for a lossy interferometer, originating in optical loss. I show that internal squeezing plays the crucial role in achieving this bound. Finally, I discuss the standard sensitivity-bandwidth limit on the sensitivity of

cavity-enhanced detectors, and how in different configurations internal squeezing allows to overcome this limit.

The approaches introduced in this thesis will need more research into the practical aspects of their implementation in the gravitational-wave detectors. They target the future detectors: the extensions to the third generation and beyond. However, they can find applications in a smaller scale metrological devices. Optomechanical ring cavity features unusual properties, which can prove useful for quantum state engineering in certain regimes [68]. I anticipate that internal squeezing and quantum expander will become standard tools in the toolbox of quantum metrology.

Appendix

A.1 Appendix: quantum expander

In this section we use the transfer matrix approach [35] to compute the sensitivity of the detector taking into account the radiation pressure noise and optical losses. We start by writing down the input-output relations as propagation of the field amplitudes in terms of transfer matrices for each optical element. The description is broader than strictly needed to compute the spectral density in the main text (e.g. it includes the effects of dynamical back action), but we find it helpful to use a general approach.

Input-output relations

We describe a two-cavity system, as shown on Fig. A.1, in terms of input and output quantum fields. Based on two-photon quadrature amplitudes we define the vector $\hat{a}(\Omega) = \{\hat{a}^{(c)}(\Omega), \hat{a}^{(s)}(\Omega)\}^T$. The signal extraction cavity can rotate the quadratures due to its detuning from resonance. The optical parametric amplification process also squeezes and rotates the quadratures. The effect of

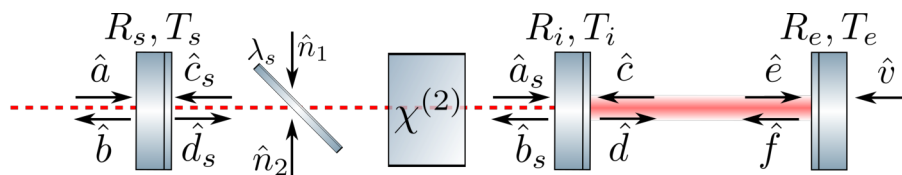


Fig. A.1. Quantum fields in the model of a two-cavity system. $R_{s,i,e}$, $T_{s,i,e}$ are the amplitude reflectivities and transmissivities of the signal extraction, input and end test mirrors correspondingly; a beamsplitter with power reflectivity λ_s represents a source of intra-cavity loss, which causes vacuum noises $\hat{n}_{1,2}$ to enter the system.

the signal recycling cavity can be described as a set of rotations and squeezing operations:

$$\hat{a}_s = O(\varphi)O(\theta)\mathcal{S}O^\dagger(\theta)O(\phi)(\sqrt{1-\lambda_s}\hat{d}_s + \sqrt{\lambda_s}\hat{n}_1)e^{i\Omega\tau_{SE}}, \quad (\text{A.1})$$

$$\hat{b}_s = -R_i\hat{a}_s + T_i\hat{c}_s, \quad (\text{A.2})$$

$$\hat{c}_s = \sqrt{1-\lambda_s}O(\phi)O(\theta)\mathcal{S}O^\dagger(\theta)O(\varphi)\hat{b}_se^{i\Omega\tau_{SE}} + \sqrt{\lambda_s}\hat{n}_2, \quad (\text{A.3})$$

$$\hat{d}_s = T_s\hat{a} + R_s\hat{c}_s, \quad (\text{A.4})$$

where we denote the amplitude reflectivity and transmissivity of the signal recycling and input mirrors by $R_{s,i}$, $T_{s,i}$, the power loss inside the cavity (before the crystal) is λ_s ; signal recycling cavity global delay $\tau_{SE} = L_{SE}/c$ and the phase delay due to the cavity detuning before and after the crystal by ϕ , φ . We now introduce the squeeze angle θ and the rotation matrix

$$\forall\phi, \quad O(\phi) = \begin{bmatrix} \cos\phi & -\sin\phi \\ \sin\phi & \cos\phi \end{bmatrix}, \quad (\text{A.5})$$

$$\mathcal{Y} = O(\pi/2) = \begin{bmatrix} 0 & -1 \\ 1 & 0 \end{bmatrix}, \quad (\text{A.6})$$

and squeezing matrix

$$\mathcal{S} = \begin{bmatrix} e^q & 0 \\ 0 & e^{-q} \end{bmatrix}, \quad (\text{A.7})$$

with q being the single-pass squeeze factor.

For the arm cavity the corresponding set of equations reads

$$\hat{b} = -R_s\hat{a} + T_s\hat{c}_s, \quad (\text{A.8})$$

$$\hat{d} = R_i\hat{c} + T_i\hat{a}, \quad (\text{A.9})$$

$$\hat{c} = O(\delta_{\text{arm}}\tau_{\text{arm}})\hat{f}e^{i\Omega\tau_{\text{arm}}}, \quad (\text{A.10})$$

$$\hat{e} = O(\delta_{\text{arm}}\tau_{\text{arm}})\hat{d}e^{i\Omega\tau_{\text{arm}}}, \quad (\text{A.11})$$

$$\hat{f} = R_e\hat{e} + T_e\hat{v} + 2kR_eO(\pi/2)\text{E}\hat{x}_-(\Omega), \quad (\text{A.12})$$

where $k = \omega/c$ is the wave vector of the main field, δ_{arm} is the arm cavity detuning and $\tau_{\text{arm}} = L_{\text{arm}}/c$ is the propagation time with L_{arm} being the length of the arm

cavity, and c the speed of light. The field E corresponds to the classical amplitude of the field impinging on the end mirror.

We find the solution to these equations, first for the complex transmissivity and reflectivity of the signal recycling cavity

$$\hat{b}_s = \mathcal{D}_b [-R_i T_s \mathcal{M}[\varphi, \phi] \hat{a} + T_i \hat{c}] , \quad (\text{A.13})$$

$$\hat{d}_s = \mathcal{D}_d [R_s T_i \mathcal{M}[\phi, \varphi] \hat{c} + T_s \hat{a}] , \quad (\text{A.14})$$

$$\hat{a}_s = \mathcal{M}[\varphi, \phi] \mathcal{D}_d [R_s T_i \mathcal{M}[\phi, \varphi] \hat{c} + T_s \hat{a}] , \quad (\text{A.15})$$

$$\hat{c}_s = \mathcal{M}[\phi, \varphi] \mathcal{D}_b [-R_i T_s \mathcal{M}[\varphi, \phi] \hat{a} + T_i \hat{c}] , \quad (\text{A.16})$$

$$(\text{A.17})$$

where we defined

$$\mathcal{M}[\phi, \psi] = O(\phi) O(\theta) S O^\dagger(\theta) O(\psi) e^{i\Omega\tau_{\text{SE}}} , \forall \phi, \psi , \quad (\text{A.18})$$

$$\mathcal{D}_b = (\mathcal{I} + R_i R_s (1 - \lambda_s) \mathcal{M}[\varphi, \phi] \mathcal{M}[\phi, \varphi])^{-1} , \quad (\text{A.19})$$

$$\mathcal{D}_d = (\mathcal{I} + R_i R_s (1 - \lambda_s) \mathcal{M}[\phi, \varphi] \mathcal{M}[\varphi, \phi])^{-1} . \quad (\text{A.20})$$

That provides the input-output relations for the signal extraction cavity

$$\hat{b} = -\mathcal{R}_b \hat{a} + \mathcal{T}_b \hat{c} + \mathcal{L}_{b1} \hat{n}_1 + \mathcal{L}_{b2} \hat{n}_2 , \quad (\text{A.21})$$

$$\hat{d} = \mathcal{R}_d \hat{c} + \mathcal{T}_d \hat{a} + \mathcal{L}_{d1} \hat{n}_1 + \mathcal{L}_{d2} \hat{n}_2 , \quad (\text{A.22})$$

where we introduced the transfer matrices for the fields

$$\mathcal{R}_b = R_s + R_i T_s^2 (1 - \lambda_s) \mathcal{M}[\phi, \varphi] \mathcal{D}_b \mathcal{M}[\varphi, \phi] , \quad (\text{A.23})$$

$$\mathcal{R}_d = R_i + R_s T_i^2 (1 - \lambda_s) \mathcal{M}[\varphi, \phi] \mathcal{D}_d \mathcal{M}[\phi, \varphi] , \quad (\text{A.24})$$

$$\mathcal{T}_b = T_i T_s \sqrt{1 - \lambda_s} \mathcal{M}[\phi, \varphi] \mathcal{D}_b , \quad (\text{A.25})$$

$$\mathcal{T}_d = T_i T_s \sqrt{1 - \lambda_s} \mathcal{M}[\varphi, \phi] \mathcal{D}_d , \quad (\text{A.26})$$

$$\mathcal{L}_{b1} = -T_s R_i \sqrt{1 - \lambda_s} \lambda_s \mathcal{M}[\varphi, \phi] \mathcal{D}_b \mathcal{M}[\phi, \varphi] , \quad (\text{A.27})$$

$$\mathcal{L}_{b2} = T_s R_i R_s \sqrt{\lambda_s} (1 - \lambda_s) \mathcal{M}[\varphi, \phi] \mathcal{D}_b \mathcal{M}[\phi, \varphi] - \sqrt{\lambda_s} , \quad (\text{A.28})$$

$$\mathcal{L}_{d1} = -T_i R_i R_s \sqrt{\lambda_s} (1 - \lambda_s) \mathcal{M}[\phi, \varphi] \mathcal{D}_d \mathcal{M}[\varphi, \phi] + \sqrt{\lambda_s} , \quad (\text{A.29})$$

$$\mathcal{L}_{d2} = T_i R_s \sqrt{\lambda_s} (1 - \lambda_s) \mathcal{M}[\phi, \varphi] \mathcal{D}_d . \quad (\text{A.30})$$

Now we can derive the fields for the arm cavity yielding

$$\begin{aligned}\hat{c} = & R_e \mathcal{D}_c O(\delta_{\text{arm}} \tau_{\text{arm}})^2 \mathcal{T}_d \hat{a} e^{2i\Omega \tau_{\text{arm}}} + T_e \mathcal{D}_c O(\delta_{\text{arm}} \tau_{\text{arm}}) \hat{v} e^{i\Omega \tau_{\text{arm}}} + \\ & + R_e \mathcal{D}_c O(\delta_{\text{arm}} \tau_{\text{arm}})^2 (\mathcal{L}_{d1} \hat{n}_1 + \mathcal{L}_{d2} \hat{n}_2) e^{2i\Omega \tau_{\text{arm}}} + \\ & + 2k R_e \mathcal{D}_c O(\delta_{\text{arm}} \tau_{\text{arm}}) \mathcal{Y} E \hat{x}_-(\Omega) e^{i\Omega \tau_{\text{arm}}}\end{aligned}\quad (\text{A.31})$$

$$\begin{aligned}\hat{e} = & \mathcal{D}_e O(\delta_{\text{arm}} \tau_{\text{arm}}) \mathcal{T}_d \hat{a} e^{i\Omega \tau_{\text{arm}}} + \\ & + T_e \mathcal{D}_e O(\delta_{\text{arm}} \tau_{\text{arm}}) \mathcal{R}_d O(\delta_{\text{arm}} \tau_{\text{arm}}) \hat{v} e^{2i\Omega \tau_{\text{arm}}} + \\ & + \mathcal{D}_e O(\delta_{\text{arm}} \tau_{\text{arm}}) (\mathcal{L}_{d1} \hat{n}_1 + \mathcal{L}_{d2} \hat{n}_2) e^{i\Omega \tau_{\text{arm}}} + \\ & + 2k R_e \mathcal{D}_e O(\delta_{\text{arm}} \tau_{\text{arm}}) \mathcal{R}_d O(\delta_{\text{arm}} \tau_{\text{arm}}) \mathcal{Y} E \hat{x}_-(\Omega) e^{2i\Omega \tau_{\text{arm}}},\end{aligned}\quad (\text{A.32})$$

where

$$\mathcal{D}_c = \left(\mathcal{I} - R_e O(\delta_{\text{arm}} \tau_{\text{arm}})^2 \mathcal{R}_d e^{2i\Omega \tau_{\text{arm}}} \right)^{-1}, \quad (\text{A.33})$$

$$\mathcal{D}_e = \left(\mathcal{I} - R_e O(\delta_{\text{arm}} \tau_{\text{arm}}) \mathcal{R}_d O(\delta_{\text{arm}} \tau_{\text{arm}}) e^{2i\Omega \tau_{\text{arm}}} \right)^{-1}. \quad (\text{A.34})$$

Finally, we find the outgoing field to be

$$\hat{b} = -\mathcal{R} \hat{a} + \mathcal{T} \hat{v} + \mathcal{Z} \hat{x}_-(\Omega) + \mathcal{L}_1 \hat{n}_1 + \mathcal{L}_2 \hat{n}_2, \quad (\text{A.35})$$

where we defined the transfer matrices:

$$\mathcal{R} = \mathcal{R}_b - R_e \mathcal{T}_b \mathcal{D}_c O(\delta_{\text{arm}} \tau_{\text{arm}})^2 \mathcal{T}_d e^{2i\Omega \tau_{\text{arm}}}, \quad (\text{A.36})$$

$$\mathcal{T} = T_e \mathcal{T}_b \mathcal{D}_c O(\delta_{\text{arm}} \tau_{\text{arm}}) e^{i\Omega \tau_{\text{arm}}}, \quad (\text{A.37})$$

$$\mathcal{Z} = 2k R_e \mathcal{T}_b \mathcal{D}_c O(\delta_{\text{arm}} \tau_{\text{arm}}) \mathcal{Y} E e^{i\Omega \tau_{\text{arm}}}, \quad (\text{A.38})$$

$$\mathcal{L}_1 = R_e \mathcal{T}_b \mathcal{D}_c O(\delta_{\text{arm}} \tau_{\text{arm}}) O(\delta_{\text{arm}} \tau_{\text{arm}}) \mathcal{L}_{d1} e^{2i\Omega \tau_{\text{arm}}} + \mathcal{L}_{b1}, \quad (\text{A.39})$$

$$\mathcal{L}_2 = R_e \mathcal{T}_b \mathcal{D}_c O(\delta_{\text{arm}} \tau_{\text{arm}}) O(\delta_{\text{arm}} \tau_{\text{arm}}) \mathcal{L}_{d2} e^{2i\Omega \tau_{\text{arm}}} + \mathcal{L}_{b2}. \quad (\text{A.40})$$

$$(\text{A.41})$$

Radiation pressure

The radiation pressure force acting on the mirrors has three contributions. First, there is a constant force due to the classical high-power optical field. It induces a constant shift of the mirror, which can be compensated with classical feedback.

Second, there is a dynamical classical part, which is amplified by optomechanical parametric amplification and which belongs to the optical spring, and third a fluctuating force due to the uncertainty in the amplitude quadrature of the light. The latter corresponds to the quantum back-action force of the carrier light. Following [196], we assume the input test mass to be fixed, and twice the back action imposed on the back mirror instead (which leads to introduction of effective light power). Such approximation is valid when the transmission of front mirror is small, such that the amplitudes of the fields acting on the front and back mirrors are almost equal (which is the case in our consideration).

$$F^{ba} = \hbar k(E^\dagger \hat{e}(\Omega) + F^\dagger \hat{f}(\Omega)) = F^{fl}(\Omega) - \mathcal{K}(\Omega)x_-(\Omega), \quad (\text{A.42})$$

where we split the back-action into the noise part $F^{fl}(\Omega)$ and position-dependent optical spring force with spring constant $\mathcal{K}(\Omega)$. Taking into account that $F = R_e E$, we find the equations for these contributions:

$$F^{fl}(\Omega) = \hbar k(1 + R_e^2)E^\dagger \mathcal{D}_e O(\delta_{\text{arm}} \tau_{\text{arm}}) e^{i\Omega \tau_{\text{arm}}} (\mathcal{T}_d \hat{a} + \mathcal{L}_{d1} \hat{n}_1 + \mathcal{L}_{d2} \hat{n}_2) + \hbar k T_e E^\dagger \mathcal{L}_v \hat{v}, \quad (\text{A.43})$$

$$\mathcal{L}_v = (1 + R_e^2) \mathcal{D}_e O(\delta_{\text{arm}} \tau_{\text{arm}}) \mathcal{R}_d O(\delta_{\text{arm}} \tau_{\text{arm}}) e^{i\Omega \tau_{\text{arm}}} + R_e, \quad (\text{A.44})$$

$$\mathcal{K}(\Omega) = -2\hbar k^2(1 + R_e^2)R_e E^\dagger \mathcal{D}_e O(\delta_{\text{arm}} \tau_{\text{arm}}) \mathcal{R}_d O(\delta_{\text{arm}} \tau_{\text{arm}}) \mathcal{Y} E e^{2i\Omega \tau_{\text{arm}}} - 2\hbar k^2 R_e^2 E^\dagger \mathcal{Y} E. \quad (\text{A.45})$$

Without loss of generality we choose the phase of the classical amplitude such that:

$$E = \sqrt{2E}\{1, 0\}^T, \quad (\text{A.46})$$

where the amplitude E is connected to the power in the cavity as $P_c = 2P_{\text{arm}} = \hbar \omega_p |E|^2$, where P_{arm} is a power in the corresponding Michelson interferometer [196].

The equation of motion for the test mass taking into account the radiation pressure force:

$$\hat{x}_-(\Omega) = \chi(\Omega) \left[F^{fl}(\Omega) - \mathcal{K}(\Omega)x_-(\Omega) \right], \quad (\text{A.47})$$

where $\chi(\Omega) = (-m\Omega^2)^{-1}$ is the mechanical susceptibility for the free mass m . This allows us to introduce an effective susceptibility:

$$\chi_{\text{eff}}(\Omega) = (\chi^{-1} + \mathcal{K}(\Omega))^{-1}, \quad (\text{A.48})$$

such that $x_-(\Omega) = \chi_{\text{eff}}(\Omega)F^{fl}(\Omega)$.

Detection

The presence of optical loss in the readout path, including the detection loss, leads to a loss of quantum correlations due to mixing with vacuum. We model this loss with a beamsplitter of power transmissivity $\eta = 1 - \lambda_r$ and reflectivity (loss) $1 - \eta = \lambda_r$ which mixes in vacuum \mathbf{n} :

$$\tilde{\mathbf{b}}(\Omega) = \sqrt{\eta}\mathbf{b}(\Omega) + \sqrt{1 - \eta}\mathbf{n}. \quad (\text{A.49})$$

The balanced homodyne detection on the output $\tilde{\mathbf{b}}$ at homodyne angle ζ provides the values

$$\begin{aligned} y(\Omega) &= \{\cos \zeta, \sin \zeta\}^T \tilde{\mathbf{b}}(\Omega) = \mathcal{H}^T \tilde{\mathbf{b}}(\Omega) = \\ &= \sqrt{\eta} \mathcal{H}^T (-\mathcal{R}\hat{\mathbf{a}} + \mathcal{T}\hat{\mathbf{v}} + \mathcal{L}_{b_1}\hat{\mathbf{n}}_1 + \mathcal{L}_{b_2}\hat{\mathbf{n}}_2) + \\ &\quad + \sqrt{\eta} \mathcal{H}^T \mathcal{Z}\hat{\mathbf{x}}_-(\Omega) + \sqrt{1 - \eta} \mathcal{H}^T \mathbf{n}(\Omega), \end{aligned} \quad (\text{A.50})$$

which we renormalize to the differential mirror displacement

$$\tilde{\mathbf{y}} = \frac{\mathcal{H}^T (-\mathcal{R}\hat{\mathbf{a}} + \mathcal{T}\hat{\mathbf{v}} + \mathcal{L}_{b_1}\hat{\mathbf{n}}_1 + \mathcal{L}_{b_2}\hat{\mathbf{n}}_2)}{\mathcal{H}^T \mathcal{Z}} + \frac{\sqrt{1 - \eta} \mathcal{H}^T \mathbf{n}}{\sqrt{\eta} \mathcal{H}^T \mathcal{Z}} + \hat{\mathbf{x}}_-(\Omega). \quad (\text{A.51})$$

We implement the injection of the squeezing from the outside, by defining an action of the squeezing operation on the input field $\hat{\mathbf{a}}$ as:

$$\hat{\mathbf{a}} = \mathcal{S}_{\text{ext}}[\phi_{\text{ext}}]\hat{\mathbf{a}}^{\text{vac}}, \quad (\text{A.52})$$

where \hat{a}^{vac} is the vacuum field before squeezing, and the squeezing matrix with squeeze factor q_{ext} and squeeze angle ϕ_{ext} is defined as

$$\mathcal{S}_{\text{ext}} = O(\phi_{\text{ext}}) \begin{bmatrix} e^{q_{\text{ext}}} & 0 \\ 0 & e^{-q_{\text{ext}}} \end{bmatrix} O(-\phi_{\text{ext}}). \quad (\text{A.53})$$

All other fields $\hat{v}, \hat{n}, \hat{n}_1, \hat{n}_2$ are in the vacuum state.

From this we get the spectral density for this output

$$S_x(\Omega) = S_{xx}(\Omega) + 2\Re[\chi_{\text{eff}}^*(\Omega)S_{xF}(\Omega)] + |\chi_{\text{eff}}(\Omega)|^2 S_{FF}(\Omega), \quad (\text{A.54})$$

where

$$S_{xx} = \frac{\mathcal{H}^T (\mathcal{R} \mathcal{S}_{\text{ext}} \mathcal{S}_{\text{ext}}^\dagger \mathcal{R}^\dagger + \mathcal{T} \mathcal{T}^\dagger + \mathcal{L}_{b1} \mathcal{L}_{b1}^\dagger + \mathcal{L}_{b2} \mathcal{L}_{b2}^\dagger) \mathcal{H}}{|\mathcal{H}^T \mathcal{Z}|^2} + \frac{1 - \eta}{\eta} \frac{1}{|\mathcal{H}^T \mathcal{Z}|^2}, \quad (\text{A.55})$$

$$S_{FF} = \hbar^2 k^2 (1 + R_e^2)^2 \mathcal{E}^\dagger \mathcal{D}_e O(\delta_{\text{arm}} \tau_{\text{arm}}) \times \left(\mathcal{T}_d \mathcal{S}_{\text{ext}} \mathcal{S}_{\text{ext}}^\dagger \mathcal{T}_d^\dagger + \mathcal{L}_{d1} \mathcal{L}_{d1}^\dagger + \mathcal{L}_{d2} \mathcal{L}_{d2}^\dagger \right) \times O^\dagger(\delta_{\text{arm}} \tau_{\text{arm}}) \mathcal{D}_e^\dagger \mathcal{E} + \hbar^2 k^2 T_e^2 \mathcal{E}^\dagger \mathcal{L}_v \mathcal{L}_v^\dagger \mathcal{E}, \quad (\text{A.56})$$

$$S_{xF} = \frac{\hbar k}{\mathcal{H}^T \mathcal{Z}} \left((1 + R_e^2) \mathcal{H}^T \left(-\mathcal{R} \mathcal{S}_{\text{ext}} \mathcal{S}_{\text{ext}}^\dagger \mathcal{T}_d^\dagger + \mathcal{L}_{b1} \mathcal{L}_{d1}^\dagger + \mathcal{L}_{b2} \mathcal{L}_{d2}^\dagger \right) \times O^\dagger(\delta_{\text{arm}} \tau_{\text{arm}}) \mathcal{D}_e^\dagger \mathcal{E} e^{-i\Omega \tau_{\text{arm}}} + T_e \mathcal{H}^T \mathcal{T} \mathcal{L}_v^\dagger \mathcal{E} \right). \quad (\text{A.57})$$

Finally we normalize the spectral density to the gravitational-wave strain yielding (taking into account the effects of high-frequency corrections [260])

$$S_h(\Omega) = S_x(\Omega) \frac{4}{m^2 L^2 \Omega^4 |\chi_{\text{eff}}(\Omega)|^2} \frac{\Omega^2 \tau_{\text{arm}}^2}{\sin^2 \Omega \tau_{\text{arm}}}. \quad (\text{A.58})$$

Filter cavities

Filter cavities on the can be used to create a necessary frequency dependence of quantum correlations, such that the QRPN is suppressed or evaded completely. There are two scenarios, input filter cavity, where the injected squeezing becomes frequency dependent, and output filter cavity, where the homodyne detection

becomes frequency dependent. We follow [35] and consider a lossless filter cavity, so that the only effect of the cavity is a frequency-dependent rotation of the input squeezed state $\hat{a} \rightarrow O[\theta_f(\Omega)]\hat{a}$ or output $b(\Omega) \rightarrow O[\theta_f(\Omega)]b(\Omega)$, by the angle

$$\theta_f(\Omega) = \arctan \frac{2\gamma_f \delta_f}{\gamma_f^2 - \delta_f^2 + \Omega^2}, \quad (\text{A.59})$$

where γ_f is the filter cavity bandwidth, and δ_f is its detuning from resonance. To obtain the spectral corresponding spectral densities it's sufficient to modify the squeeze angle $\phi_{\text{ext}} \rightarrow \phi_{\text{ext}} + \theta_f(\Omega)$ or homodyne angle $\zeta \rightarrow \zeta - \theta_f(\Omega)$ in the equations for the spectral density Eq. A.54. The optimal detuning is on the slope of the cavity resonance $\delta_f = \gamma_f$, and the exact choice of cavity linewidth depends on the parameters of the detector, including the internal squeezing strength and readout loss.

A.2 Appendix: optical spring detector

Input-output relations for coupled cavities

It is helpful to consider the input-output relations of our optomechanical system in the 'two-photon formalism' [165, 166], where the amplitude and phase quadrature amplitudes \hat{a}^c and \hat{a}^s of the modulation field at frequency Ω are linked to the optical fields $\hat{a}(\omega \pm \Omega)$ via

$$\hat{a}^c(\Omega) = \frac{\hat{a}(\omega + \Omega) + \hat{a}^\dagger(\omega - \Omega)}{\sqrt{2}}, \quad (\text{A.60})$$

$$\hat{a}^s(\Omega) = \frac{\hat{a}(\omega + \Omega) - \hat{a}^\dagger(\omega - \Omega)}{i\sqrt{2}}. \quad (\text{A.61})$$

Based on these quadrature amplitudes we define the vector $\hat{\mathbf{a}}(\Omega) = \{\hat{a}^c(\Omega), \hat{a}^s(\Omega)\}^T$.

The signal recycling cavity rotates the quadratures due to its detuning and squeezes and rotates additionally due to intra-cavity optical-parametric amplification. The phase shift due to the cavity length can be neglected since the cavity length is much shorter than the wavelengths of the sideband modulations

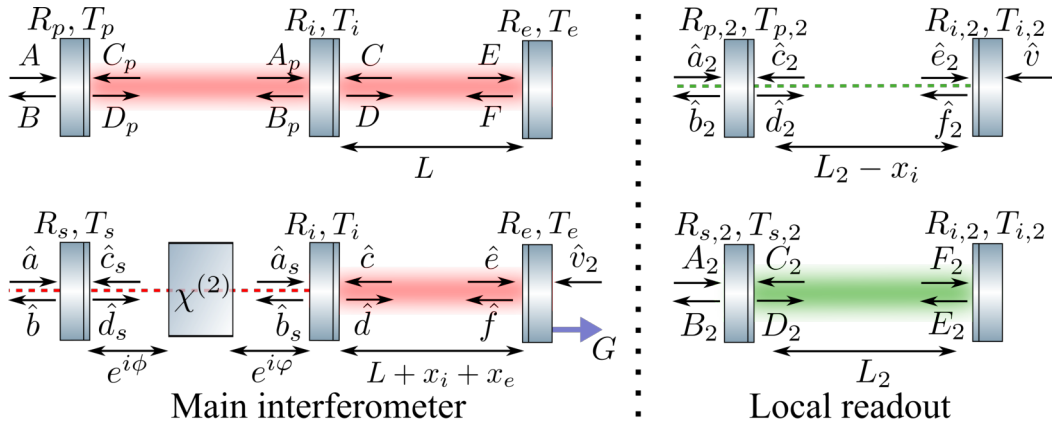


Fig. A.2. Notations of the optical fields for the PR cavity together with the common mode of the arm cavities at ω (top left), for the SE cavity together with the differential mode of the arm cavities at ω (bottom left), and respective parts of the interferometer in Fig. 9.1 at ω_2 , which belongs to the local readout (top and bottom right). Operators are annihilation operators and denote complex amplitudes including their uncertainties. Capital letters A to F denote complex amplitudes whose uncertainties are irrelevant. Subscript ‘ s ’: signal extraction; ‘ p ’: power recycling; ‘ i ’: input to arm cavity; ‘ e ’: end of arm cavity; ‘ 2 ’: optical frequency ω_2 . R, T : amplitude reflectivity and transmissivity of mirrors. L is the average length of the arm resonators, L_2 is the relevant average length of the local read out, and $x_{i,e}$ represent their dynamical parts due to differential test mass motion. ϕ and φ are additional phases accumulated by the light field inside the SE cavity due to the cavity detuning. The gravitational-wave signal (‘ G ’) corresponds to a differential change of the arm length L .

considered here. The effect of the signal recycling cavity can be described as a set of rotations and squeezing operations:

$$\hat{\mathbf{a}}_s = \mathbb{O}(\varphi)\mathbb{O}(\theta)\mathbb{S}\mathbb{O}^\dagger(\theta)\mathbb{O}(\phi)\hat{\mathbf{d}}_s, \quad (\text{A.62})$$

$$\hat{\mathbf{b}}_s = -R_i\hat{\mathbf{a}}_s + T_i\hat{\mathbf{c}}, \quad (\text{A.63})$$

$$\hat{\mathbf{c}}_s = \mathbb{O}(\phi)\mathbb{O}(\theta)\mathbb{S}\mathbb{O}^\dagger(\theta)\mathbb{O}(\varphi)\hat{\mathbf{b}}_s, \quad (\text{A.64})$$

$$\hat{\mathbf{d}}_s = T_s\hat{\mathbf{a}} + R_s\hat{\mathbf{c}}_s, \quad (\text{A.65})$$

where we denote the amplitude reflectivity and transmissivity of the signal recycling and input mirrors by $R_{s,i}, T_{s,i}$ and the phase delay due to the cavity detuning

before and after the crystal by ϕ , φ , see Fig. A.2. We now introduce the squeeze angle θ and the rotation matrix

$$\forall \phi, \quad \mathbb{O}(\phi) = \begin{bmatrix} \cos \phi & -\sin \phi \\ \sin \phi & \cos \phi \end{bmatrix}, \quad (\text{A.66})$$

$$\mathbb{Y} = \mathbb{O}(\pi/2) = \begin{bmatrix} 0 & -1 \\ 1 & 0 \end{bmatrix} \quad (\text{A.67})$$

and squeezing matrix

$$\mathbb{S} = \begin{bmatrix} e^q & 0 \\ 0 & e^{-q} \end{bmatrix}, \quad (\text{A.68})$$

with q being the single-pass squeeze factor. For the arm cavity the corresponding set of equations reads

$$\hat{\mathbf{b}} = -R_s \hat{\mathbf{a}} + T_s \hat{\mathbf{c}}_s, \quad (\text{A.69})$$

$$\hat{\mathbf{d}} = R_i \hat{\mathbf{c}} + T_i \hat{\mathbf{a}}, \quad (\text{A.70})$$

$$\hat{\mathbf{c}} = \mathbb{O}(\delta_a \tau_a) \hat{\mathbf{f}} e^{i\Omega \tau_a}, \quad (\text{A.71})$$

$$\hat{\mathbf{e}} = \mathbb{O}(\delta_a \tau_a) \hat{\mathbf{d}} e^{i\Omega \tau_a}, \quad (\text{A.72})$$

$$\hat{\mathbf{f}} = R_e \hat{\mathbf{e}} + T_e \hat{\mathbf{v}} + 2k \mathbb{O}(\pi/2) \mathbf{E} \hat{\mathbf{x}}_-(\Omega), \quad (\text{A.73})$$

where $k = \omega/c$ is the wave vector of the main field, δ_a is the arm cavity detuning and $\tau_a = L/c$ is the propagation time with L being the length of the arm cavity, and c the speed of light. The field \mathbf{E} corresponds to the classical amplitude of the field impinging on the end mirror. This set of equations can be resolved for the outgoing field $\hat{\mathbf{b}}$ and intra-cavity fields $\hat{\mathbf{c}}$, $\hat{\mathbf{d}}$, $\hat{\mathbf{e}}$, $\hat{\mathbf{f}}$. We find the solution to these equations, first for the complex transmissivity and reflectivity of the signal recycling cavity

$$\hat{\mathbf{b}}_s = \mathbb{D}_b [-R_i T_s \mathbb{M}[\varphi, \phi] \hat{\mathbf{a}} + T_i \hat{\mathbf{c}}], \quad (\text{A.74})$$

$$\hat{\mathbf{d}}_s = \mathbb{D}_d [R_s T_i \mathbb{M}[\phi, \varphi] \hat{\mathbf{c}} + T_s \hat{\mathbf{a}}], \quad (\text{A.75})$$

$$\hat{\mathbf{a}}_s = \mathbb{M}[\varphi, \phi] \mathbb{D}_d [R_s T_i \mathbb{M}[\phi, \varphi] \hat{\mathbf{c}} + T_s \hat{\mathbf{a}}], \quad (\text{A.76})$$

$$\hat{\mathbf{c}}_s = \mathbb{M}[\phi, \varphi] \mathbb{D}_b [-R_i T_s \mathbb{M}[\varphi, \phi] \hat{\mathbf{a}} + T_i \hat{\mathbf{c}}], \quad (\text{A.77})$$

where we defined

$$\mathbb{M}[\phi, \psi] = \mathbb{O}(\phi)\mathbb{O}(\theta)\mathbb{S}\mathbb{O}^\dagger(\theta)\mathbb{O}(\psi), \forall \phi, \psi, \quad (\text{A.78})$$

$$\mathbb{D}_b = (\mathbb{I} + R_i R_s \mathbb{M}[\phi, \phi] \mathbb{M}[\phi, \phi])^{-1}, \quad (\text{A.79})$$

$$\mathbb{D}_d = (\mathbb{I} + R_i R_s \mathbb{M}[\phi, \phi] \mathbb{M}[\phi, \phi])^{-1}. \quad (\text{A.80})$$

That provides the solution for the signal extraction cavity

$$\hat{\mathbf{b}} = -\mathbb{R}_b \hat{\mathbf{a}} + \mathbb{T}_b \hat{\mathbf{c}}, \quad (\text{A.81})$$

$$\hat{\mathbf{d}} = -\mathbb{R}_d \hat{\mathbf{c}} + \mathbb{T}_d \hat{\mathbf{a}}, \quad (\text{A.82})$$

where

$$\mathbb{R}_b = R_s + R_i T_s^2 \mathbb{M}[\phi, \phi] \mathbb{D}_b \mathbb{M}[\phi, \phi], \quad (\text{A.83})$$

$$\mathbb{R}_d = R_i + R_s T_i^2 \mathbb{M}[\phi, \phi] \mathbb{D}_d \mathbb{M}[\phi, \phi], \quad (\text{A.84})$$

$$\mathbb{T}_b = T_i T_s \mathbb{M}[\phi, \phi] \mathbb{D}_b, \quad (\text{A.85})$$

$$\mathbb{T}_d = T_i T_s \mathbb{M}[\phi, \phi] \mathbb{D}_d. \quad (\text{A.86})$$

Now we can derive the fields for the arm cavity yielding

$$\begin{aligned} \hat{\mathbf{c}} = & R_e \mathbb{D}_c \mathbb{O}(\delta_a \tau_a)^2 \mathbb{T}_d \hat{\mathbf{a}} e^{2i\Omega\tau_a} + \\ & + T_e \mathbb{D}_c \mathbb{O}(\delta_a \tau_a) \hat{\mathbf{v}} e^{i\Omega\tau_a} \\ & + 2k \mathbb{D}_c \mathbb{O}(\delta_a \tau_a) \mathbb{Y} \mathbf{E} \hat{\mathbf{x}}_-(\Omega) e^{i\Omega\tau_a} \end{aligned} \quad (\text{A.87})$$

$$\begin{aligned} \hat{\mathbf{e}} = & \mathbb{D}_e \mathbb{O}(\delta_a \tau_a) \mathbb{T}_d \hat{\mathbf{a}} e^{i\Omega\tau_a} + \\ & + T_e \mathbb{D}_e \mathbb{O}(\delta_a \tau_a) \mathbb{R}_d \mathbb{O}(\delta_a \tau_a) \hat{\mathbf{v}} e^{2i\Omega\tau_a} + \\ & + 2k \mathbb{D}_e \mathbb{O}(\delta_a \tau_a) \mathbb{R}_d \mathbb{O}(\delta_a \tau_a) \mathbb{Y} \mathbf{E} \hat{\mathbf{x}}_-(\Omega) e^{2i\Omega\tau_a} \end{aligned} \quad (\text{A.88})$$

where

$$\mathbb{D}_c = \left(\mathbb{I} - R_e \mathbb{O}(\delta_a \tau_a)^2 \mathbb{R}_d e^{2i\Omega\tau_a} \right)^{-1} \quad (\text{A.89})$$

$$\mathbb{D}_e = \left(\mathbb{I} - R_e \mathbb{O}(\delta_a \tau_a) \mathbb{R}_d \mathbb{O}(\delta_a \tau_a) e^{2i\Omega\tau_a} \right)^{-1} \quad (\text{A.90})$$

Finally, we find the outgoing field to be

$$\hat{\mathbf{b}} = \left(-\mathbb{R}_b + R_e \mathbb{T}_b \mathbb{D}_c \mathbb{O}(\delta_a \tau_a)^2 \mathbb{T}_d e^{2i\Omega\tau_a} \right) \mathbf{a} + \quad (\text{A.91})$$

$$+ T_e \mathbb{T}_b \mathbb{D}_c \mathbb{O}(\delta_a \tau_a) \hat{\mathbf{v}} e^{i\Omega\tau_a} + \quad (\text{A.92})$$

$$+ 2k \mathbb{T}_b \mathbb{D}_c \mathbb{O}(\delta_a \tau_a) \mathbb{Y} \mathbf{E} \hat{x}_-(\Omega) e^{i\Omega\tau_a} = \quad (\text{A.93})$$

$$= -\mathbb{R} \hat{\mathbf{a}} + \mathbb{T} \hat{\mathbf{v}} + \mathbb{Z} \hat{x}_-(\Omega) \quad (\text{A.94})$$

Radiation pressure and optical spring

The radiation pressure force acting on the mirrors has three contributions. First, there is a constant force due to the classical high-power optical field. It induces a constant shift of the mirror, which can be compensated with classical feedback. Second, there is a dynamical classical part, which is amplified by optomechanical parametric amplification and which belongs to the optical spring, and third a fluctuating force due to the uncertainty in the amplitude quadrature of the light. The latter corresponds to the quantum back-action force of the carrier light and can be written for the input and end mirrors as

$$F_i^{ba} = \hbar k (\mathbf{C}^\dagger \hat{\mathbf{c}}(\Omega) + \mathbf{D}^\dagger \hat{\mathbf{d}}(\Omega)), \quad (\text{A.95})$$

$$F_e^{ba} = \hbar k (\mathbf{E}^\dagger \hat{\mathbf{e}}(\Omega) + \mathbf{F}^\dagger \hat{\mathbf{f}}(\Omega)). \quad (\text{A.96})$$

In the single-mode approximation, these two forces become equal and read

$$F_{i,e}^{ba}(\Omega) = 2\hbar k \mathbf{E}^\dagger \hat{\mathbf{e}}(\Omega) = F_{fl}(\Omega) - \mathcal{K}(\Omega) x_-(\Omega), \quad (\text{A.97})$$

where

$$F^{fl}(\Omega) = 2\hbar k \mathbf{E}^\dagger \mathbb{D}_e \mathbb{O}(\delta_a \tau_a) e^{i\Omega\tau_a} \left(\mathbb{T}_d \hat{\mathbf{a}} + \right. \quad (\text{A.98})$$

$$\left. + T_e \mathbb{R}_d \mathbb{O}(\delta_a \tau_a) \hat{\mathbf{v}} e^{i\Omega\tau_a} \right)$$

$$\mathcal{K}(\Omega) = -4\hbar k^2 \mathbf{E}^\dagger \mathbb{D}_e \mathbb{O}(\delta_a \tau_a) \mathbb{R}_d \mathbb{O}(\delta_a \tau_a) \mathbb{Y} \mathbf{E} \hat{x}_-(\Omega) e^{2i\Omega\tau_a} \quad (\text{A.99})$$

Ignoring the effect of the second-harmonic beam, we get for the differential motion

$$\hat{x}_-(\Omega) = \chi(\Omega) \left[F^{fl} - \mathcal{K}(\Omega) x_-(\Omega) \right], \quad (\text{A.100})$$

which allows us to introduce an effective susceptibility:

$$\chi_{\text{eff}}(\Omega) = (\chi^{-1} + \mathcal{K}(\Omega))^{-1}, \quad (\text{A.101})$$

such that $x_-(\Omega) = \chi_{\text{eff}}(\Omega)F^{fl}(\Omega)$.

Detection

The balanced homodyne detection on the output $\hat{\mathbf{b}}$ at homodyne angle ζ provides the values

$$\begin{aligned} y(\Omega) &= \begin{bmatrix} \cos \zeta & \sin \zeta \end{bmatrix} \hat{\mathbf{b}}(\Omega) = \mathbb{H}^T \hat{\mathbf{b}}(\Omega) = \\ &= -\mathbb{H}^T \mathbb{R} \hat{\mathbf{a}} + \mathbb{H}^T \mathbb{T} \hat{\mathbf{v}} + \mathbb{H}^T \mathbb{Z} \hat{x}_-(\Omega) \end{aligned} \quad (\text{A.102})$$

which we renormalize to the differential mirror displacement

$$\tilde{y} = \frac{-\mathbb{H}^T \mathbb{R} \hat{\mathbf{a}} + \mathbb{H}^T \mathbb{T} \hat{\mathbf{v}}}{\mathbb{H}^T \mathbb{Z}} + \hat{x}_-(\Omega) = -\frac{-\mathbb{H}^T \mathbb{R} \hat{\mathbf{a}} + \mathbb{H}^T \mathbb{T} \hat{\mathbf{v}}}{\mathbb{H}^T \mathbb{Z}} + \chi_{\text{eff}} F^{fl} \quad (\text{A.103})$$

From this we get the spectral density for this output

$$S_x(\Omega) = S_{xx}(\Omega) + 2\Re[\chi_{\text{eff}}^*(\Omega)S_{xF}(\Omega)] + |\chi_{\text{eff}}(\Omega)|^2 S_{FF}(\Omega), \quad (\text{A.104})$$

where

$$S_{xx} = \frac{\mathbb{H}^T (\mathbb{R} \mathbb{R}^\dagger + \mathbb{T} \mathbb{T}^\dagger) \mathbb{H}}{|\mathbb{H}^T \mathbb{Z}|^2}, \quad (\text{A.105})$$

$$\begin{aligned} S_{FF} &= 4\hbar^2 k^2 \mathbf{E}^\dagger \mathbb{D}_e \mathbb{O}(\delta_a \tau_a) \times \\ &\quad \times \left(\mathbb{T}_d \mathbb{T}_d^\dagger + T_e^2 \mathbb{R}_d \mathbb{R}_d^\dagger \right) \mathbb{O}^\dagger(\delta_a \tau_a) \mathbb{D}_e^\dagger \mathbf{E}, \end{aligned} \quad (\text{A.106})$$

$$\begin{aligned} S_{xF} &= \frac{2\hbar k}{\mathbb{H}^T \mathbb{Z}} \left(-\mathbb{H}^T \mathbb{R} \mathbb{T}_d^\dagger \mathbb{O}^\dagger(\delta_a \tau_a) \mathbb{D}_e^\dagger \mathbf{E} e^{-i\Omega \tau_a} + \right. \\ &\quad \left. + T_e \mathbb{H}^T \mathbb{T} \mathbb{O}^\dagger(\delta_a \tau_a) \mathbb{R}_d \mathbb{O}^\dagger(\delta_a \tau_a) \mathbb{D}_e^\dagger \mathbf{E} e^{-2i\Omega \tau_a} \right). \end{aligned} \quad (\text{A.107})$$

Finally we normalize the spectral density to the gravitational-wave strain yielding

$$S_h(\Omega) = S_x(\Omega) \frac{4}{m^2 L^2 \Omega^4 |\chi_{\text{eff}}(\Omega)|^2}. \quad (\text{A.108})$$

A.3 Appendix: paired carriers

In this Appendix, we consider the single carrier features and therefore omit for brevity the indices enumerated the carriers.

A.3.1 Speedmeter-like frequency dependence of the shot noise

Consider the ultimate case of the condition (5.24), assuming that

$$\zeta = \beta. \quad (\text{A.109})$$

This assumption gives the exact speedmeter-like frequency dependence of the shot noise:

$$S_{xx}(\Omega) = \frac{\hbar}{4MJ\Gamma \cos \beta \sin^2 \beta} \frac{A\Gamma^4 + 2B\Gamma^2\Omega^2 + C\Omega^4}{\Omega^2}, \quad (\text{A.110})$$

where

$$A = e^{2r} \cos^2(\beta + \theta) + e^{-2r} \sin^2(\beta + \theta), \quad (\text{A.111a})$$

$$B = e^{2r} \cos(\beta + \theta) \cos(\theta - \beta) + e^{-2r} \sin(\beta + \theta) \sin(\theta - \beta), \quad (\text{A.111b})$$

$$C = e^{2r} \cos^2(\theta - \beta) + e^{-2r} \sin^2(\theta - \beta). \quad (\text{A.111c})$$

The low- and high-frequency asymptotics of (A.110) are equal to

$$S_{xx}(\Omega \rightarrow 0) = \frac{\hbar\Gamma^3}{4MJ\Omega^2 \cos \beta \sin^2 \beta} A, \quad (\text{A.112a})$$

$$S_{xx}(\Omega \rightarrow \infty) = \frac{\hbar\Omega^2}{4MJ\Gamma \cos \beta \sin^2 \beta} C, \quad (\text{A.112b})$$

The minimum of (A.110) is equal to

$$S_{xx}(\Omega_0) = \frac{\hbar\Gamma}{2MJ \cos \beta \sin^2 \beta} (\sqrt{AC} + B), \quad (\text{A.113})$$

where

$$\Omega_0 = \Gamma \left(\frac{A}{C} \right)^{1/4}. \quad (\text{A.114})$$

A.3.2 Sub-optimal regimes of the dual carrier interferometer

Here we analytically calculate a sub-optimal parameters values of the antisymmetric dual-carrier regime which we use in the plots in Sec. 5.3. We enumerate the carriers by the index j , assuming the condition (5.46) for the odd and the even components.

One pair of carriers or low-frequency pair of the xylophone

Start with requirement, that the low frequency asymptotic of the total quantum noise spectral density has to be equal to the SQL:

$$S_{\text{sum}}(\Omega \rightarrow 0) = \frac{\hbar}{M\Omega^2}. \quad (\text{A.115})$$

With account of Eqs. (5.1, 5.46, 5.47, A.112a), it gives:

$$S_{xx}^{\text{eff}}(\Omega \rightarrow 0) = \frac{S_{xx}^{(j)}(\Omega \rightarrow 0)}{2} = \frac{\hbar}{2M\Omega^2} \Rightarrow \quad (\text{A.116})$$

$$\Gamma_j = \left(\frac{4J_j \cos \beta_j \sin^2 \beta}{A_j} \right)^{1/3}, \quad (\text{A.117})$$

where $j = 1, 2$.

The corresponding high-frequency asymptotic of the total quantum noise is equal to

$$S_{\text{sum}}(\Omega \rightarrow \infty) \approx \frac{S_{xx}^{(j)}(\Omega \rightarrow \infty)}{2} = \frac{\hbar\Omega^2}{2M(4J_j)^{4/3}} F^{1/3}(\beta_j, \theta_j), \quad (\text{A.118})$$

e^{2r}	Γ/Ω_0	β	θ
1.0 (0 db)	1.0	$-\arccos(1/\sqrt{3})$	—
2.0 (3 db)	0.75	-1.02	0.51
4.0 (6 db)	0.54	-1.04	0.52
10.0 (10 db)	0.34	-1.05	0.52
> 10.0	$e^{-r}/\sin 2\beta$	-1.047	$\pi/2 + \beta$

Tab. A.1. Values of Γ , β , and θ which minimize function (A.122)

where

$$F(\beta, \theta) = \frac{AC^3}{\cos^4 \beta \sin^8 \beta}. \quad (\text{A.119})$$

The values of β and θ which provide the minimum of this function are shown in Table A.1 for some characteristic values of squeezing. Note that in all cases, $\theta \approx \pi/2 + \beta$, which cancels the term proportional to e^{2r} in A , giving

$$F(\beta, \theta) \propto e^{-4r}. \quad (\text{A.120})$$

Therefore, the high-frequency part of the total noise scales with the power and with the squeezing as follows:

$$S_{\text{sum}}(\Omega \rightarrow \infty) \propto \frac{1}{(Je^r)^{4/3}}. \quad (\text{A.121})$$

Higher-frequency components of xylophon

At high frequency, the radiation pressure noise can be neglected. In this case, our goal is to get the most broadband shot noise spectral density centered at some given frequency Ω_0 . Therefore, we minimize the product of the low- and high-frequency asymptotics

$$\begin{aligned} S_{xx}(\Omega \rightarrow 0)^{\text{eff}} \times S_{xx}^{\text{eff}}(\Omega \rightarrow \infty) \\ &= \frac{1}{4} S_{xx}^{(j)}(\Omega \rightarrow 0) \times S_{xx}^{(j)}(\Omega \rightarrow \infty) \\ &= \frac{1}{4} \left(\frac{\hbar}{4MJ_j} \right)^2 \frac{\Gamma_j^2 A_j C_j}{\cos^2 \beta_j \sin^4 \beta_j} \quad (\text{A.122}) \end{aligned}$$

where $j = \{2p + 1, 2p + 2\}$ and $p = 2, \dots$ is the pair number, in Γ_j , β_j , and θ_j for a given value of Ω_0 :

Eq. (A.114) gives Γ_j :

$$\Gamma_j = \Omega_0 \left(\frac{C_j}{A_j} \right)^{1/4}. \quad (\text{A.123})$$

Therefore,

$$S_{xx}^{(j)}(\Omega \rightarrow 0) \times S_{xx}^{(j)}(\Omega \rightarrow \infty) = \left(\frac{\hbar}{4MJ_j} \right)^2 \sqrt{F(\beta_j, \theta_j)}, \quad (\text{A.124})$$

with the same optimal values of β_j and θ_j as for the low-frequency pair.

In this case, the noise scales with the power and with the squeezing as follows:

$$S_{\text{sum}}(\Omega \rightarrow \infty) \propto \frac{1}{Je^r}. \quad (\text{A.125})$$

Narrowband optimization

The minimum of (A.113) in θ is provided by

$$\theta_j = \frac{\pi}{2}. \quad (\text{A.126})$$

In this case,

$$S_{xx}^{(j)}(\Omega) = \frac{\hbar}{4MJ_j\Gamma_j\Omega^2 \cos \beta_j \sin^2 \beta_j} \times \left[(\Omega^2 - \Gamma_j^2)^2 e^{2r} \sin^2 \beta_j + (\Omega^2 + \Gamma_j^2)^2 e^{-2r} \cos^2 \beta_j \right]. \quad (\text{A.127})$$

If

$$\left| \alpha_j = \frac{\pi}{2} - \beta_j \right| \ll 1, \quad (\text{A.128})$$

then this spectral density has a sharp minimum at $\Omega = \Gamma_j$. In this case

$$S_{xx}^{(j)}(\Omega_0 + \nu) \approx \frac{\hbar}{MJ\Gamma_j\alpha_j} \left(\nu^2 e^{2r_j} + \Gamma_j^2 \alpha_j^2 e^{-2r_j} \right). \quad (\text{A.129})$$

Therefore, the value of the minimum and its width are equal to

$$S_{xx}(\Gamma) \approx \frac{\hbar\Gamma_j\alpha_j e^{-2r_j}}{MJ}, \quad (\text{A.130})$$

$$\Delta\Omega = 2\Gamma_j\alpha_j e^{-2r_j}. \quad (\text{A.131})$$

Bibliography

- [1] LIGO Scientific Collaboration and Virgo Collaboration. “Observation of gravitational waves from a binary black hole merger”. In: *Physical Review Letters* 116.6 (2016). doi: [10.1103/PhysRevLett.116.061102](https://doi.org/10.1103/PhysRevLett.116.061102) (cited on pages [ix](#), [xi](#), [1](#), [14](#)).
- [2] B. P. Abbott, R. Abbott, T. D. Abbott, et al. “GWTC-1: A gravitational-wave transient catalog of compact binary mergers observed by LIGO and Virgo during the first and second observing runs”. In: *Physical Review X* 9.3 (2019), p. 31040 (cited on pages [ix](#), [xi](#), [1](#)).
- [3] B. P. Abbott, R. Abbott, T. D. Abbott, et al. “GW170104: Observation of a 50-Solar-Mass Binary Black Hole Coalescence at Redshift 0.2”. In: *Physical Review Letters* 118.22 (2017), p. 221101. doi: [10.1103/PhysRevLett.118.221101](https://doi.org/10.1103/PhysRevLett.118.221101) (cited on pages [ix](#), [xi](#), [201](#)).
- [4] LIGO Scientific Collaboration and Virgo Collaboration, F. G.-r. B. Monitor, A. C. Z. T. I. Team, et al. “Multi-messenger observations of a binary neutron star merger”. In: *Astrophysical Journal Letters* 848.2 (2017). doi: [10.3847/2041-8213/aa91c9](https://doi.org/10.3847/2041-8213/aa91c9) (cited on pages [ix](#), [xi](#), [1](#)).
- [5] B. P. Abbott, R. Abbott, T. D. Abbott, et al. “Gravitational Waves and Gamma-Rays from a Binary Neutron Star Merger: GW170817 and GRB 170817A”. In: *The Astrophysical Journal* 848.2 (2017), p. L13. doi: [10.3847/2041-8213/aa920c](https://doi.org/10.3847/2041-8213/aa920c) (cited on pages [ix](#), [xi](#), [1](#)).
- [6] LIGO Scientific Collaboration and Virgo Collaboration. “A gravitational-wave standard siren measurement of the Hubble constant”. In: *Nature* 551.7678 (2017). doi: [10.1038/nature24471](https://doi.org/10.1038/nature24471) (cited on pages [ix](#), [xi](#), [2](#)).
- [7] A. Einstein. “Näherungsweise Integration der Feldgleichungen der Gravitation”. In: *Sitzungsberichte der Königlich Preußischen Akademie der Wis-*

senschaften. Wiley, 2016, pp. 688–696. DOI: [10.1002/3527608958.ch7](https://doi.org/10.1002/3527608958.ch7) (cited on page [↑1](#)).

- [8] M. E. Gertsenshtein and V. I. Pustovoit. “On the detection of low frequency gravitational waves”. In: *Journal of Experimental and Theoretical Physics (U.S.S.R.)* 43.2 (1962), pp. 605–607 (cited on page [↑1](#)).
- [9] R. Weiss. *Electromagnetically Coupled Broadband Gravitational Antenna*. 1972. DOI: [P720002-00-R](https://doi.org/10.720002-00-R) (cited on page [↑1](#)).
- [10] J. Aasi, B. P. Abbott, R. Abbott, et al. “Advanced LIGO”. In: *Classical and Quantum Gravity* 32.7 (2015), p. 074001. DOI: [10.1088/0264-9381/32/7/074001](https://doi.org/10.1088/0264-9381/32/7/074001). arXiv: [1411.4547](https://arxiv.org/abs/1411.4547) (cited on pages [↑1](#), [3](#), [20](#), [21](#), [83](#), [137](#), [141](#), [221](#), [231](#)).
- [11] B. Caron, A. Dominjon, C. Drezen, et al. “The Virgo interferometer”. In: *Classical and Quantum Gravity* 14 (1997), p. 1461 (cited on page [↑1](#)).
- [12] F. Acernese, M. Agathos, K. Agatsuma, et al. “Advanced Virgo: A second-generation interferometric gravitational wave detector”. In: *Classical and Quantum Gravity* 32.2 (2015), p. 024001. DOI: [10.1088/0264-9381/32/2/024001](https://doi.org/10.1088/0264-9381/32/2/024001). arXiv: [1408.3978](https://arxiv.org/abs/1408.3978) (cited on pages [↑1](#), [231](#)).
- [13] B. F. Schutz, H. Lück, P. Aufmuth, et al. “The status of GEO600”. In: *Third Edoardo Amaldi Conference*. 2000, pp. 119–127 (cited on page [↑1](#)).
- [14] A. Rüdiger and K. Danzmann. “The GEO 600 Gravitational Wave Detector Status, Research, Development”. In: *Gyros, Clocks, Interferometers...: Testing Relativistic Gravity in Space*. 2001, pp. 131–140. DOI: [10.1007/3-540-40988-2_7](https://doi.org/10.1007/3-540-40988-2_7) (cited on page [↑1](#)).
- [15] Y. Aso, Y. Michimura, K. Somiya, et al. “Interferometer design of the KAGRA gravitational wave detector”. In: *Physical Review D - Particles, Fields, Gravitation and Cosmology* 88.4 (2013), p. 043007. DOI: [10.1103/PhysRevD.88.043007](https://doi.org/10.1103/PhysRevD.88.043007). arXiv: [1306.6747](https://arxiv.org/abs/1306.6747) (cited on page [↑1](#)).
- [16] D. V. Martynov, E. D. Hall, B. P. Abbott, et al. “Sensitivity of the Advanced LIGO detectors at the beginning of gravitational wave astronomy”. In: *Physical Review D* 93.11 (2016), p. 112004. DOI: [10.1103/PhysRevD.93.112004](https://doi.org/10.1103/PhysRevD.93.112004). arXiv: [1604.00439](https://arxiv.org/abs/1604.00439) (cited on pages [↑1](#), [20](#), [21](#), [25](#), [26](#)).

- [17] B. P. Abbott, R. Abbott, T. D. Abbott, et al. “Tests of general relativity with GW170817”. In: *Physical Review Letters* 123.1 (2019), p. 11102 (cited on page ↑2).
- [18] B. P. Abbott, R. Abbott, T. D. Abbott, et al. “Tests of General Relativity with GW150914”. In: *Physical Review Letters* 116.22 (2016), p. 221101. DOI: [10.1103/PhysRevLett.116.221101](https://doi.org/10.1103/PhysRevLett.116.221101) (cited on page ↑2).
- [19] D. Kasen, B. Metzger, J. Barnes, E. Quataert, and E. Ramirez-Ruiz. “Origin of the heavy elements in binary neutron-star mergers from a gravitational-wave event”. In: *Nature* 551.7678 (2017), pp. 80–84. DOI: [10.1038/nature24453](https://doi.org/10.1038/nature24453) (cited on page ↑2).
- [20] B. P. Abbott, R. Abbott, T. D. Abbott, et al. “Estimating the Contribution of Dynamical Ejecta in the Kilonova Associated with GW170817”. In: *The Astrophysical Journal* 850.2 (2017), p. L39. DOI: [10.3847/2041-8213/aa9478](https://doi.org/10.3847/2041-8213/aa9478). arXiv: [1710.05836](https://arxiv.org/abs/1710.05836) (cited on page ↑2).
- [21] S. Jana and S. Mohanty. “Constraints on $f(R)$ theories of gravity from GW170817”. In: *Physical Review D* 99.4 (2019). DOI: [10.1103/PhysRevD.99.044056](https://doi.org/10.1103/PhysRevD.99.044056). arXiv: [1807.04060](https://arxiv.org/abs/1807.04060) (cited on page ↑2).
- [22] B. Abbott, R. Abbott, T. Abbott, et al. “Constraints on cosmic strings using data from the first Advanced LIGO observing run”. In: *Physical Review D* 97.10 (2018). DOI: [10.1103/PhysRevD.97.102002](https://doi.org/10.1103/PhysRevD.97.102002) (cited on page ↑2).
- [23] J. García-Bellido. “Massive Primordial Black Holes as Dark Matter and their detection with Gravitational Waves”. In: *Journal of Physics: Conference Series*. Vol. 840. 1. 2017. DOI: [10.1088/1742-6596/840/1/012032](https://doi.org/10.1088/1742-6596/840/1/012032). arXiv: [1702.08275](https://arxiv.org/abs/1702.08275) (cited on page ↑2).
- [24] S. Wang, Y. F. Wang, Q. G. Huang, and T. G. Li. “Constraints on the Primordial Black Hole Abundance from the First Advanced LIGO Observation Run Using the Stochastic Gravitational-Wave Background”. In: *Physical Review Letters* 120.19 (2018). DOI: [10.1103/PhysRevLett.120.191102](https://doi.org/10.1103/PhysRevLett.120.191102). arXiv: [1610.08725](https://arxiv.org/abs/1610.08725) (cited on page ↑2).

- [25] L. Amendola, M. Kunz, I. D. Saltas, and I. Sawicki. “Fate of Large-Scale Structure in Modified Gravity after GW170817 and GRB170817A”. In: *Physical Review Letters* 120.13 (2018). DOI: [10.1103/PhysRevLett.120.1311101](https://doi.org/10.1103/PhysRevLett.120.1311101). arXiv: [1711.04825](https://arxiv.org/abs/1711.04825) (cited on page [↑2](#)).
- [26] K. Yamada, T. Narikawa, and T. Tanaka. “Testing massive-field modifications of gravity via gravitational waves”. In: *Progress of Theoretical and Experimental Physics* 2019.10 (2019). DOI: [10.1093/ptep/ptz103](https://doi.org/10.1093/ptep/ptz103). arXiv: [1905.11859](https://arxiv.org/abs/1905.11859) (cited on page [↑2](#)).
- [27] H. K. Guo, K. Riles, F. W. Yang, and Y. Zhao. “Searching for dark photon dark matter in LIGO O1 data”. In: *Communications Physics* 2.1 (2019). DOI: [10.1038/s42005-019-0255-0](https://doi.org/10.1038/s42005-019-0255-0). arXiv: [1905.04316](https://arxiv.org/abs/1905.04316) (cited on page [↑2](#)).
- [28] J. M. Ezquiaga and M. Zumalacárregui. “Dark Energy in Light of Multi-Messenger Gravitational-Wave Astronomy”. In: *Frontiers in Astronomy and Space Sciences* 5 (2018). DOI: [10.3389/fspas.2018.00044](https://doi.org/10.3389/fspas.2018.00044). arXiv: [1807.09241](https://arxiv.org/abs/1807.09241) (cited on page [↑2](#)).
- [29] M. Du, W. Yang, L. Xu, S. Pan, and D. F. Mota. “Future constraints on dynamical dark-energy using gravitational-wave standard sirens”. In: *Physical Review D* 100.4 (2019). DOI: [10.1103/PhysRevD.100.043535](https://doi.org/10.1103/PhysRevD.100.043535). arXiv: [1812.01440](https://arxiv.org/abs/1812.01440) (cited on page [↑2](#)).
- [30] X. Calmet, I. Kuntz, and S. Mohapatra. “Gravitational Waves in Effective Quantum Gravity”. In: *European Physical Journal C* 76.8 (2016). DOI: [10.1140/epjc/s10052-016-4265-8](https://doi.org/10.1140/epjc/s10052-016-4265-8). arXiv: [1607.02773](https://arxiv.org/abs/1607.02773) (cited on page [↑2](#)).
- [31] S. B. Giddings. “Gravitational wave tests of quantum modifications to black hole structure - With post-GW150914 update”. In: *Classical and Quantum Gravity* 33.23 (2016). DOI: [10.1088/0264-9381/33/23/235010](https://doi.org/10.1088/0264-9381/33/23/235010). arXiv: [1602.03622](https://arxiv.org/abs/1602.03622) (cited on page [↑2](#)).
- [32] G. Calcagni, S. Kuroyanagi, S. Marsat, et al. “Quantum gravity and gravitational-wave astronomy”. In: *Journal of Cosmology and Astroparticle Physics* 2019.10 (2019). DOI: [10.1088/1475-7516/2019/10/012](https://doi.org/10.1088/1475-7516/2019/10/012). arXiv: [1907.02489](https://arxiv.org/abs/1907.02489) (cited on page [↑2](#)).

- [33] G. Calcagni, S. Kuroyanagi, S. Marsat, et al. “Gravitational-wave luminosity distance in quantum gravity”. In: *Physics Letters, Section B: Nuclear, Elementary Particle and High-Energy Physics* 798 (2019). DOI: [10.1016/j.physletb.2019.135000](https://doi.org/10.1016/j.physletb.2019.135000). arXiv: [1904.00384](https://arxiv.org/abs/1904.00384) (cited on page [↑2](#)).
- [34] V. B. Braginsky and F. Y. Khalili. *Quantum Measurement*. Cambridge University Press, 1992. Chap. V, p. 64 (cited on pages [↑2](#), [27](#), [29](#), [39](#), [83](#), [160](#), [162](#)).
- [35] S. L. Danilishin and F. Y. Khalili. “Quantum Measurement Theory in Gravitational-Wave Detectors”. In: *Living Reviews in Relativity* 15.1 (2012), pp. 1–147. DOI: [10.12942/lrr-2012-5](https://doi.org/10.12942/lrr-2012-5). arXiv: [1203.1706](https://arxiv.org/abs/1203.1706) (cited on pages [↑2](#), [39](#), [60](#), [83](#), [85](#), [95](#), [136](#), [142](#), [143](#), [156](#), [202](#), [214](#), [232](#), [235](#), [249](#), [256](#)).
- [36] G. Milburn and M. Woolley. “An Introduction to Quantum Optomechanics”. In: *Acta Physica Slovaca. Reviews and Tutorials* 61.5 (2011), pp. 483–601. DOI: [10.2478/v10155-011-0005-7](https://doi.org/10.2478/v10155-011-0005-7) (cited on pages [↑2](#), [39](#)).
- [37] M. Aspelmeyer, T. J. Kippenberg, and F. Marquardt. “Cavity optomechanics”. In: *Reviews of Modern Physics* 86.December (2014). DOI: [10.1103/RevModPhys.86.1391](https://doi.org/10.1103/RevModPhys.86.1391). arXiv: [0712.1618](https://arxiv.org/abs/0712.1618) (cited on pages [↑2](#), [230](#), [231](#)).
- [38] F. Y. Khalili and S. L. Danilishin. “Quantum Optomechanics”. In: *Progress in Optics*. 1st ed. Elsevier B.V., 2016, pp. 113–236. DOI: [10.1016/bs.po.2015.09.001](https://doi.org/10.1016/bs.po.2015.09.001) (cited on pages [↑2](#), [39](#)).
- [39] Y. Chen. “Macroscopic quantum mechanics: theory and experimental concepts of optomechanics”. In: *Journal of Physics B: Atomic, Molecular and Optical Physics* 46.10 (2013), p. 104001. DOI: [10.1088/0953-4075/46/10/104001](https://doi.org/10.1088/0953-4075/46/10/104001). arXiv: [1302.1924](https://arxiv.org/abs/1302.1924) (cited on page [↑2](#)).
- [40] R. Schnabel, N. Mavalvala, D. E. McClelland, and P. K. Lam. “Quantum metrology for gravitational wave astronomy”. In: *Nature Communications* 1.8 (2010), p. 121. DOI: [10.1038/ncomms1122](https://doi.org/10.1038/ncomms1122) (cited on pages [↑2](#), [39](#), [160](#)).
- [41] The LIGO Scientific Collaboration. “A gravitational wave observatory operating beyond the quantum shot-noise limit”. In: *Nature Physics* 7.12 (2011), pp. 962–965. DOI: [10.1038/nphys2083](https://doi.org/10.1038/nphys2083). arXiv: [1109.2295](https://arxiv.org/abs/1109.2295) (cited on pages [↑2](#), [160](#), [180](#)).

- [42] The LIGO Scientific Collaboration. “Enhanced sensitivity of the LIGO gravitational wave detector by using squeezed states of light”. In: *Nature Photonics* 7.8 (2013), pp. 613–619. DOI: [10.1038/nphoton.2013.177](https://doi.org/10.1038/nphoton.2013.177). arXiv: [arXiv:1310.0383v1](https://arxiv.org/abs/1310.0383v1) (cited on pages [↑2, 27, 160](#)).
- [43] R. Schnabel. “Squeezed states of light and their applications in laser interferometers”. In: *Physics Reports* 684 (2017), pp. 1–51. DOI: [10.1016/j.physrep.2017.04.001](https://doi.org/10.1016/j.physrep.2017.04.001) (cited on pages [↑2, 29, 41, 207](#)).
- [44] F. Acernese, M. Agathos, L. Aiello, et al. “Increasing the Astrophysical Reach of the Advanced Virgo Detector via the Application of Squeezed Vacuum States of Light”. In: *Physical Review Letters* 123.23 (2019). DOI: [10.1103/PhysRevLett.123.231108](https://doi.org/10.1103/PhysRevLett.123.231108) (cited on pages [↑2, 27, 160, 180](#)).
- [45] M. Tse, H. Yu, N. Kijbunchoo, et al. “Quantum-Enhanced Advanced LIGO Detectors in the Era of Gravitational-Wave Astronomy”. In: *Physical Review Letters* 123.23 (2019), p. 231107. DOI: [10.1103/PhysRevLett.123.231107](https://doi.org/10.1103/PhysRevLett.123.231107) (cited on pages [↑2, 29, 160, 180](#)).
- [46] R. W. P. Drever, J. L. Hall, F. V. Kowalski, et al. “Laser phase and frequency stabilization using an optical resonator”. In: *Applied Physics B Photophysics and Laser Chemistry* 31.2 (1983), pp. 97–105. DOI: [10.1007/BF00702605](https://doi.org/10.1007/BF00702605) (cited on pages [↑2, 113, 171](#)).
- [47] E. D. Black. “An introduction to Pound–Drever–Hall laser frequency stabilization”. In: *American Journal of Physics* 69.1 (2001), p. 79. DOI: [10.1119/1.1286663](https://doi.org/10.1119/1.1286663) (cited on pages [↑2, 113, 171](#)).
- [48] M. D. Álvarez. “Optical Cavities for Optical Atomic Clocks, Atom Interferometry and Gravitational-Wave Detection”. In: *Book* September (2019), pp. 1–25. DOI: [10.1007/978-3-030-20863-9](https://doi.org/10.1007/978-3-030-20863-9) (cited on page [↑2](#)).
- [49] A. V. Cumming, L. Cunningham, G. D. Hammond, et al. “Silicon mirror suspensions for gravitational wave detectors”. In: *Classical and Quantum Gravity* 31.2 (2014). DOI: [10.1088/0264-9381/31/2/025017](https://doi.org/10.1088/0264-9381/31/2/025017) (cited on page [↑2](#)).

- [50] F. Matichard, B. Lantz, R. Mittleman, et al. “Seismic isolation of Advanced LIGO: Review of strategy, instrumentation and performance”. In: *Classical and Quantum Gravity* 32.18 (2015). DOI: [10.1088/0264-9381/32/18/185003](https://doi.org/10.1088/0264-9381/32/18/185003). arXiv: [1502.06300](https://arxiv.org/abs/1502.06300) (cited on pages [↑2](#), [25](#)).
- [51] A. M. A. Van Veggel. *Quasi-monolithic mirror suspensions in ground-based gravitational-wave detectors: An overview and look to the future*. 2018. DOI: [10.1098/rsta.2017.0281](https://doi.org/10.1098/rsta.2017.0281) (cited on page [↑2](#)).
- [52] R. Flaminio, J. Franc, C. Michel, et al. “A study of coating mechanical and optical losses in view of reducing mirror thermal noise in gravitational wave detectors”. In: *Classical and Quantum Gravity* 27.8 (2010). DOI: [10.1088/0264-9381/27/8/084030](https://doi.org/10.1088/0264-9381/27/8/084030) (cited on page [↑2](#)).
- [53] M. Principe. “Reflective coating optimization for interferometric detectors of gravitational waves”. In: *Optics Express* 23.9 (2015), p. 10938. DOI: [10.1364/oe.23.010938](https://doi.org/10.1364/oe.23.010938) (cited on page [↑2](#)).
- [54] J. Steinlechner. “Development of mirror coatings for gravitational-wave detectors”. In: *Philosophical Transactions of the Royal Society A: Mathematical, Physical and Engineering Sciences* 376.2120 (2018). DOI: [10.1098/rsta.2017.0282](https://doi.org/10.1098/rsta.2017.0282) (cited on pages [↑2](#), [25](#), [215](#)).
- [55] J. Steinlechner, I. W. Martin, A. S. Bell, et al. “Silicon-Based Optical Mirror Coatings for Ultrahigh Precision Metrology and Sensing”. In: *Physical Review Letters* 120.26 (2018). DOI: [10.1103/PhysRevLett.120.263602](https://doi.org/10.1103/PhysRevLett.120.263602) (cited on page [↑2](#)).
- [56] B. P. Abbott, R. Abbott, T. D. Abbott, et al. “Prospects for observing and localizing gravitational-wave transients with Advanced LIGO, Advanced Virgo and KAGRA”. In: *Living Reviews in Relativity* 21.1 (2018), p. 3 (cited on page [↑2](#)).
- [57] L. collaboration, V. collaboration, and K. collaboration. “Advanced LIGO, Advanced Virgo and KAGRA observing run plans”. In: (2019), pp. 1–6 (cited on page [↑2](#)).
- [58] The LIGO Scientific Collaboration. “Exploring the Sensitivity of Next Generation Gravitational Wave Detectors”. In: (2016), pp. 1–11. arXiv: [1607.08697](https://arxiv.org/abs/1607.08697) (cited on pages [↑2](#), [19](#)).

- [59] R. X. Adhikari, O. Aguiar, K. Arai, et al. “A Cryogenic Silicon Interferometer for Gravitational-wave Detection”. In: *arXiv preprint arXiv:2001.11173* (2020). arXiv: [2001.11173](https://arxiv.org/abs/2001.11173) (cited on page [↑2](#)).
- [60] M. Punturo, M. Abernathy, F. Acernese, et al. “The Einstein Telescope: A third-generation gravitational wave observatory”. In: *Classical and Quantum Gravity* 27.19 (2010). DOI: [10.1088/0264-9381/27/19/194002](https://doi.org/10.1088/0264-9381/27/19/194002) (cited on page [↑2](#)).
- [61] M. Maggiore, C. van den Broeck, N. Bartolo, et al. “Science Case for the Einstein Telescope”. In: (2019). arXiv: [1912.02622](https://arxiv.org/abs/1912.02622) (cited on pages [↑2, 3](#)).
- [62] D. Reitze, R. X. Adhikari, S. Ballmer, et al. “Cosmic Explorer: The U.S. Contribution to Gravitational-Wave Astronomy beyond LIGO”. In: (2019). arXiv: [1907.04833](https://arxiv.org/abs/1907.04833) (cited on page [↑2](#)).
- [63] R. X. Adhikari, P. Ajith, Y. Chen, et al. “Astrophysical science metrics for next-generation gravitational-wave detectors”. In: *Classical and Quantum Gravity* 36.24 (2019). DOI: [10.1088/1361-6382/ab3cff](https://doi.org/10.1088/1361-6382/ab3cff). arXiv: [1905.02842](https://arxiv.org/abs/1905.02842) (cited on page [↑3](#)).
- [64] H. Miao, H. Yang, and D. Martynov. “Towards the design of gravitational-wave detectors for probing neutron-star physics”. In: *Physical Review D* 98.4 (2018), p. 044044. DOI: [10.1103/PhysRevD.98.044044](https://doi.org/10.1103/PhysRevD.98.044044). arXiv: [1712.07345](https://arxiv.org/abs/1712.07345) (cited on pages [↑3, 214, 222](#)).
- [65] H. P. Yuen and V. W. S. Chan. “Noise in homodyne and heterodyne detection”. In: *Optics Letters* 8 (1983), p. 177 (cited on pages [↑3, 27](#)).
- [66] C. M. Caves. “Quantum-mechanical noise in an interferometer”. In: *Physical Review D* 23 (1981), p. 1693. DOI: <http://dx.doi.org/10.1103/PhysRevD.23.1693> (cited on pages [↑3, 27, 160, 186](#)).
- [67] C. M. Caves. “Quantum-Mechanical Radiation-Pressure Fluctuations in an Interferometer”. In: *Physical Review Letters* 45.2 (1980), pp. 75–79. DOI: [10.1103/PhysRevLett.45.75](https://doi.org/10.1103/PhysRevLett.45.75). arXiv: [arXiv:1011.1669v3](https://arxiv.org/abs/1011.1669v3) (cited on pages [↑3, 20, 160](#)).

- [68] X. Li, M. Korobko, Y. Ma, R. Schnabel, and Y. Chen. “Coherent coupling completing an unambiguous optomechanical classification framework”. In: *Physical Review A* 100.5 (2019), p. 053855. DOI: [10.1103/PhysRevA.100.053855](https://doi.org/10.1103/PhysRevA.100.053855). arXiv: [1908.03372](https://arxiv.org/abs/1908.03372) (cited on pages [↑4](#), [90](#), [108](#), [110](#), [111](#), [246](#), [247](#)).
- [69] M. Korobko, N. Voronchev, H. Miao, and F. Y. Khalili. “Paired carriers as a way to reduce quantum noise of multicarrier gravitational-wave detectors”. In: *Physical Review D* 91.4 (2015), p. 042004. DOI: [10.1103/PhysRevD.91.042004](https://doi.org/10.1103/PhysRevD.91.042004) (cited on pages [↑4](#), [135](#), [156](#), [157](#)).
- [70] M. Korobko, L. Kleybolte, S. Ast, et al. “Beating the Standard Sensitivity-Bandwidth Limit of Cavity-Enhanced Interferometers with Internal Squeezed-Light Generation”. In: *Physical Review Letters* 118.14 (2017), p. 143601. DOI: [10.1103/PhysRevLett.118.143601](https://doi.org/10.1103/PhysRevLett.118.143601) (cited on pages [↑4](#), [159](#), [176](#), [183](#), [202](#), [221](#)).
- [71] M. Korobko, Y. Ma, Y. Chen, and R. Schnabel. “Quantum expander for gravitational-wave observatories”. In: *Light: Science & Applications* 8.1 (2019), p. 118. DOI: [10.1038/s41377-019-0230-2](https://doi.org/10.1038/s41377-019-0230-2). arXiv: [1903.05930](https://arxiv.org/abs/1903.05930) (cited on pages [↑5](#), [183](#), [203](#)).
- [72] M. Korobko, F. Y. Khalili, and R. Schnabel. “Engineering the optical spring via intra-cavity optical-parametric amplification”. In: *Physics Letters A* 382.33 (2018), pp. 2238–2244. DOI: [10.1016/j.physleta.2017.08.008](https://doi.org/10.1016/j.physleta.2017.08.008). arXiv: [1709.03055](https://arxiv.org/abs/1709.03055) (cited on pages [↑5](#), [203](#), [221](#), [229](#)).
- [73] J. C.W. Misner, K.S. Thorne. *Gravitation*. W. H. Freeman and Company, San Francisco, 1973 (cited on pages [↑13](#), [14](#)).
- [74] Sean M. Carroll. *Spacetime and Geometry: An Introduction to General Relativity*. Addison-Wesley, 2003 (cited on pages [↑13](#), [14](#)).
- [75] J. M. Weisberg, J. H. Taylor, and L. A. Fowler. “Gravitational Waves from an Orbiting Pulsar”. In: *Scientific American* 245.4 (1981), pp. 74–82. DOI: [10.1038/scientificamerican1081-74](https://doi.org/10.1038/scientificamerican1081-74) (cited on page [↑14](#)).
- [76] B. Pang and Y. Chen. “Quantum interactions between a laser interferometer and gravitational waves”. In: *Physical Review D* 98.12 (2018). DOI: [10.1103/PhysRevD.98.124006](https://doi.org/10.1103/PhysRevD.98.124006). arXiv: [1808.09122](https://arxiv.org/abs/1808.09122) (cited on page [↑15](#)).

- [77] M. Rakhmanov. “Response of test masses to gravitational waves in the local Lorentz gauge”. In: *Physical Review D - Particles, Fields, Gravitation and Cosmology* 71.8 (2005), pp. 1–12. doi: [10.1103/PhysRevD.71.084003](https://doi.org/10.1103/PhysRevD.71.084003) (cited on page [↑15](#)).
- [78] L. Gottardi, A. De Waard, O. Usenko, et al. “Sensitivity of the spherical gravitational wave detector MiniGRAIL operating at 5 K”. In: *Physical Review D - Particles, Fields, Gravitation and Cosmology* 76.10 (2007). doi: [10.1103/PhysRevD.76.102005](https://doi.org/10.1103/PhysRevD.76.102005) (cited on page [↑17](#)).
- [79] G. Hobbs, A. Archibald, Z. Arzoumanian, et al. “The international pulsar timing array project: Using pulsars as a gravitational wave detector”. In: *Classical and Quantum Gravity* 27.8 (2010). doi: [10.1088/0264-9381/27/8/084013](https://doi.org/10.1088/0264-9381/27/8/084013). arXiv: [0911.5206](https://arxiv.org/abs/0911.5206) (cited on page [↑17](#)).
- [80] M. P. Robbins, N. Afshordi, and R. B. Mann. “Bose-Einstein condensates as gravitational wave detectors”. In: *Journal of Cosmology and Astroparticle Physics* 2019.7 (2019). doi: [10.1088/1475-7516/2019/07/032](https://doi.org/10.1088/1475-7516/2019/07/032). arXiv: [1811.04468](https://arxiv.org/abs/1811.04468) (cited on page [↑17](#)).
- [81] S. Dimopoulos, P. W. Graham, J. M. Hogan, M. A. Kasevich, and S. Rajendran. “Gravitational wave detection with atom interferometry”. In: *Physics Letters, Section B: Nuclear, Elementary Particle and High-Energy Physics* 678.1 (2009), pp. 37–40. doi: [10.1016/j.physletb.2009.06.011](https://doi.org/10.1016/j.physletb.2009.06.011). arXiv: [0712.1250](https://arxiv.org/abs/0712.1250) (cited on page [↑17](#)).
- [82] B. F. Schutz and M. Tinto. “Antenna patterns of interferometric detectors of gravitational waves - I. Linearly polarized waves”. In: *Monthly Notices of the Royal Astronomical Society* 224.1 (1987), pp. 131–154. doi: [10.1093/mnras/224.1.131](https://doi.org/10.1093/mnras/224.1.131) (cited on page [↑18](#)).
- [83] B. F. Schutz. “Networks of gravitational wave detectors and three figures of merit”. In: *Classical and Quantum Gravity* 28.12 (2011). doi: [10.1088/0264-9381/28/12/125023](https://doi.org/10.1088/0264-9381/28/12/125023). arXiv: [1102.5421](https://arxiv.org/abs/1102.5421) (cited on page [↑18](#)).
- [84] M. Armano, H. Audley, G. Auger, et al. “Sub-Femto- g Free Fall for Space-Based Gravitational Wave Observatories: LISA Pathfinder Results”. In: *Physical Review Letters* 116.23 (2016). doi: [10.1103/PhysRevLett.116.231101](https://doi.org/10.1103/PhysRevLett.116.231101) (cited on page [↑19](#)).

- [85] P. Amaro-Seoane, S. Aoudia, S. Babak, et al. “eLISA: Astrophysics and cosmology in the millihertz regime”. In: (2012). arXiv: [1201.3621](https://arxiv.org/abs/1201.3621) (cited on page [↑19](#)).
- [86] S. Sato, S. Kawamura, M. Ando, et al. “DECIGO: The Japanese space gravitational wave antenna”. In: *Journal of Physics: Conference Series* 154 (2009), p. 12040. doi: [10.1088/1742-6596/154/1/012040](https://doi.org/10.1088/1742-6596/154/1/012040) (cited on page [↑19](#)).
- [87] W. R. Hu and Y. L. Wu. *The Taiji Program in Space for gravitational wave physics and the nature of gravity*. 2017. doi: [10.1093/nsr/nwx116](https://doi.org/10.1093/nsr/nwx116) (cited on page [↑19](#)).
- [88] J. Luo, L. S. Chen, H. Z. Duan, et al. “TianQin: A space-borne gravitational wave detector”. In: *Classical and Quantum Gravity* 33.3 (2016). doi: [10.1088/0264-9381/33/3/035010](https://doi.org/10.1088/0264-9381/33/3/035010). arXiv: [1512.02076](https://arxiv.org/abs/1512.02076) (cited on page [↑19](#)).
- [89] V. B. Braginsky and I. I. Minakova. “Influence of the small displacement measurements on the dynamical properties of mechanical oscillating systems”. In: *Moscow Univ. Phys. Bull.* 1 (1964), pp. 83–85 (cited on pages [↑20](#), [230](#)).
- [90] *pyGWINC*, <https://git.ligo.org/gwinc/pygwinc> (cited on page [↑21](#)).
- [91] D. Walls and G. J. Milburn. *Quantum Optics*. Springer, 2008 (cited on pages [↑22](#), [39](#)).
- [92] G. M. Harry, H. Armandula, E. Black, et al. “Thermal noise from optical coatings in gravitational wave detectors”. In: *Appl. Opt.* 45.7 (2006), pp. 1569–1574. doi: [10.1364/AO.45.001569](https://doi.org/10.1364/AO.45.001569) (cited on page [↑24](#)).
- [93] G. Gonzalez. “Suspensions thermal noise in the LIGO gravitational wave detector”. In: *Class. Quantum Grav.* 17 (2000), pp. 4409–4435. doi: [10.1088/0264-9381/17/21/305](https://doi.org/10.1088/0264-9381/17/21/305). arXiv: [0006053](https://arxiv.org/abs/0006053) [gr-qc] (cited on page [↑25](#)).
- [94] N. A. Robertson, R. W. P. Drever, I. Kerr, and J. Hough. “Passive and active seismic isolation for gravitational radiation detectors and other instruments”. In: *Journal of Physics E: Scientific Instruments* 15.10 (1982), pp. 1101–1105. doi: [10.1088/0022-3735/15/10/032](https://doi.org/10.1088/0022-3735/15/10/032) (cited on page [↑25](#)).

- [95] P. R. Saulson. “Terrestrial gravitational noise on a gravitational wave antenna”. In: *Physical Review D* 30.4 (1984), pp. 732–736. doi: [10.1103/PhysRevD.30.732](https://doi.org/10.1103/PhysRevD.30.732) (cited on page [↑25](#)).
- [96] J. Harms. *Terrestrial gravity fluctuations*. 2019. doi: [10.1007/s41114-019-0022-2](https://doi.org/10.1007/s41114-019-0022-2) (cited on page [↑25](#)).
- [97] J. C. Driggers, J. Harms, and R. X. Adhikari. “Subtraction of Newtonian noise using optimized sensor arrays”. In: *Physical Review D - Particles, Fields, Gravitation and Cosmology* 86.10 (2012). doi: [10.1103/PhysRevD.86.102001](https://doi.org/10.1103/PhysRevD.86.102001) (cited on page [↑26](#)).
- [98] H. Vahlbruch, S. Chelkowski, K. Danzmann, and R. Schnabel. “Quantum engineering of squeezed states for quantum communication and metrology”. In: *New Journal of Physics* 9.10 (2007), p. 371. doi: [10.1088/1367-2630/9/10/371](https://doi.org/10.1088/1367-2630/9/10/371) (cited on page [↑26](#)).
- [99] The LIGO Scientific Collaboration. “Characterization of transient noise in Advanced LIGO relevant to gravitational wave signal GW150914”. In: *Classical and Quantum Gravity* 33.13 (2016). doi: [10.1088/0264-9381/33/13/134001](https://doi.org/10.1088/0264-9381/33/13/134001) (cited on page [↑26](#)).
- [100] B. P. Abbott, R. Abbott, T. D. Abbott, et al. “A guide to LIGO–Virgo detector noise and extraction of transient gravitational-wave signals”. In: *Classical and Quantum Gravity* 37.5 (2020), p. 055002. doi: [10.1088/1361-6382/ab685e](https://doi.org/10.1088/1361-6382/ab685e) (cited on page [↑26](#)).
- [101] R. Schnabel. ““Quantum Weirdness” in Exploitation by the International Gravitational-Wave Observatory Network”. In: *Annalen der Physik* 532.3 (2020), p. 1900508. doi: [10.1002/andp.201900508](https://doi.org/10.1002/andp.201900508) (cited on page [↑26](#)).
- [102] W. G. Unruh. “Quantum noise in the interferometer detector”. In: *Quantum Optics, Experimental Gravitation, and Measurement Theory*. Ed. by P. Meystre and M. O. Scully. Plenum, 1983, pp. 647–660 (cited on pages [↑27](#), [57](#)).
- [103] D. F. Walls. “Squeezed states of light”. In: *Nature* 306.5939 (1983), pp. 141–146. doi: [10.1038/306141a0](https://doi.org/10.1038/306141a0) (cited on page [↑27](#)).

- [104] H. Vahlbruch, S. Chelkowski, B. Hage, et al. “Demonstration of a Squeezed-Light-Enhanced Power- and Signal-Recycled Michelson Interferometer”. In: *Physical Review Letters* 95.21 (2005), p. 211102. DOI: [10.1103/PhysRevLett.95.211102](https://doi.org/10.1103/PhysRevLett.95.211102) (cited on page [↑27](#)).
- [105] K. Goda, O. Miyakawa, E. E. Mikhailov, et al. “A quantum-enhanced prototype gravitational-wave detector”. In: *Nature Physics* 4.6 (2008), pp. 472–476. DOI: [10.1038/nphys920](https://doi.org/10.1038/nphys920) (cited on page [↑27](#)).
- [106] M. Mehmet, S. Ast, T. Eberle, et al. “Squeezed light at 1550 nm with a quantum noise reduction of 123 dB”. In: *Optics Express* 19.25 (2011), p. 25763. DOI: [10.1364/OE.19.025763](https://doi.org/10.1364/OE.19.025763). arXiv: [1110.3737](https://arxiv.org/abs/1110.3737) (cited on pages [↑27](#), [171](#), [177](#)).
- [107] H. Vahlbruch, M. Mehmet, K. Danzmann, and R. Schnabel. “Detection of 15 dB Squeezed States of Light and their Application for the Absolute Calibration of Photoelectric Quantum Efficiency”. In: *Physical Review Letters* 117.11 (2016), pp. 1–5. DOI: [10.1103/PhysRevLett.117.110801](https://doi.org/10.1103/PhysRevLett.117.110801) (cited on pages [↑27](#), [177](#)).
- [108] J. Abadie, B. P. Abbott, R. Abbott, et al. “A gravitational wave observatory operating beyond the quantum shot-noise limit”. In: *Nature Physics* 7.12 (2011), pp. 962–965. DOI: [10.1038/NPHYS2083](https://doi.org/10.1038/NPHYS2083). arXiv: [1109.2295](https://arxiv.org/abs/1109.2295) (cited on page [↑27](#)).
- [109] H.Vahlbruch, A.Khalaidovski, N.Lastzka, C.Graef, K.Danzmann, R.Schnabel. “The GEO600 squeezed light source”. In: *Classical and Quantum Gravity* 27 (2010), p. 84027 (cited on page [↑27](#)).
- [110] M.T.Jaekel and S.Reynaud. “Quantum Limits in Interferometric Measurements”. In: *Europhysics Letters* 13 (1990), p. 301 (cited on page [↑27](#)).
- [111] S. Chelkowski, H. Vahlbruch, B. Hage, et al. “Experimental characterization of frequency-dependent squeezed light”. In: *Physical Review A* 71.1 (2005), p. 13806. DOI: [10.1103/PhysRevA.71.013806](https://doi.org/10.1103/PhysRevA.71.013806) (cited on pages [↑27](#), [155](#)).
- [112] H. J. Kimble, Y. Levin, A. B. Matsko, K. S. Thorne, and S. P. Vyatchanin. “Conversion of conventional gravitational-wave interferometers into QND interferometers by modifying their input and/or output optics”. In: *Physical Review D* 3 (2008), p. 33. DOI: [10.1103/PhysRevD.65.022002](https://doi.org/10.1103/PhysRevD.65.022002). arXiv:

0008026v2 [arXiv:gr-qc] (cited on pages ↑27, 58, 60, 141, 202, 214, 215, 217).

- [113] F. Y. Khalili. “Optimal configurations of filter cavity in future gravitational-wave detectors”. In: *Physical Review D* 81.12 (2010), pp. 1–11. doi: [10.1103/PhysRevD.81.122002](https://doi.org/10.1103/PhysRevD.81.122002). arXiv: [arXiv: 1003.2859v1](https://arxiv.org/abs/1003.2859v1) (cited on pages ↑27, 155).
- [114] M. Evans, L. Barsotti, P. Kwee, J. Harms, and H. Miao. “Realistic filter cavities for advanced gravitational wave detectors”. In: *Physical Review D - Particles, Fields, Gravitation and Cosmology* 88.2 (2013). doi: [10.1103/PhysRevD.88.022002](https://doi.org/10.1103/PhysRevD.88.022002). arXiv: [1305.1599](https://arxiv.org/abs/1305.1599) (cited on page ↑27).
- [115] J. B. Hertzberg, T. Rocheleau, T. Ndukum, et al. “Back-action Evading Measurements of Nanomechanical Motion”. In: *Nature Physics* 6.3 (2009), p. 19. doi: [10.1038/nphys1479](https://doi.org/10.1038/nphys1479). arXiv: [0906.0967](https://arxiv.org/abs/0906.0967) (cited on page ↑27).
- [116] G. Vasilakis, H. Shen, K. Jensen, et al. “Generation of a squeezed state of an oscillator by stroboscopic back-action-evading measurement”. In: *Nature Physics* advance on.March (2015), pp. 1–4. doi: [10.1038/nphys3280](https://doi.org/10.1038/nphys3280) (cited on page ↑27).
- [117] S. Danilishin and F. Khalili. “Stroboscopic variation measurement”. In: *Physics Letters A* 300.August (2002), pp. 547–558 (cited on page ↑27).
- [118] F. Y. Khalili. “Quantum variational measurement in the next generation gravitational-wave detectors”. In: *Physical Review D* (2007). arXiv: [0609058v2](https://arxiv.org/abs/0609058v2) [arXiv:gr-qc] (cited on page ↑27).
- [119] V. Braginsky and F. Y. Khalili. “Gravitational wave antenna with QND speed meter”. In: *Physics Letters A* 147.5-6 (1990), pp. 251–256. doi: [10.1016/0375-9601\(90\)90442-Q](https://doi.org/10.1016/0375-9601(90)90442-Q) (cited on pages ↑29, 83).
- [120] F. Ya. Khalili, Yu. Levin. “Speed meter as a quantum nondemolition measuring device for force”. In: *Physical Review D* 54 (1996), pp. 4735–4737 (cited on page ↑29).
- [121] P.Purdue, Y.Chen. “Practical speed meter design for QND gravitational-wave interferometers”. In: *Physical Review D* 66 (2002), p. 122004 (cited on pages ↑29, 84, 141, 142, 156).

- [122] C. Gräf, B. W. Barr, A. S. Bell, et al. “Design of a speed meter interferometer proof-of-principle experiment”. In: (2014). arXiv: [1405.2783](#) (cited on pages [↑29, 84](#)).
- [123] S. H. Huttner, S. L. Danilishin, B. W. Barr, et al. “Candidates for a possible third-generation gravitational wave detector: Comparison of ring-Sagnac and sloshing-Sagnac speedmeter interferometers”. In: *Classical and Quantum Gravity* 34.2 (2017). doi: [10.1088/1361-6382/34/2/024001](#) (cited on pages [↑29, 84](#)).
- [124] S. L. Danilishin, F. Y. Khalili, and H. Miao. *Advanced quantum techniques for future gravitational-wave detectors*. 2019. doi: [10.1007/s41114-019-0018-y](#). arXiv: [1903.05223](#) (cited on pages [↑29, 39, 84](#)).
- [125] S. L. Danilishin, E. Knyazev, N. V. Voronchev, et al. “A new quantum speed-meter interferometer: Measuring speed to search for intermediate mass black holes article”. In: *Light: Science and Applications* 7.1 (2018). doi: [10.1038/s41377-018-0004-2](#) (cited on pages [↑29, 84](#)).
- [126] T. Zhang, E. Knyazev, S. Steinlechner, et al. “Quantum noise cancellation in asymmetric speed metres with balanced homodyne readout”. In: *New Journal of Physics* 20.10 (2018). doi: [10.1088/1367-2630/aae86e](#). arXiv: [1806.05488](#) (cited on pages [↑29, 84](#)).
- [127] V. B. Braginsky, M. L. Gorodetsky, and F. Y. Khalili. “Optical bars in gravitational wave antennas”. In: *Physics Letters A* 232.August (1997), pp. 340–348 (cited on pages [↑29, 230](#)).
- [128] F. Khalili. “Frequency-dependent rigidity in large-scale interferometric gravitational-wave detectors”. In: *Physics Letters A* 288.October (2001), pp. 251–256 (cited on pages [↑29, 240](#)).
- [129] A. Buonanno and Y. Chen. “Laser-interferometer gravitational-wave optical-spring detectors”. In: *Classical and Quantum Gravity* July 2001 (2002), pp. 8–13. arXiv: [0201063v2 \[arXiv:gr-qc\]](#) (cited on pages [↑29, 136, 230, 237](#)).
- [130] J. Harms, Y. Chen, and S. Chelkowski. “Squeezed-input, optical-spring, signal-recycled gravitational-wave detectors”. In: *Physical Review D* (2003), pp. 1–10. arXiv: [0303066v2 \[arXiv:gr-qc\]](#) (cited on pages [↑29, 232](#)).

- [131] H. Rehbein, H. Mueller-Ebhardt, K. Somiya, et al. “Double optical spring enhancement for gravitational wave detectors”. In: *Physical Review D* (2008), pp. 1–11. doi: [10.1103/PhysRevD.78.062003](https://doi.org/10.1103/PhysRevD.78.062003) (cited on pages [↑29](#), [136](#), [137](#), [149](#), [156](#), [244](#)).
- [132] F. Y. Khalili, S. L. Danilishin, H. Müller-Ebhardt, et al. “Negative optical inertia for enhancing the sensitivity of future gravitational-wave detectors”. In: *Physical Review D - Particles, Fields, Gravitation and Cosmology* 83.6 (2011), pp. 1–7. doi: [10.1103/PhysRevD.83.062003](https://doi.org/10.1103/PhysRevD.83.062003) (cited on pages [↑29](#), [244](#)).
- [133] G. S. Pati, M. Salit, K. Salit, and M. S. Shahriar. “Demonstration of a Tunable-Bandwidth White-Light Interferometer Using Anomalous Dispersion in Atomic Vapor”. In: *Physical Review Letters* 99.13 (2007), p. 133601. doi: [10.1103/PhysRevLett.99.133601](https://doi.org/10.1103/PhysRevLett.99.133601). arXiv: [0610022](https://arxiv.org/abs/0610022) [quant-ph] (cited on pages [↑29](#), [160](#), [201](#)).
- [134] Y. Ma, H. Miao, C. Zhao, and Y. Chen. “Quantum noise of a white-light cavity using a double-pumped gain medium”. In: *Physical Review A* 92.2 (2015), p. 023807. doi: [10.1103/PhysRevA.92.023807](https://doi.org/10.1103/PhysRevA.92.023807). arXiv: [1501.01349](https://arxiv.org/abs/1501.01349) (cited on pages [↑29](#), [180](#), [201](#)).
- [135] H. N. Yum, J. Scheuer, M. Salit, P. R. Hemmer, and M. S. Shahriar. “Demonstration of white light cavity effect using stimulated Brillouin scattering in a fiber loop”. In: *Lightwave Technology, Journal of* 31 (2013), p. 3865 (cited on pages [↑29](#), [160](#), [201](#)).
- [136] M. Zhou, Z. Zhou, and S. M. Shahriar. “Quantum noise limits in white-light-cavity-enhanced gravitational wave detectors”. In: *Physical Review D* 92.8 (2015), p. 082002. doi: [10.1103/PhysRevD.92.082002](https://doi.org/10.1103/PhysRevD.92.082002). arXiv: [1410.6877](https://arxiv.org/abs/1410.6877) (cited on pages [↑29](#), [160](#), [201](#)).
- [137] H. Miao, Y. Ma, C. Zhao, and Y. Chen. “Enhancing the Bandwidth of Gravitational-Wave Detectors with Unstable Optomechanical Filters”. In: *Physical Review Letters* 115.21 (2015), pp. 1–5. doi: [10.1103/PhysRevLett.115.211104](https://doi.org/10.1103/PhysRevLett.115.211104). arXiv: [1506.00117v1](https://arxiv.org/abs/1506.00117v1) (cited on pages [↑29](#), [160](#), [201](#)).

- [138] J. Bentley, P. Jones, D. Martynov, A. Freise, and H. Miao. “Converting the signal-recycling cavity into an unstable optomechanical filter to enhance the detection bandwidth of gravitational-wave detectors”. In: *Physical Review D* 99.10 (2019). doi: [10.1103/PhysRevD.99.102001](https://doi.org/10.1103/PhysRevD.99.102001). arXiv: [1903.04965](https://arxiv.org/abs/1903.04965) (cited on page [↑29](#)).
- [139] J. Bentley, H. Nurdin, Y. Chen, and H. Miao. “A systematic approach to realising quantum filters for high-precision measurements using network synthesis theory”. In: (2020), pp. 1–6 (cited on page [↑29](#)).
- [140] F. Y. Khalili and E. S. Polzik. “Overcoming the Standard Quantum Limit in Gravitational Wave Detectors Using Spin Systems with a Negative Effective Mass”. In: *Physical Review Letters* 121.3 (2018). doi: [10.1103/PhysRevLett.121.031101](https://doi.org/10.1103/PhysRevLett.121.031101). arXiv: [1710.10405](https://arxiv.org/abs/1710.10405) (cited on page [↑29](#)).
- [141] Y. Ma, H. Miao, B. H. Pang, et al. “Proposal for Gravitational-Wave Detection Beyond the Standard Quantum Limit via EPR Entanglement”. In: 13.May (2016), pp. 776–780. doi: [10.1038/nphys4118](https://doi.org/10.1038/nphys4118). arXiv: [1612.06934](https://arxiv.org/abs/1612.06934) (cited on pages [↑29](#), [76](#), [80](#), [137](#), [158](#)).
- [142] Y. Ma, F.-L. Lin, H. Miao, C. Zhao, and Y. Chen. “Application of optomechanical frequency conversion on gravitational wave detection”. In: (2019). arXiv: [1912.01246](https://arxiv.org/abs/1912.01246) (cited on page [↑29](#)).
- [143] J. Südbeck, S. Steinlechner, M. Korobko, and R. Schnabel. “Demonstration of interferometer enhancement through Einstein–Podolsky–Rosen entanglement”. In: *Nature Photonics* 14.4 (2020), pp. 240–244. doi: [10.1038/s41566-019-0583-3](https://doi.org/10.1038/s41566-019-0583-3). arXiv: [1908.09602](https://arxiv.org/abs/1908.09602) (cited on pages [↑29](#), [76](#), [77](#), [79–81](#), [137](#), [158](#)).
- [144] M. J. Yap, P. Altin, T. G. McRae, et al. “Generation and control of frequency-dependent squeezing via Einstein–Podolsky–Rosen entanglement”. In: *Nature Photonics* (2020). doi: [10.1038/s41566-019-0582-4](https://doi.org/10.1038/s41566-019-0582-4). arXiv: [1908.08685](https://arxiv.org/abs/1908.08685) (cited on pages [↑29](#), [76](#), [137](#), [158](#)).
- [145] M. Szczykulska, T. Baumgratz, and A. Datta. “Multi-parameter quantum metrology”. In: *Advances in Physics: X* 1.4 (2016), pp. 621–639. doi: [10.1080/23746149.2016.1230476](https://doi.org/10.1080/23746149.2016.1230476). arXiv: [1604.02615](https://arxiv.org/abs/1604.02615) (cited on page [↑30](#)).

- [146] V. Giovannetti, S. Lloyd, and L. MacCone. *Advances in quantum metrology*. 2011. DOI: [10.1038/nphoton.2011.35](https://doi.org/10.1038/nphoton.2011.35). arXiv: [1102.2318](https://arxiv.org/abs/1102.2318) (cited on page [↑30](#)).
- [147] M. A. Taylor and W. P. Bowen. “Quantum metrology and its application in biology”. In: *Physics Reports* 615 (2016), pp. 1–59. DOI: [10.1016/j.physrep.2015.12.002](https://doi.org/10.1016/j.physrep.2015.12.002). arXiv: [1409.0950](https://arxiv.org/abs/1409.0950) (cited on pages [↑30](#), [198](#)).
- [148] F. Guzmán Cervantes, L. Kumanchik, J. Pratt, and J. M. Taylor. “High sensitivity optomechanical reference accelerometer over 10 kHz”. In: *Applied Physics Letters* 104.22 (2014). DOI: [10.1063/1.4881936](https://doi.org/10.1063/1.4881936). arXiv: [1303.1188](https://arxiv.org/abs/1303.1188) (cited on page [↑30](#)).
- [149] P. Cheiney, L. Fouché, S. Templier, et al. “Navigation-Compatible Hybrid Quantum Accelerometer Using a Kalman Filter”. In: *Physical Review Applied* 10.3 (2018). DOI: [10.1103/PhysRevApplied.10.034030](https://doi.org/10.1103/PhysRevApplied.10.034030). arXiv: [1805.06198](https://arxiv.org/abs/1805.06198) (cited on page [↑30](#)).
- [150] B.-B. Li, J. Bílek, U. B. Hoff, et al. “Quantum enhanced optomechanical magnetometry”. In: *Optica* 5.7 (2018), p. 850. DOI: [10.1364/OPTICA.5.000850](https://doi.org/10.1364/OPTICA.5.000850) (cited on pages [↑30](#), [198](#)).
- [151] V. B. Braginsky, M. L. Gorodetsky, K. S. Thorne, and F. Y. Khalili. “Energetic Quantum Limit in Large-Scale Interferometers”. In: *Gravitational waves. Third Edoardo Amaldi Conference, Pasadena, California 12-16 July*. Ed. by S. Meshkov. Melville NY: AIP Conf. Proc. 523, 2000, pp. 180–189 (cited on pages [↑34](#), [160](#), [162](#)).
- [152] H. L. V. Trees. *Detection, Estimation, and Modulation Theory*. Wiley, 2001 (cited on page [↑34](#)).
- [153] M. Tsang, H. M. Wiseman, and C. M. Caves. “Fundamental Quantum Limit to Waveform Estimation”. In: *Physical Review Letters* 106.9 (2011), p. 090401. DOI: [10.1103/PhysRevLett.106.090401](https://doi.org/10.1103/PhysRevLett.106.090401). arXiv: [1006.5407](https://arxiv.org/abs/1006.5407) (cited on pages [↑34](#), [160](#)).
- [154] H. Miao, R. X. Adhikari, Y. Ma, B. Pang, and Y. Chen. “Towards the Fundamental Quantum Limit of Linear Measurements of Classical Signals”. In: *Physical Review Letters* 119.5 (2017). DOI: [10.1103/PhysRevLett.119.050801](https://doi.org/10.1103/PhysRevLett.119.050801). arXiv: [1608.00766](https://arxiv.org/abs/1608.00766) (cited on pages [↑35](#), [160](#), [213](#)).

- [155] J. Mizuno. “Comparison of optical configurations for laser-interferometric gravitational-wave detectors”. PhD Thesis. Albert-Einstein-Institut Hannover, 1995 (cited on pages [↑37](#), [160](#)).
- [156] P. R. Saulson. *Fundamentals of Interferometric Gravitational Wave Detectors*. World Scientific Publishing Company, 1994 (cited on page [↑39](#)).
- [157] D. Reitze, P. Saulson, and H. Grote. *Advanced Interferometric Gravitational-Wave Detectors*. Vol. 05. 100 Years of General Relativity. World Scientific, 2019. DOI: [10.1142/10181](#) (cited on page [↑39](#)).
- [158] W. Vogel and D. Welsch. *Quantum Optics*. 3rd. Wiley-VCH Verlag GmbH, 2006, p. 520 (cited on page [↑39](#)).
- [159] C. C. Gerry and P. L. Knight. *Introductory Quantum Optics*. Cambridge University Press, 2005, p. 317 (cited on page [↑39](#)).
- [160] H.-A. Bachor and T. C. Ralph. *A Guide to Experiments in Quantum Optics*. Ed. by H.-A. Bachor and T. C. Ralph. Weinheim, Germany: Wiley, 2004. DOI: [10.1002/9783527619238](#) (cited on page [↑39](#)).
- [161] M. Pitkin, S. Reid, S. Rowan, and J. Hough. “Gravitational Wave Detection by Interferometry (Ground and Space)”. In: *Living Reviews in Relativity* 14.1 (2011), p. 5. DOI: [10.12942/lrr-2011-5](#). arXiv: [1102.3355](#) (cited on page [↑39](#)).
- [162] C. Bond, D. Brown, A. Freise, and K. A. Strain. “Interferometer techniques for gravitational-wave detection”. In: *Living Reviews in Relativity* 19.1 (2016), p. 3. DOI: [10.1007/s41114-016-0002-8](#) (cited on page [↑39](#)).
- [163] D. G. Blair, L. Ju, C. Zhao, and E. J. Howell, eds. *Advanced Gravitational Wave Detectors*. Cambridge: Cambridge University Press, 2012. DOI: [10.1017/CB09781139046916](#) (cited on page [↑39](#)).
- [164] G. Hammond, S. Hild, and M. Pitkin. “Advanced technologies for future ground-based, laser-interferometric gravitational wave detectors”. In: *Journal of Modern Optics* 61.sup1 (2014), S10–S45. DOI: [10.1080/09500340.2014.920934](#). arXiv: [1402.4616](#) (cited on page [↑39](#)).

- [165] B. L. Schumaker and C. M. Caves. “New formalism for two-photon quantum optics. II. Mathematical foundation and compact notation”. In: *Physical Review A* 31.5 (1985), pp. 3093–3111. doi: [10.1103/PhysRevA.31.3093](https://doi.org/10.1103/PhysRevA.31.3093) (cited on pages [↑41](#), [208](#), [256](#)).
- [166] C. M. Caves and B. L. Schumaker. “New formalism for two-photon quantum optics. I. Quadrature phases and squeezed states”. In: *Physical Review A* 31.5 (1985), pp. 3068–3092. doi: [10.1103/PhysRevA.31.3068](https://doi.org/10.1103/PhysRevA.31.3068) (cited on pages [↑41](#), [208](#), [256](#)).
- [167] M. Reid. “Demonstration of the Einstein-Podolsky-Rosen paradox using nondegenerate parametric amplification”. In: *Physical Review A* 40.2 (1989), pp. 913–923. doi: [10.1103/PhysRevA.40.913](https://doi.org/10.1103/PhysRevA.40.913) (cited on page [↑48](#)).
- [168] G. Milburn and D. Walls. “Production of squeezed states in a degenerate parametric amplifier”. In: *Optics Communications* 39.6 (1981), pp. 401–404. doi: [10.1016/0030-4018\(81\)90232-7](https://doi.org/10.1016/0030-4018(81)90232-7) (cited on pages [↑49](#), [165](#), [168](#)).
- [169] M. J. Collett and C. W. Gardiner. “Squeezing of intracavity and traveling-wave light fields produced in parametric amplification”. In: *Physical Review A* 30.3 (1984), pp. 1386–1391. doi: [10.1103/PhysRevA.30.1386](https://doi.org/10.1103/PhysRevA.30.1386) (cited on pages [↑49](#), [165](#), [168](#)).
- [170] A. Sambrowski, C. E. Laukötter, N. Grosse, P. K. Lam, and R. Schnabel. “Two Color Entanglement”. In: *AIP Conference Proceedings*. Vol. 1363. 2011, pp. 219–222. doi: [10.1063/1.3630183](https://doi.org/10.1063/1.3630183). arXiv: [1011.5766](https://arxiv.org/abs/1011.5766) (cited on page [↑50](#)).
- [171] V. B. Braginsky and A. B. Manukin. “Ponderomotive Effects of electromagnetic radiation”. In: *Soviet Physics JETP* 25.4 (1967), pp. 653–655 (cited on pages [↑57](#), [230](#)).
- [172] P. Kwee and V. D. Fakult. “Laser Characterization and Stabilization for Precision Interferometry”. In: (2010) (cited on pages [↑69](#), [74](#)).
- [173] P. Kwee, C. Bogan, K. Danzmann, et al. “Stabilized high-power laser system for the gravitational wave detector advanced LIGO”. In: *Optics Express* 20.10 (2012), p. 10617. doi: [10.1364/OE.20.010617](https://doi.org/10.1364/OE.20.010617) (cited on pages [↑69](#), [74](#)).

- [174] J. H. Pold. “Design , Implementation and Characterization of the Advanced LIGO 200 W Laser System”. In: (2014) (cited on pages [↑69, 74](#)).
- [175] V. B. Braginsky, M. L. Gorodetsky, F. Y. Khalili, and K. S. Thorne. “Dual-resonator speed meter for a free test mass”. In: *Physical Review D* 61 (2000), p. 44002 (cited on page [↑84](#)).
- [176] Y.Chen. “Sagnac Interferometer as a Speed-Meter-Type, Quantum-Nondemolition Gravitational-Wave detector”. In: *Physical Review D* 67 (2003), p. 122004 (cited on pages [↑84, 141, 156](#)).
- [177] G. De Vine, M. Gray, D. E. McClelland, Y. Chen, and S. Whitcomb. “Measurement of the frequency response of a bench-top quantum speed meter interferometer”. In: *Physics Letters, Section A: General, Atomic and Solid State Physics* 316.1-2 (2003), pp. 17–23. doi: [10.1016/S0375-9601\(03\)01102-2](#). arXiv: [9605103 \[cs\]](#) (cited on page [↑84](#)).
- [178] A. Xuereb, P. Horak, and T. Freearge. “Amplified optomechanics in a unidirectional ring cavity”. In: (2011), pp. 1–9. doi: [10.1080/09500340.2011.559316](#). arXiv: [1101.0130](#) (cited on page [↑84](#)).
- [179] S. Chesi, Y. D. Wang, and J. Twamley. “Diabolical points in multi-scatterer optomechanical systems”. In: *Scientific Reports* 5 (2015). doi: [10.1038/srep07816](#). arXiv: [1402.0926](#) (cited on page [↑84](#)).
- [180] A. Yilmaz, S. Schuster, P. Wolf, et al. “Optomechanical damping of a nanomembrane inside an optical ring cavity”. In: *New Journal of Physics* 19.1 (2017), p. 013038. doi: [10.1088/1367-2630/aa55ee](#). arXiv: [1608.02799](#) (cited on page [↑84](#)).
- [181] A. M. Jayich, J. C. Sankey, B. M. Zwickl, et al. “Dispersive optomechanics: a membrane inside a cavity”. In: *New Journal of Physics* 10.9 (2008), p. 095008. doi: [10.1088/1367-2630/10/9/095008](#) (cited on page [↑95](#)).
- [182] J. D. Thompson, B. M. Zwickl, A. M. Jayich, et al. “Strong dispersive coupling of a high-finesse cavity to a micromechanical membrane”. In: *Nature* 452.7183 (2008), pp. 72–75. doi: [10.1038/nature06715](#) (cited on page [↑95](#)).

- [183] R. W. Peterson, T. P. Purdy, N. S. Kampel, et al. “Laser cooling of a micromechanical membrane to the quantum backaction limit”. In: (2015), pp. 1–13. arXiv: [1510.03911](https://arxiv.org/abs/1510.03911) (cited on page [↑95](#)).
- [184] P. Piergentili, L. Catalini, M. Bawaj, et al. “Two-membrane cavity optomechanics”. In: 2019, F5A.66. DOI: [10.1364/qim.2019.f5a.66](https://doi.org/10.1364/qim.2019.f5a.66) (cited on page [↑95](#)).
- [185] J. Chen, M. Rossi, D. Mason, and A. Schliesser. “Entanglement of propagating optical modes via a mechanical interface”. In: *Nature Communications* 11.1 (2020). DOI: [10.1038/s41467-020-14768-1](https://doi.org/10.1038/s41467-020-14768-1). arXiv: [1911.05729](https://arxiv.org/abs/1911.05729) (cited on page [↑95](#)).
- [186] B.M.Zwickl, W.E.Shanks, A.M.Jayich, C.Yang, A.C.Bleszynski, A.M.Jayich, J.D.Thompson, and J.G.E.Harris. “High quality mechanical and optical properties of commercial silicon nitride membranes”. In: *Appl. Phys. Lett.* 92 (2008), p. 103125 (cited on page [↑120](#)).
- [187] V. B. Braginsky, F. Ya. Khalili. “Low-noise rigidity in quantum measurements”. In: *Physics Letters A* 257 (1999), pp. 241–246 (cited on page [↑136](#)).
- [188] F. Y. Khalili. “Frequency-dependent rigidity in large-scale interferometric gravitational-wave detectors”. In: *Physics Letters A* 288.October (2001), pp. 251–256 (cited on page [↑136](#)).
- [189] F. Khalili, S. Danilishin, H. Müller-Ebhardt, et al. “Negative optical inertia for enhancing the sensitivity of future gravitational-wave detectors”. In: *Phys. Rev. D* 83.6 (2011), p. 62003. DOI: [10.1103/PhysRevD.83.062003](https://doi.org/10.1103/PhysRevD.83.062003) (cited on page [↑136](#)).
- [190] N. V. Voronchev, S. L. Danilishin, and F. Y. Khalili. “Negative optical inertia in optomechanical systems”. In: *Optics and Spectroscopy* 112.3 (2012), pp. 377–385. DOI: [10.1134/S0030400X12030216](https://doi.org/10.1134/S0030400X12030216) (cited on pages [↑136](#), [244](#)).
- [191] T. Corbitt, Y. Chen, E. Innerhofer, et al. “An All-Optical Trap for a Gram-Scale Mirror”. In: *Phys. Rev. Lett.* 98.15 (2007), p. 150802. DOI: [10.1103/PhysRevLett.98.150802](https://doi.org/10.1103/PhysRevLett.98.150802) (cited on pages [↑136](#), [231](#)).

- [192] V. B. Braginsky, F. Ya. Khalili. “Gravitational wave antenna with QND speed meter”. In: *Physics Letters A* 147 (1990), pp. 251–256 (cited on page [↑141](#)).
- [193] V. B. Braginsky, M. L. Gorodetsky, F. Ya. Khalili and K. S. Thorne. “Dual-resonator speed meter for a free test mass”. In: *Physical Review D* 61.4 (2000), p. 44002 (cited on page [↑141](#)).
- [194] P. Purdue. “An analysis of a QND speed-meter interferometer”. In: *Physical Review D* 66 (2002), p. 22001 (cited on pages [↑141](#), [156](#)).
- [195] S.L. Danilishin. “Sensitivity limitations in optical speed meter topology of gravitational-wave antennae.” In: *Physical Review D* 69 (2004), p. 102003 (cited on pages [↑141](#), [156](#)).
- [196] A. Buonanno and Y. Chen. “Scaling law in signal recycled laser-interferometer gravitational-wave detectors”. In: *Physical Review D* (2003), pp. 1–23. arXiv: [0208048v1 \[arXiv:gr-qc\]](#) (cited on pages [↑146](#), [180](#), [203](#), [207](#), [216](#), [224](#), [233](#), [237](#), [253](#)).
- [197] A. A. Abdo, M. Ackermann, M. Ajello, et al. “DISCOVERY OF PULSED γ -RAYS FROM PSR J0034–0534 WITH THE FERMI LARGE AREA TELESCOPE: A CASE FOR CO-LOCATED RADIO AND γ -RAY EMISSION REGIONS”. In: *The Astrophysical Journal* 712.2 (2010), pp. 957–963. DOI: [10.1088/0004-637X/712/2/957](#) (cited on page [↑155](#)).
- [198] A. Wicht, K. Danzmann, M. Fleischhauer, et al. “White-light cavities, atomic phase coherence, and gravitational wave detectors”. In: *Optics Communications* 134.1-6 (1997), pp. 431–439. DOI: [10.1016/S0030-4018\(96\)00579-2](#) (cited on pages [↑160](#), [201](#)).
- [199] A. Wicht, M. Müller, R. H. Rinkleff, A. Rocco, and K. Danzmann. “Experimental demonstration of negative dispersion without absorption”. In: *Optics Communications* 179.1 (2000), pp. 107–115. DOI: [10.1016/S0030-4018\(99\)00528-3](#) (cited on page [↑160](#)).
- [200] S. Wise, G. Mueller, D. Reitze, D. B. Tanner, and B. F. Whiting. “Linewidth-broadened Fabry–Perot cavities within future gravitational wave detectors”. In: *Classical and Quantum Gravity* 21.5 (2004), S1031–S1036. DOI: [10.1088/0264-9381/21/5/097](#) (cited on page [↑160](#)).

- [201] S. Wise, V. Quetschke, A. J. Deshpande, et al. “Phase effects in the diffraction of light: Beyond the grating equation”. In: *Physical Review Letters* 95.1 (2005), pp. 1–4. doi: [10.1103/PhysRevLett.95.013901](https://doi.org/10.1103/PhysRevLett.95.013901) (cited on page [↑160](#)).
- [202] J. Qin, C. Zhao, Y. Ma, L. Ju, and D. G. Blair. “Linear negative dispersion with a gain doublet via optomechanical interactions”. In: *Optics Letters* 40.10 (2015), p. 2337. doi: [10.1364/OL.40.002337](https://doi.org/10.1364/OL.40.002337). arXiv: [1502.06083](https://arxiv.org/abs/1502.06083) (cited on pages [↑160](#), [180](#), [201](#)).
- [203] H. Rehbein, J. Harms, R. Schnabel, and K. Danzmann. “Optical Transfer Functions of Kerr Nonlinear Cavities and Interferometers”. In: *Physical Review Letters* 95.19 (2005), p. 193001. doi: [10.1103/PhysRevLett.95.193001](https://doi.org/10.1103/PhysRevLett.95.193001) (cited on pages [↑162](#), [203](#)).
- [204] V. Peano, H. G. L. Schwefel, C. Marquardt, and F. Marquardt. “Intracavity Squeezing Can Enhance Quantum-Limited Optomechanical Position Detection through Deamplification”. In: *Physical Review Letters* 115.24 (2015), p. 243603. doi: [10.1103/PhysRevLett.115.243603](https://doi.org/10.1103/PhysRevLett.115.243603). arXiv: [1502.06423](https://arxiv.org/abs/1502.06423) (cited on page [↑162](#)).
- [205] K. Somiya, Y. Kataoka, J. Kato, N. Saito, and K. Yano. “Parametric signal amplification to create a stiff optical bar”. In: *Physics Letters A* 380.4 (2016), pp. 521–524. doi: [10.1016/j.physleta.2015.11.010](https://doi.org/10.1016/j.physleta.2015.11.010). arXiv: [1403.1222](https://arxiv.org/abs/1403.1222) (cited on pages [↑162](#), [203](#), [231](#)).
- [206] R. Schnabel. “Squeezed states of light and their applications in laser interferometers”. In: *ArXiv* (2016). arXiv: [1611.03986](https://arxiv.org/abs/1611.03986) (cited on pages [↑165](#), [180](#)).
- [207] J. Steinlechner, S. Ast, C. Krüger, et al. “Absorption Measurements of Periodically Poled Potassium Titanyl Phosphate (PPKTP) at 775 nm and 1550 nm”. In: *Sensors* 13.1 (2013), pp. 565–573. doi: [10.3390/s130100565](https://doi.org/10.3390/s130100565) (cited on pages [↑177](#), [219](#), [221](#)).
- [208] L. Kleybolte. “Sensitivity Enhancement of Optomechanical Measurements using Squeezed Light”. PhD thesis. Universität Hamburg, 2019 (cited on page [↑177](#)).

- [209] K. Mosegaard and A. Tarantola. “Monte Carlo sampling of solutions to inverse problems”. In: *Journal of Geophysical Research: Solid Earth* 100.B7 (1995), pp. 12431–12447. DOI: [10.1029/94JB03097](https://doi.org/10.1029/94JB03097) (cited on page [↑179](#)).
- [210] J. Mizuno, K. A. Strain, P. G. Nelson, et al. “Resonant sideband extraction: a new configuration for interferometric gravitational wave detectors”. In: *Physics Letters A* 175.5 (1993), pp. 273–276. DOI: [10.1016/0375-9601\(93\)90620-F](https://doi.org/10.1016/0375-9601(93)90620-F) (cited on pages [↑181, 230](#)).
- [211] H. Miao, N. D. Smith, and M. Evans. “Quantum limit for laser interferometric gravitational wave detectors from optical dissipation”. In: (2018), pp. 1–6. arXiv: [1807.11734](https://arxiv.org/abs/1807.11734) (cited on pages [↑183, 186–189, 192, 198](#)).
- [212] V.B.Braginsky, M.L.Gorodetsky, V.S.Ilchenko. “Optical whispering-gallery microresonators”. In: *Proceedings of SPIE* 2097 (1993), p. 283 (cited on page [↑184](#)).
- [213] M.L.Gorodetsky, V.S.Ilchenko. “High-Q optical whispering-gallery microresonators: precession approach for spherical mode analysis and emission patterns with prism couplers”. In: *Optics Communications* 113 (1994), pp. 133–143 (cited on page [↑184](#)).
- [214] A. Schliesser and T. J. Kippenberg. “Cavity optomechanics with whispering-gallery-mode optical micro-resonators”. In: *arXiv* April (2010), p. 121. arXiv: [1003.5922](https://arxiv.org/abs/1003.5922) (cited on page [↑184](#)).
- [215] G. Grynberg, A. Aspect, and C. Fabre. *Introduction to Quantum Optics: From the Semi-classical Approach to Quantized Light*. 2010, p. 696 (cited on pages [↑184, 215](#)).
- [216] E. Knyazev, K. Y. Spasibko, M. V. Chekhova, and F. Y. Khalili. “Quantum tomography enhanced through parametric amplification”. In: *New Journal of Physics* 20.1 (2018), p. 13005 (cited on page [↑186](#)).
- [217] S. Ramelow, A. Farsi, Z. Vernon, et al. “Strong Nonlinear Coupling in a Si₃N₄ Ring Resonator”. In: *Physical Review Letters* 122.15 (2019), p. 153906. DOI: [10.1103/PhysRevLett.122.153906](https://doi.org/10.1103/PhysRevLett.122.153906) (cited on page [↑198](#)).

- [218] D. V. Strekalov, C. Marquardt, A. B. Matsko, H. G. L. Schwefel, and G. Leuchs. “Nonlinear and quantum optics with whispering gallery resonators”. In: *Journal of Optics* 18.12 (2016), p. 123002. doi: [10.1088/2040-8978/18/12/123002](https://doi.org/10.1088/2040-8978/18/12/123002) (cited on page [↑198](#)).
- [219] M. R. Foreman, J. D. Swaim, and F. Vollmer. “Whispering gallery mode sensors”. In: *Advances in Optics and Photonics* 7.2 (2015), p. 168. doi: [10.1364/aop.7.000168](https://doi.org/10.1364/aop.7.000168) (cited on page [↑198](#)).
- [220] J. A. Faber and F. A. Rasio. “Binary Neutron Star Mergers”. In: *Living Rev. Relativity* 15 (2012), p. 8. doi: [10.12942/lrr-2012-8](https://doi.org/10.12942/lrr-2012-8) (cited on page [↑201](#)).
- [221] L. Baiotti and L. Rezzolla. “Binary neutron star mergers: A review of Einstein’s richest laboratory”. In: *Reports on Progress in Physics* 80.9 (2017). doi: [10.1088/1361-6633/aa67bb](https://doi.org/10.1088/1361-6633/aa67bb). arXiv: [1607.03540](https://arxiv.org/abs/1607.03540) (cited on page [↑201](#)).
- [222] R. S. Conklin, B. Holdom, and J. Ren. “Gravitational wave echoes through new windows”. In: *Physical Review D* 98.4 (2017), p. 44021. doi: [10.1103/PhysRevD.98.044021](https://doi.org/10.1103/PhysRevD.98.044021). arXiv: [1712.06517](https://arxiv.org/abs/1712.06517) (cited on page [↑201](#)).
- [223] S. Chelkowski, H. Vahlbruch, B. Hage, et al. “Experimental characterization of frequency dependent squeezed light”. In: *Physical Review A - Atomic, Molecular, and Optical Physics* 71.1 (2007), pp. 1–8. doi: [10.1103/PhysRevA.71.013806](https://doi.org/10.1103/PhysRevA.71.013806). arXiv: [0706.4479](https://arxiv.org/abs/0706.4479) (cited on pages [↑202, 214](#)).
- [224] H. Miao, H. Yang, R. X Adhikari, and Y. Chen. “Quantum limits of interferometer topologies for gravitational radiation detection”. In: *Classical and Quantum Gravity* 31.16 (2014), p. 165010. doi: [10.1088/0264-9381/31/16/165010](https://doi.org/10.1088/0264-9381/31/16/165010). arXiv: [1305.3957](https://arxiv.org/abs/1305.3957) (cited on pages [↑202, 214](#)).
- [225] D. Martynov, H. Miao, H. Yang, et al. “Exploring the sensitivity of gravitational wave detectors to neutron star physics”. In: *Phys. Rev. D* 99 (10 2019), p. 102004. doi: [10.1103/PhysRevD.99.102004](https://doi.org/10.1103/PhysRevD.99.102004) (cited on pages [↑207, 214](#)).
- [226] T. Corbitt, N. Mavalvala, and S. Whitcomb. “Optical cavities as amplitude filters for squeezed fields”. In: *Physical Review D* 70 (2004), p. 22002. doi: [10.1103/PhysRevD.70.022002](https://doi.org/10.1103/PhysRevD.70.022002) (cited on page [↑214](#)).

- [227] M. Korobko. *Supplementary code for "Quantum expander for gravitational - wave observatories"*. 2020. DOI: [10 . 5281 / zenodo . 3597327](https://doi.org/10.5281/zenodo.3597327) (cited on page [↑215](#)).
- [228] E. Oelker, L. Barsotti, S. Dwyer, D. Sigg, and N. Mavalvala. "Squeezed light for advanced gravitational wave detectors and beyond". In: *Optics Express* 22.17 (2014), p. 21106. DOI: [10 . 1364/OE . 22 . 021106](https://doi.org/10.1364/OE.22.021106) (cited on page [↑218](#)).
- [229] E. Schreiber. "Gravitational-wave detection beyond the quantum shot-noise limit". PhD thesis. Leibniz Universität Hannover, 2017 (cited on page [↑218](#)).
- [230] A. Bauswein and H.-T. Janka. "Measuring Neutron-Star Properties via Gravitational Waves from Neutron-Star Mergers". In: *Phys. Rev. Lett.* 108.1 (2012), p. 11101. DOI: [10 . 1103 / PhysRevLett . 108 . 011101](https://doi.org/10.1103/PhysRevLett.108.011101) (cited on page [↑222](#)).
- [231] H. Yang, W. E. East, V. Paschalidis, F. Pretorius, and R. F. P. Mendes. "Evolution of highly eccentric binary neutron stars including tidal effects". In: *Phys. Rev. D* 98.4 (2018), p. 44007. DOI: [10 . 1103/PhysRevD . 98 . 044007](https://doi.org/10.1103/PhysRevD.98.044007) (cited on page [↑222](#)).
- [232] H. Yang, V. Paschalidis, K. Yagi, et al. "Gravitational wave spectroscopy of binary neutron star merger remnants with mode stacking". In: *Phys. Rev. D* 97.2 (2018), p. 24049. DOI: [10 . 1103/PhysRevD . 97 . 024049](https://doi.org/10.1103/PhysRevD.97.024049). arXiv: [1707 . 00207 \[gr-qc\]](https://arxiv.org/abs/1707.00207) (cited on page [↑222](#)).
- [233] A. Bauswein, N. Stergioulas, and H.-T. Janka. "Exploring properties of high-density matter through remnants of neutron-star mergers". In: *The European Physical Journal A* 52.3 (2016), p. 56. DOI: [10.1140/epja/i2016-16056-7](https://doi.org/10.1140/epja/i2016-16056-7) (cited on page [↑223](#)).
- [234] H. Shen, H. Toki, K. Oyamatsu, and K. Sumiyoshi. "Relativistic equation of state of nuclear matter for supernova and neutron star". In: *Nuclear Physics A* 637.3 (1998), pp. 435–450. DOI: [https://doi.org/10.1016/S0375-9474\(98\)00236-X](https://doi.org/10.1016/S0375-9474(98)00236-X) (cited on page [↑223](#)).
- [235] F. Y. Khalili. "The "optical lever" intracavity readout scheme for gravitational-wave antennae". In: *Physics Letters A* 298.5-6 (2002), pp. 308–314. DOI: [10 . 1016/S0375-9601\(02\)00578-9](https://doi.org/10.1016/S0375-9601(02)00578-9) (cited on page [↑230](#)).

- [236] F. Y. K. S. L. Danilishin. “Practical design of the optical lever intracavity topology of gravitational-wave detectors”. In: *Physical Review D* 73 (2006), p. 22002 (cited on page [↑230](#)).
- [237] B. J. Meers. “Recycling in laser-interferometric gravitational-wave detectors”. In: *Physical Review D* 38 (1988), p. 2317 (cited on page [↑230](#)).
- [238] G. Heinzel, K. A. Strain, J. Mizuno, K. D. Skeldon, and B. Willke. “Experimental Demonstration of a Suspended Dual Recycling Interferometer for Gravitational Wave Detection”. In: *Physical Review Letters* 81 (1998), p. 5493 (cited on page [↑230](#)).
- [239] G. Heinzel, J. Mizuno, R. Schilling, et al. “An experimental demonstration of resonant sideband extraction for laser-interferometric gravitational wave detectors”. In: *Physics Letters A* 217.6 (1996), pp. 305–314. doi: [10.1016/0375-9601\(96\)00361-1](#) (cited on page [↑230](#)).
- [240] A. Schliesser, P. Del’Haye, N. Nooshi, K. Vahala, and T. Kippenberg. “Radiation Pressure Cooling of a Micromechanical Oscillator Using Dynamical Backaction”. In: *Physical Review Letters* 97.24 (2006), p. 243905. doi: [10.1103/PhysRevLett.97.243905](#) (cited on page [↑230](#)).
- [241] C. H. Metzger and K. Karrai. “Cavity cooling of a microlever.” In: *Nature* 432.7020 (2004), pp. 1002–1005. doi: [10.1038/nature03118](#) (cited on page [↑230](#)).
- [242] B. J. Meers, A. Krolak, and J. A. Lobo. “Dynamically tuned interferometers for the observation of gravitational waves from coalescing compact binaries”. In: *Physical Review D* 47.6 (1993), pp. 2184–2197. doi: [10.1103/PhysRevD.47.2184](#) (cited on page [↑231](#)).
- [243] D. A. Simakov. “Time-domain analysis of a dynamically tuned signal recycled interferometer for the detection of chirp gravitational waves from coalescing compact binaries”. In: *Physical Review D* 90.10 (2014), p. 102003. doi: [10.1103/PhysRevD.90.102003](#) (cited on page [↑231](#)).
- [244] B. S. Sheard, M. B. Gray, C. M. Mow-Lowry, D. E. McClelland, and S. E. Whitcomb. “Observation and characterization of an optical spring”. In: *Physical Review A* 69 (2004), p. 51801. doi: [10.1103/PhysRevA.69.051801](#) (cited on page [↑231](#)).

- [245] O. Miyakawa, R. Ward, R. Adhikari, et al. “Measurement of optical response of a detuned resonant sideband extraction gravitational wave detector”. In: *Physical Review D* 74.2 (2006), p. 22001. DOI: [10.1103/PhysRevD.74.022001](https://doi.org/10.1103/PhysRevD.74.022001) (cited on page [↑231](#)).
- [246] T. Corbitt, D. Ottaway, E. Innerhofer, J. Pelc, and N. Mavalvala. “Measurement of radiation-pressure-induced optomechanical dynamics in a suspended Fabry-Perot cavity”. In: *Physical Review A* 74.2 (2006), p. 21802. DOI: [10.1103/PhysRevA.74.021802](https://doi.org/10.1103/PhysRevA.74.021802) (cited on page [↑231](#)).
- [247] T. Corbitt, C. Wipf, T. Bodiya, et al. “Optical Dilution and Feedback Cooling of a Gram-Scale Oscillator to 6.9 mK”. In: *Physical Review Letters* 99.16 (2007), p. 160801. DOI: [10.1103/PhysRevLett.99.160801](https://doi.org/10.1103/PhysRevLett.99.160801) (cited on page [↑231](#)).
- [248] M. Hossein-Zadeh and K. J. Vahala. “Observation of optical spring effect in a microtoroidal optomechanical resonator”. In: *Optics Letters* 32.12 (2007), p. 1611. DOI: [10.1364/OL.32.001611](https://doi.org/10.1364/OL.32.001611) (cited on page [↑231](#)).
- [249] D. Kelley, J. Lough, F. Mangaña-Sandoval, A. Perreca, and S. W. Ballmer. “Observation of photothermal feedback in a stable dual-carrier optical spring”. In: *Physical Review D* 92.6 (2015), p. 062003. DOI: [10.1103/PhysRevD.92.062003](https://doi.org/10.1103/PhysRevD.92.062003) (cited on page [↑231](#)).
- [250] A. Sawadsky, H. Kaufer, R. M. Nia, et al. “Observation of Generalized Optomechanical Coupling and Cooling on Cavity Resonance”. In: *Physical Review Letters* 114.4 (2015), p. 43601. DOI: [10.1103/PhysRevLett.114.043601](https://doi.org/10.1103/PhysRevLett.114.043601) (cited on page [↑231](#)).
- [251] M. P. Edgar, J. Macarthur, B. W. Barr, et al. “Demonstration of an optical spring in the 100 g mirror regime”. In: *Classical and Quantum Gravity* 33.7 (2016), p. 075007. DOI: [10.1088/0264-9381/33/7/075007](https://doi.org/10.1088/0264-9381/33/7/075007) (cited on page [↑231](#)).
- [252] R. Singh, G. D. Cole, J. Cripe, and T. Corbitt. “Stable Optical Trap from a Single Optical Field Utilizing Birefringence”. In: *Physical Review Letters* 117.21 (2016), p. 213604. DOI: [10.1103/PhysRevLett.117.213604](https://doi.org/10.1103/PhysRevLett.117.213604) (cited on page [↑231](#)).

- [253] N. A. Gordon, B. W. Barr, A. Bell, et al. “Experimental demonstration of coupled optical springs”. In: *Classical and Quantum Gravity* 34.3 (2017), p. 035020. DOI: [10.1088/1361-6382/aa556f](https://doi.org/10.1088/1361-6382/aa556f) (cited on page [↑231](#)).
- [254] C. Affeldt, K. Danzmann, K. L. Dooley, et al. “Advanced techniques in GEO 600”. In: *Classical and Quantum Gravity* 31.22 (2014), p. 224002. DOI: [10.1088/0264-9381/31/22/224002](https://doi.org/10.1088/0264-9381/31/22/224002) (cited on page [↑231](#)).
- [255] K. Somiya. “Detector configuration of KAGRA—the Japanese cryogenic gravitational-wave detector”. In: *Classical and Quantum Gravity* 29.12 (2012), p. 124007. DOI: [10.1088/0264-9381/29/12/124007](https://doi.org/10.1088/0264-9381/29/12/124007) (cited on page [↑231](#)).
- [256] H. Rehbein, H. Müller-Ebhardt, K. Somiya, and H. Rehbein, H. Müller-Ebhardt, K. Somiya, C. Li, R. Schnabel, K. Danzmann, and Y. Chen. “Local readout enhancement for detuned signal-recycling interferometers”. In: *Physical Review D* 76 (2007), pp. 1–11. arXiv: [arXiv:0705.2987v3](https://arxiv.org/abs/0705.2987v3) (cited on pages [↑231, 241–243](#)).
- [257] I. S. Gradshteyn and I. M. Ryzhik. *Table of integrals, series, and products*. Seventh. Elsevier/Academic Press, Amsterdam, 2007, p. 1171 (cited on page [↑237](#)).
- [258] A. Buonanno and Y. Chen. “Optical noise correlations and beating the standard quantum limit in advanced gravitational-wave detectors”. In: *Classical and Quantum Gravity* 18.15 (2001), pp. L95–L101. DOI: [10.1088/0264-9381/18/15/102](https://doi.org/10.1088/0264-9381/18/15/102). arXiv: [0102012](https://arxiv.org/abs/0102012) [gr-qc] (cited on page [↑237](#)).
- [259] M. Korobko, N. Voronchev, H. Miao, and F. Y. Khalili. “Paired carriers as a way to reduce quantum noise of multicarrier gravitational-wave detectors”. In: *Physical Review D* 91.4 (2015), p. 042004. DOI: [10.1103/PhysRevD.91.042004](https://doi.org/10.1103/PhysRevD.91.042004) (cited on page [↑244](#)).
- [260] M. Rakhmanov, J. D. Romano, and J. T. Whelan. “High-frequency corrections to the detector response and their effect on searches for gravitational waves”. In: *Classical and Quantum Gravity* 25.18 (2008). DOI: [10.1088/0264-9381/25/18/184017](https://doi.org/10.1088/0264-9381/25/18/184017). arXiv: [0808.3805](https://arxiv.org/abs/0808.3805) (cited on page [↑255](#)).

My publications

Main publications

- [1] M. Korobko, N. Voronchev, H. Miao, and F. Y. Khalili. “Paired carriers as a way to reduce quantum noise of multicarrier gravitational-wave detectors”. In: *Physical Review D* 91.4 (2015), p. 042004. DOI: [10.1103/PhysRevD.91.042004](https://doi.org/10.1103/PhysRevD.91.042004).
- [2] M. Korobko, L. Kleybolte, S. Ast, et al. “Beating the Standard Sensitivity-Bandwidth Limit of Cavity-Enhanced Interferometers with Internal Squeezed-Light Generation”. In: *Physical Review Letters* 118.14 (2017), p. 143601. DOI: [10.1103/PhysRevLett.118.143601](https://doi.org/10.1103/PhysRevLett.118.143601).
- [3] M. Korobko, F. Y. Khalili, and R. Schnabel. “Engineering the optical spring via intra-cavity optical-parametric amplification”. In: *Physics Letters A* 382.33 (2018), pp. 2238–2244. DOI: [10.1016/j.physleta.2017.08.008](https://doi.org/10.1016/j.physleta.2017.08.008). arXiv: [1709.03055](https://arxiv.org/abs/1709.03055).
- [4] S. Steinlechner, N.-O. Rohweder, M. Korobko, et al. “Mitigating Mode-Matching Loss in Nonclassical Laser Interferometry”. In: *Physical Review Letters* 121.26 (2018), p. 263602. DOI: [10.1103/PhysRevLett.121.263602](https://doi.org/10.1103/PhysRevLett.121.263602). arXiv: [1811.00598](https://arxiv.org/abs/1811.00598).
- [5] M. Korobko, Y. Ma, Y. Chen, and R. Schnabel. “Quantum expander for gravitational-wave observatories”. In: *Light: Science & Applications* 8.1 (2019), p. 118. DOI: [10.1038/s41377-019-0230-2](https://doi.org/10.1038/s41377-019-0230-2). arXiv: [1903.05930](https://arxiv.org/abs/1903.05930).
- [6] X. Li, M. Korobko, Y. Ma, R. Schnabel, and Y. Chen. “Coherent coupling completing an unambiguous optomechanical classification framework”. In: *Physical Review A* 100.5 (2019), p. 053855. DOI: [10.1103/PhysRevA.100.053855](https://doi.org/10.1103/PhysRevA.100.053855). arXiv: [1908.03372](https://arxiv.org/abs/1908.03372).

- [7] M. Korobko. *Supplementary code for "Quantum expander for gravitational - wave observatories"*. 2020. doi: [10.5281/zenodo.3597327](https://doi.org/10.5281/zenodo.3597327).
- [8] J. Südbeck, S. Steinlechner, M. Korobko, and R. Schnabel. "Demonstration of interferometer enhancement through Einstein–Podolsky–Rosen entanglement". In: *Nature Photonics* 14.4 (2020), pp. 240–244. doi: [10.1038/s41566-019-0583-3](https://doi.org/10.1038/s41566-019-0583-3). arXiv: [1908.09602](https://arxiv.org/abs/1908.09602).

Publications in collaboration

- [1] J. Aasi, B. P. Abbott, R. Abbott, et al. "Directed search for gravitational waves from Scorpius X-1 with initial LIGO data". In: *Physical Review D* 91.6 (2015), p. 62008.
- [2] J. Aasi, B. P. Abbott, R. Abbott, et al. "Narrow-band search of continuous gravitational-wave signals from Crab and Vela pulsars in Virgo VSR4 data". In: *Physical Review D* 91.2 (2015), p. 22004.
- [3] J. Aasi, B. P. Abbott, R. Abbott, et al. "SEARCHES FOR CONTINUOUS GRAVITATIONAL WAVES FROM NINE YOUNG SUPERNOVA REMNANTS". In: *The Astrophysical Journal* 813.1 (2015), p. 39. doi: [10.1088/0004-637X/813/1/39](https://doi.org/10.1088/0004-637X/813/1/39).
- [4] J. Aasi, B. P. Abbott, R. Abbott, et al. "Advanced LIGO". In: *Classical and Quantum Gravity* 32.7 (2015), p. 074001. doi: [10.1088/0264-9381/32/7/074001](https://doi.org/10.1088/0264-9381/32/7/074001). arXiv: [1411.4547](https://arxiv.org/abs/1411.4547).
- [5] J. Aasi, B. P. Abbott, R. Abbott, et al. "First low frequency all-sky search for continuous gravitational wave signals". In: *Physical Review D* 93.4 (2016), p. 42007.
- [6] J. Aasi, B. P. Abbott, R. Abbott, et al. "Search of the Orion spur for continuous gravitational waves using a loosely coherent algorithm on data from LIGO interferometers". In: *Physical Review D* 93.4 (2016), p. 42006.
- [7] B. P. Abbott, R. Abbott, T. D. Abbott, et al. "ASTROPHYSICAL IMPLICATIONS OF THE BINARY BLACK HOLE MERGER GW150914". In: *The Astrophysical Journal* 818.2 (2016), p. L22. doi: [10.3847/2041-8205/818/2/L22](https://doi.org/10.3847/2041-8205/818/2/L22).

- [8] B. P. Abbott, R. Abbott, T. D. Abbott, et al. “Observation of Gravitational Waves from a Binary Black Hole Merger”. In: *Physical Review Letters* 116.6 (2016), p. 061102. DOI: [10.1103/PhysRevLett.116.061102](https://doi.org/10.1103/PhysRevLett.116.061102). arXiv: [1602.03837](https://arxiv.org/abs/1602.03837).
- [9] B. P. Abbott, R. Abbott, T. D. Abbott, et al. “Properties of the Binary Black Hole Merger GW150914”. In: *Physical Review Letters* 116.24 (2016), p. 241102. DOI: [10.1103/PhysRevLett.116.241102](https://doi.org/10.1103/PhysRevLett.116.241102). arXiv: [1602.03840](https://arxiv.org/abs/1602.03840).
- [10] B. P. Abbott, R. Abbott, T. D. Abbott, et al. “Tests of General Relativity with GW150914”. In: *Physical Review Letters* 116.22 (2016), p. 221101. DOI: [10.1103/PhysRevLett.116.221101](https://doi.org/10.1103/PhysRevLett.116.221101).
- [11] B. Abbott, R. Abbott, T. Abbott, et al. “All-sky search for long-duration gravitational wave transients with initial LIGO”. In: *Physical Review D* 93.4 (2016). DOI: [10.1103/PhysRevD.93.042005](https://doi.org/10.1103/PhysRevD.93.042005).
- [12] B. Abbott, R. Abbott, T. Abbott, et al. “First targeted search for gravitational-wave bursts from core-collapse supernovae in data of first-generation laser interferometer detectors”. In: *Physical Review D* 94.10 (2016). DOI: [10.1103/PhysRevD.94.102001](https://doi.org/10.1103/PhysRevD.94.102001).
- [13] B. Abbott, R. Abbott, T. Abbott, et al. “GW150914: The advanced LIGO detectors in the era of first discoveries”. In: *Physical Review Letters* 116.13 (2016). DOI: [10.1103/PhysRevLett.116.131103](https://doi.org/10.1103/PhysRevLett.116.131103).
- [14] B. Abbott, R. Abbott, T. Abbott, et al. “Observing gravitational-wave transient GW150914 with minimal assumptions”. In: *Physical Review D* 93.12 (2016). DOI: [10.1103/PhysRevD.93.122004](https://doi.org/10.1103/PhysRevD.93.122004).
- [15] B. Abbott, R. Abbott, T. Abbott, et al. “Results of the deepest all-sky survey for continuous gravitational waves on LIGO S6 data running on the Einstein@Home volunteer distributed computing project”. In: *Physical Review D* 94.10 (2016). DOI: [10.1103/PhysRevD.94.102002](https://doi.org/10.1103/PhysRevD.94.102002).
- [16] B. Abbott, R. Abbott, T. Abbott, et al. “Search for transient gravitational waves in coincidence with short-duration radio transients during 2007-2013”. In: *Physical Review D* 93.12 (2016). DOI: [10.1103/PhysRevD.93.122008](https://doi.org/10.1103/PhysRevD.93.122008).

- [17] B. Abbott, R. Abbott, T. Abbott, et al. “Supplement: The Rate Of Binary Black Hole Mergers Inferred From Advanced Ligo Observations Surrounding Gw150914”. In: *Astrophysical Journal, Supplement Series* 227.2 (2016). DOI: [10.3847/0067-0049/227/2/14](https://doi.org/10.3847/0067-0049/227/2/14).
- [18] B. Abbott, R. Abbott, T. Abbott, et al. “UPPER LIMITS on the RATES of BINARY NEUTRON STAR and NEUTRON STAR-BLACK HOLE MERGERS from ADVANCED LIGO’S FIRST OBSERVING RUN”. In: *Astrophysical Journal Letters* 832.2 (2016). DOI: [10.3847/2041-8205/832/2/L21](https://doi.org/10.3847/2041-8205/832/2/L21).
- [19] B. P. Abbott, R. Abbott, T. D. Abbott, et al. “Binary black hole mergers in the first advanced LIGO observing run”. In: *Physical Review X* 6.4 (2016), p. 41015.
- [20] B. P. Abbott, R. Abbott, T. D. Abbott, et al. “Characterization of transient noise in Advanced LIGO relevant to gravitational wave signal GW150914”. In: *Classical and Quantum Gravity* 33.13 (2016), p. 134001.
- [21] B. P. Abbott, R. Abbott, T. D. Abbott, et al. “GW150914: First results from the search for binary black hole coalescence with Advanced LIGO”. In: *Physical Review D* 93.12 (2016), p. 122003.
- [22] B. P. Abbott, R. Abbott, T. D. Abbott, et al. “Localization and broadband follow-up of the gravitational-wave transient GW150914”. In: *The Astrophysical journal letters* 826.1 (2016), p. L13.
- [23] B. P. Abbott, R. Abbott, T. D. Abbott, et al. “Comprehensive all-sky search for periodic gravitational waves in the sixth science run LIGO data”. In: *Physical Review D* 94.4 (2016), p. 42002.
- [24] B. P. Abbott, R. Abbott, T. D. Abbott, et al. “Improved analysis of GW150914 using a fully spin-precessing waveform model”. In: *Physical Review X* 6.4 (2016), p. 41014.
- [25] B. P. Abbott, R. Abbott, T. D. Abbott, et al. “Directly comparing GW150914 with numerical solutions of Einstein’s equations for binary black hole coalescence”. In: *Physical Review D* 94.6 (2016), p. 64035.
- [26] S. Adrián-Martínez, A. Albert, M. André, et al. “High-energy neutrino follow-up search of gravitational wave event GW150914 with ANTARES and IceCube”. In: *Physical Review D* 93.12 (2016), p. 122010.

- [27] The LIGO Scientific Collaboration. “Exploring the Sensitivity of Next Generation Gravitational Wave Detectors”. In: (2016), pp. 1–11. arXiv: [1607.08697](https://arxiv.org/abs/1607.08697).
- [28] B. P. Abbott, R. Abbott, T. D. Abbott, et al. “VizieR Online Data Catalog: Gravitational waves search from known PSR with LIGO (Abbott+, 2017)”. In: *VizieR Online Data Catalog* 183 (2017).
- [29] B. P. Abbott, R. Abbott, T. D. Abbott, et al. “On the Progenitor of Binary Neutron Star Merger GW170817”. In: *The Astrophysical Journal* 850.2 (2017), p. L40. DOI: [10.3847/2041-8213/aa93fc](https://doi.org/10.3847/2041-8213/aa93fc). arXiv: [1710.05838](https://arxiv.org/abs/1710.05838).
- [30] B. P. Abbott, R. Abbott, T. D. Abbott, et al. “Search for Post-merger Gravitational Waves from the Remnant of the Binary Neutron Star Merger GW170817”. In: *The Astrophysical Journal* 851.1 (2017), p. L16. DOI: [10.3847/2041-8213/aa9a35](https://doi.org/10.3847/2041-8213/aa9a35).
- [31] B. P. Abbott, R. Abbott, T. D. Abbott, et al. “A gravitational-wave standard siren measurement of the Hubble constant”. In: *Nature* 551.7678 (2017), pp. 85–88. DOI: [10.1038/nature24471](https://doi.org/10.1038/nature24471). arXiv: [1710.05835](https://arxiv.org/abs/1710.05835).
- [32] B. P. Abbott, R. Abbott, T. D. Abbott, et al. “Estimating the Contribution of Dynamical Ejecta in the Kilonova Associated with GW170817”. In: *The Astrophysical Journal* 850.2 (2017), p. L39. DOI: [10.3847/2041-8213/aa9478](https://doi.org/10.3847/2041-8213/aa9478). arXiv: [1710.05836](https://arxiv.org/abs/1710.05836).
- [33] B. P. Abbott, R. Abbott, T. D. Abbott, et al. “Gravitational Waves and Gamma-Rays from a Binary Neutron Star Merger: GW170817 and GRB 170817A”. In: *The Astrophysical Journal* 848.2 (2017), p. L13. DOI: [10.3847/2041-8213/aa920c](https://doi.org/10.3847/2041-8213/aa920c).
- [34] B. P. Abbott, R. Abbott, T. D. Abbott, et al. “GW170104: Observation of a 50-Solar-Mass Binary Black Hole Coalescence at Redshift 0.2”. In: *Physical Review Letters* 118.22 (2017), p. 221101. DOI: [10.1103/PhysRevLett.118.221101](https://doi.org/10.1103/PhysRevLett.118.221101).
- [35] B. P. Abbott, R. Abbott, T. Abbott, et al. “First low-frequency Einstein@Home all-sky search for continuous gravitational waves in Advanced LIGO data”. In: *Physical Review D* 96.12 (2017), p. 122004. DOI: [10.1103/PhysRevD.96.122004](https://doi.org/10.1103/PhysRevD.96.122004).

- [36] B. P. Abbott, R. Abbott, T. Abbott, et al. “First narrow-band search for continuous gravitational waves from known pulsars in advanced detector data”. In: *Physical Review D* 96.12 (2017), p. 122006. DOI: [10.1103/PhysRevD.96.122006](https://doi.org/10.1103/PhysRevD.96.122006).
- [37] B. Abbott, R. Abbott, T. Abbott, et al. “All-sky search for short gravitational-wave bursts in the first Advanced LIGO run”. In: *Physical Review D* 95.4 (2017). DOI: [10.1103/PhysRevD.95.042003](https://doi.org/10.1103/PhysRevD.95.042003).
- [38] B. Abbott, R. Abbott, T. Abbott, et al. “Effects of waveform model systematics on the interpretation of GW150914”. In: *Classical and Quantum Gravity* 34.10 (2017). DOI: [10.1088/1361-6382/aa6854](https://doi.org/10.1088/1361-6382/aa6854).
- [39] B. Abbott, R. Abbott, T. Abbott, et al. “First Search for Gravitational Waves from Known Pulsars with Advanced LIGO”. In: *Astrophysical Journal* 839.1 (2017). DOI: [10.3847/1538-4357/aa677f](https://doi.org/10.3847/1538-4357/aa677f).
- [40] B. Abbott, R. Abbott, T. Abbott, et al. “Search for continuous gravitational waves from neutron stars in globular cluster NGC 6544”. In: *Physical Review D* 95.8 (2017). DOI: [10.1103/PhysRevD.95.082005](https://doi.org/10.1103/PhysRevD.95.082005).
- [41] B. P. Abbott, R. Abbott, T. D. Abbott, et al. “Calibration of the Advanced LIGO detectors for the discovery of the binary black-hole merger GW150914”. In: *Physical Review D* 95.6 (2017), p. 62003.
- [42] B. P. Abbott, R. Abbott, T. D. Abbott, et al. “Directional limits on persistent gravitational waves from Advanced LIGO’s first observing run”. In: *Physical review letters* 118.12 (2017), p. 121102.
- [43] B. P. Abbott, R. Abbott, T. D. Abbott, et al. “GW170608: Observation of a 19 Solar-mass Binary Black Hole Coalescence”. In: *The Astrophysical Journal* 851.2 (2017), p. L35. DOI: [10.3847/2041-8213/aa9f0c](https://doi.org/10.3847/2041-8213/aa9f0c).
- [44] B. P. Abbott, R. Abbott, T. D. Abbott, et al. “GW170814: a three-detector observation of gravitational waves from a binary black hole coalescence”. In: *Physical review letters* 119.14 (2017), p. 141101.
- [45] B. P. Abbott, R. Abbott, T. D. Abbott, et al. “Upper limits on gravitational waves from Scorpius X-1 from a model-based cross-correlation search in Advanced LIGO data”. In: *The Astrophysical Journal* 847.1 (2017), p. 47.

- [46] B. P. Abbott, R. Abbott, T. D. Abbott, et al. “All-sky search for periodic gravitational waves in the O1 LIGO data”. In: *Physical Review D* 96.6 (2017), p. 62002.
- [47] A. Albert, M. André, M. Anghinolfi, et al. “Search for high-energy neutrinos from gravitational wave event GW151226 and candidate LVT151012 with ANTARES and IceCube”. In: *Physical Review D* 96.2 (2017), p. 22005.
- [48] LIGO Scientific Collaboration and Virgo Collaboration, F. G.-r. B. Monitor, A. C. Z. T. I. Team, et al. “Multi-messenger observations of a binary neutron star merger”. In: *Astrophysical Journal Letters* 848.2 (2017). DOI: [10.3847/2041-8213/aa91c9](https://doi.org/10.3847/2041-8213/aa91c9).
- [49] L. Scientific, V. Collaborations, B. P. Abbott, et al. “The basic physics of the binary black hole merger GW150914”. In: *Annalen der Physik* 529.1-2 (2017), p. 1600209.
- [50] B. P. Abbott, R. Abbott, T. D. Abbott, et al. “GW170817: Measurements of Neutron Star Radii and Equation of State”. In: *Physical review letters* 121.16 (2018), p. 161101.
- [51] B. Abbott, R. Abbott, T. Abbott, et al. “Constraints on cosmic strings using data from the first Advanced LIGO observing run”. In: *Physical Review D* 97.10 (2018). DOI: [10.1103/PhysRevD.97.102002](https://doi.org/10.1103/PhysRevD.97.102002).
- [52] B. P. Abbott, R. Abbott, T. D. Abbott, et al. “All-sky search for long-duration gravitational wave transients in the first Advanced LIGO observing run”. In: *Classical and quantum gravity* 35.6 (2018), p. 65009.
- [53] B. P. Abbott, R. Abbott, T. D. Abbott, et al. “Effects of data quality vetoes on a search for compact binary coalescences in Advanced LIGO’s first observing run”. In: *Classical and Quantum Gravity* 35.6 (2018), p. 65010.
- [54] B. P. Abbott, R. Abbott, T. D. Abbott, et al. “Full band all-sky search for periodic gravitational waves in the O1 LIGO data”. In: *Physical Review D* 97.10 (2018), p. 102003.
- [55] B. P. Abbott, R. Abbott, T. D. Abbott, et al. “GW170817: implications for the stochastic gravitational-wave background from compact binary coalescences”. In: *Physical review letters* 120.9 (2018), p. 91101.

- [56] B. P. Abbott, R. Abbott, T. D. Abbott, et al. “Prospects for observing and localizing gravitational-wave transients with Advanced LIGO, Advanced Virgo and KAGRA”. In: *Living Reviews in Relativity* 21.1 (2018), p. 3.
- [57] B. P. Abbott, R. Abbott, T. D. Abbott, et al. “Search for tensor, vector, and scalar polarizations in the stochastic gravitational-wave background”. In: *Physical review letters* 120.20 (2018), p. 201102.
- [58] B. P. Abbott, R. Abbott, T. D. Abbott, et al. “First search for nontensorial gravitational waves from known pulsars”. In: *Physical review letters* 120.3 (2018), p. 31104.
- [59] B. P. Abbott, R. Abbott, T. D. Abbott, et al. “All-sky search for short gravitational-wave bursts in the second Advanced LIGO and Advanced Virgo run”. In: *Physical Review D* 100.2 (2019), p. 24017.
- [60] B. P. Abbott, R. Abbott, T. D. Abbott, et al. “Constraining the p-mode–g-mode tidal instability with GW170817”. In: *Physical review letters* 122.6 (2019), p. 61104.
- [61] B. P. Abbott, R. Abbott, T. D. Abbott, et al. “Directional limits on persistent gravitational waves using data from Advanced LIGO’s first two observing runs”. In: *Physical Review D* 100.6 (2019), p. 62001.
- [62] B. P. Abbott, R. Abbott, T. D. Abbott, et al. “GWTC-1: A gravitational-wave transient catalog of compact binary mergers observed by LIGO and Virgo during the first and second observing runs”. In: *Physical Review X* 9.3 (2019), p. 31040.
- [63] B. P. Abbott, R. Abbott, T. D. Abbott, et al. “Narrow-band search for gravitational waves from known pulsars using the second LIGO observing run”. In: *Physical Review D* 99.12 (2019), p. 122002.
- [64] B. P. Abbott, R. Abbott, T. D. Abbott, et al. “Properties of the binary neutron star merger GW170817”. In: *Physical Review X* 9.1 (2019), p. 11001.
- [65] B. P. Abbott, R. Abbott, T. D. Abbott, et al. “Search for intermediate mass black hole binaries in the first and second observing runs of the Advanced LIGO and Virgo network”. In: *Physical Review D* 100.6 (2019), p. 64064.

- [66] B. P. Abbott, R. Abbott, T. D. Abbott, et al. “Search for the isotropic stochastic background using data from Advanced LIGO’s second observing run”. In: *Physical Review D* 100.6 (2019), pp. 1–16.
- [67] B. P. Abbott, R. Abbott, T. D. Abbott, et al. “Searches for continuous gravitational waves from 15 supernova remnants and Fomalhaut b with Advanced LIGO”. In: *The Astrophysical Journal* 875.2 (2019), p. 122.
- [68] B. P. Abbott, R. Abbott, T. D. Abbott, et al. “Tests of general relativity with GW170817”. In: *Physical Review Letters* 123.1 (2019), p. 11102.
- [69] B. P. Abbott, R. Abbott, T. D. Abbott, et al. “Binary Black Hole Population Properties Inferred from the First and Second Observing Runs of Advanced LIGO and Advanced Virgo”. In: *The Astrophysical Journal* 882.2 (2019), p. L24. DOI: [10.3847/2041-8213/ab3800](https://doi.org/10.3847/2041-8213/ab3800). arXiv: [1811.12940](https://arxiv.org/abs/1811.12940).
- [70] B. P. Abbott, R. Abbott, T. D. Abbott, et al. “Low-latency gravitational-wave alerts for multimessenger astronomy during the second Advanced LIGO and Virgo observing run”. In: *The Astrophysical Journal* 875.2 (2019), p. 161.
- [71] A. Albert, M. André, M. Anghinolfi, et al. “Search for multimessenger sources of gravitational waves and high-energy neutrinos with advanced LIGO during its first observing run, ANTARES, and IceCube”. In: *The Astrophysical Journal* 870.2 (2019), p. 134.
- [72] E. Burns, A. Goldstein, C. M. Hui, et al. “A Fermi Gamma-ray Burst Monitor search for electromagnetic signals coincident with gravitational-wave candidates in advanced LIGO’s first observing run”. In: *The Astrophysical Journal* 871.1 (2019), p. 90.
- [73] M. Soares-Santos, A. Palmese, W. Hartley, et al. “First measurement of the Hubble constant from a dark standard siren using the Dark Energy Survey galaxies and the LIGO/Virgo binary–black-hole merger GW170814”. In: *The Astrophysical Journal Letters* 876.1 (2019), p. L7.
- [74] B. P. Abbott, R. Abbott, T. D. Abbott, et al. “Model comparison from LIGO–Virgo data on GW170817’s binary components and consequences for the merger remnant”. In: *Classical and Quantum Gravity* 37.4 (2020), p. 45006.

- [75] R. X. Adhikari, O. Aguiar, K. Arai, et al. “A Cryogenic Silicon Interferometer for Gravitational-wave Detection”. In: *arXiv preprint arXiv:2001.11173* (2020). arXiv: [2001.11173](https://arxiv.org/abs/2001.11173).

Acknowledgments

I was lucky to work under the supervision of Roman Schnabel, whose continuous support and encouragement made my doctorate time so enjoyable and productive. He introduced me to an exciting world of correlated states of light, which never cease to amaze me and continue to open their new sides. I learned many things from Roman, but most notably the skill of seeing a physical picture behind the technical details and numbers. It is still a long way for me to master this skill, but now I see clearly see the road ahead. Thank you Roman for all the guidance you gave me over these years, it has been an exciting journey.

I thank Farid Khalili for showing me how to think outside the box and see the physics behind equations. His support made it possible for me to move to Germany and pursue my scientific goals by doing a PhD there. Our discussions over these years have been a great inspiration for my work. I also thank Stefan Danilishin, whose comments have always been so precise and deep. The works by Stefan and Farid have been my main guidance in the world of equations.

I'm really grateful to Yanbei Chen, Haixing Miao and Yiqiu Ma for many insightful and interesting discussions we had over the years, without which this thesis wouldn't be possible. I also thank all the members of the MQM discussion group, our discussions have been a great source of inspiration and excitement for me.

The Optoboy: Sacha, Paolo & Ramon, you made the beginning of my PhD the greatest experience! Even at difficult times, you had been the best colleagues and friends. Our time together will always be the warmest memories. Sacha, I owe you a debt of my deepest gratitude for all your support, which I doubt I will ever be able to pay you back. Paolo, when building electronics, I still use all the emotional self-support you taught me (but really, you're the best!). Ramon, I've never had as much fun working in the lab as when you were there.

I thank my colleagues for making my time with you so comfortable and enjoyable, both at work and outside it. Steini, I have always admired your expertise and understanding of the inner working of the experiments, and electronics in particular. This has been a great inspiration for me. Jan, Axel, Christoph, Daniela, Lisa, you taught me so much about doing experiments! Thank you for all your patience with my weird questions and for being there when I needed help. Jascha & Pascal, you always make my day better, managing to lift my spirit even in difficult times. I also thank all my colleagues and friends for their encouragement, shared knowledge and the interesting time we spent together.

I'm most grateful to my wife Lina, for all the unconditional support and acceptance over these years. Thank you for traveling to another country with me, for me to pursue my dream of becoming a scientist. I would never be able to go through this journey without you. You made everything for this thesis to become possible. That is unlike my two kids, Arthur and Felix, who made everything for the thesis to not become possible, but instead brought so much happiness into my life. I could've done with a bit more sleep, but the joy you gave me every day was so worth it. Arthur, all my best ideas came to me when I was rocking you back to sleep in the middle of the night. In some way, you were really instrumental to this work.

Мама и папа, огромное вам спасибо за вашу поддержку, понимание и помощь. Вы помогали развивать мое любопытство и любовь к науке с самых ранних лет и вложили столько сил в мое образование. Эта диссертация была бы совершенно невозможна без вас. Катюша, твоя эмоциональная поддержка всегда помогала мне в сложные минуты! Дядя Сережа, спасибо, что прививал любовь к электронике с ранних лет, и я, наконец, могу применять ее на практике.

Membership and funding

The work in this thesis was performed as the part of a scientific research program in the LIGO Scientific Collaboration. The work was funded by the Deutsche Forschungsgemeinschaft (DFG, German Research Foundation, SCHN 757/6-1), by the European REsearch Council (ERC) project "MassQ" (Grant No. 339897) and by the Marie Curie Initial Training Network cQOM.

Mikhail Korobko | Curriculum vitæ

Luruper Chaussee 149, Hamburg – 22761, Germany

☎ +49 40 89985103 • ✉ mkorobko@physnet.uni-hamburg.de

Personal Information

Name: Mikhail Korobko

Born: June 18, 1990, Krasnogorsk, Moscow Region, USSR

Current employment: Institute for Laser Physics, University of Hamburg, Hamburg, Germany

Education

University of Hamburg, Insitute for Laser Physics **2014–current**
Topic: quantum optomechanics, quantum optics and gravitational wave detection *PhD*

Address: Luruper Chaussee, 149, Geb. 69, 22761 Hamburg, Germany

Phone: +494089985103

M.V.Lomonosov Moscow State University, Faculty of Physics **2007–2013**
*Major: physics, **summa cum laude**, GPA: 3.9/4.0* *Specialist Degree*

Title of the thesis: "*Adaptive quantum measurements for gravitational-wave detectors*"

Address: Leninskie Gory 1-2, Moscow 119991, GSP-1, Russia

Phone: +7(495)939-16-82

California Institute of Technology **July – August 2013**
LIGO SURF 2013 Research Fellow *Research Fellow*

Address: 1200 E.California Blvd. 250-862 Pasadena, CA 91125

Web: http://www.ligo.caltech.edu/LIGO_web/students/SURF/

California Institute of Technology **June – August 2012**
LIGO SURF 2012 Research Fellow *Research Fellow*

Address: 1200 E.California Blvd. 250-862 Pasadena, CA 91125

Web: http://www.ligo.caltech.edu/LIGO_web/students/SURF/

Moscow High School #1199 **2002–2007**
Moscow, Russia

Krasnogorsk Lyceum #4 **2000–2002**
Krasnogorsk, Moscow region, Russia

Krasnogorsk Gymnasium #2 **1997–2000**
Krasnogorsk, Moscow region, Russia

Employment history

University of Hamburg **Researcher**
Institute of Laser Physics *June 2016–Present*

University of Hamburg **EU Researcher**
Institute of Laser Physics *December 2014–May 2016*

University of Hamburg **Researcher**
Institute of Laser Physics *September 2014–November 2014*

Awards

Personal

- Gold medal for special achievements in studies, Lomonosov Moscow State University (2014)
- Caltech Summer Undergraduate Research Fellowship (2012, 2013)
- Special Honours Russian Government stipend (2011,2012,2013)

As a part of LIGO Scientific Collaboration

- 2016 Special Breakthrough Prize in Fundamental Physics for the observation of gravitational waves, opening new horizons in astronomy and physics.
- 2016 Gruber Cosmology Prize
- 2016 National Space Club Distinguished Science Award
- 2017 Bruno Rossi Prize
- 2017 Royal Astronomy Society Group Achievement Award
- 2017 Princess of Asturias Award for Technical and Scientific Research
- 2017 Einstein Medal

Professional membership

- LIGO Scientific Collaboration (LSC), 2012–current
- LSC Academic Advisory Council (PhD representative, 2019–current)
- LSC Quantum Noise Working group
- LSC Advanced Interferometer Configuration working group
- LSC GEO 600 interferometer group
- Center in Hamburg for astro-,mathematical and particle physics (CHAMPP)

Languages

Russian: Native speaker

English: Proficient (C2)

German: Basic (A2)